Ice Giant Stratospheres from the Spitzer Space Telescope's Infrared Spectrometer

Naomi Rowe-Gurney MPhys
School of Physics and Astronomy
University of Leicester

A thesis submitted for the degree of
Doctor of Philosophy

August 2021

Abstract

The ice giants are the least explored planets in the Solar System. Many questions regarding their entire planetary systems and their role in shaping the solar system remain unanswered. NASA's Spitzer Infrared Spectrometer (IRS) acquired mid-infrared ($5 - 37$ μm) disc-averaged spectra of Uranus and Neptune multiple times between 2004 and 2007. Analysing all the sets of data with multiple separate longitudes gives us a unique opportunity to compare the longitudinal variability in the thermal emission of the two planets for the first time. At Uranus, there was a considerable variation in stratospheric emission detected for multiple epochs. A variation is not present at Neptune for the majority of the observed epochs.

The observations of Uranus in 2007 and Neptune in 2005 were used to develop a consistent retrieval framework for ice giant middle atmospheres. Building on the forward-modelling analysis of the global average study of Uranus by Orton et al. (2014), and conducting novel analysis on the Neptune data, we present full optimal estimation inversions (using NEMESIS) of the spectra of both planets. At Uranus, we perform spectral inversions for each longitude to distinguish between thermal and compositional variability, showing that longitudinal variations in stratospheric temperature are the cause of Uranus' rotational variability. At Neptune, we constrain the temperature profile and the abundances of the stratospheric hydrocarbons, including the first retrieval of methyl (CH_3), and a statistical study of the methane D/H ratio.

This disc-averaged thermal and chemical structure from Spitzer will likely be our best characterisation of ice giant thermal structure until the James Webb Space Telescope acquires spatially-resolved mid-infrared spectroscopy in 2022. We present the first stages of modelling the JWST observations of both planets and discuss the advancements that the observatory's guaranteed time observations will give with respect to Spitzer.

Acknowledgements

I am grateful to be supported by a European Research Council Consolidator Grant (under the European Union's Horizon 2020 research and innovation programme, grant agreement No 723890) at the University of Leicester (through Leigh N. Fletcher). This work is based, in part, on observations made with the Spitzer Space Telescope, which is operated by the Jet Propulsion Laboratory, California Institute of Technology under a contract with NASA. This research used the ALICE High Performance Computing Facility at the University of Leicester. We used some images from the W. M. Keck Observatory telescopes on Maunakea in Hawaii and recognize the significant cultural role of Maunakea within the indigenous Hawaiian community, and appreciate the opportunity to use data gained from observations from this revered site.

Dedication

I should start at the beginning. To my Mama, for giving me life and for giving me love and support since I can remember. Along with my sister Lyssa and aunties Deborah and Judy, I have always had strong Black women to look up to and show me that anything is possible. To my grandparents, for always asking how my thesis is going and being proud of me no matter what.

To my supervisor Leigh, thank you for giving me this opportunity and for having my back, even through unprecedented times. To all of team NEMESIS across the globe for making me feel welcome in this world.

To all my friends and office mates. Everyone on the list below supported me and showed me love, especially Harneet. How lucky we were to find each other, I wouldn't have been able to do this without you. To Onya, for giving me an outlet and keeping me sane.

To my wife, Lydia. I can't put into words how much you have helped me through this process. It was because of your encouragement that I became a teacher, which drove me to do a PhD in the first place. For the endless cups of tea and encouragement hugs and speeches. Marrying you was the best decision I ever made. To my puppy Pungyoh, who spent a lot of nights sitting at my side while I wrote and gave me cuddles at just the right times.

And finally, to all the white men who doubted me and told me I wasn't good enough at each and every stage of my life. Working to complete this thesis through a pandemic and a civil rights movement has been one of the hardest things I've ever done and so I ultimately dedicate this to me, as an act of self-love.

Declaration

I, Naomi Rowe-Gurney, hereby declare that the work presented in this thesis is my own. Information taken from other sources and material which is reproduced has been suitably referenced.

Contents

List of Figures

List of Tables

Glossary of Acronyms

BCD – Basic calibrated data
CIA – Collision-induced absorption
DDT – Directors discretionary time
FIR – Far-infrared
GDS – Great Dark Spot
GTO - Guaranteed time observation
HST – Hubble Space Telescope
IRIS - Infrared Interferometer Spectrometer (Voyager-2)
IRS – Infrared Spectrometer (Spitzer)
IRTF – NASA Infrared Telescope Facility
ISO - Infrared Space Observatory
JWST – James Webb Space Telescope
LH – Long-high module
LL – Long-low module
LTE – Local thermodynamic equilibrium
MIR – Mid-infrared
MIRI – Mid-Infrared Instrument (Webb)
NEMESIS – Non-Linear Optimal Estimator for Multivariate Spectral Analysis
NIR – Near-infrared
PBCD – Post-basic calibrated data
PSF - Point spread function
RTE – Radiative transfer equation
SH – Short-high module
SHA – Spitzer Heritage Archive
SL – Short-low module
SPICE – Spitzer IRS Custom Extraction
SSC – Spitzer Science Centre
SST – Spitzer Space Telescope
STIS – Space Telescope Imaging Spectrograph (Hubble)
UVS - Ultraviolet Spectrograph (Voyager-2)
VLT - Very Large Telescope
VMR - Volume mixing ratio (approx. equivalent to mole fraction)
WFC3 – Wide Field Camera 3 (Hubble)

Chapter 1

Introduction

1.1 Overview

The ice giants are the least explored planets in the solar system. We have only visited each planet once with the Voyager-2 flybys in the late 1980s (Smith et al. 1986, 1989, Fig. 1.1) and all other observations have happened remotely. Due to their distant orbits they prove to be the hardest to investigate and even the largest telescopes on Earth struggle to provide adequate spatial resolution. Their distance also makes them extremely cold and therefore very difficult to observe with mid-infrared (MIR) spectroscopy because the emitted spectrum has such low power. As a result, many major questions regarding their entire planetary systems and their role in shaping the solar system remain unanswered.

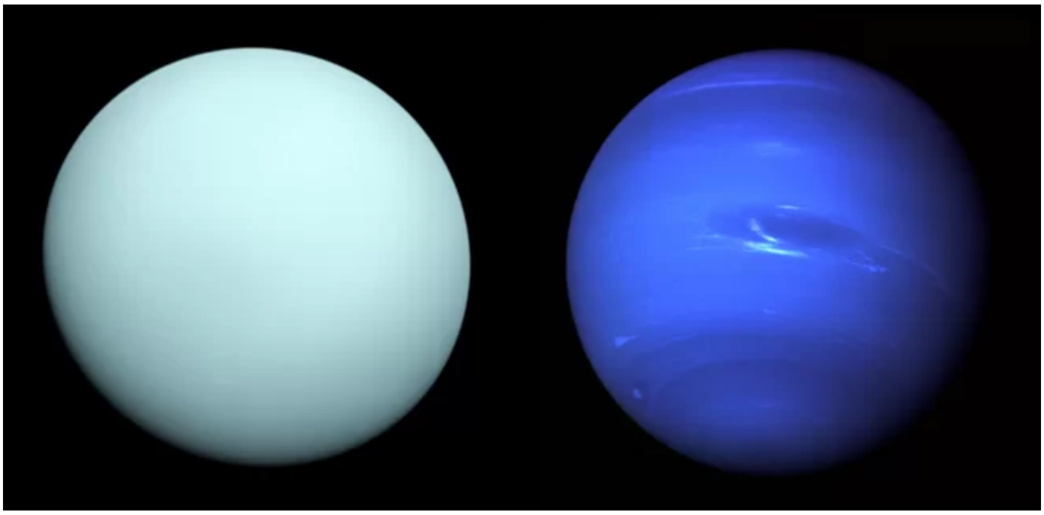

Figure 1.1: Images of Uranus and Neptune that were obtained from Voyager-2 during its flyby in 1986 and 1989 respectively. Image credit NASA/JPL-Caltech (Smith et al., 1986, 1989).

Uranus and Neptune represent a unique class of planet. The ice giants are much smaller than their gas giant cousins Jupiter and Saturn though they are a lot denser due to the higher fraction of heavy elements within. They also have slower rotations and cooler temperatures. The term 'ice giants' reflects the consensus that, by mass, they are thought to be predominantly made of water and other elements that are capable of forming ices, such as methane and ammonia. Those species were likely in an icy state during the early stages of solar system formation, but today virtually all of the water in an ice giant is thought to be in fluid phases (Hofstadter et al. 2019, Fig. 1.2). To demonstrate how little we know about these planets, it is not even known whether these heavier elements are even ice-dominated. Observed properties have been found to also fit with rock-dominated compositions Helled et al. (2020). In fact, it has been recently suggested that Neptune could be a 'Rock Giant' by Teanby et al. (2020) based on measured atmospheric abundances.

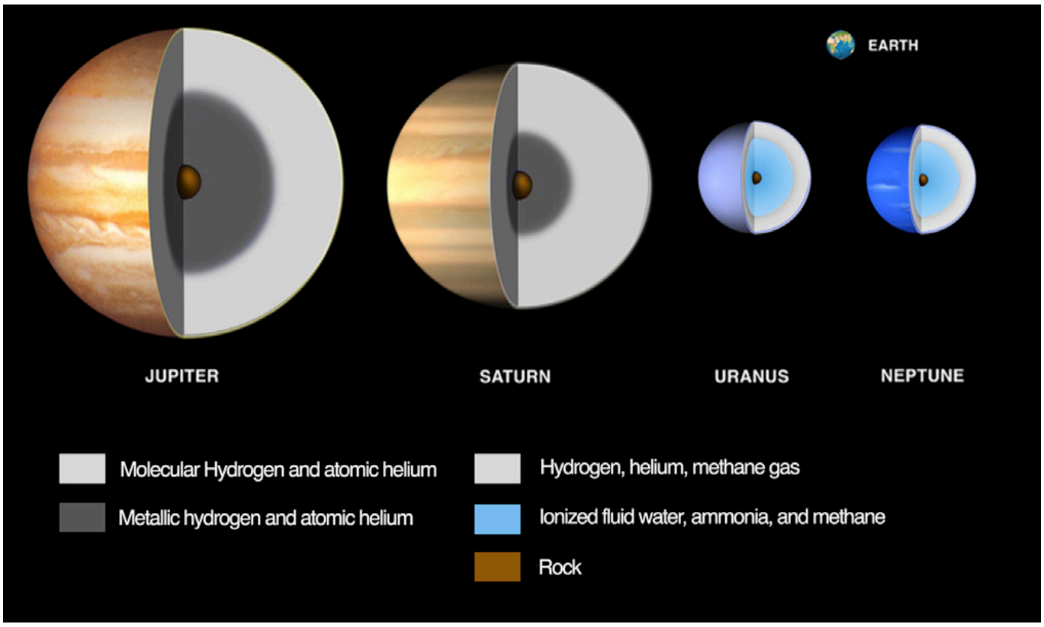

Figure 1.2: Illustration of compositional and structural differences among the giant planets and their relative sizes. Earth is shown for comparison. Jupiter and Saturn are primarily made of hydrogen and helium, the terrestrial planets are almost pure rock, while Uranus and Neptune are thought to be largely super-critical water (Hofstadter et al., 2019).

Though Uranus and Neptune are the same class of planet and exhibit many similarities, they show evidence of having remarkably different evolutionary paths from their shared origins. A major difference between the two planets is in their orbital obliquities. With its 98° rotational tilt from its orbital plane, Uranus is subject to an 84 year cycle of daylight and darkness. During our first and only close up encounter of Uranus in 1986 by Voyager-2 it was near its southern summer solstice. This means that its south pole and sparse rings were face on to us. The response of the atmosphere to these extremes were determined during the flyby (Flasar et al., 1987; Conrath et al., 1990), where it measured the north pole in the middle of its long winter darkness. This is the only time that the winter hemisphere has been observed (Orton et al., 2015). Another quarter of the way through its 84-year orbit, in 2007, it arrived at its northern spring equinox with its rings now edge-on. Every 42 years the equinox allows the northern and southern hemispheres to be viewed simultaneously. We took advantage of this in the dataset that will be a central part of this investigation, though this will be made clearer in Chapter 3.

Parameter	**(Unit)**	**Uranus**	**Neptune**
Mass	(Earth masses)	14.5	17.1
Radius	(Earth radii)	4.0	3.9
Mean radius	(km)	25559	24764
Oblateness	-	0.023	0.017
Rotation period	(hours)	17.24	16.11
Axial tilt	(degrees)	98	29
Solar distance	(AU)	19.2	30.1
Orbital period	(Earth years)	84.01	164.79
Solar constant	(Wm^{-2})	3.5-3.9	1.5
T_{eff}	(K)	59	59
Flux ratio $(T_{eff}/T_{eq})^4$	-	1.06	2.61
Atmospheric:			
T at 1 bar	(K)	79	70
Scale height	(km)	27.7	20
Hydrogen mole fraction	-	0.825	0.80
Helium mole fraction	-	0.152	0.19
Methane mole fraction	-	0.023	0.015

Table 1.1: Planetary and atmospheric parameters of Uranus and Neptune adapted from Hueso and Sánchez-Lavega (2019). T_{eff} is the effective temperature and T_{eq} is the equilibrium temperature (the theoretical temperature of the planet assuming no internal heat source). The flux ratio therefore represents the ratio between thermal emission and irradiation. The scale height is the increase in altitude for which the atmospheric pressure decreases by a factor of e.

The seasonal changes are very challenging to observe due to their extremely long orbits. We have only been able to resolve atmospheric features for about 1.5 Uranian seasons (each lasting 21 years). Neptune's 164-year orbit has meant that we are yet to see in detail even a complete 41-year season (Fletcher et al., 2020).

Uranus is considered the atypical ice giant when compared to Neptune because it is unique in our solar system for more than one reason. Another unique feature is its cold stratosphere. It is colder than Neptune's, even though Neptune's distance from the Sun is so much larger (Table 1.1). The amount of heat emitted by the planet is only around 1.06 times that received from the Sun, making it near equilibrium with solar insolation (Pearl et al., 1990; Pearl and Conrath, 1991). Neptune's flux ratio of 2.61 implies that it is still cooling.

As the farthest-known planet from the Sun, Neptune is considered to be typical for an ice giant. It has a 29° tilt that is similar to other planets in our solar system and it has a 'standard' heat flux that you could expect for the cooling of a planet with an adiabatic interior (Fortney et al., 2011). An adiabatic interior assumes that no heat is transferred to or from the surroundings and the only internal energy change is done by work. So, it is Uranus' heat flux value that is far lower than expected and indicates that it has either lost all its energy or that the energy is still captured inside. Investigations have shown that its interior may not be fully convective, and/or it contains compositional gradients (Vazan and Helled, 2020) or thermal boundary layers (Nettelmann et al., 2016) that hinder convection (Helled et al., 2020). A popular theory is that a large impact early on in Uranus' formation released its internal heat rapidly instead of the slow cooling being undergone by Neptune (Reinhardt et al., 2020). This impact also provides an explanation for the planet's extreme tilt.

The answers as to why Uranus and Neptune are so different are still unknown. This comes from the fact that we are still unclear on how an ice giant forms. Traditional core-accretion planetary-formation models have had difficulty getting the timing of the formation to match the data (Helled and Bodenheimer, 2014). Core accretion is where solid core formation is accompanied by slow gas accretion and then followed by more rapid gas accretion as it grows. In these models, a planet must form fast enough to ensure that gas is accreted onto the core but slow enough in order to remain small in mass and not become a gas giant like Jupiter and Saturn. This balance is difficult to achieve for Uranus and Neptune but clues to better understand how they form can come from the study of their atmospheres (Moses et al., 2020).

This introduction will detail the theory and history behind ice giant atmospheres. A brief history of the observations of both planets is given in Section 1.2. Here, we will also further explain the significance and value of infrared remote sensing for atmospheric science. Section 1.3 will go through what knowledge we have gained from these observations, from the atmosphere's thermal structures and compositions to their dynamics and smaller scale weather systems. This will provide the tools and information needed to understand the significance and impact of this study (Section 1.4) of arguably the most intriguing planets in our solar system.

1.2 Observing the Ice Giants

Uranus had been observed on many occasions before its recognition as a planet, but it was generally mistaken for a star or a comet (Wright, 1987). It was finally recognised and recorded as a planet in 1781. Neptune was the first planet to be discovered through mathematical prediction in 1846. It was actively searched for after astronomers had detected a series of irregularities in Uranus' orbit that could be explained by the gravity of another planet.

Due to their extreme distance from us, these worlds have still been relatively unexplored. Neptune is so distant and dim that it couldn't be viewed at all before the invention of the telescope. Molecular hydrogen was first identified through the hydrogen quadrupole lines on Uranus by Herzberg (1952). Other than this, most of the discoveries used in ice giant atmospheric science today were made after the flybys conducted by Voyager-2.

1.2.1 The Voyager-2 Encounters

To take advantage of the geometric arrangement of the outer planets in the late 1970s and 1980s, NASA's Voyager programme was designed. It allowed for a four-planet tour for a minimum of propellant and trip time. Voyager-2 was launched on August 20, 1977 and encountered Uranus on January 24, 1986. It came within 81,500 km of the cloud-tops and returned detailed photos and other data on the planet, its moons, magnetic field and rings in the midst of its southern summer solstice (Stone and Miner, 1986). Its closest approach to Neptune was on August 25, 1989, passing about 4,950 km above the north pole (Stone and Miner, 1989). Data were gathered over about three months centered on the encounter date (Sánchez-Lavega et al., 2019).

The fleeting flybys of Voyager-2 remain the only in-situ investigation of both planets; the famous images seen in Figure 1.1 still being the ones thought of today when picturing them. The flybys provided data on atmospheric chemistry, thermal structure and dynamics, which has helped constrain and therefore better understand the pre-Voyager data.

Radio-occultation measurements were conducted and provided many useful results. They helped to determine many variables including gas refractivity, number density, pressure, temperature and methane abundance in the troposphere and stratosphere. They also helped to constrain the zonal wind velocities and the rotation periods (Lindal et al., 1987).

Breakthroughs in ice giant mid-infrared science were once dominated by Voyager Infrared Interferometer Spectrometer (IRIS) data (e.g., Hanel et al., 1986; Flasar et al., 1987; Conrath et al., 1989; Pearl et al., 1990). The IRIS instrument aboard Voyager-2 had the capacity to provide infrared spectra between 4 and 55 μm. The measurements at Uranus between 25 and 50 μm were used to determine the vertical temperature structure between 60 - 900 mbar and the upper limit for the effective temperature was found to be 59.4 K (Hanel et al., 1986). Individual spectra were taken at Neptune between 31 and 50 μm as this was the only region with enough signal to overcome the noise. Averages of many spectra were used to achieve a large enough signal-to-noise to observe in the same bands as Uranus. By averaging a vast number (sometimes hundreds) of observations, spectra all the way out to the acetylene band at 13.8 μm and vertical temperature profiles between 30 and 1000 mbar were obtained at multiple latitudes (Conrath et al., 1989). Temperature maps of the planet were able to be made at two different levels, lower stratosphere and upper troposphere, giving the first glimpse at the planet's zonal mean temperature structure with warmer pole and equator and cooler mid-latitudes. The effective temperature of Neptune was estimated at 59.3 K (Conrath et al., 1989).

Data collected in the present day is still being compared to this relatively reliable Voyager data. For example, the IRIS experiment yielded atmospheric temperature distributions for the upper troposphere of Uranus which have been compared to ground-based data from Very Large Telescope (VLT) VISIR, Subaru Telescope COMICS, and the Long-Wavelength Spectrometer (LWS) on the Keck-1 Telescope (Orton et al., 2015). For Neptune, IRIS mapping of tropospheric temperatures has been re-analysed and compared to thermal emission from Keck/LWS, Gemini-N/MICHELLE, Gemini-S/TReCS and VLT/VISIR from multiple epochs (Fletcher et al., 2014).

1.2.2 Remote Sensing

Earth based observatories and space telescopes now provide the majority of the data used to investigate the ice giants via remote sensing (Mousis et al., 2018). Post-Voyager, in the 1990s and 2000s, most observations were made by the Hubble Space Telescope (HST) and large ground-based telescopes that are capable of resolving the small 2-4″ discs. Despite the planets' large distance from Earth, they have been observed in many different wavelength bands using many different instruments.

Each wavelength has a slightly different application in atmospheric remote sensing. The spectral regions can be split roughly into reflectance spectra (wavelengths shorter than around 4 μm) and thermal emission (wavelengths longer than around 4 μm). The reflectance bands consist of ultraviolet, visible and near-infrared. Thermal emission is visible in the MIR and the far-infrared (FIR), as well as in the much longer microwave and radio bands.

The MIR is where thermal emission is the most dominant. It contains the rotational-vibrational (ro-vibrational) emission and absorption features of gases that can then be used to measure temperature and therefore composition. Chapter 2 will go into detail about these processes.

Figure 1.3 shows the vertical sounding of the most popular wavelength bands for remote sensing of ice giant atmospheres along with some example images of Uranus in these bands. This is generalised to be relevant to both Uranus and Neptune. This clearly indicates the strength of mid-infrared remote sensing and why this investigation needs it to probe the stratosphere. Though much of this thesis will be talking about the mid-infrared wavelength bands from 5 - 40 μm, this section gives an opportunity to highlight why the MIR is so important by comparing it to the other wavelength bands.

Ultraviolet

UV (0.2 - 0.4 μm) is dominated by high energy scattering effects like Raman and Rayleigh scattering. In most of the UV, high-sensitivity observations generally must be made in space, either from Earth-orbiting or planet-encountering spacecraft. The Voyager-2 Ultraviolet Spectrograph (UVS), the HST Space Telescope Imaging Spectrograph (STIS) and some filters in the HST Wide Field Camera 3 (WFC3) are considered some of the most important for UV observations of the ice giants.

UV occultation observations by the UVS have characterized the temperature, energy deposition, and compositional profiles of these atmospheres above the 0.1-1 mbar level (Herbert and Sandel, 1999). The UVS also directly observed auroral emissions at Uranus through detection of excited H and H_2 emissions from the upper stratosphere (Broadfoot et al., 1986), giving an insight into atmospheric energy balance at the planet (Melin, 2020). These observations are consistent with more recent observations by HST (e.g. Lamy et al., 2012) that show emission in the form of discrete

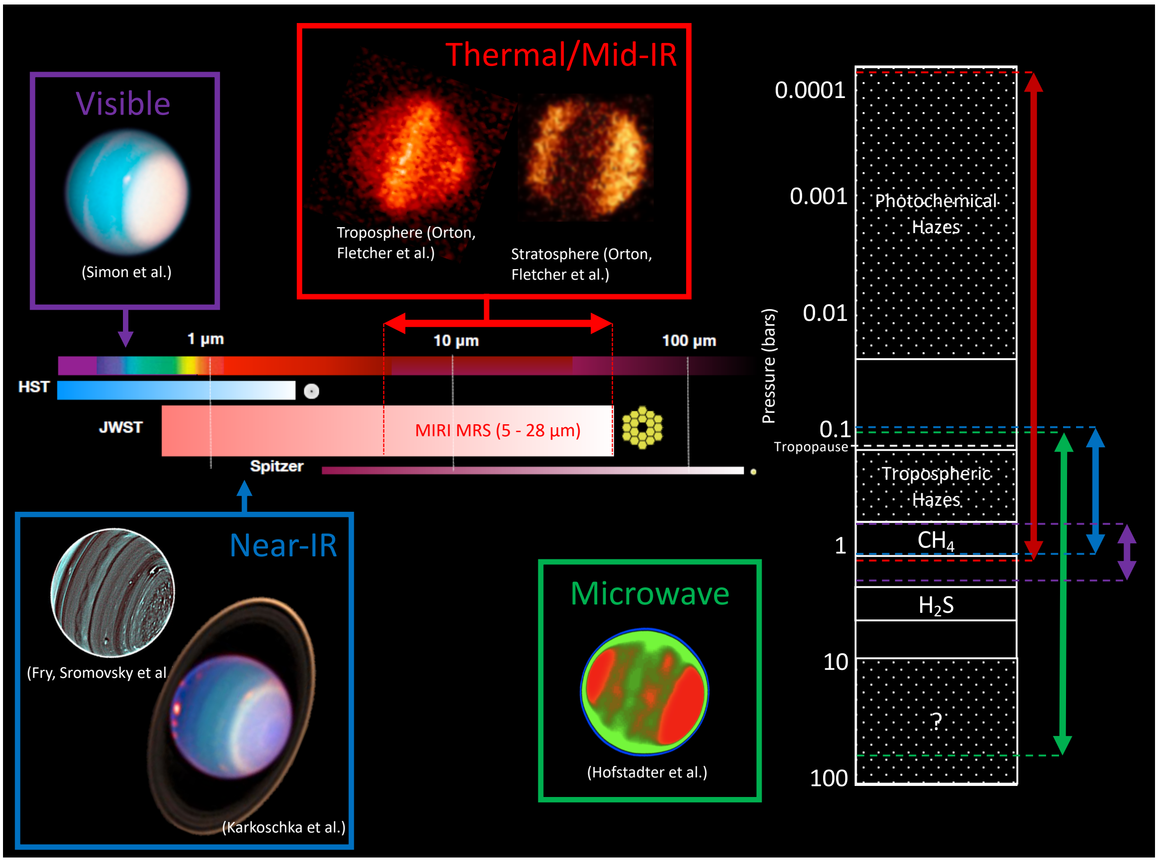

Figure 1.3: Atmospheric sounding of the stratosphere and upper-troposphere from different wavelength ranges at Uranus (applicable to Neptune) with example images from various instruments (ground- and space-based). The thermal infrared images are from two different filters of the VLT-VISIR instrument sensing two different depths: the 18.7 micron Q2 filter sensitive to the continuum emission of the troposphere and the 13.0 micron NeII_2 filter sensitive to stratospheric acetylene. Cloud layers adapted from Hueso and Sánchez-Lavega (2019).

faint spots. No auroral emission has ever been detected at Neptune (Broadfoot et al., 1989).

Visible and Near-Infrared

Visible (0.4 – 0.9 μm) and near-infrared (NIR) spectra (1 – 4 μm) contain features from reflected sunlight and hence are useful in sensing the upper atmosphere and the aerosols distributed within. They sound the cloud decks and surrounding areas of the tropopause (Fig. 1.3). Observations in the visible and near-infrared have tracked cloud features across both ice giants, constraining the zonal wind structures seen later in Figure 1.10. The winds have been measured from Voyager-2, HST, and Keck over multiple decades (Mousis et al., 2018).

The large storm system at Uranus in 2014 was observed in these wavelengths using the HST/WFC3 and compared to the VLT's SINFONI Integral Field Unit Spectrometer and the NASA Infrared Telescope Facility (IRTF) SpeX instrument (Irwin et al., 2017). It is not just the large storms that can be tracked; up to 28 separate cloud features were tracked up to high latitudes of 74°N. Again, this used space-based (HST) combined with ground-based (Keck telescope) observations to determine atmospheric motions and define changes in atmospheric band structure (Sromovsky et al., 2009). Discrete cloud features being observed at mid-latitudes ties into the upwelling theory shown later in Figure 1.11.

Neptune has exhibited pronounced atmospheric activity throughout the last 30 years at both visible and near-infrared wavelengths (Hammel et al., 2007; Hueso et al., 2017). This has been attributed to the variability of CH_4-condensate cloud brightnesses and distributions (Hammel and Lockwood, 2007). HST visible wavelength imaging revealed the first observation of the formation of a dark vortex on Neptune (Simon et al., 2019). This new Great Dark Spot (GDS) feature, discovered in 2018, was nearly identical in shape and size to the famous Voyager-era GDS. Dark spots can only be definitively identified in visible wavelengths because of their strong absorption at blue-wavelengths. Near-infrared is optimised for viewing the bright companion clouds of features like the GDS (Hammel et al., 2009).

Mid-Infrared

Beyond the solar spectrum of the NIR, thermal emission now dominates. The MIR or thermal-infrared (5 - 40 μm) is an invaluable tool in investigating atmospheric temperatures, composition and dynamics. These wavelengths at the ice giants are dominated by the collision induced opacity of H_2 and He along with the collection of hydrocarbons that result from the photolysis of methane (see Section 1.3 and Chapter 2). MIR spectroscopy and imaging provide the only methods of deducing atmospheric thermal structure and composition above the cloud tops (Fletcher et al., 2014).

By using instruments like Spitzer, it is possible to measure relatively continuous spectra over a broad wavelength range free of telluric contamination, despite the disadvantage of distance and low temperature that the ice giants have. This thesis utilises data in the MIR from the Spitzer Space Telescope Infrared Spectrometer (IRS) between 5 and 37 μm that sounds the stratosphere and upper troposphere from around one nanobar to around two bars of pressure (Fig. 1.3). These altitudes contain the complex hydrocarbon hazes that dominate the stratospheric processes we are looking to investigate.

At present, observations are mostly obtained using ground-based telescope facilities, but they have limitations in the mid-infrared due to telluric absorption at critical wavelengths (see Fig. 1.4). Most of the N-band (7-14 μm) spectrum can be viewed through the largest atmospheric window at thermal wavelengths visible in the figure and contains the spectral features of methane, ethane and also acetylene. Some examples are Orton et al. (1992) who used IRTF to view these species at Neptune, later followed by Fletcher et al. (2014) using multiple ground-based MIR instruments. The Q-band (17-25 μm) allows the viewing of the hydrogen-helium continuum through windows such as the 18.7 μm window used to view Uranus with the Q2 filter on the VLT/VISIR (Roman et al., 2020) and the multiple windows out at 20-25 μm observable with Subaru/COMICS (Orton et al., 2015).

An important feature of the giant planets that can provide key atmospheric information is the para-H_2 fraction, also called the ortho-para ratio and is explained further in Chapter 2 and below when we talk about temperatures. The para-H_2 fraction is observable at around 25 μm at Uranus and corresponds to the ratio at around 200 mbar (Orton et al., 2015). This is one of the wavelength bands that is visible from ground-based observations. These values were compared to the Voyager IRIS para-H_2 fractions which were also obtained using observations in the MIR (Conrath et al., 1998).

Larger and larger diameter telescope mirrors combined with new and advanced instruments are responsible for many scientific advances but it is unsurprising that the Spitzer Space Telescope, especially the IRS instrument, has provided a significant leap in mid-infrared observation capabilities with its sensitivity being two orders of magnitude greater than previous missions (Houck et al., 2004).

Far-infrared, Radio and Microwave

Beyond the MIR, the FIR, radio and microwave observations of the ice giants investigate the deep troposphere down to pressures of tens of bars (Fig. 1.3). The FIR (40 – 500 μm) is dominated by the hydrogen and helium collision induced continuum that is also present in some of the MIR. Microwave to radio ranges (1 mm and larger) used to be less commonly used for remote sensing due to planetary discs being difficult to resolve at longer wavelengths, but they were used instead to search for and track seasonal changes below the visible clouds. Using modern instruments and techniques, it is now possible to resolve the discs of both planets and conduct investigations on tropospheric composition and temperatures (Tollefson et al., 2019; Molter et al., 2020).

Radio data probe much deeper than the visible and NIR (Klein and Hofstadter, 2006). Temporal variations have been observed at these ranges at Uranus, but these findings are not conclusive because long wavelengths are challenging to work with in remote sensing. Despite these difficulties, radio observations are especially effective at the ice giants because their upper tropospheres are depleted in ammonia, making them much less opaque than at Jupiter and Saturn (Hofstadter and Butler, 2003).

Disc-averaged microwave measurements of Uranus have been made since 1965 and show that the planet has brightened between the 1960s and mid-1970s, peaking in the late 1980s (Klein and Hofstadter, 2006). The first radio telescope to clearly map Uranus was the Very Large Array (VLA) and was used throughout the 1980s and 90s to do a plethora of investigations (Hofstadter and Butler, 2003). Spatial maps can be taken at these longer wavelengths like the most recent of Uranus using both the Atacama Large Millimeter/submillimeter Array (ALMA) and the VLA by Molter et al. (2020).

The Infrared Space Observatory (ISO) has observed Neptune in the FIR between 46 and 185 μm and combined these results with MIR observations to determine a disk-averaged temperature profile and derive several physical quantities (Burgdorf et al., 2003). Neptune's south pole is considerably enhanced in both MIR and radio wavelengths (de Pater et al., 2014). This is interpreted as being due to subsidence into the deep troposphere all the way from the stratosphere. The brightness at radio wavelengths reveals that the subsiding air is very dry, showing how it can tell us something different from the MIR, which would be interpreted as adiabatic heating of the subsiding air by compression. Latitudinal variations in the microwave have been viewed from Earth by Tollefson et al. (2019) in spatially resolved maps using instruments like ALMA.

Space Telescopes

Only space-based telescopes can measure species such as some of the complex hydrocarbons found in ice giant atmospheres because the ro-vibration bands, situated in the infrared, are blocked by the Earth's atmosphere (Burgdorf et al. 2006; Norwood et al. 2016 and see Figure 1.4). This lack of spectral windows, especially in the MIR, makes calibration very difficult and therefore reduces the practicality of ground-based instruments in these investigations. This is where facilities like NASA's Hubble Space Telescope (HST) and Spitzer Space Telescope become instrumental in our understanding of the giant planet atmospheres.

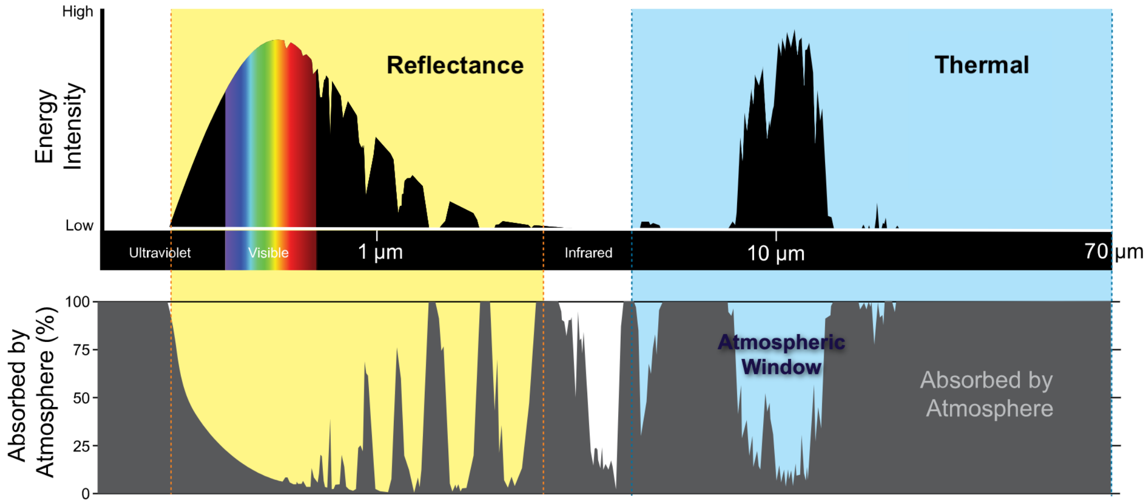

Figure 1.4: Absorption spectra caused by telluric absorption for a vertical column from the surface to space. Rough areas show where reflectance spectra and thermal emission are demarcated. Adapted from an image from the Nation Weather Service, National Oceanic and Atmospheric Administration (NOAA) - weather.gov

Spatially resolved remote sensing in reflected sunlight at both Uranus and Neptune have relied heavily on the HST (Karkoschka and Tomasko, 2009; Karkoschka, 2011; Sromovsky et al., 2014). Achieving adequate spatial resolution is more challenging at longer MIR wavelengths. Observations from the Infrared Space Observatory (ISO, Encrenaz 2002), Herschel Space Telescope (Lellouch et al., 2010) and AKARI Space Telescope (Fletcher et al., 2010) along with the Spitzer Space Telescope all captured data that were disc-integrated and without spatial resolution. Even though they lack the spatial resolution, the absence of telluric contamination makes them all perfect for the study of the ice giants, especially Spitzer (Trilling et al., 2020).

The Spitzer Space Telescope and its Infrared Spectrometer (IRS) observe in the mid-infrared between around 5 and 35 μm (Werner et al., 2004; Houck et al., 2004). The IRS has observed both ice giants multiple times between 2004 and 2007 and the data have been used for multiple studies. The first observations of Uranus (Burgdorf et al., 2006) and Neptune (Meadows et al., 2008) were used in groundbreaking studies that identified new hydrocarbons and constrained others. Alongside previously determined abundances of methane and acetylene (Orton et al., 1987; Encrenaz et al., 1998, etc.), Burgdorf et al. (2006) obtained the first clear detections at Uranus of ethane, propyne, diacetylene and carbon dioxide in this wavelength range using data from the Spitzer/IRS acquired in 2004. Orton et al. (2014a,b) have analysed the 2007 data of Uranus in a detailed study of the abundance and temperature profiles.

The data from 2007 are not only the most optimised observation campaign of Uranus from the IRS but also perfectly timed to coincide with the equinox. The target was observed several times during a rotation period, meaning that we can explore the longitudinal contrasts in emission. The separate longitude observations make the most of the equinox because, with Uranus' unique 98° tilt, both northern and southern hemispheres are only discernible around this time. Chapter 4 and 5 follow on from their study using new and updated data reductions (Chapter 3), updated photochemical models, and a more generalised optimal estimation retrieval technique. Chapter 4 extends Orton et al.'s study of Uranus to discover evidence of rotational variability in 2007, and compares this to all other Uranus observations 2004-2007, and also to Neptune. Chapter 5 then performs the first full spectral inversion of the Uranus data, a significant enhancement on the approach used by Orton. Chapter 6 does the same for the completely unpublished Neptune data. A more thorough explanation of the previous findings from the IRS in these studies is discussed in Chapter 3.

The James Webb Space Telescope (JWST) will be launched in December of 2021 and has a mirror diameter of 6.5 m along with the capability to observe from 0.6 to 28 μm. This combination of wavelength range and sensitivity will provide groundbreaking science when it observes the ice giants during their viewing windows in 2022. We will discuss the advances that JWST will make and what that means for both Uranus and Neptune in Chapter 7.

1.3 Ice Giant Atmospheres

Even though Uranus and Neptune have hardly been explored, their atmospheres have become synonymous with dynamic and beautiful. Neptune is known for its vibrant blue colour, fast winds and dynamic weather. It has pronounced features, including bright clouds and dark spots like those observed at Jupiter. Uranus is known for its almost featureless blue-green skies but, as it has slowly changed seasons, more and more discrete cloud features have been observed (Taylor, 2010).

The composition of the atmospheres of the ice giants is similar to the gas giants, but where Jupiter and Saturn are composed primarily of hydrogen and helium, the total mass of heavier elements at Uranus and Neptune is comparable to or greater than these lighter elements (Fig. 1.2). By mass, they consist of around 10-20% hydrogen and helium and 80-90% heavier elements (Podolak et al., 2019). The relative proportions of rocky materials and more volatile elements that form ices are unclear (Helled and Fortney, 2020). Ice refers to any condensable compound and not just water ice. The planets' distinctive blueish hues are thought to be due, in part, to the gaseous form of one of those ices, methane (Irwin, 2009). Methane possesses prominent absorption bands in the visible and near-infrared which absorbs red light from the Sun but reflects the blue light back into space.

The atmospheres can be divided into three main regions: the troposphere, the stratosphere and the thermosphere (Fig. 1.5). The lowest region, the troposphere, is where convection occurs and temperatures are hot at depth and decrease with increasing altitude. The stratosphere is above the tropopause temperature minimum and is where radiative processes dominate and temperature increases or is constant with increasing altitude. The bulk compositions of both planets are split into the stratospheric and tropospheric species and are displayed in Table 1.2.

The thermosphere is the uppermost region of the atmosphere where temperatures increase more sharply as heat is conducted downward from a hot exosphere at high altitudes. For completeness, in the altitudes above Figure 1.5, the exobase is the atmospheric level above which the integrated column density produces just one mean free collision path for an atom. This means that the gas above this is essentially collisionless and is referred to as the exosphere (Lunine, 1993).

The data from Spitzer used in this investigation are sensitive to what we will refer to as the middle atmosphere. This region comprises the stratosphere and upper troposphere where methane and its photolysis products dominate the composition and temperature structure (Moses et al., 2018). The complex hydrocarbons produced in solar-driven reactions in the stratosphere are the main trace gases present in this region. These species are observable at mid-infrared wavelengths sensitive to emission from altitudes between approximately one nanobar and two bars of pressure (Orton et al., 2014a).

We have split up this section into temperatures, chemistry, clouds, and dynamics even though they are all very much interlinked. This inter-connectivity is addressed throughout.

1.3.1 Temperatures

The vertical temperature structure is important as a fundamental constraint on both the dynamics and chemistry of any planetary atmosphere. The temperatures in the stratosphere and upper troposphere vary between around 55 K and 300 K (Fig. 1.5) with the stratospheric temperatures at Uranus being up to around 40 K cooler than at Neptune (Irwin, 2009, p. 77). Voyager-2 radio occultation results have provided these temperature profiles (Lindal et al., 1987; Lindal, 1992), however, these results cannot

Species		Uranus	Neptune
Troposphere:			
Helium	He	15.2%	14.9%
Methane[1]	CH_4	1.4-4%	2-5%
Ammonia[2]	NH_3	30-90 ppm	40-200 ppm
Water[3]	H_2O	<5%	27%
Phosphine	PH_3	<2 ppm	<1 ppb at 0.7 bar
Hydrogen sulfide[4]	H_2S	0.4–0.8 ppm	1–3 ppm
Stratosphere:			
Methane	CH_4	16 ppm at 50 mbar	0.115% at 5 mbar
Acetylene	C_2H_2	0.25 ppm at 0.2 mbar	0.033 ppm at 0.5 mbar
Ethylene	C_2H_4	$<2 \times 10^{-14}$ at 10 mbar	0.8 ppb at 0.2 mbar
Ethane	C_2H_6	0.13 ppm at 0.2 mbar	0.85 ppm at 0.3 mbar
Methylacetylene/propyne	C_3H_4	0.36 ppb at 0.4 mbar	0.12 ppb at 0.1 mbar
Diacetylene	C_4H_2	0.13 ppb at 0.4 mbar	0.003 ppb at 0.1 mbar
Carbon dioxide[5]	CO_2	0.08 ppb at 0.14 mbar	0.78 ppm at 0.1 mbar
Carbon monoxide[5]	CO	6 ppb at 0.5 mbar	1.1 ppm at 0.1 mbar
Water[5]	H_2O	3.8 ppb at 0.03 mbar	2.5 ppm at 0.16 mbar

Table 1.2: Composition by volume in the atmospheres of Uranus and Neptune. [1]Latitude dependent. [2]Inferred from microwave photometry. [3]Indirect determination. [4]At the hydrogen sulphide cloud top. [5]From external source. For references of each source see original tables in Moses et al. (2020).

be interpreted with 100% reliability due our lack of understanding of both planets' bulk compositions, chemistry and dynamics (Mousis et al., 2018), and differences have been noted from recent models using data from remote observations (Orton et al., 2014a; Fletcher et al., 2014). The findings of Orton et al. (2014a) for Uranus will be detailed in chapter 3. Discussion of the temperature profile of Neptune will be detailed in chapter 6.

An important parameter in defining a vertical temperature profile is the lapse rate of the atmosphere, which is the rate of change of temperature with height. This is a free parameter which is dependant on the many factors that can affect convection (e.g. abundances, chemical processes). The adiabatic lapse rate is the rate at which the temperature of an air parcel changes in response to the compression or expansion associated with an altitude change, under the assumption that no heat exchange occurs between the given air parcel and its surroundings. This is differentiated into dry adiabatic lapse rate (DALR) and saturated adiabatic lapse rate (SALR). The DALR is a useful starting point for many models and depends only on the gravitational acceleration acting on the air parcel and the specific heat capacity of the parcel, making it easily estimated. The SALR, however, depends on the amount of condensable

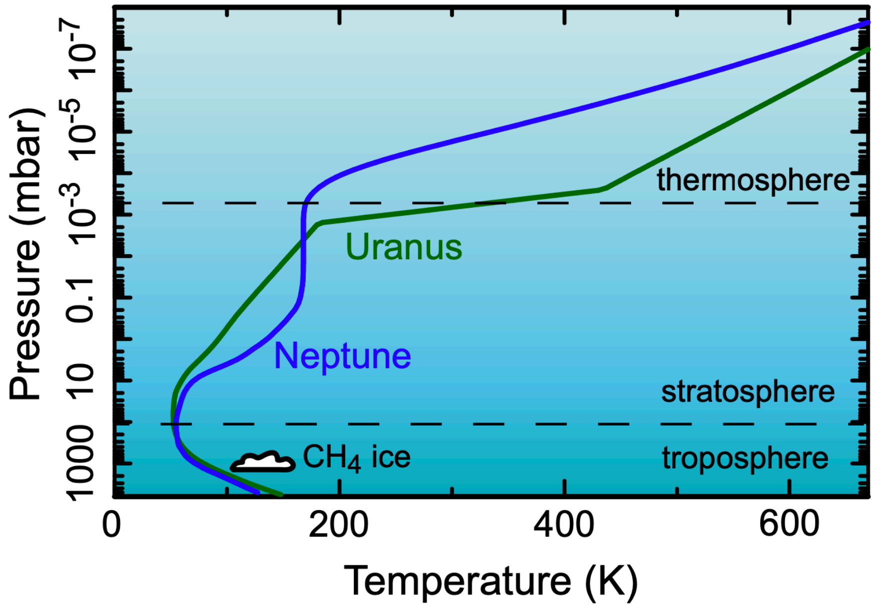

Figure 1.5: Global-average temperature-pressure profile of the atmosphere of Uranus and Neptune. Modified from Moses et al. (2020).

species in the parcel and can be highly variable. Condensation processes release latent heat causing the parcel to rise upward, transporting heat upwards and therefore decreasing the lapse rate. Spitzer spectra provide the vertical temperature profile, and hence the lapse rate, allowing us to evaluate the importance of condensation processes, convection, and radiative heating on the vertical temperature structure.

Tropospheric temperatures, derived from the 17 - 50 micron region of the spectrum, are governed by the collision-induced continuum of hydrogen and helium (Conrath et al., 1998). This collision-induced absorption (CIA) provides a thermometer to measure the thermal structure of the upper tropospheres of the ice giants (Fletcher et al., 2018). This will be explained further in Chapter 2.

The para-H_2 fraction is dependant on temperature and over time it will assume the thermodynamic equilibrium value of the lower temperatures but only after an equilibration time. This equilibration is also thought to modify the lapse rate (Smith and Gierasch, 1995; Baines et al., 1995). The degree of disequilibrium depends on the dynamic transport time and therefore relates directly to the dynamics of the atmosphere, as long as the equilibration time can be accurately estimated (Conrath et al., 1998). At deeper atmospheric levels where temperatures exceed 300 K, the ortho-para ratio is expected to be around 3:1. This is the high temperature limit and is considered the normal value. Since transitions between the states are strongly forbidden, an air parcel will retain its initial ratio as it moves from hotter depths to cooler shallows. Figure 1.6 shows an example of the relationship between temperature and para-H_2 fraction at Neptune. Super-equilibrium conditions are present at the equator and high-southern latitudes, whereas sub-equilibrium conditions are seen at mid-latitudes in both hemispheres, coincident with the coldest atmospheric temperatures (Fletcher et al., 2014).

Radiation is the dominant mechanism for heat transport in the stratosphere and above (Conrath et al., 1990). The temperature profile at the pressure levels of the stratosphere and upper troposphere are determined by radiative equilibrium. Efficiency is determined by the abundance of radiatively active molecules, especially methane. The increase of temperature with height in the stratosphere is caused by radiative heating from the absorption of NIR sunlight and solar-UV by methane gas absorption bands, and also the absorption of sunlight by aerosols. To achieve equilibrium or balance, these sources must be transported or radiated away. The cooling in the stratosphere at the ice giants is mainly due to the radiative cooling from the thermal emission of the collision-induced continuum and hydrocarbons (products of UV photolysis of methane) like acetylene and ethane (Irwin, 2009). The amount of methane that is lofted into the stratosphere from its condensation level, at around 1-2 bar, directly influences the vertical temperature structure through these processes and chemical reactions that we will discuss in the following Chemistry subsection. Because these chemical products absorb solar radiation, the abundance of species and the temperatures of the altitudes they occupy are degenerate, and are a main source of uncertainty in the radiative transfer and retrieval models we discuss in Chapter 2.

The Voyager-2 data showed meridional differences in the upper tropospheric (80 mbar) temperature structure (Conrath et al., 1998), with cool mid-latitudes compared to a warmer equator and poles. Uranus receives more net insolation at its poles than its equator (Fig. 1.7), a unique feature in our solar system. Ground-based observations over the past decade have shown the latitudinal temperature contrast has not changed significantly over time, despite the dramatic change in season (Orton et al., 2015; Roman et al., 2020).

1.3.2 Chemistry

Characterizing the three-dimensional distribution of atmospheric constituents on Uranus and Neptune is necessary in order to fully grasp how various chemical and physical processes are affecting said composition, and how the composition relates to the large-scale motion of the atmosphere (Orton et al., 2015). To understand the temperature

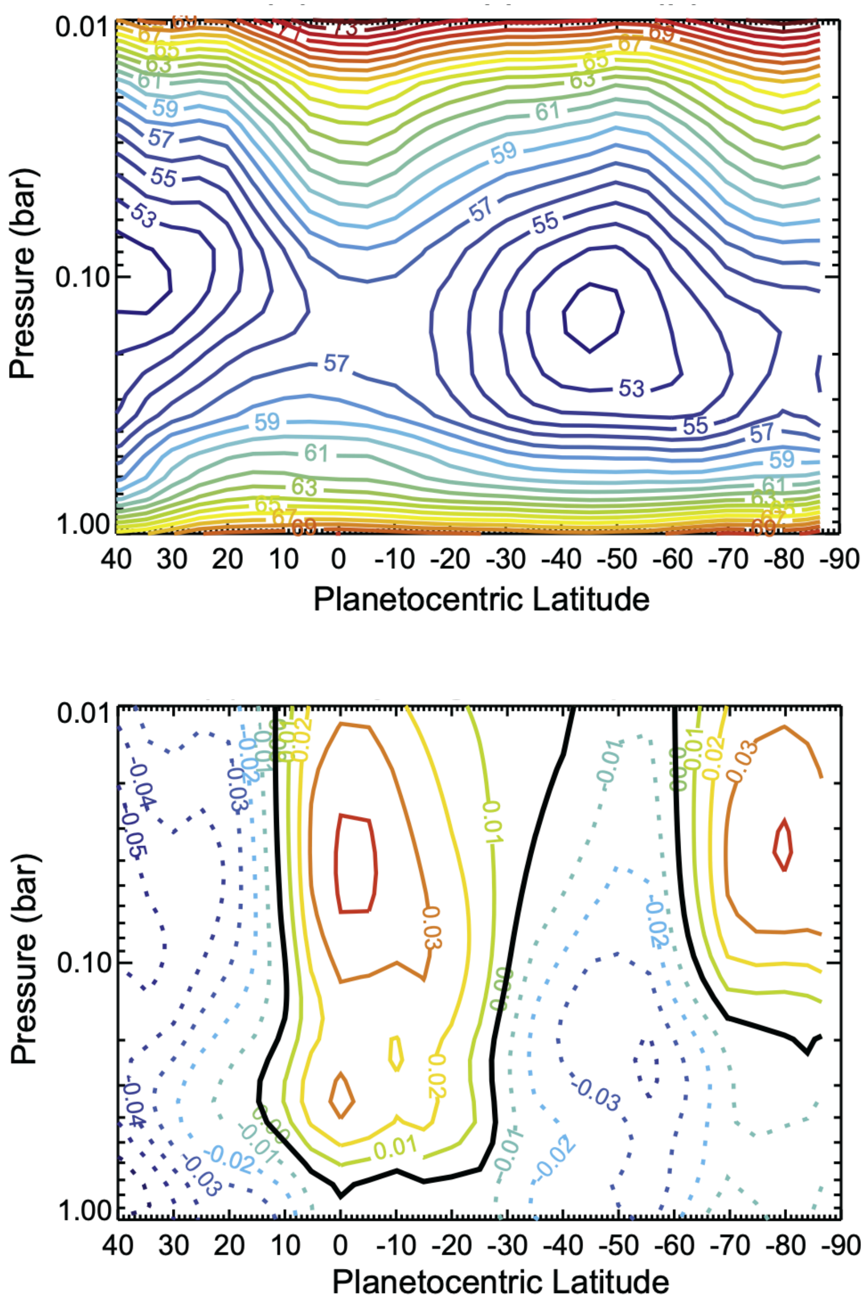

Figure 1.6: Comparison of Neptune's two-dimensional temperatures (top panel) and the para-H_2 disequilibrium (bottom panel) from closest-approach Voyager-2 IRIS maps demonstrating similarities between the two. Temperature contours are given at 1-K intervals covering the 10-1000 mbar pressure range. Adapted from Fletcher et al. (2014).

structures discussed above requires characterising the sources of opacity, and hence composition.

Despite receiving a much weaker solar flux than the gas giants, Uranus and Nep-

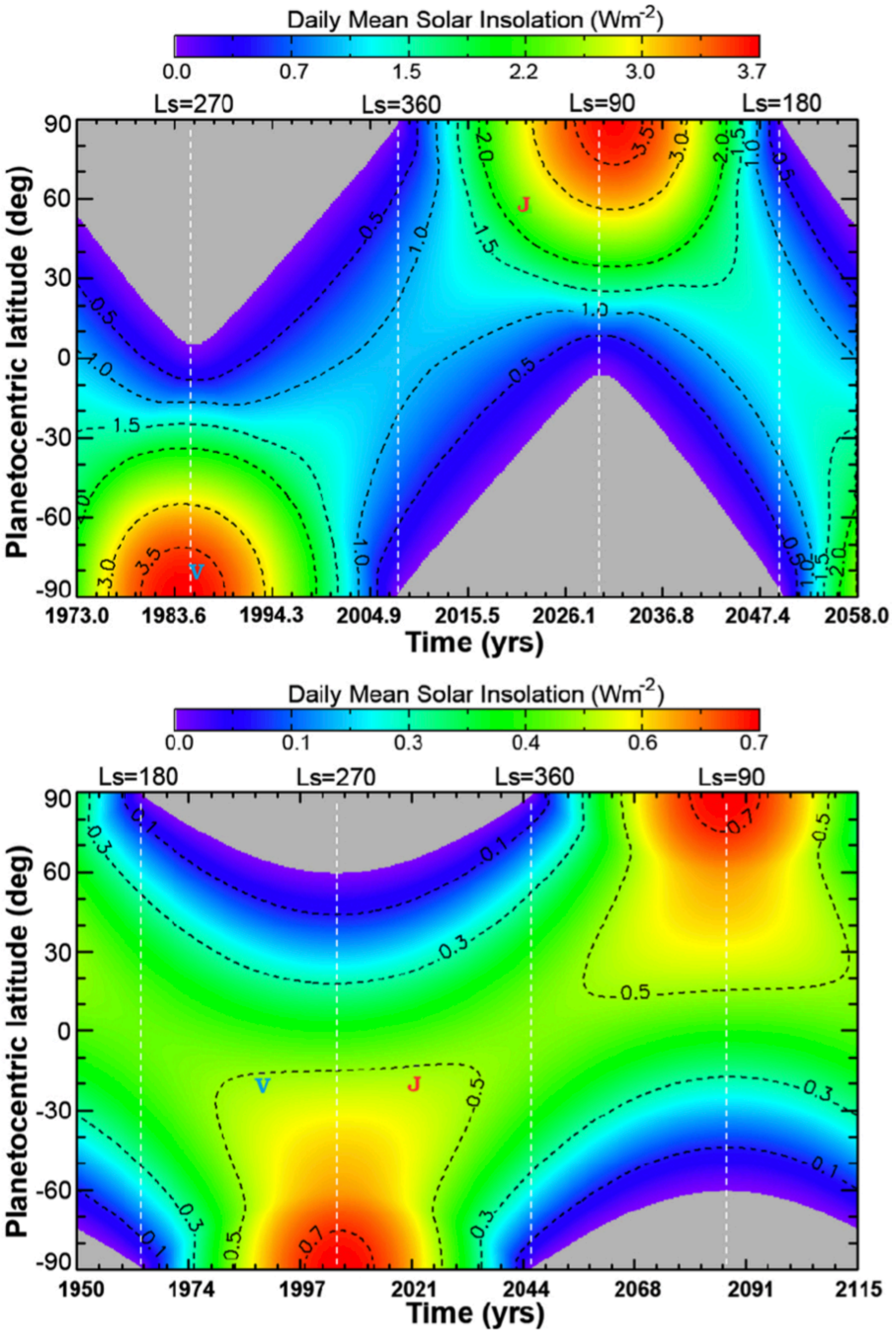

Figure 1.7: Mean daily solar insolation (Wm^{-2} averaged per planetary rotation period) incident at the top of the atmosphere over a full planetary year. Top panel shows Uranus and bottom panel shows Neptune. Grey areas are regions of the planet that do not receive direct light from the Sun. Solstices and equinoxes are marked with white dashed lines showing their solar longitude. Letters V and J show the year and sub-solar planetocentric latitude corresponding to the Voyager-2 flyby (V in blue) and the 2022 GTO for JWST (J in red) (Hueso and Sánchez-Lavega, 2019).

tune have relatively active and vigorous photochemical processes taking place in their atmospheres. The most abundant of the trace gases in ice giant atmospheres are hydrocarbons that come from the photodissociation/photolysis of methane in the upper stratosphere caused by the interaction of photons with the molecules. Chemical reaction chains begin with this process then products can either recycle back to methane or recombine into complex hydrocarbons (Moses and Poppe, 2017) like the ones listed in Table 1.2. For example, acetylene in the atmosphere of Uranus was first discovered in UV data from 1980 (Encrenaz et al., 1986). Ethane at Neptune was first noted by Gillett and Rieke (1977) using the University of Arizona 1.5 m and 2.2 m telescopes in the MIR. The first firm identification of ethylene at Neptune was from MIR ISO photometry in 1997 (Schulz et al., 1999).

Diffusion distributes these hydrocarbons downwards where they condense at low temperatures in the middle atmosphere (Burgdorf et al., 2006). Sluggish vertical mixing at Uranus prevents methane from being carried to high altitudes. This is one of the key differences when comparing to the atmosphere of Neptune (see Figure 1.8). This indicates that Uranus' photochemical processes occur at higher pressures than on any other world (Moses et al., 2020). The methane homopause at Uranus is much lower than it is on Neptune, causing certain species to play different photochemical roles on each planet (see Dynamics subsection 1.3.4 for definition of the homopause).

CO and H_2O are dominant trace molecules at pressures below around 10 microbars. This is most likely due to external sources such as satellite or ring debris as well as cometary impacts (Moses and Poppe, 2017). Photolysis of both CO and CO_2 can lead to secondary peaks of hydrocarbon production at higher altitudes (Moses et al., 2018).

Re-analysis of the Voyager-2 radio occultation data of Uranus in more recent years, combined with comparison to HST/STIS data, revealed a suspected methane depletion toward the poles (Sromovsky et al., 2011). Both Uranus and Neptune show this polar depletion of methane at their south poles in the NIR spectrum from Hubble (Karkoschka and Tomasko, 2009, 2011). This same pattern has also been seen in millimeter observations sensitive primarily to H_2S gas (Tollefson et al., 2019; Molter et al., 2020). There is evidence that might support this depletion in the stratosphere of Neptune from Keck data in 2003 (Fletcher et al., 2014). Latitudinal changes at Neptune in the distributions of acetylene and ethane were observed using the TEXES instrument on the Gemini North 8-m telescope. The abundances of both hydrocarbons appeared to be meridionally invariant (Greathouse et al., 2011). Spatially-resolved ground-based imaging of Uranus in the mid-infrared has revealed

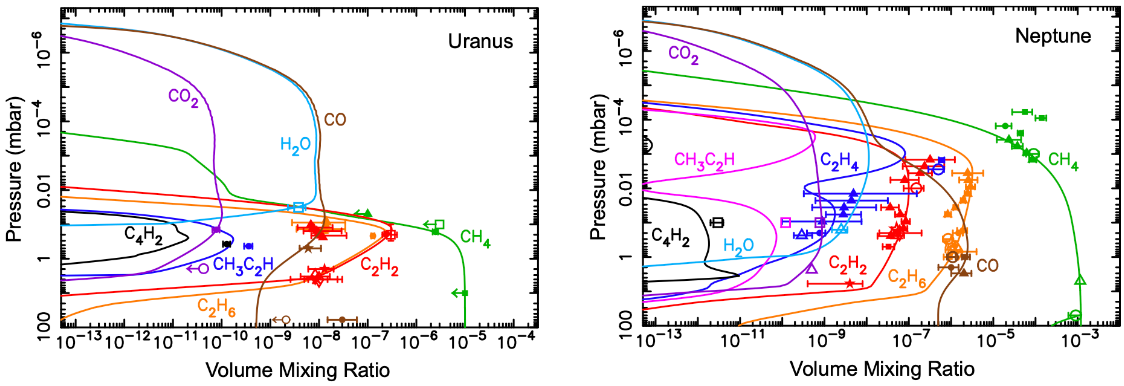

Figure 1.8: Comparison of the vertical distributions of hydrocarbons and oxygen compounds in the stratospheres of Uranus (left) and Neptune (right) from Moses and Poppe (2017). The volume mixing ratio (vmr) that is used to define the abundances of each species relative to that of all other components of the atmosphere. Points with error bars are measurements from a wide variety of sources.

that emission from stratospheric acetylene is relatively enhanced at mid and high latitudes compared to that at the equator (Roman et al., 2020). Roman et al. (2020) found these spatial differences to be consistent with either a 16-K latitudinal gradient in the stratospheric temperatures or a factor of 10 gradient in the stratospheric acetylene abundance, arguing in favor of the latter based on the vertical motions implied by complementary upper-tropospheric observations. Until these observations in 2009 and 2018, there had been no mid-infrared measurements of spatial structure in the stratosphere of Uranus, and these will be used to assess the sources of longitudinal variability observed by Spitzer (see Chapter 4). H_2S absorption features have only just recently been detected in the NIR (Irwin et al., 2018, 2019b) but the latitudinal distribution has already been shown to exhibit the same polar depletion and mid-latitude enhancement as can be seen in methane and the hydrocarbons (Irwin et al., 2019a). This consistent pattern of latitudinal abundances connects with the circulation model outlined in section 1.3.4 and in Figure 1.11.

1.3.3 Clouds and Hazes

Observations can only probe down to the few-bar-level because gas and cloud opacity and Rayleigh scattering limit the penetration any deeper (Hueso and Sánchez-Lavega, 2019). Figure 1.9 shows the thermochemical equilibrium scenario where most clouds form deep in the troposphere. This is modelled by thermochemical equilibrium cloud condensation (ECC) models that are based on vertical temperature and composition

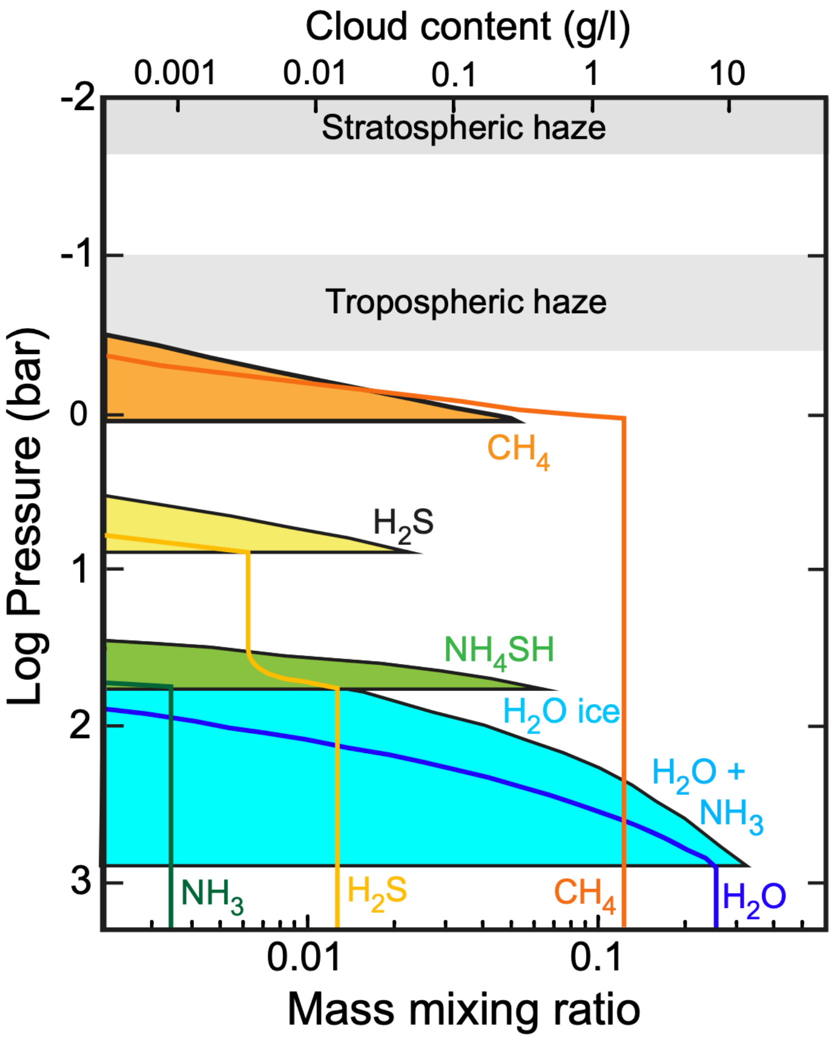

Figure 1.9: Thermochemical equilibrium prediction of the upper-tropospheric cloud structure on Uranus (results for Neptune are similar). The predicted mass mixing ratios of condensible gases are shown as colored solid lines, and the maximum cloud density as solid black lines with color-shaded regions (modified from Hueso and Sánchez-Lavega (2019) by Moses et al. (2020)).

distributions. They give the altitude of the formation of the cloud bases and vertical distribution of the density in the cloud according to the different species that condense following the saturation vapour pressure curves based on the Clausius-Clapeyron equation (Sánchez-Lavega et al., 2004). These models suggest the formation of hazes made of H_2O, C_6H_6, C_4H_2, C_4H_{10}, CO_2, C_3H_8, C_2H_2, and C_2H_6 from top to bottom (Romani and Atreya, 1988; Romani et al., 1993; Baines and Hammel, 1994; Baines et al., 1995; Moses et al., 1995, 2005; Moses and Poppe, 2017, etc.).

Water and ammonia are expected to condense at very deep levels (between 50 and

1000 bar), an ammonia hydrosulphide cloud forms somewhere around 40-50 bar, a hydrogen sulphide cloud forms around 8 bar and methane condenses near 1.5-2 bar (Hueso and Sánchez-Lavega, 2019). These depths vary from Uranus to Neptune but only two cloud decks are actually observed at both planets. An optically thin cloud at around the methane condensation level of 1.5 bar and an optically thick cloud around 3-4 bar (Baines et al., 1995). Modeling and observations appear to show some seasonal variations of dynamics and aerosol distributions over time (Hofstadter and Butler, 2003). For example, at Neptune, Toledo et al. (2020) reported a haze opacity that had grown by up to 3.5 times in the 15 years since that observed by Voyager-2.

The long chain hydrocarbons that are created at high altitudes through the photodissociation of CH_4, condensate into stratospheric hazes that play a role in dynamics and radiative balance (Moses and Poppe, 2017; Li et al., 2018; Toledo et al., 2018). The condensation of the hydrocarbons into their respective ices results in the formation of initial haze particles at different altitudes (Toledo et al., 2020). These haze particles can only be detected once they coagulate, due to their small size (radii <0.1 μm), but in this process they also sink deeper and into the troposphere.

Orton et al. (2007) and then Fletcher et al. (2018), revised the CIA opacity and found there was no need for consideration of aerosols and clouds in the model of both ice giants to reproduce the spectra at these MIR wavelengths. Because of this, we treat the hazes as optically thin at the altitudes that the MIR are sensitive to and so the models we use in chapter 5 and 6 are cloudless and scatter free (see Chapter 2).

1.3.4 Dynamics, Meteorology and Waves

Atmospheric dynamics are governed by the same fundamental physics on all planets. These processes can be described by fluid momentum and the conservation of mass and energy. The relative dominance of certain physical processes over others result in various atmospheric flow phenomena, ultimately shaping the motion, energetics, and cloud distributions that we observe. Vertical transport in atmospheres happens by three main mechanisms: convection, atmospheric waves and turbulence.

At the ice giants this transport is assumed to operate via eddy and molecular diffusion as well as by general atmospheric circulation (e.g., upwelling and subsidence). Eddy diffusion is the process of the atmosphere mixing due to turbulence. This process is extremely complicated and is simplified for use in atmospheric modelling (Moses et al., 2005, 2018). Eddy diffusion, its simplification and the effect it has on ice giant atmospheric models will be discussed further in Chapter 2.

The term used to describe the boundary between the two levels of significance for the kinetic transport of species is the homopause. The homopause is defined as the level of the atmosphere at which the coefficients of molecular diffusion and eddy (turbulent) diffusion are equal. Below the homopause, strong vertical mixing dominates and above it molecular species separate diffusively. Strictly speaking, the homopause must be defined for each species (we have previously used the term methane homopause) but on the ice giants both the homopause and methane homopause are generally understood to refer to the level at which methane begins to separate diffusively from the background gas and can be used interchangeably (Lunine, 1993).

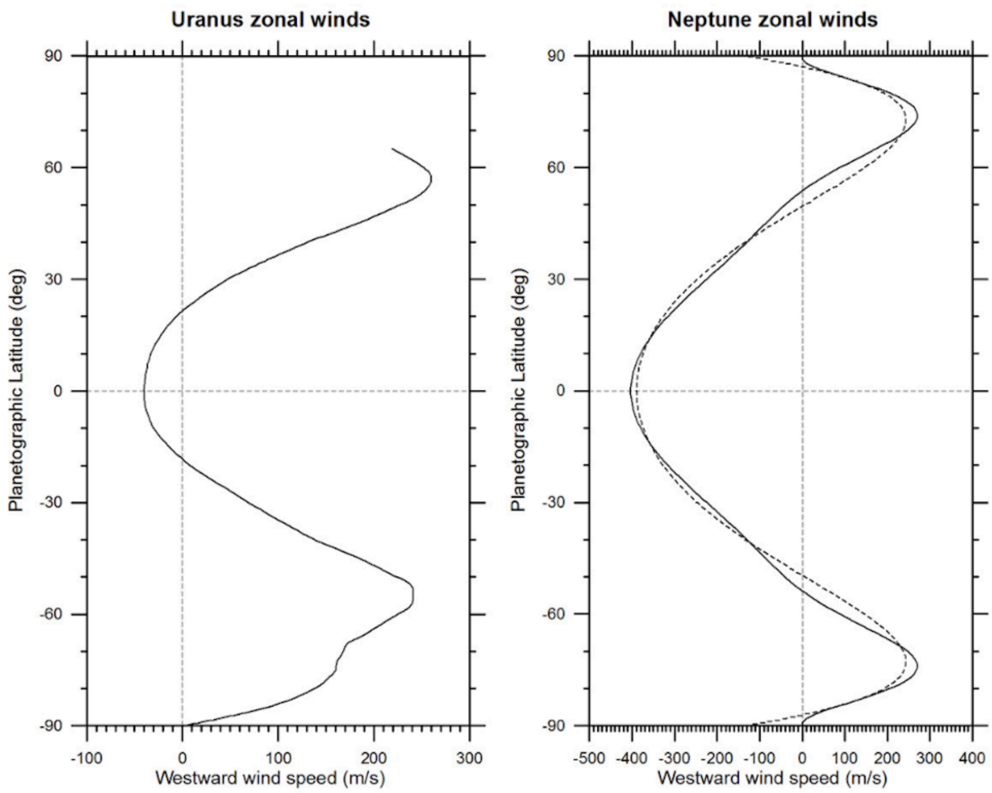

Figure 1.10: Uranus and Neptune zonal winds. Uranus winds (left panel) are a combination of Keck results from 2012 to 2014 and a reanalysis of 1986 voyager images by Karkoschka (2015) and adopted from Sromovsky et al. (2015). Neptune winds (right panel) are from Voyager measurements showing different fits to Voyager wind speeds (Sromovsky et al., 1993). Figure and caption adapted from Mousis et al. (2018).

Mean-zonal circulation is characterized on both ice giants by a broad retrograde tropospheric jet centered on the equator and prograde broad tropospheric jets in the mid-latitudes (Fig. 1.10). They have none of the fast-moving latitudinal structure (i.e. belts and zones) associated with Jupiter and Saturn. There is a banded structure at depth (i.e. below the hazes) that has been observed but, unlike the two larger planets, there's no notable connection between the winds and the bands (Karkoschka, 2015; Sromovsky et al., 2015). For Uranus, the retrograde equatorial zone peaks at around 50 m/s. At both northern and southern mid-latitudes, a prograde jet blows at around 250 m/s, making it fairly symmetric between hemispheres. The equatorial jet of Uranus is comparatively sluggish compared to Neptune. Neptune has some of the highest wind speeds in the solar system with its retrograde equatorial zone peaking at around 400 m/s and the prograde jets blowing at almost 300 m/s (Sromovsky et al., 1993).

Both planets have discrete cloud activity that is both episodic and continuous. Unlike Jupiter and Saturn, most large scale systems at the ice giants are episodic and relatively short lived, disappearing after a few years. Some features, like the Berg feature at Uranus (Sromovsky et al., 2015) and the South Polar Feature at Neptune (Karkoschka, 2011) are more continuous and long-lived.

Uranus shows less discrete cloud activity than Neptune, though it does have some, infrequent, storms. Uranus' meteorology was perceived to be relatively dormant during the Voyager-2 fly-by but has since then increased in activity as Uranus approached its northern spring equinox in 2007, as shown most prominently at near-infrared wavelengths. Episodic bright and dark features were observed in 2011 that were changing and moving over relatively short timescales (Sromovsky et al., 2012) and bright, long-lived cloud features have been observed multiple times (de Pater et al., 2011; Sromovsky et al., 2009; Roman et al., 2018). One of the largest and brightest of these features was called the "Bright Northern Complex", which attained its peak brightness in 2005 with clouds reaching pressures as low as 240 to 300 mbar (Sromovsky et al., 2007; Roman et al., 2018). In 2014 a similarly bright feature was observed in the near-infrared and estimated to reach to similar heights (de Pater et al., 2015). These features may be tied to vortex systems that exist in the upper troposphere, such as the prominent dark spot observed in 2006 at depths in the 1-4 bar pressure range (Hammel et al., 2009). This feature had bright cloud companions manifesting at lower pressures of around 220 mbars (Sromovsky and Fry, 2005), which could be evidence of deep-seated features influencing the structure of the upper troposphere at certain longitudes.

To date, only two dark spots have been observed on Uranus and six on Neptune, and only one has been witnessed forming (Simon et al., 2019). Dark spots are the third most prominent cloud type after zonal banding and bright clouds on the ice giants. They are dark ovals that are most notable on Neptune where they are usually dark blue-green in colour. The most famous dark spot is the Great Dark Spot (GDS) first observed by Voyager-2 in visible wavelengths (Smith et al., 1989). It drifted slowly from around 20° South towards the equator where is disappeared about a year later (Sromovsky et al., 2002). Simulations of the GDS demonstrated that such vortices responded strongly to variations in the structure of the zonal wind, temperature profile and distribution of aerosols (Hadland et al., 2020). Bright clouds often accompany these dark oval features and are thought to be orographic clouds that are the result of air being forced upwards by the vortex (Stratman et al., 2001). These same bright clouds were seen in relation to Uranus' first definitive detection of a dark spot in 2006 (Hammel et al., 2009).

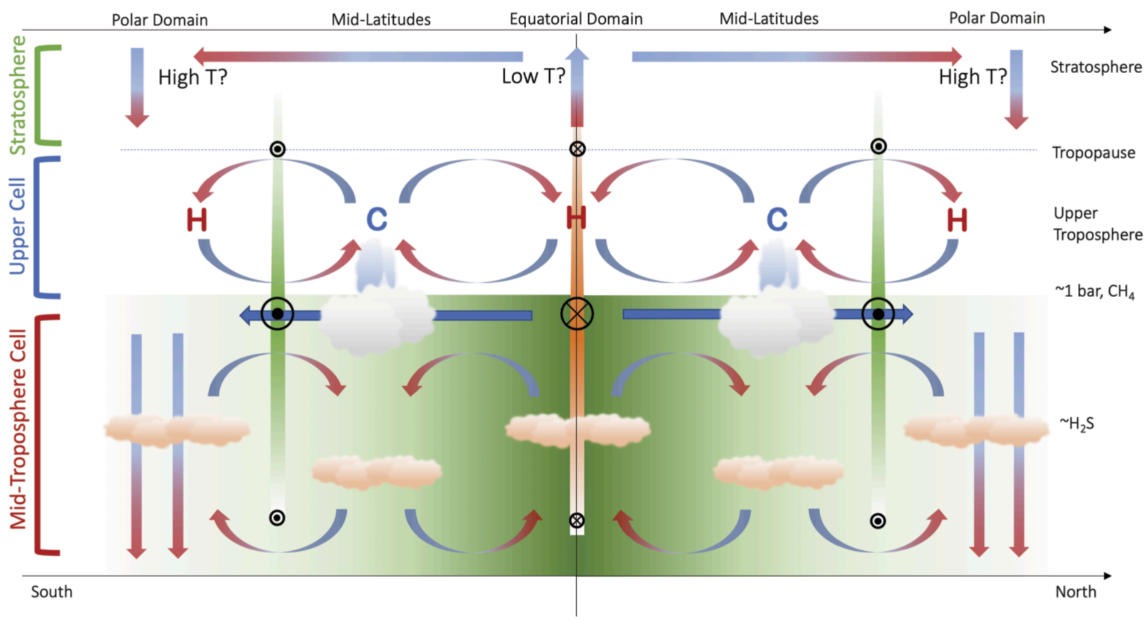

Figure 1.11: Schematic of the potential circulation in the troposphere and stratosphere of an ice giant. **Mid-Troposphere Cell:** Extends down to around 50 bar from the 1 bar CH_4 condensation level. Retrograde winds are shown by orange bars and circles with crosses. Prograde winds are shown by green bars and circles with dots. **Upper Cell:** Layer between the tropopause and the CH_4 condensation level. Tropospheric temperatures are denoted by 'C' and 'H' for cold and hot. Inferred decay of horizontal winds with altitude. **Stratosphere:** Large scale equator to pole motions inferred from latitudinal temperature variations. Figure from Fletcher et al. (2020).

The upper tropospheric temperatures on both planets derived from Voyager-2 show cool mid-latitudes in the 80-800 mbar range, contrasted with warm equator and poles (Flasar et al., 1987; Conrath et al., 1998). The temperature contrasts suggest rising motion with adiabatic cooling at mid-latitudes, accompanied by subsidence and adiabatic warming at the equator and poles (Fig. 1.11). The upwelling at low latitudes condenses into discrete methane cloud features. Dry air would then be transported poleward and descend, thus inhibiting methane condensation at high latitudes (Sromovsky et al., 2011). We discussed in the Chemistry subsection how the latitudinal variations in abundances of species like CH_4 and H_2S hint to the same meridional circulation model at both planets. This again shows how temperatures, abundances and dynamics are all connected.

Geostrophy implies that temperatures and winds are in balance with one another via the thermal wind equation. If we know the wind speeds at a certain pressure level (for example, at the cloud tops by discrete cloud tracking) then the wind speeds at other levels can be estimated by using the three dimensional temperature field. This is complicated by the molecular weight of the atmosphere, which does not always remain constant as is assumed in the general thermal wind equations (Irwin, 2009). Uranus and Neptune have large fractions of condensable gases that mean that the equations have to be slightly modified like in recent work by Tollefson et al. (2018) for Neptune where they had to consider global methane variations in their calculations.

Stratospheric circulation is not yet understood and the schematic in Figure 1.11 is only one possible option if we consider observed brightness to be a direct result of latitudinal temperature variations. However, an alternative stratospheric circulation model has been put forward by Roman et al. (2020) assuming that observed brightness of Uranus is the result of latitudinal hydrocarbon variations rather than temperatures. In this case, mid-latitude upwelling from the troposphere carries CH_4 aloft to be broken down into C_2H_2 which is transported to the equator and pole. Atmospheric dynamics are a direct cause of spatial variation in emissions and will be discussed further when analysing the longitudinal variations at Uranus in Chapter 5. However, it is important to note, that much of the latitudinal variability discussed here would not be detectable in the disc-averaged Spitzer data like the longitudinal variations were. This is where the JWST's spatially resolved MIR observations will be invaluable.

Voyager observations of Neptune in MIR revealed the planet's large internal heat source (Pearl and Conrath, 1991). The IRIS instrument also identified latitudinal variations in brightness, with maxima near the equator and south pole and minima at southern mid-latitudes, similar to Uranus (Fig. 1.11). This is consistent with a meridional circulation, with cold air rising at mid-latitudes and subsiding at both the poles and the equator (Fig. 1.11). This was observed at Uranus by Conrath et al. (1998) and again after reanalysis and comparison by Orton et al. (2015). The para-H_2 fraction is at its minimum in areas of upwelling observed in the mid-latitudes yet at a much higher value in the high-latitude areas of the northern hemisphere that exhibited cooler temperatures. This same pattern is observed at Neptune and can be seen in Figure 1.6 where para-H_2 super-equilibrium conditions are shown to be linked to areas of hotter atmospheric subsidence at the equator and high-latitudes (Fletcher et al., 2014).

The observations of Uranus at the 1986 southern summer solstice and the recent observations a season later (around northern spring equinox between 2003 and 2011) showed no detectable changes in upper-tropospheric/lower stratospheric temperatures. This goes against what was expected as the atmosphere should only be influenced by convective energy transport which changes drastically during Uranus' extreme seasons (Orton et al. 2015 and see Fig. 1.7).

Vigorous upwelling of hot gases from the deep atmospheres of giant planets can cause changes in both the temperature and chemistry of the stratosphere, as has been observed at Saturn. A large stratospheric anomaly called the Saturn stratospheric beacon, observed in 2011-2012, was likely due to waves propagating into the stratosphere from a tropospheric storm, interacting with the background zonal flow, breaking and depositing their energy (Fletcher et al., 2012; Moses et al., 2015; Cavalié et al., 2015). This shows how the troposphere can potentially influence the stratosphere, and we seek in chapter 4 and 5 to investigate whether similar processes might be at work on Uranus.

1.4 Context and Significance

Ice giants are important because they challenge our models of planet formation and evolution, and because they, along with their rings, moons, and magnetospheres, exhibit structures not yet understood.

The next generation of space telescope, the James Webb Space Telescope (JWST), is set to be launched in late 2021. Its 6.5 m-diameter mirror will be able to spatially resolve Uranus and Neptune in the MIR. The main reason for this investigation with Spitzer is to provide a comprehensive characterisation of these atmospheres, to allow more targeted questions to be developed ahead of JWST operations. The JWST has Guaranteed Time Observations (GTO) for both Uranus and Neptune scheduled within the first 12 months of operation. This should be in Summer 2022 and makes this study extremely timely (Fletcher et al., 2021). This is discussed thoroughly in Chapter 7.

Ice giants are the last remaining class of planet to not have a dedicated orbital explorer. Since the Voyager encounters, atmospheric processes at the gas giants have been well characterised by the Galileo and Juno orbiters at Jupiter, and the Cassini orbiter at Saturn (Mousis et al., 2018). The motivations for this study, that have already been pointed out above, are why the international science community are collectively pushing towards a dedicated mission to one or both of the ice giants (Mousis et al., 2018; Hofstadter et al., 2019; Guillot, 2019; Fletcher et al., 2019; Dahl et al., 2020; Fletcher et al., 2020, etc.).

Exoplanet science is one of the fastest growing areas in astronomy. Understanding Uranus and Neptune will be critical in understanding the origins of our own solar system and consequently the hundreds of extra-solar systems being discovered every year. Planets between the size of Earth and Neptune constitute a dominant fraction of the planets discovered (Batalha et al., 2013). Most of these worlds are close to their parent star and therefore would have very different environments to our cold ice giants but, since nothing like that is present in our solar system, Uranus and Neptune provide a rich laboratory to explore the diverse chemical and dynamical processes in the unique parameter space that they occupy (Helled and Bodenheimer, 2014; Mousis et al., 2018; Dahl et al., 2020).

The work done in this thesis ultimately provides an improved context to understand the chemistries, processes, origin, and evolution of ice giant atmospheres. Untangling the mysteries surrounding these planets in our own solar system will lead to fundamental insights into the formation and evolution of planetary systems in general.

1.5 Thesis Structure

This chapter has outlined the background behind the planets and their atmospheres. Chapter 2 outlines radiative transfer and retrieval theory, introduces NEMESIS (the retrieval suite used) and how it will be used in this investigation to model the data. The Spitzer Space Telescope and its Infrared Spectrometer instrument are described in Chapter 3 in addition to an outline of how the data were reduced and calibrated.

The results are then split into the following four chapters. The first results chapter (Chapter 4) displays and discusses the stratospheric longitudinal variations that can be detected at both Uranus and Neptune. Chapter 5 and 6 are the results from the optimal estimation retrievals of Uranus and Neptune respectively. Both chapters discuss the vertical temperature and chemical structures of the planets from the best data available from Spitzer. At Uranus we also investigate the longitudinal variation discussed in the first results chapter using the radiative transfer model. The content from Chapters 3, 4 and 5 have been published in Icarus by Rowe-Gurney et al. (2021). The last results chapter (Chapter 7) shows how the data from Spitzer and our results from the previous chapters have helped us to model future observations from JWST MIRI and speculate on what new discoveries may be made with it. A brief description of the JWST MIRI instrument and its capabilities for the ice giants is also included in this chapter for reference. Much of this chapter describes latitudinally-varying temperature, cloud, and gas properties. Although Spitzer can't resolve these, it can provide a global average, as well as the longitudinal study, and these are all required for JWST.

In brief, this thesis uses the data from the Spitzer IRS to investigate the composition and temperature structure of the stratosphere and upper troposphere of Uranus and Neptune in preparation for the JWST. The aim of the thesis is to answer the following questions:

- Is there a longitudinal variation at Uranus and Neptune from Spitzer IRS data?
- Is there a connection between the troposphere and stratosphere in the variability?
- What is the thermal structure and composition of Uranus' stratosphere in 2007 and can this tell us the likely cause of the variation?
- What is the thermal structure and composition of Neptune's stratosphere in 2005?
- How will spatially-resolved MIR observations from JWST MIRI extend the disc-integrated analysis described in this thesis?

Chapter 8 returns to these questions to discuss if and how they have been answered. We also bring together the conclusions made throughout the results sections and present any opportunities for future work.

Chapter 2

Radiative Transfer and Retrieval Theory

2.1 Introduction

The atmospheres of the ice giants have never been directly sampled. Even though Voyager-2 flew close to each planet, it did not have an atmospheric probe to directly measure the composition, temperature, or dynamics. All the knowledge we have of the atmospheres has come indirectly from analysing features in their electromagnetic spectrum. The spectrum is split into reflectance and thermal emission (see Figure 2.1 and also section 1.2 where the parts of the spectrum and their contributions to observing the atmospheres of the ice giants are explained).

In this chapter we will examine how the spectra of Uranus and Neptune are formed through the process of radiative transfer. Electromagnetic radiation interacts with molecules in the atmosphere in a way that we can model a synthetic spectrum generated from initial assumptions. This is our radiative transfer model, sometimes called a *forward model*. The first section will give a brief background of spectroscopy and how the spectra we observe are formed. We then explain radiative transfer and how it is a basis for the modelling done in this thesis.

The differences between the observed spectra and the spectra modelled using radiative transfer can then be used to revise the atmospheric profile assumptions and improve the fit. This process is called inversion. Derivation of the vertical temperature and composition profiles require the use of the optimal estimation retrieval algorithm, NEMESIS, to fit the disc-averaged Spitzer observations (Irwin et al., 2008). The process of doing retrievals using NEMESIS will be explained in the last section, along with the parameters of our reference atmospheres for Uranus and Neptune that are used in Chapter 5 and 6 respectively.

2.2 Spectroscopy

As radiation propagates through an atmospheric medium it is modified by absorption, emission and scattering of radiant energy on a microscopic scale. The study of the interaction between matter and electromagnetic radiation is called spectroscopy. A spectrum, in this context, is commonly displayed as a plot of intensity, flux or power as a function of frequency or wavelength (Fig. 2.1).

An atom can lose or gain energy by emitting or absorbing photons. The energy and thus frequency of these transitions between energy levels are specifically quantised and are what produce the spectra. Therefore, the discrete line pattern in a spectrum is characteristic of the chemical species producing it. These fingerprints are what make spectra useful for compositional analysis via remote sensing in planetary atmospheres. In reality, it is not quite as simple because it is not single atoms that planetary atmospheres consist of. The grouping of atoms into molecules leads to the creation of unique transitions between states due to combinations of spins, rotations and vibrations that will be discussed later in this section.

Figure 2.1 shows the continuum from a hypothetical planet with an atmosphere. The two distinct sections of the continuum, reflectance spectra and thermal emission, are visible. Superimposed on top of these are the discrete line and band absorption and emission spectra. The emission lines are produced by ions, atoms and molecules excited by various processes, typically at high temperatures. So, if the light emitted by an excited sample is analysed then this is an emission spectrum. If the intensity of light transmitted through a sample is measured, then this is an absorption spectrum. The absorption lines and bands are produced by atoms and molecules when they absorb specific frequencies of the continuum (Sanchez-Lavega, 2010).

The thermal part of the continuum is derived from the assumption that the planet is a blackbody that emits according to equation 2.1, the Planck radiation law:

$$B_\lambda(T) = \frac{2hc^2}{\lambda^5(e^{hc/\lambda k_B T} - 1)} \tag{2.1}$$

where $B_\lambda(T)$ is the specific intensity or brightness as a function of wavelength (λ), h is the Planck constant, k_B is the Boltzmann constant, c is the speed of light in a vacuum and T is the effective temperature of the atmosphere. A blackbody is an idealised object that absorbs 100% of the electromagnetic radiation incident upon it. Because it is a perfect absorber, Kirchhoff's law states that, at thermal equilibrium, is must also be a perfect emitter.

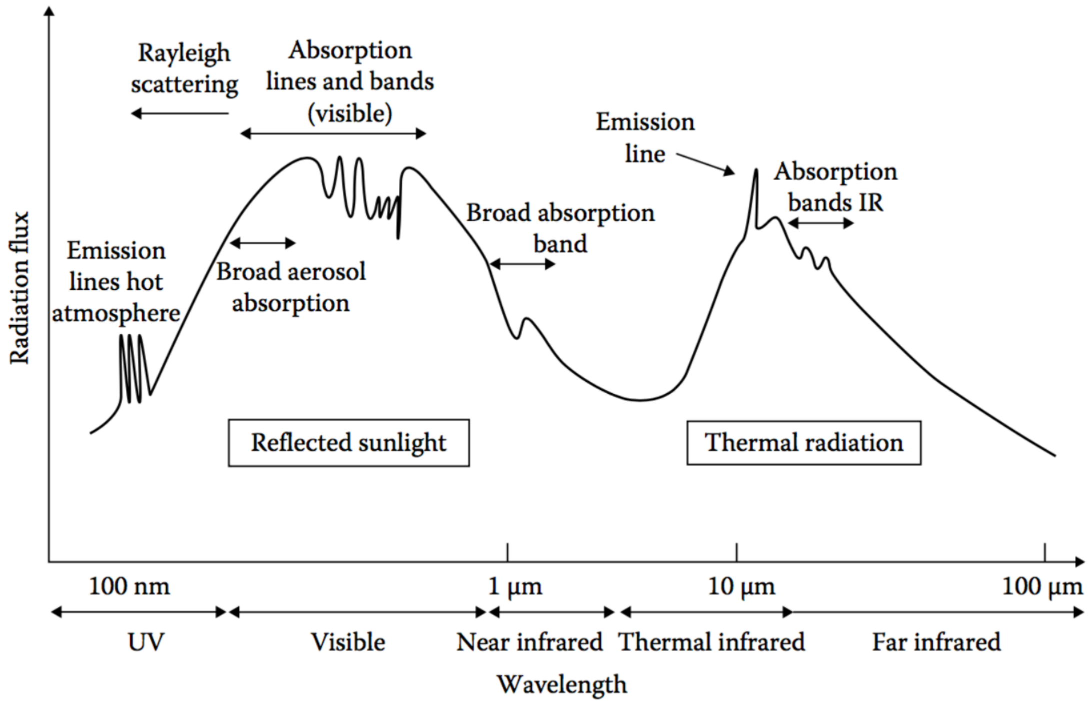

Figure 2.1: Typical spectrum of a hypothetical planet with an atmosphere (Sanchez-Lavega, 2010, p. 116).

At a certain temperature, the wavelength at which this brightness has a maximum is known as the Wein displacement law:

$$\lambda_{max} = \frac{2897.8}{T} \tag{2.2}$$

with the wavelength in microns and temperature in kelvin. Integrating equation 2.1 over all wavelengths and solid angles obtains another important equation called the Stephan-Boltzmann law, where the total flux (in Wm^{-2}) from a blackbody is given by:

$$F = \int_0^\infty B_\lambda(T)\, d\lambda = \frac{\sigma_B}{\pi} T^4 \tag{2.3}$$

Here, σ_B is the Stephan-Boltzmann constant.

A useful parameter to look at the spectra of a planet, and one that is used frequently in the results chapters, is the brightness temperature, T_B. This is the idealisation and therefore approximation of the real temperature found by fitting the measured radiance to a blackbody curve with the same temperature and is equivalent to the effective temperature in equation 2.1 (Sanchez-Lavega, 2010).

2.2.1 Ro-vibrational Transitions

In the infrared, the gaseous absorption is primarily dependent on the vibrational and rotational modes of the molecules in the atmosphere. Molecules vibrate with different modes like balls attached with springs. Each band of spectral lines exhibited by the molecule corresponds to a single vibrational transition. Fine structure is also introduced by accompanying rotational transitions. These vibration-rotation (ro-vibration) bands that are produced have a complex structure of lines that often overlap each other. Using molecular spectroscopy theory, both the energy levels and the transition probabilities can be calculated. These properties give the positions of the spectral lines and bands that allow us to derive the unique species that produce them. These bands are not always the same shape and strength, with this depending on the physical conditions in which the molecules exist, especially temperature and pressure. These can be calculated using quantum mechanics but are more often found physically in the laboratory using spectrometers.

2.2.2 Line Shapes and Broadening

The strength and shape of a band can change for different reasons. For example, the strength of an absorption line depends on the transition probability and on the population of the lower energy level. Whether bands appear in absorption or emission depends on the environmental conditions of the line-forming region. Both emission and absorption happen simultaneously resulting in a combination of gains and losses in radiance at the same spectral point.

The band-shape depends on the population of states and the symmetry of the molecule, this determines the quantum-mechanical selection rules for allowed transitions between states. For spherical or linear diatomic molecules there are usually three branches (P, Q and R). The central band at the fundamental vibrational frequency is called the Q branch. The P branch is at lower frequencies and the R branch is at higher frequencies. At both ice giants, this Q, P, R configuration can be clearly seen in the acetylene, C_2H_2, feature centred at around 13.5 μm (see Figure 3.5 and 3.7 in later chapters).

There is a natural broadening of a line due to the time it takes for the photon to be absorbed or emitted by an atom or molecule. This natural broadening process however is extremely small compared to other line-broadening processes. The first process is collision broadening otherwise called pressure broadening. The spreading of wavelengths in a line profile is caused when, during absorption or emission, molecules collide with each other. This effect is dominant in the troposphere due to higher pressures and therefore higher probabilities of collisions.

Doppler broadening occurs in the stratosphere where pressures are lower. As molecules are emitting and absorbing, they move with a Maxwell-Boltzmann distribution of speeds. The absorption will happen at a different frequency depending on whether the molecules are moving towards or away from the observer. This is dependent on the temperature and molecular weight of the gas being observed. For intermediate pressures, where both mechanisms may be at work, the combined process is called Voigt broadening (Irwin, 2009).

2.2.3 Collision-Induced Absorption

In homonuclear molecules like the hydrogen molecule, no permanent dipoles can exist due to their symmetric charge distribution. However, temporary, collision-induced dipole transitions can occur in dense atmospheres like that on the ice giants. Collisions between hydrogen molecules and hydrogen and helium molecules form broad absorption bands called collision-induced absorptions (CIAs, Sanchez-Lavega 2010). These homonuclear molecules may also engage in electric quadrupole transitions. The most common of these in the giant planets are S-branch vibrational transitions given the designation S(0-3).

The shape of this continuum is dependant on the ratio of the two spin isomers of hydrogen: the S(1) absorption (near 17 μm) and S(0) absorption (near 28 μm). S(1) is formed from transitions within ortho-H_2 and S(1) from transitions within para-H_2. Para-H_2 is the even spin state of hydrogen with anti-parallel spins and ortho-H_2 is the odd spin state with parallel spins. Transitions from state to state are forbidden yet they occur in the giant planets over long periods of time.

The para-hydrogen fraction (or ortho-para ratio) is the ratio of molecular hydrogen in the one state to that in the other. The ratio has a “normal distribution” of around 3:1 at temperatures of over 300K that are observed in the deep atmosphere. In the cooler, upper atmosphere the ratio tends towards thermodynamic equilibrium (1:1) but any parcels of gas moving upwards from warmer temperatures will retain their initial para-hydrogen fraction for a certain amount of time (Conrath et al., 1998). As mentioned previously in Chapter 1, the degree of disequilibrium measured in the upper troposphere can tell us a lot about deep atmospheric circulation. To measure this ratio, analysis can be done on the solar reflected light in the 4-0 quadrupole lines of hydrogen and from interpreting the collision-induced hydrogen continuum (Fouchet et al., 2003).

The abundance of H_2 in the ice giants is so high that their infrared spectra (especially at longer wavelengths) are dominated by CIA opacity from H_2-H_2 and H_2-He collision pairs. Molecular pairs may be free (collisional complexes) or bound by van der Waals forces (e.g., dimers), and undergo bound-bound, bound-free or free-free transitions between rotational or translational states. As a consequence of the Uncertainty Principle, the short lifetimes of the states creates a broad continuum feature in planetary spectra (Irwin, 2009). Both the line data for the individual species, and the collision induced absorption, will be needed to generate our forward model, as described in the next section.

2.3 Radiative Transfer

Radiative transfer theory is the basis for understanding the transfer of energy within a climate system and therefore interpreting atmospheric remote sensing measurements (Taylor, 2005). In reality, a body like Uranus or Neptune is not a perfect blackbody as represented by equation 2.1 because it not only emits but absorbs, reflects/scatters and transmits radiation. All of these processes must be taken into account if we are to construct the equations needed to accurately describe the behaviour of a single layer of atmosphere. A layer has incident radiance that is reflected by clouds or aerosols. Energy is conserved between this reflectance as well as the absorptance and transmittance. Layers like this can be stacked together to represent the entire atmosphere (Fig. 2.2).

Looking at the thermal emission from all the layers used to simulate the atmosphere, as in Figure 2.2, the radiative transfer equation (RTE) can be written as

$$I_1 = I_0\tau_0 + \int_{z_0}^{z_1} B_\nu(z)\frac{d\tau}{dz}\,dz \tag{2.4}$$

where, B_ν is the Planck function at a certain wavenumber and temperature, τ_0 is the transmission from z_0 to z_1 at angle θ and $d\tau/dz$ is the transmission weighting function. I_0 and I_1 are the radiant intensity, or radiance, at the bottom and top of the atmosphere respectively (see Fig. 2.2), typically measured in units of W cm^{-2} sr^{-1} $(cm^{-1})^{-1}$. The peak of the transmission weighting function varies with altitude depending on the wavelength and is at maximum roughly where the optical depth is one. Each atmospheric layer contributes to the measured radiance depending on the wavelength at which the measurement is made. The contribution as a function of height is described by the product of the transmission weighting function and the Planck function. This is called the contribution function and shows the vertical

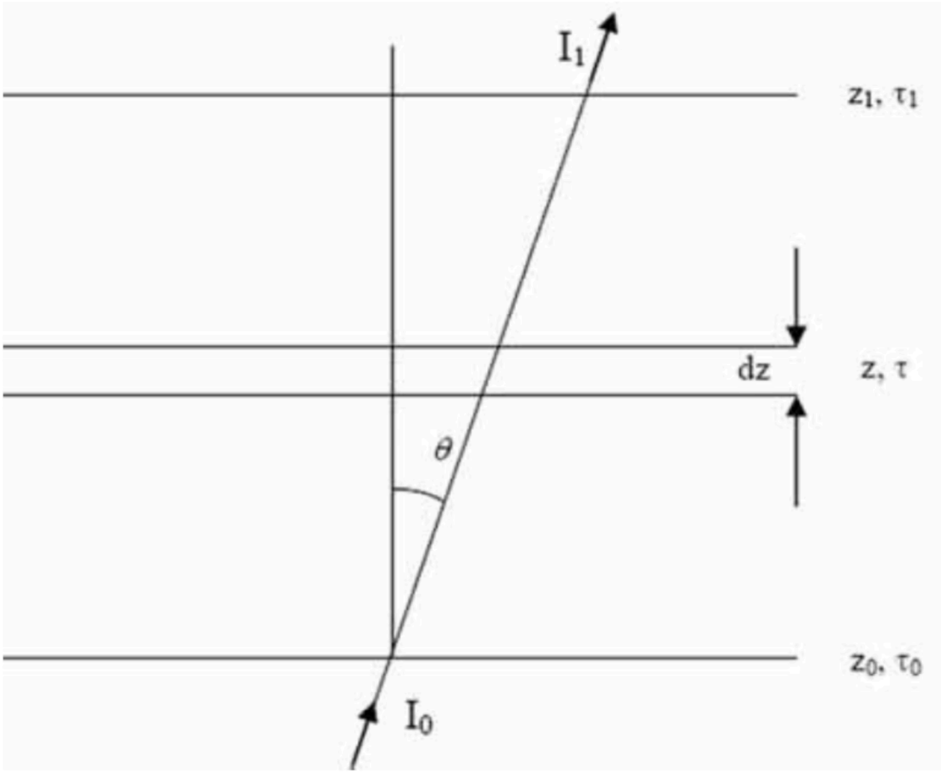

Figure 2.2: Radiative transfer in a plane-parallel atmosphere (Irwin, 2009, p.214). A thick slab of atmosphere between levels z_0 and z_1, with radiant intensity I_0 incident upwards at z_0 at an angle θ. This radiance itself is attenuated by the overlying layer before reaching the top and thus the contribution to I_1 can be written as Equation 2.4.

sensitivity of the spectrum. The calculation of this function requires the abundances of the principal absorbers in the spectral intervals chosen. For nadir viewing ($\theta = 0$) a smoothly varying function indicates the altitudes to which each region of the spectrum is sensitive. Figure 2.3 shows the normalised contribution functions for the wavelengths of the hydrogen quadrupole on Uranus.

2.3.1 Line-by-line Modelling

The different species in a planet's atmosphere all have spectral lines that overlap to contribute to the overall transmission/opacity. Using the identified ro-vibrational bands, the transmission and emission of an atmosphere can be calculated using the RTE (Equation 2.4). A line-by-line model will calculate the absorption coefficient for each line of each gas from the line strength and shape and is the most accurate way to calculate the overall transmission because it takes into account the contribution of

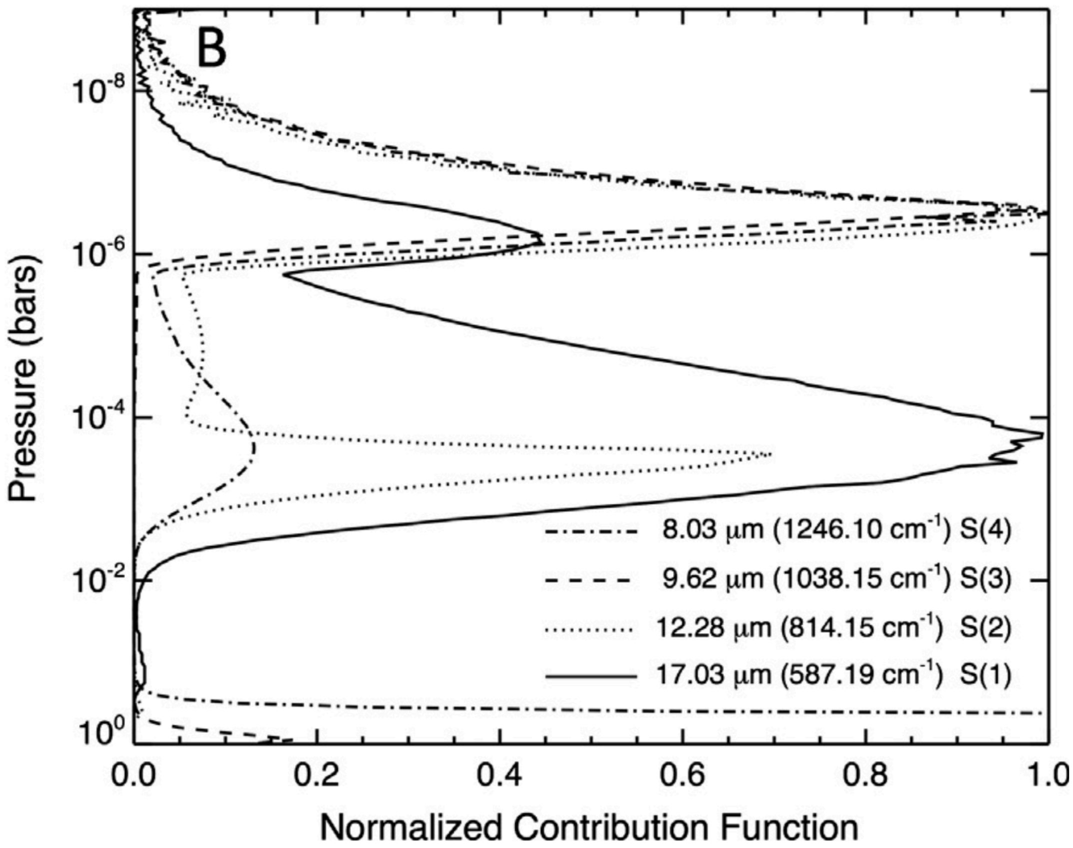

Figure 2.3: Normalised contribution functions for spectral points at the peaks of the H_2 quadrupole lines at the spectral resolution of Spitzer IRS data for Uranus (Orton et al., 2014a).

every single individual line. Each line has a line strength and line width, functions of temperature and pressure that vary across the atmosphere.

Depending on the number of lines and the spectral resolution, this can be extremely computationally intensive and there is a need for a faster, more efficient method. This is the case with the Spitzer spectra we analyse in Chapter 5 and 6 where the correlated-k approximation, explained in the following subsection, is used. The line-by-line technique has been used in previous analyses of Spitzer data, but prevents accurate modelling of the entire spectrum at once.

2.3.2 Correlated-k Approximation

There can be thousands of lines per wavelength band and each of them will vary with pressure and temperature causing line-by-line calculations to be extremely computationally intensive. It is therefore necessary to use a model with the aim to accurately approximate the results of the more accurate line-by-line method whilst drastically reducing the computation time needed. A correlated-k approximation is one method used frequently in radiative transfer calculations in the MIR.

To be able to calculate the mean transmission, only the fraction of high to low absorption needs to be known for each spectral interval. This approach uses a Gaussian quadrature scheme to approximate the definite integral of the rapidly varying absorption-coefficient function. The spectrum is reshuffled and ordered by absorption coefficient making a smoothly varying function whose integral can be calculated with much less computing power. The approximation is a smoother, more easily integrated function of the absorption coefficients that is a weighted sum of function values at specified points within the domain of integration. This reshuffled spectrum is called a k-distribution (Goody and Yung, 1995). The k-distribution tables as a function of temperature and pressure can be calculated just once then used multiple times without the need to calculate them again.

The number of quadrature points to integrate over (g-ordinates) is chosen to achieve the best trade-off between accurate sampling and computational speed (Irwin et al., 2008). Tables computed at the lowest resolution of Spitzer with 20 g-ordinates for integration did not reproduce the opacity in the very fine line-features such as the quadrupole features and in some of the hydrocarbon features. 20 quadrature points are the typical number used by NEMESIS. Increasing the resolution of the k-tables improved this a small amount, but increasing the number of g-ordinates to 50 has proven to be the most effective at reproducing the observed spectrum at both high and low-resolution.

The k-tables for both planets were generated from a high-resolution line-by-line spectrum with sufficient sampling to capture the narrow Doppler-broadened lines at low pressures, based on a correction identified by the erratum of Roman et al. (2020).

Physically realistic atmospheres are inhomogeneous with pressures and temperatures that vary rapidly with position. It has been found that there is a correlation between the k-distributions for adjacent layers and means that an inhomogeneous atmosphere can be modelled by summing together homogeneous layers (Goody and Yung, 1995; Lacis and Oinas, 1991).

2.4 NEMESIS and Retrieval Theory

NEMESIS is a retrieval algorithm that can be used for many different planets and spectral intervals. NEMESIS stands for the Non-Linear Optimal Estimator for Multivariate Spectral Analysis. It is a diverse suit of software that is capable of using line-by-line or correlated-k calculations at nadir or limb viewing geometries. It uses non-linear optimal estimation that we will explain in this section. The forward model that underlies the NEMESIS inverse model is called *Radtrans*. The radiative transfer parameters used for the models will be specified in this section after we outline the way the inverse model works, using retrieval theory.

Radiative transfer describes how radiation interacts with the atmosphere and allows the calculation of a modelled spectra from the composition and temperature profile. This process is called forward modelling and is the most direct approach. Retrieval theory, however, is the inverse method and calculates the most likely atmospheric properties and structure that would result in the radiances observed in a given spectrum. The atmospheric structure is modified within physical limitations until the difference between the modelled and observed spectra is as small as possible. This section is based on content from Irwin et al. (2008), Irwin (2009) and Rodgers (2000).

The atmospheric profile can be described by a set of parameters, $\mathbf{x}$, and the spectrum can be described by a set of measurements, $\mathbf{y}$. In the forward model, $\mathbf{x}$ is used to calculate $\mathbf{y}$, which can be expressed as,

$$\mathbf{y} = \mathbf{K}(\mathbf{x} - \mathbf{x}_a) + \epsilon \tag{2.5}$$

where $\mathbf{K}$ is the matrix of functional derivatives describing the rate of change of radiance with respect to the an atmospheric parameter. $\mathbf{x}_a$ is the *a priori* estimate of $\mathbf{x}$ and ϵ is the measurement error.

Equation 2.5 is for a forward model, whereas in reality, we do the inverse and use observations to measure $\mathbf{y}$ so that we can find $\mathbf{x}$. Most inversion/retrieval methods are based on least-squares fitting of the modelled versus observed radiances. However, the least squares method does not work well when there are more parameters to fit than there are measurements (i.e., an under-constrained problem). Retrievals will have more than one realistic solution to the problem and one, hopefully the best one, must be chosen from all those possibilities.

We use the technique of 'optimal estimation' to identify the family of potential solutions. This involves not only relying on the measured radiances for comparison, but also an additional set of constraints called an *a priori*. An *a priori* is based on the results and data from historical observations and relevant experiments. In a relatively simple linear optimal estimation, the modelled spectra must give a close fit to the measured spectrum and to the *a priori* profile. In this inverse model,

$$\mathbf{x} = \mathbf{x}_a + (\mathbf{K}^T\mathbf{S}_\epsilon^{-1}\mathbf{K} + \mathbf{S}_a^{-1})^{-1}\mathbf{K}^T\mathbf{S}_\epsilon^{-1}(\mathbf{y} - \mathbf{K}\mathbf{x}_a) \tag{2.6}$$

where $\mathbf{S}_a$ is the error assigned to the *a priori* assumption (called the *a priori* covariance matrix) and $\mathbf{S}_\epsilon$ is the combination of the measurement and modelling error, including any forward-modelling errors (measurement covariance matrix). The *a priori* covariance matrix contains not only the error but also the assumed vertical smoothing, represented by non-zero off-diagonal elements (representing the correlation between different pressure levels, p_i and p_j) which is set as,

$$S_{ij} = S_{ii}S_{jj}\text{exp}(((p_i - p_j)/l)^2) \tag{2.7}$$

where l is the correlation length, the scale in terms of the logarithm of the pressure over which the inter-level correlation drops off by $1/e$. The smoothing of the retrieved profiles is controlled by this correlation length parameter and a value of 1.5 is assumed for all profiles after being tested to approximate a scale height in vertical resolution.

The linear solution in equation 2.6 is too large a simplification and ends in very large errors. Instead, non-linear optimal estimation is a better solution using a Newtonian iteration technique. This iterates the retrieval a chosen number of times until the fit converges to a solution within the errors specified. The initial reference state ($\mathbf{x}_a$) is used to calculate a new estimate of the solution and then that is used as the reference state for the next iteration and so on.

$$\begin{aligned}\mathbf{x}_{n+1} &= \mathbf{x}_a + \mathbf{S}_a\mathbf{K}_n^T(\mathbf{K}_n\mathbf{S}_a\mathbf{K}_n^T + \mathbf{S}_\epsilon)^{-1}(\mathbf{y}_m - \mathbf{y}_n - \mathbf{K}_n(\mathbf{x}_a - \mathbf{x}_n)) \\ &= \mathbf{x}_a + \mathbf{G}_n(\mathbf{y}_m - \mathbf{y}_n) + \mathbf{G}_n\mathbf{K}_n(\mathbf{x}_a - \mathbf{x}_n)\end{aligned} \tag{2.8}$$

where n is the iteration number and therefore $\mathbf{K}_n$ is the weighting function matrix for the nth iteration. $\mathbf{y}_m$ is the measured spectrum and $\mathbf{y}_n$ is the synthetic spectrum calculated from the nth solution, $\mathbf{x}_n$. This can be defined in terms of $\mathbf{G}$, the gain matrix, which is the derivative of the estimated state with respect to the measurement and gives the contribution of each measurement in $\mathbf{y}$ to the estimated state vector.

The inclusion of the *a priori* covariance matrix, $\mathbf{S}_a$, and the *a priori* state vector, $\mathbf{x}_a$ is what makes this process 'optimal estimation' and modifies the cost-function. The cost-function, ϕ, quantifies the error between predicted values and expected values,

$$\phi = (\mathbf{y}_m - \mathbf{y}_n)^T\mathbf{S}_\epsilon^{-1}(\mathbf{y}_m - \mathbf{y}_n) + (\mathbf{x}_n - \mathbf{x}_a)^T\mathbf{S}_a^{-1}(\mathbf{x}_n - \mathbf{x}_a) \tag{2.9}$$

where the first term describes how well the spectrum fits the data (i.e., the standard 'least squares' value, albeit recast with an error covariance matrix), and the second term describes how far the solution deviates from the assumed *a priori* state vector. The process of iteration is what NEMESIS uses to minimize this cost-function. The optimal solution to the state vector is found and the degree to which it deviates from the *a priori* will depend upon the relative size of the errors contained within the *a priori* and measurement covariance matrices.

Non-linear retrievals can become rapidly unstable, with the solution to each iteration quickly diverging from the optimal solution so that the cost function, ϕ, increases without bound. A type of braking/damping parameter (NEMESIS uses a Levenberg-Marquardt braking parameter) is used to stabilise the model and is altered according to the change in the cost function at each stage of the iteration. The retrieval is deemed to have converged when ϕ alters by less than 10% (an arbitrary limit), the braking parameter tends to zero and the solution tends to the optimal estimate.

For cases where $\mathbf{K}_n$ varies greatly between steps, in the case of most non-linear inversions, then the number of iterations required is usually 10-20. 15 iteration steps was enough for the the convergence to happen in the models for both ice giants.

The quality of fits can be assessed by considering the goodness-of-fit parameter, the reduced chi-squared (χ^2/n) reported by NEMESIS. This value is the weighted sum of squared errors, χ^2, divided by n. The value of n is difficult to assess and is typically approximated as the number of points in the spectrum. Technically this should be reduced by the number of degrees of freedom in the model but that is hard to assess when doing a full-profile retrieval where the atmospheric levels cannot be considered as independent. The reduced chi-squared is optimally a value around unity and a much larger value suggests the model is underfitting the data. A much smaller value suggests the model is overfitting the data. We use the term chi-squared and reduced chi-squared interchangeably throughout the results chapters but, when we are referring to a value close to 1, we mean the χ^2/n value.

Another value that can be used to assess the quality of the fits is the retrieval error,

$$\hat{\mathbf{S}} = (\mathbf{S}_a^{-1} + \mathbf{K}_n^T \mathbf{S}_\epsilon^{-1} \mathbf{K}_n)^{-1} \tag{2.10}$$

which combines the measurement error, modelling error and the error on the *a priori* assumptions. $\hat{\mathbf{S}}$ is only an estimate of the error on the retrieved parameters but it has been shown that when the data is of a relatively high spectral resolution and signal-to-noise this assumption is valid (Line et al., 2013). This means the retrieved errors of the low-resolution modules on Spitzer that will be described in the next chapter should be viewed with some caution but are valid for the high-resolution module spectra, as long as errors from other sources have also been accounted for.

An error is defined as the difference between the measurement result and the value of the measurand. The uncertainty however, describes the reliability of the assertion that the stated measurement result represents the value of the measurand. Though the error can be calculated in a quantitative fashion as discussed above, the uncertainty in the retrieval process comes from many different factors:

- The measurement and modelling errors are not always well known
- Optimal estimation assumes that the errors on the parameters are Gaussian, which is not always true
- Incorrect paramaterisation, for example, the assumption that a gas is well-mixed when it is not
- Incomplete physical description of the radiative transfer, for example, any missing gases, aerosols or unaccounted for processes like fluorescence
- The uncertainty involved in constructing the k-tables and how well the approximation handles simulating the features (especially very small ones)

Therefore the $\hat{\mathbf{S}}$ value is likely to provide an underestimate of the true retrieval error. This is where the tuning process of the retrievals comes in, where we try to test any assumptions that have been made in order to reduce the uncertainties. We can also account for a poor model description or a calibration problem by loosening the constraints and adding forward-modelling error in the first stages of the retrieval. This prevents 'exact' fits that exhibit non-physical oscillations and is accounted for in $\hat{\mathbf{S}}$.

In summary, optimal estimation is sensitive to prior assumptions and is therefore reliant on there being a hypothesis to test. This means that not only could a completely unexpected process be overlooked, but also that only the best solution out of many possibilities can be chosen. These limitations must be kept in mind throughout the investigation and are discussed throughout Chapter 5 and 6. Spectral retrieval is a robust tool for interpreting planetary remote sensing observations that has been used worldwide in numerous areas of atmospheric science. This thesis takes advantage of the many strengths of this technique to characterise the atmospheres of both Uranus and Neptune using NEMESIS.

2.4.1 Running NEMESIS

To run NEMESIS, input files are manipulated to see what effect they have on the output calculated spectrum. Every user generally has their own mechanisms for running NEMESIS, with pipelines in IDL and Python to distribute large batch jobs to supercomputer clusters. The basic operation remains the same no matter the user. Input files are generated to run in NEMESIS, then using code in IDL we plot and interpret the output.

The input files are subdivided into four categories: (i) those setting up the atmospheric structure for Uranus or Neptune, (ii) those telling NEMESIS how to run, (iii) those specifying the sources of opacity, and (iv) those specifying the measurement. There are many of these files, but below we discuss the ones that contain the most information and are therefore adapted the most throughout the retrieval process.

NEMESIS is not hard-wired to a particular planet, so needs to be given the basic atmospheric structure as a starting point for fitting a spectrum. The most important file is the *.ref* file, which contains the reference height, pressure, temperature and composition grid for each gas on every atmospheric level. This file also has a flag to say which planet we're looking at and a list of identifiers for the gases to be included in the reference model.

The *.inp* file contains a list of flags allowing you to specify many parameters. Some important examples are whether wavenumber or wavelength space is to be used, whether to use line-by-line or ktables, whether to add forward modelling error, the number of iterations and which units the output spectrum will be in.

When you run a retrieval, NEMESIS will calculate the spectrum based on the contents of the reference profile but modified with the profiles you're actually retrieving. In the *.apr* file, you can specify exactly what you wish to retrieve. NEMESIS can use different retrieval models for different parameters in the same inversion. We use only two of those models in our experiments, model 0 and model 3. Model 0 retrieves a continuous vertical profile of the specified parameter. For example, after testing, we decided that the temperature profile can always be retrieved using model 0 with *a priori* errors of 3 K. The full profile, containing the temperatures at the number of pressure levels in the model, is output by NEMESIS along with the associated errors at every level. Model 3 retrieves a scaled parameter and only one scale factor value and associated error are output by NEMESIS. Model 3 takes up a lot less computing power than model 0 and so is used, typically, when there are a lot of parameters present in the model, but as long as we can converge on a good fit with model 3, model 0 is not needed. Model 3 was applied to gases, assuming an *a priori* vertical profile.

With these input files and various others, NEMESIS can run the retrievals over multiple iterations. It will generate multiple intermediate files during the process and produce the output files that are used in analysis.

There are multiple output files but the most important is the *.mre* file containing the final result. This file contains two matrices. The first is a matrix showing the fit of the spectrum to the data and can be used to plot the results of the spectral fit and to estimate the reduced chi-squared value. The second matrix contains the retrieved properties. These results are displayed in multiple ways using IDL with examples shown throughout Chapter 5 and 6.

2.4.2 Ice Giant Reference Atmospheres

The reference atmospheres we use for the ice giants are similar and contain the same building blocks. They do, however, have some fundamental differences. There are some different chemicals present in their spectra. For example, ethylene and methyl are present at Neptune but are not visible in the spectra at Uranus. These species have to be contained in the reference files and also present in k-distribution lists. They are based on the *a priori* assumptions of the vertical thermal and gaseous profiles that are based on the results of previous studies and therefore come from different literature sources and models. All of these specifics are detailed in Chapter 5 for Uranus and Chapter 6 for Neptune. This section will explain the parts and methods for generating the reference atmospheres that are the same for both planets.

Sources of Line Data

A number of databases list the molecular absorption lines of important gases, as well as the intensities, half-widths and temperature-dependent broadening parameters that are needed to generate the k-distributions. The NEMESIS group mainly uses lines from the HITRAN (Rothman et al., 2009, 2013) and GEISA (Jacquinet-Husson et al., 2003, 2011, 2016) molecular databases. However, there are some differences that have been listed in Table 2.1. For example, one type of underlying collision-induced absorption (CIA), that of $H_2{-}H_2$, is taken from Fletcher et al. (2018) so as to include the contributions of hydrogen dimers. The databases also provide data for the air-broadened line widths and temperature coefficients. Air-broadened values are measured/calculated using a mixture of nitrogen and oxygen, as found on Earth but at the ice giants the atmosphere is primarily H_2, making H_2-broadening coefficients more useful. It is only CO_2 that has air-broadened parameters and this serves as an adequate estimate for H_2-broadened lines. We are assuming thermochemical equilibrium para-H_2 fraction throughout this work. A species not found in the usual databases is methyl (CH_3), which is included in the Neptune model, and is explained in detail in Chapter 6.

Disc-Averaging

NEMESIS provides two methods of calculating the disc-averaged spectrum - a faster technique using exponential integrals (Goody and Yung, 1995) to compute the emission into a hemisphere (used by Fletcher et al., 2014, for the study of AKARI spectra of Neptune), and a slower but more accurate technique splitting the disc into a number of paths at different emission angles (used by Teanby and Irwin, 2013, to analyse Uranus' disc-averaged spectrum from Herschel/SPIRE). We select the latter, more accurate technique for this study.

To simulate the disc-averaged spectrum we used the same method used by Teanby and Irwin (2013) and detailed in Teanby et al. (2013). Ten discrete atmospheric paths are used with finer spacing near the limb to account for rapid changes due to limb brightening and darkening. We tested between 50 and 5 field of view points and ten points proved the best when balancing computation speeds and spectrum reproducability. NEMESIS calculates the spectrum along these ten paths and sums them up using the weightings in Table 5.1. The weighting is:

$$w_i = \frac{x_i x_{i+1} - x_{i-1} x_i}{r^2} \tag{2.11}$$

Where x is the offset from the sub-observer point and is associated with an emission angle and r is the radius of the planet with any added limb. This equation is adapted from Teanby et al. (2013).

This method was chosen over the NEMESIS variant that computes the disc-average using the exponential integral technique due to better model fits to the data. This variant was designed for use with secondary-eclipse spectra of exoplanets, but was found to be unable to reproduce the coldest limb-darkened parts of the Uranian spectrum, and proved too sensitive to the choice of lower pressure boundary that represents the planetary limb (Orton et al., 2014a). The method chosen is slower but much more effective in allowing more reliable coverage of the limb, taking into account the limb brightening and darkening effects just as the 10-stream trapezoidal quadrature method in emission angle cosine used by Orton et al. (2014a) for Uranus.

This method was first tested for Uranus and then applied to Neptune due to its effectiveness in reproducing the spectrum.

To make sure we capture the rapid changes happening at the limb, we had to extend the limb of both planets above the 1-bar level. NEMESIS can compute the spectral radiance and irradiance in numerous different formats. We have chosen to compute the integrated spectral power of the planet with units of W/μm. To convert to these units we use the extended radius value (Teanby et al., 2013). The weightings in equation 2.11 are also calculated using these same extended radius values. The atmospheric level that we have defined the zenith angle of the observation from is the 0 km (1 bar) altitude.

Eddy Diffusion Coefficient

We discussed what eddy diffusion is in Chapter 1 when we talked about the dynamics of ice giant atmospheres. In 1D photochemical models, vertical transport is assumed to operate through eddy and molecular diffusion. To understand the effects of these processes on the vertical abundance profiles, we need a more general way to parameterise the vertical flux of the molecules. A parcel of air displaced vertically will carry the mean abundances of its original level for a characteristic distance analogous to the mean free path in molecular diffusion. This displacement will create a turbulent fluctuation in the composition of the new level. The magnitude of this depends on the characteristic distance and the vertical gradient of the mean composition. This means we can model the process by defining an eddy-mixing coefficient, K and takes into account both the molecular and eddy diffusion processes. The vertical flux of species, i is defined as,

$$\phi_i = n_i \left[-D_i \left(\frac{1}{n_i}\frac{\partial n_i}{\partial z} + \frac{1}{H_i} + \frac{1}{T}\frac{\partial T}{\partial z} \right) - K \left(\frac{1}{n_i}\frac{\partial n_i}{\partial z} + \frac{1}{H_a} + \frac{1}{T}\frac{\partial T}{\partial z} \right) \right] \tag{2.12}$$

where D_i is the molecular diffusion coefficient of the ith species, T is the temperature, H is the pressure scale height and K is the eddy diffusion coefficient that we can attempt to determine via observations (Irwin, 2009). H_i is the pressure scale height of the species and H_a is that of the bulk atmosphere. The level where molecular diffusion becomes dominant (i.e. the species tends to its own profile with its own scale height) is called the homopause. The homopause level, where $D_i = K$, at the ice giants is the level at which methane begins to separate diffusively from the background gas (see Chapter 1).

The eddy diffusion coefficient (K_{zz}) profile is one of the major free parameters for photochemical models. K_{zz} has units of cm^2s^{-1} and can be constant with altitude like is assumed at Uranus, or change depending on the pressure/density of the atmosphere like is assumed at Neptune (Moses et al., 2018). The suffix zz reminds us that K has a functional dependence on the altitude. It is parameterised as,

$$\begin{aligned} K_{zz} &= K_H \left(\frac{n_H}{n_{zz}}\right)^{\gamma}, \text{ for P} \leq \text{P}_T \\ &= K_T \left(\frac{n}{n_0}\right) \text{ or, } = K_T, \text{ for P} > \text{P}_T \end{aligned} \tag{2.13}$$

where P_T is the pressure at the tropopause, n_{zz} is the total number density, and γ is a coefficient close to 0.5 (Atreya, 2013). n_H is the number density at the homopause and K_H is the eddy mixing coefficient at this same level. Equation 2.13 also shows that this coefficient, and therefore the entire model, is dependant on where the homopause level is defined. We discuss the K_{zz} and homopause levels for each planet model in Chapter 5 and 6.

Local Thermodynamic Equilibrium (LTE)

The internal energy of a gas in local thermodynamic equilibrium (LTE) is characterised by a single temperature, applicable to all degrees of freedom. This temperature specifies the populations of states according to a Boltzmann distribution which is maintained by collisions. At low pressures, radiative processes usually control the populations of states and departures from LTE can occur.

The RTE (equation 2.4) assumes LTE because it uses the Planck function and the current model used in NEMESIS also assumes LTE. At high-enough pressures, the molecular collisions are sufficiently rapid to keep the atmosphere in this state. However, at low pressure, the time between collisions becomes much larger, making the Planck function unusable and there are departures from the usual Boltzmann distribution for populations of states. Under these non-LTE conditions, the Planck function is replaced with the Source function making calculations much more complicated (Irwin, 2009).

Evidence suggests that this is suitable for the gas giants at these wavelengths but not for the extreme cold of the ice giants (Orton et al., 2014b). This means corresponding atmospheric temperatures can differ significantly from the local kinetic temperature assumed, which could generate a systematic offset in retrieved temperatures and abundances at low pressures. Appleby (1990) found that a temperature difference of up to 20 K is possible at Uranus due to non-LTE effects at pressures of around 0.1 μbar. This is higher than the Spitzer data is sensing but significant deviations from LTE for methane at 1300 cm^{-1} were found to occur starting at pressures of around 0.1 mbar. At Neptune, the differences were smaller and the thermal structure is not significantly altered when comparing LTE to non-LTE. As the source functions for the hydrocarbons remain poorly constrained under ice giant conditions, a hybrid radiative transfer code combining LTE and non-LTE effects is planned for future work.

2.5 Summary

This chapter provided an introduction to spectroscopy and radiative transfer as well as an insight into the processes happening inside the NEMESIS retrieval software. This software will be used in Chapter 5 for Uranus and 6 for Neptune. It will also be used in forward modelling mode in Chapter 7. The reference atmosphere we use for both ice giants has been outlined with the specifics talked about in their respective results chapters. The measured spectra that are needed for the retrieval process are from the Spitzer Space Telescope Infrared Spectrometer and these data are the subject of the next Chapter.

Gas	Line intensities	Broadening half-width	Temperature dependence
H_2 quadrupoles	Rothman et al. (2013)	0.0017 $cm^{-1}atm^{-1}$	n = 0.75 assumed
H_2-H_2 CIA	Fletcher et al. (2018)	Fletcher et al. (2018)	Fletcher et al. (2018)
H_2-He CIA	Borysow et al. (1988)	Borysow et al. (1988)	Borysow et al. (1988)
H_2-CH_4 CIA	Borysow and Frommhold (1986)	Borysow and Frommhold (1986)	Borysow and Frommhold (1986)
CH_4 and isotopes	Brown et al. (2003)	H_2 broadened using a half-width of 0.059 $cm^{-1}atm^{-1}$ at 296 K	n = 0.44 Margolis (1993)
C_2H_6	Vander Auwera et al. (2007)	0.11 $cm^{-1}atm^{-1}$ at 296 K Blass et al. (1987)	n = 0.94 Halsey et al. (1988)
C_2H_2	Jacquinet-Husson et al. (2003)	Fits to data in Varanasi (1992)	Varanasi (1992)
CO_2	Rothman et al. (2009)	Air-broadened	-
C_4H_2	Jacquinet-Husson et al. (2011)	0.1 $cm^{-1}atm^{-1}$ for all lines	n = 0.75 assumed
C_3H_4	Jacquinet-Husson et al. (2011)	0.075 $cm^{-1}atm^{-1}$ for all lines	n = 0.50 assumed
C_2H_4	Jacquinet-Husson et al. (2003)	Polynomial fits to data from Bouanich et al. (2003, 2004)	n = 0.73 Bouanich et al. (2004)
C_3H_8	Jacquinet-Husson et al. (2011)	0.08 $cm^{-1}atm^{-1}$ for all lines	n = 0.75 assumed
CH_3	Stancu et al. (2005)	0.035 $cm^{-1}atm^{-1}$ (Bézard et al., 1999)	0.75 (Bézard et al., 1999)

Table 2.1: Table of the sources of line data used in the radiative transfer models of Uranus and Neptune. Ethylene (C_2H_4), propane (C_3H_8) and methyl (CH_3) are only in the model for Neptune and CH_3 k-table construction is discussed in Chapter 6.

Chapter 3

Data

3.1 Introduction

This thesis is based on the mid-infrared observations of Uranus and Neptune from NASA's *Spitzer Space Telescope (SST)*. The telescope was a 3-axis stabilised pointing and scanning observatory launched on the 25 August 2003 into an Earth-trailing heliocentric orbit.

Spitzer's novel cryogenic architecture and overall configuration of the flight system is shown in Figure 3.1. It consists of an all-Beryllium telescope, with an 85-cm primary mirror and a secondary mirror that can be moved in an axial direction to focus the telescope on-orbit. Spitzer's predecessors (e.g. ISO) packaged the whole telescope inside the cryogen so it was cold even from launch. Spitzer is novel in design because it launched with the greater part of it at room temperature. It was cooled on-orbit by a combination of active cooling by evaporating helium and passive cooling by always orienting the solar panels to shade the telescope from the sun.

The science payload consisted of three cryogenically-cooled focal plane instruments with capabilities from the near to the far infrared: the InfraRed Array Camera (IRAC), the Multiband Imaging Photometer for Spitzer (MIPS), and the Infrared Spectrograph/Spectrometer (IRS). Spitzer's great scientific power follows directly from the size and quality of the arrays used at all wavelengths for both imaging and spectroscopy. The cryogen was depleted on 15 May 2009 with the warm mission continuing until the observatory's decommissioning on 30 January 2020. Only the IRAC instrument was partially operational during the warm mission. However, this investigation solely uses data from the IRS instrument.

The IRS (Houck et al., 2004) acquired 5 - 37 micron spectra of Uranus and Neptune between 2004 and 2007. Uranus was observed twice in Cycle-1 time in November 2004 (Burgdorf et al., 2006), July 2005, then again during Directors Discretionary Time

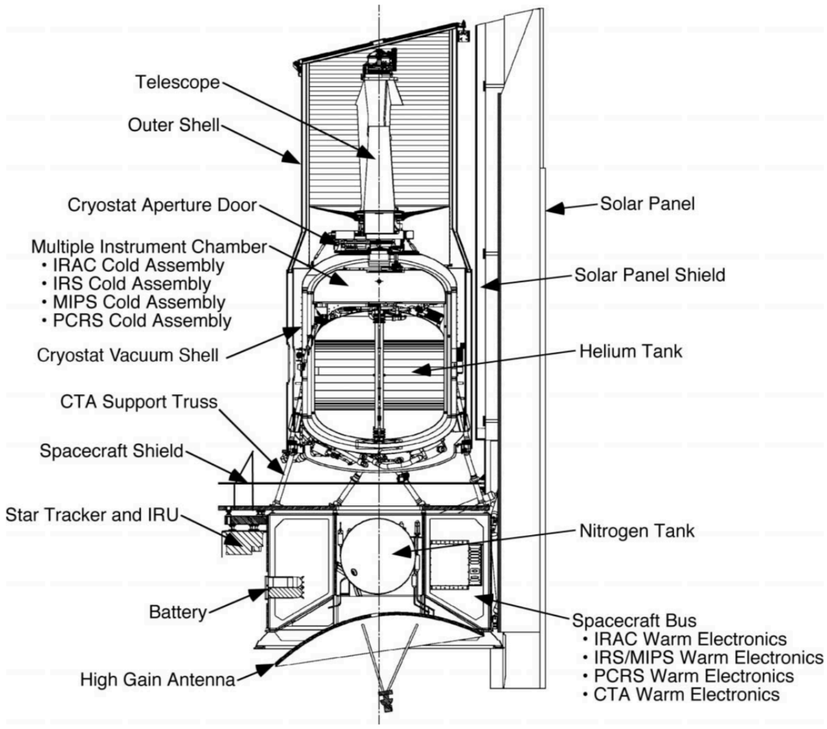

Figure 3.1: Spitzer flight hardware diagram (Werner et al., 2004). The observatory is approximately 4.5 m tall and 2.1 m in diameter.

(DDT) very near its equinox in December 2007. The mean of the four observed longitudes in 2007, spaced equally around the planet, have provided the opportunity for the most comprehensive characterisation of Uranus' vertical structure (temperature and hydrocarbon composition) ever obtained (Orton et al., 2014a,b; Rowe-Gurney et al., 2021). The IRS acquired a similar set of spectra for Neptune in May 2004 (Meadows et al., 2008), November 2004, November 2005, and May 2006. Meadows et al. (2008) discovered and derived the abundances of Neptune's complex hydrocarbons methylacetylene and diacetylene. The rest of the Neptune data has yet to be published.

These data are used throughout the results in Chapters 4, 5 and 6. In this chapter we describe the IRS instrument and outline the available data. We discuss the methods used to reduce and calibrate it and the associated errors. The data reduction process outlined in Sub-section 3.4.1 and the Uranus-specific information throughout this chapter are published in Rowe-Gurney et al. (2021).

3.2 Spitzer Infrared Spectrometer (IRS)

The IRS instrument is the main source of the data used throughout this thesis and the only instrument used that is aboard the SST. The IRS has four modules of varying resolution and wavelength capabilities (Short-Low, Short-High, Long-Low and Long-High; see Table 3.1 and Figure 3.2). Two modules provide low spectral resolution (R$\sim$60 – 130) over 5.2 – 38 μm, and two provide higher spectral resolution (R$\sim$600) over 9.9 – 37.2 μm.

Spitzer has a mirror diameter of 0.85 m so the data obtained are disc-averaged, with no spatial resolution. The spatial or angular resolution of a telescope is dependent on the wavelength, λ, of the observed radiation and can be approximated by

$$R_\theta = \frac{\lambda}{D} \tag{3.1}$$

where D is the diameter of the telescope's mirror. The resulting R_θ is measured in radians with sources larger than the angular resolution called extended sources and sources smaller than the resolution called point sources. In Spitzer's case, both ice giants are treated like point sources because at the centre of its range (at 20 μm) the resolution is around 3.5 arcsec, approximately the same diameter as Uranus and larger than Neptune's.

What Spitzer lacks in spatial resolution it makes up for in spectral resolution. A spectrometer, like the IRS, is the scientific instrument used to do spectroscopy. They are characterised by their resolving power R_λ and by what wavelength band they can detect. The resolving power is defined as:

$$R_\lambda = \frac{\lambda_0}{\Delta\lambda} \tag{3.2}$$

i.e. the capability to distinguish between two neighbouring wavelengths. The spectral resolution, $\Delta\lambda$, is the smallest difference in wavelengths that can be distinguished at the observed wavelength, λ_0 (Sanchez-Lavega, 2010, p.565). The resolving power R of the different Spitzer IRS modules can be found in Table 3.1. It quotes this resolving power of 600 for the SH and LH data. This number, however, is for faint sources where Gaussian smoothing must be applied in order to boost the signal to noise ratio. Uranus and Neptune are much brighter and therefore have plenty of signal to noise for this smoothing to not be necessary. The effective resolving power is therefore variable with the wavelength/wavenumber and is for example, around 750 at the 17 μm S(1) quadrupole feature of Neptune. We discuss how the variability of the resolving power of the IRS high-resolution modules affects the results in Chapter 5 and 6.

The wavelength range acquired for this investigation is 5.2 – 37.2 μm utilising all four modules and using the astronomical observation template (AOT) called "staring" mode that gives a spectrum of an individual fixed or, in this case, moving target. The IRS contains no moving parts and its four modules are in separate, fixed boxes that allow only one module to take observations at a time. This means that to switch from module to module the telescope has to move to point at the target each time.

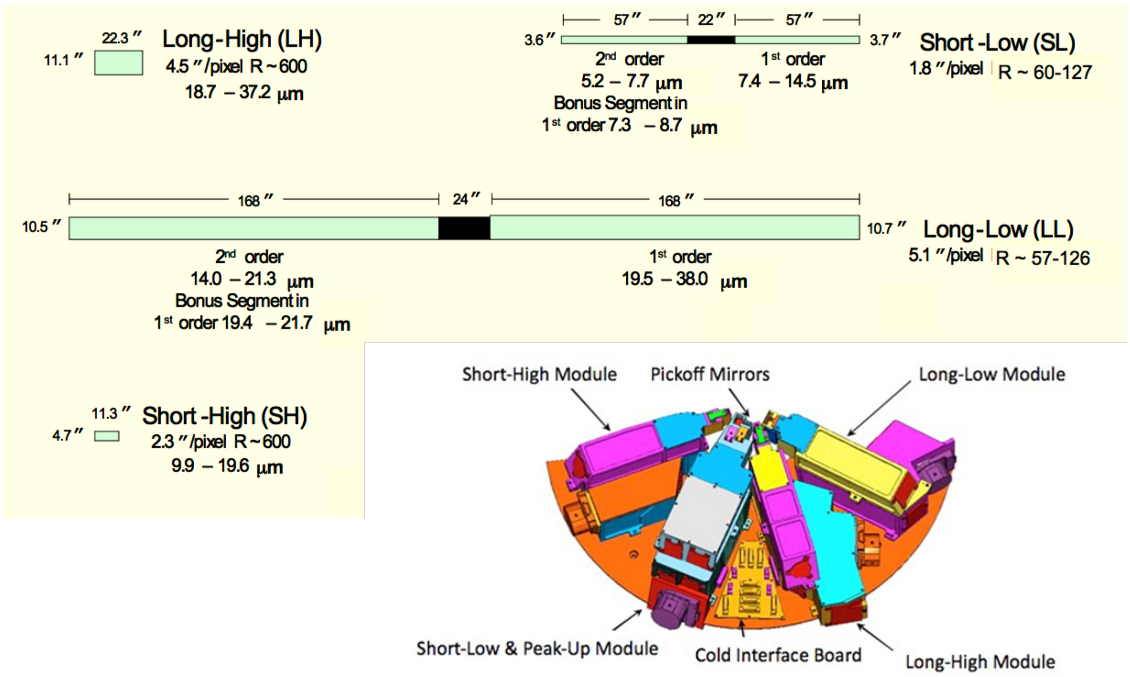

Figure 3.2: IRS module assembly and summary of properties. Wavelengths labeled in this figure are approximate with more accurate values in Table 3.1. The slits are not parallel as depicted in this figure. The actual slit position angles relative to a Spitzer roll angle of 0° are SL = +84.7°, LL = +181.2°, SH = +221.5° and LH = +136.7° (Houck et al., 2004, and IRS Pocket Guide v3.1).

The low-resolution modules are split into two separate sub-slits and therefore have three orders, two main orders and a bonus third order caused by overlapping regions between the two. These two modules (SL and LL) are both grating spectrographs that utilise a diffraction grating for optical dispersion. The high-resolution modules have a single slit but have ten orders each and use a cross-dispersed echelle design that allows broad spectral coverage for each exposure. An echelle grating, which is a type of diffraction grating, has a low groove density optimised for high incidence angles

Module	Detector	λ (μm)	R	Slit Width ($''$)	Slit Length ($''$)
SL1		7.46-14.29			
SL2	Si:As	5.13-7.60	60-127	3.6-3.7	57
SL3		7.33-8.66			
LL1		19.91-39.90			
LL2	Si:Sb	13.90-21.27	57-126	10.5-10.7	168
LL3		19.23-21.61			
SH	Si:As	9.89-19.51	600	4.7	11.3
LH	Si:Sb	18.83-37.14	600	11.1	22.3

Table 3.1: Spitzer IRS module characteristics (Houck et al., 2004). The detector substrate, wavelength range (λ) in μm, resolving power (R), and the slit sizes in arc-seconds for each module.

and therefore increased dispersion of features. The grating is also cross dispersed, which spreads the features out more so they can be differentiated easier. The SH module has a small overlap of wavelengths with the LH. As can be seen in Table 3.1 the short wavelength detectors are both arsenic-doped silicon arrays whereas the long wavelength detectors are both antimony-doped silicon arrays. Examples of detector images from the four modules can be seen in Figures 3.3 and 3.4.

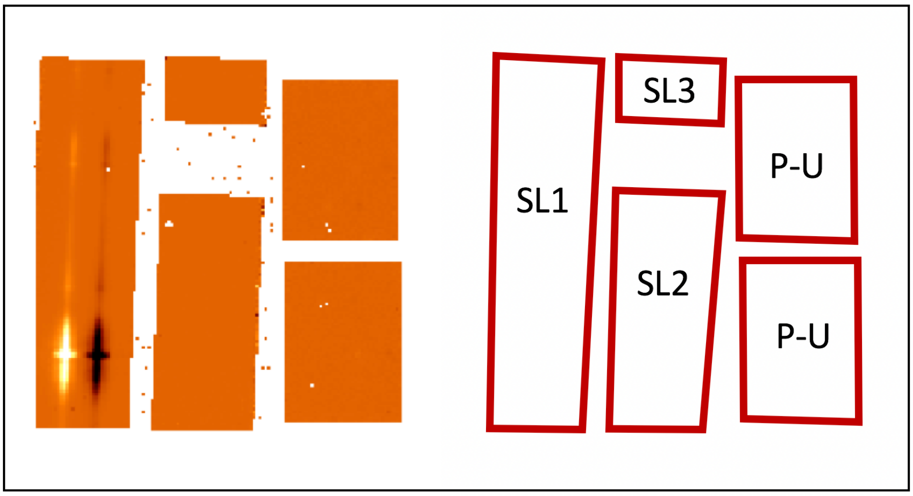

Figure 3.3: SL module detector image showing an example of two nods of data (inverted for clarity) in SL1 module. SL1, 2 and bonus order 3 identified along with the peak-up (P-U) modules that were not used for the ice giants.

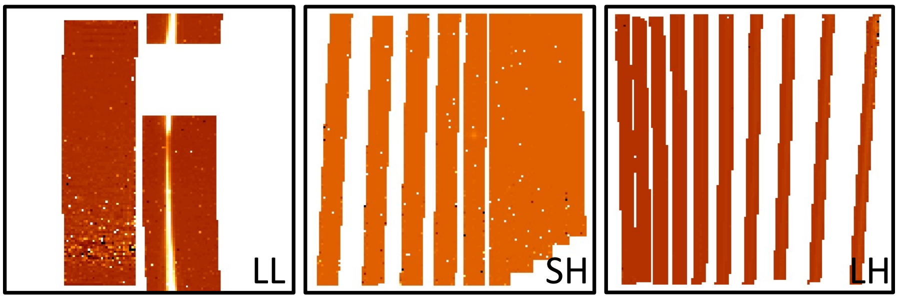

Figure 3.4: Detector images from LL, SH and LH modules. Source shown clearly in module LL2 and bonus order 3 with LL1 (on the left) not used for the ice giants due to expected saturation.

3.3 Ice Giant Data

The discs of Uranus and Neptune, with approximate angular diameter 3.35-arcsec and 2.22-arcsec respectively, are treated as unresolved sources and therefore the resulting spectra are disc-averaged. The discs fit into all of the slit sizes in Table 3.1 and therefore no mapping or mosaicking was needed when taking exposures of either planet. A program was needed to account for the overfilling of some of the narrower slits due to the spreading caused by the PSF (Point Spread Function) of the instrument but we will detail this in Section 3.4.1.

Table 3.2 summarises the observations made with Spitzer. We have three epochs of Uranus and four epochs of Neptune available from the archive. The highest quality data with optimised exposure times (Table 3.3) and therefore lowest noise are the latest datasets, Uranus-2007 and Neptune-2005. These are the datasets that have been used most extensively in the longitude study in Chapter 4 and both the retrieval Chapters (5 and 6). The other epochs have been used for reference, mostly using the more reliable low-resolution modules (Fig. 3.6 and 3.8).

Planet	**Cycle**	**Date**	**Modules**	n_{long}	**Program ID**	**PI**	**Primary Reference**
Uranus	1	12/11/2004 - 13/11/2004	SL, SH, LH	3	71	James R. Houck	Burgdorf et al. (2006)
Uranus	1	06/07/2005 - 07/07/2005	SL, SH, LH	4	3534	Glenn S. Orton	Rowe-Gurney et al. (2021)
Uranus	2 (DDT)	16/12/2007 - 17/12/2007	SL, LL, SH, LH	4	467	Dean C. Hines	Orton et al. (2014a,b)
Neptune	1	15/05/2004	SL, SH, LH	3	71	James R. Houck	Meadows et al. (2008)
Neptune	1	15/11/2004 - 16/11/2004	SL, SH, LH	4	3534	Glenn S. Orton	-
Neptune	2	19/11/2005 - 22/11/2005	SL, SH, LH	3	20500	Glenn S. Orton	-
Neptune	2	31/05/2006	SL, SH, LH	1	20500	Glenn S. Orton	-

Table 3.2: Table of observations of Uranus and Neptune made using Spitzer IRS. n_{long} is the number of distinct central meridian longitudes observed. Data were downloaded from the Spitzer Heritage Archive (`https://sha.ipac.caltech.edu/applications/Spitzer/SHA/`) and reduced and stored at `https://doi.org/10.5281/zenodo.4617490` and `https://doi.org/10.5281/zenodo.5254503` for Uranus and Neptune respectively.

An important characteristic of the data is the exposure time for each module, shown in Table 3.3. The earlier campaigns (2004) were integrated over shorter time periods for most modules, resulting in noisier data. We will discuss how this impacts our ability to use the data later on.

Planet	**Module**	**Program ID**	**Epoch**	**Integration Time (s)**
Uranus	SL	467	2007	700
		3534	2005	700
		71	2004	48
Uranus	SH	467	2007	1800
		3534	2005	480
		71	2004	48
Uranus	LH	467	2007	24
		3534	2005	24
		71	2004	48
Uranus	LL	467	2007	90
Neptune	SL	20500	2005/06	316
		3534	2004	140
		71	2004	48
Neptune	SH	20500	2005/06	360
		3534	2004	480
		71	2004	48
Neptune	LH	20500	2005/06	36
		3534	2004	24
		71	2004	48

Table 3.3: Table to show the integration time for each module for each Spitzer campaign. Exposure time is the time for which the timing pattern generator was running during an IRS exposure. The integration is the exposure time summed over the multiple exposure cycles for that module. This time is per longitude observation and does not take into account the different number of longitudes per campaign. The SL times are the summation of the SL1 and SL2 exposure times. The longer the time, the better the signal-to-noise.

3.3.1 Uranus

The globally-averaged spectra from December 2007 are shown in Fig. 3.5. These data are processed using the updated reduction pipeline outlined in Section 3.4. This is the same data that were used in the Orton et al. (2014a,b) global study of Uranus. The spectrum contains several different complex hydrocarbons associated with the lower- and mid-stratosphere (Moses et al., 2018) and five hydrogen quadrupole lines sensing the upper stratosphere (Orton et al., 2014a). The hydrogen-helium collision-induced absorption (CIA) is a main feature of the spectrum present at the higher pressures of the troposphere, creating the overall shape of the entire spectrum (Orton et al., 1986). Monodeuterated methane (CH_3D) on Uranus is also associated with these higher pressures due to its low abundance, unlike CH_4 that senses the lower-pressure regions of the stratosphere. Complex hydrocarbons that are the products of methane photodissociation include ethane (C_2H_6), three ro-vibrational bands of acetylene (C_2H_2), diacetylene (C_4H_2) and methylacetylene a.k.a. propyne (CH_3C_2H a.k.a. C_3H_4).

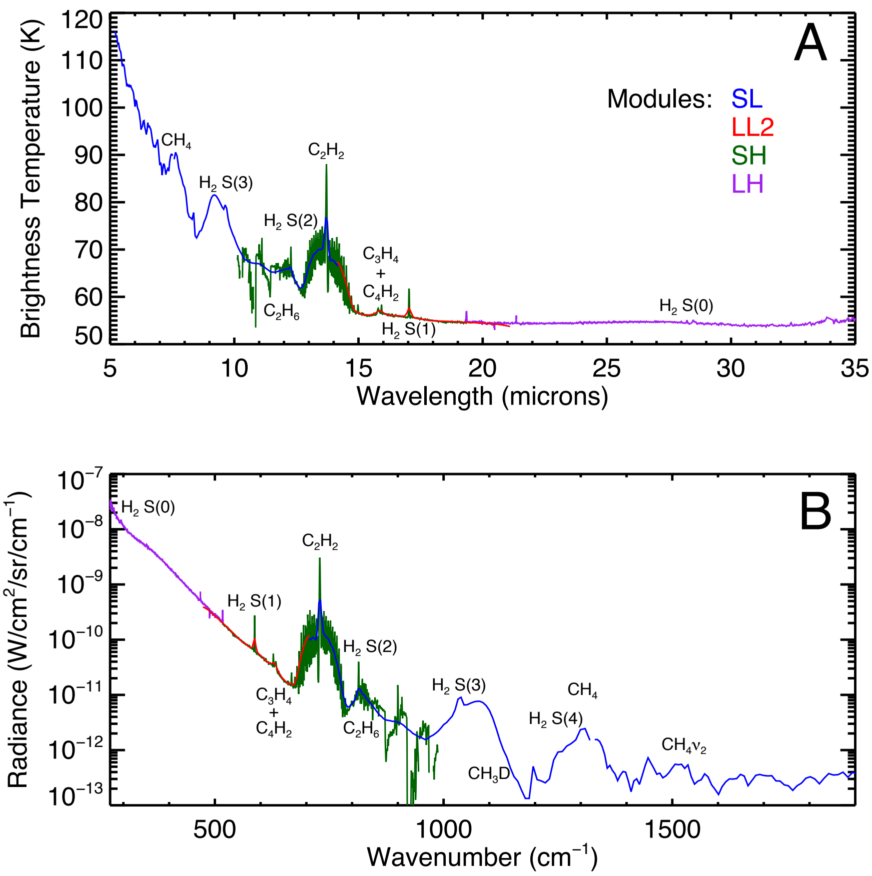

Figure 3.5: The global average spectrum of Uranus for observations made on 16th-17th December 2007 using all available modules of the Spitzer Space Telescope Infrared Spectrometer. The modules are shown in different colours: Short-Low (SL) in blue, Long-Low second order (LL2) in red, Short-High (SH) in green and Long-High (LH) in purple. Panel A shows brightness temperature vs. wavelength and panel B shows radiance vs. wavenumber. Well-defined spectral features are labelled with their chemical names.

Table 3.2 shows that data from July 2005 and November 2004 are also available for analysis. The 2004 data have been previously published by Burgdorf et al. (2006) but the 2005 data remain unpublished. The low resolution data from both epochs have been reduced using the updated pipeline so they can be properly compared. Fig. 3.6 shows that 2005 has a higher radiance than 2007 at shorter wavelengths. The 2004 data appear even brighter at these same wavelengths. This could reflect changes in the visibility of reflective aerosols associated with the southern hemisphere as it approached autumn equinox. There are no LL module data for 2004 or 2005 so only the SL module can be compared directly.

Table 3.3 shows that the SL module integration times for the 2005 observations are the same as for 2007 with around 12 minutes of exposure for each longitude observation. The 2004 data however, have an integration of less than a minute, so the signal-to-noise ratio is much lower and the resulting spectra less reliable. This can be seen in Figure 3.6 where the noise at wavenumbers greater than around 1400 cm^{-1} is visibly much more significant than the other two epochs.

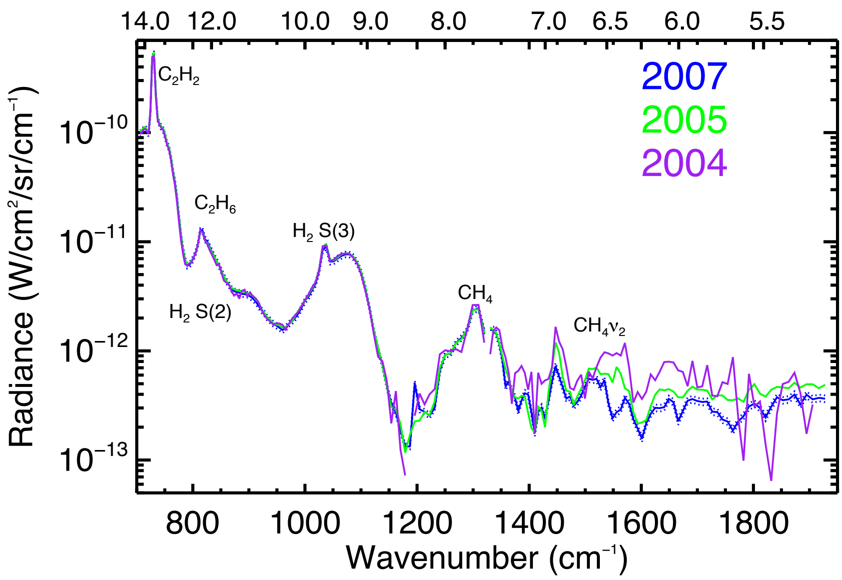

Figure 3.6: The Spitzer-IRS SL module spectra for the three epochs of Uranus (2007, 2005 and 2004) with main features labelled. Measurement error maxima and minima are shown for the 2007 data as dotted lines. Corresponding wavelength units are displayed on top x-axis in microns.

Previous study by Burgdorf *et al.* (2006)

The Burgdorf et al. (2006) paper entitled *'Detection of new hydrocarbons in Uranus' atmosphere by infrared spectroscopy'* used the first dedicated observations of Uranus from Spitzer taken in 2004 (Table 3.2). They averaged the three separate longitudes to form a global average from the SH and SL1 modules. They also used a calibration observation from November 2003 that covered the LL2 module.

Their main findings were the first clear detections of new species ethane, methylacetylene, diacetylene and carbon dioxide in the spectra between 10-20 μm with the estimation of their mixing ratios. They derived the profiles of these new species, along with known species acetylene and methane (Orton et al., 1987; Encrenaz et al., 1998, etc.), in part by utilising model A and C from Moses et al. (2005). They surmise that the presence of CO_2 is not surprising because it had already been discovered on all of the other giant planets including Neptune. Its appearance in emission only suggests that it is from external rather than tropospheric sources, a hypothesis that has been built upon in later investigations like Moses and Poppe (2017).

They anticipated that the 2005 data would improve the signal-to-noise and allow for greater constraints to be put on the models. The 2005 data did improve on signal-to-noise but the 2007 data was what provided the best improvement and was used for the following study by Orton *et al.*.

Previous study by Orton *et al.* (2014)

Our longitude study of Uranus is built upon the initial work done in the two papers by Orton *et al.* in 2014, *'Mid-infrared spectroscopy of Uranus from the Spitzer Infrared Spectrometer'*. The papers attempt to determine the mean temperature structure (Orton et al., 2014a) and mean composition (Orton et al., 2014b) of the stratosphere and upper-troposphere. They use the globally-averaged 2007 data (average of the four longitudes) that utilises all four modules of the data (SL, LL2, SH and LH).

The data reduction procedure was used as an outline for the new and updated procedure designed for this investigation that is detailed in section 3.4. Their radiative transfer method splits the spectrum into bands of different features and retrieves them using line-by-line calculations (for explanation of line-by-line and how it differs from our correlated-k approach see chapter 2). They split their temperature retrievals into steps by looking at different atmospheric layers one at a time and finding the best fit for each using the relevant bands.

Temperatures were derived from multiple bands in the SH, LL2 and SL1 modules with hydrogen, helium and methane being the only gases in the model. Their first approximation of atmospheric structure comes from the Voyager 2 results extrapolated down to 10 bars using adiabatic lapse rate assuming equilibrium mixtures of para and ortho hydrogen at local temperature without active heat exchange. H_2 was assumed at 85%, He at 15% and deep CH_4 (below condensation level) at 3.2%. Their derived stratospheric temperatures were compatible with those from Voyager 2 UV occultations (Herbert et al., 1987) but were higher than those derived from Voyager 2 radio occultations between around 1 and 10 mbar (Lindal et al., 1987; Sromovsky et al., 2011).

For the gas retrievals, model C of Moses et al. (2005) was used with methane condensation ignored. The stratospheric eddy diffusion coefficient (K_{zz}) plays a vital role in the derivation of the gas abundances. The K_{zz} profile was thoroughly investigated with a vertically uniform slope being chosen as the nominal. A large error was found in the range of plausible coefficients and this is discussed further in our investigation in Chapter 5.

They determined the abundances of acetylene, ethane, propyne, diacetylene, carbon dioxide and tentatively methyl (CH_3). This CH_3 discovery was unsuccessful by Burgdorf et al. (2006) with the noisier data from 2004. It was demonstrated that the slow vertical mixing implies that the hydrocarbons are confined to altitudes below the 0.1 mbar pressure levels. They also suggest that there is no evidence for an increase in mixing (and therefore hydrocarbon abundances) near the equinox, despite suggestions of an increase in dynamical activity in the troposphere at this time (Mousis et al., 2018). Even though there was no obvious evidence for changes in these hydrocarbon abundances with time from 1986 to 2007, the derived acetylene profile was much greater than that determined by Bishop et al. (1990) using Voyager UVS occultations. This was postulated to be a potential physical increase over time.

Their investigation revealed surprising rotational variability in the strength of the hydrocarbon emissions. Neither the hydrogen continuum nor the quadrupole seemed to vary above the noise level. This variation consistent with a longitudinal dependence was highlighted as something that needed to be addressed in a subsequent paper. This is where our investigation begins in the first results chapter of this thesis (Chapter 4).

3.3.2 Neptune

The globally-averaged spectra from November 2005 are shown in Figure 3.7 and have also been processed using the updated reduction pipeline in Section 3.4. No LL module data were available. Neptune has an overall brighter spectrum than Uranus with the same features visible that were detected in Meadows et al. (2008). This includes the strongest bands of methane (CH_4), acetylene (C_2H_2) and ethane (C_2H_6) as-well-as weaker but still clearly recognisable features of ethylene (C_2H_4), carbon dioxide, methyl (CH_3), methylacetylene (C_3H_4) and diacetylene (C_4H_2). Ethylene, not detected at Uranus, is clearly visible in both the SL and SH spectra at 10.5 μm. Monodeuterated methane (CH_3D) on Neptune is more abundant than on Uranus so appears as a stratospheric emission feature like CH_4 (Fletcher et al., 2010).

The integration times for both sets of 2004 SL data are short compared to the 2005/06 data (Table 3.3). The brighter spectrum of Neptune (in comparison to Uranus) means that this has not affected the overall shape of the globally-averaged low-resolution spectra, even at shorter wavelengths. The consistency of the different epochs of data demonstrates the reliability of the reduction process detailed in the following sub-section.

The 2006 epoch is slightly dimmer than the rest of the data. This is consistent with ground-based imaging observations of Neptune around the same period, with this long-term variability being the subject of a separate study (Roman et al., in-preparation).

Previous study by Meadows *et al.* (2008)

The paper titled *'First Spitzer observations of Neptune: Detection of new hydrocarbons'* by Meadows et al. (2008) uses the Neptune data from May 2004 to highlight the high-sensitivity of the Spitzer spectra between 10 and 20 μm specifically. They used the SH and SL2 modules with a simplified reduction process using the Spitzer default data processing pipeline. Their final reduction is essentially the second tier default product (post-BCD/PBCD) that is available directly from the Spitzer Heritage Archive. They coadd the data at all three separate longitudes to improve the signal-to-noise and therefore form a global-average.

They discovered methylacetylene and diacetylene, previously unobserved, and derived their volume mixing ratios. Methylacetylene abundances matched the model A predictions of Moses et al. (2005). Diacetylene abundances were however, significantly higher by around 13.5 times. They postulated that if more observations show similar

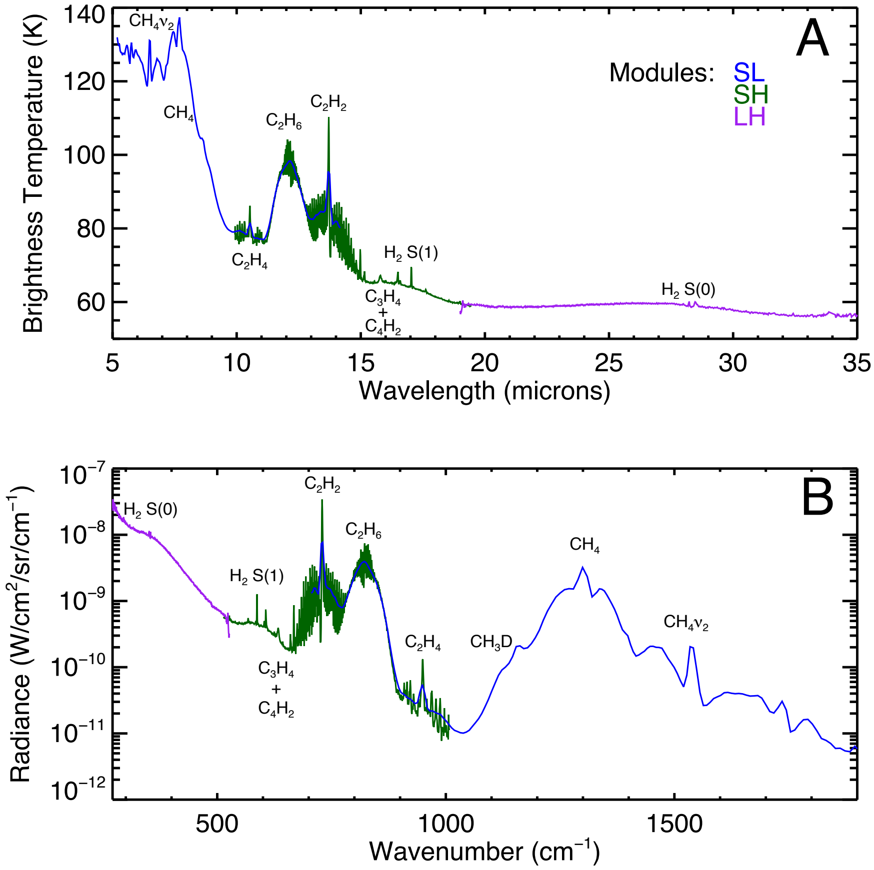

Figure 3.7: The global average spectrum of Neptune for observations made on 19th-22nd November 2005 using three available modules of the Spitzer Space Telescope Infrared Spectrometer. The modules are shown in different colours: Short-Low (SL) in blue, Short-High (SH) in green and Long-High (LH) in purple. Panel A shows brightness temperature vs. wavelength and panel B shows radiance vs. wavenumber. Well-defined spectral features are labelled with their chemical names.

abundances of diacetylene which are consistently higher than the predicted models then this shows that the discrepancy may therefore be physical instead of chemical. This could be in the predicted condensation level as both the temperature profile and vapour pressure uncertainties could be contributing.

They identified multiple features between 15 μm and 18 μm that they could not identify at the time of submission as well as a strong methyl (CH_3) double feature at 16.5 μm, which we will return to in Chapter 6.

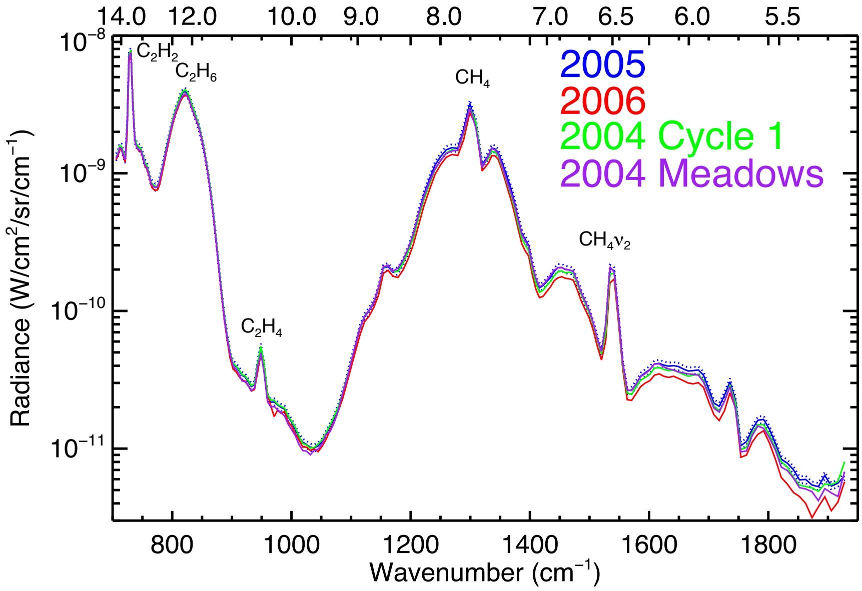

Figure 3.8: The Spitzer-IRS SL module spectra for all epochs of Neptune (2004, 2005 and 2006) with main features labelled. Measurement error maxima and minima are shown for the 2005 data as dotted lines. Corresponding wavelength units are displayed on top x-axis in microns.

3.4 Data Reduction

We now know what ice giant data we have available and what that data looks like. To ensure an accurate comparison of the different epochs, it has all been processed using the same pipeline procedure and this section will outline that process and the associated calibration and uncertainties. There are some differences in the processing of the two planets and in these cases we have stated them explicitly.

3.4.1 Process

The Spitzer data have been analysed using the most up-to-date pipeline software available from NASA's Spitzer Science Centre (SSC, `https://irsa.ipac.caltech.edu/data/SPITZER/docs/dataanalysistools`) resulting in minor changes over the previous reductions of the data by Orton et al. (2014a) and Meadows et al. (2008) that are detailed in Section 3.4.2. Most of the available software has received updates and are now the final versions that were not available when the Uranus-2007 data were reduced in 2008. We have re-reduced all of the available ice giant data listed in Table 3.2 for archiving and future use. This is available at `https://doi.org/10.5281/zenodo.4617490` and `https://doi.org/10.5281/zenodo.5254503` for Uranus and Neptune respectively.

The reduction process was the same for both Uranus and Neptune (Figure 3.9). The raw form of data that are available from the heritage archive are FITS files of the 2D detector images. Each observation has two nods that are in different parts of the same detector slit (Figure 3.3 shows an example of the nods in the SL1 module). The SSC software, *irsclean_mask v2.1.1*, was used to mitigate the effects of bad pixels on the detector that come from dark currents and historically dead pixels. The edited masks from any previous reductions were not available, so additional bad pixels that were not included in the default campaign-specific masks had to be identified by eye. Bad pixels were identified if they were clearly dead or if they exhibited intermittent large changes in brightness over multiple exposures. The multiple exposures for each module and nod were co-added using the provided *coad* software. Each campaign has varying numbers of exposure cycles and sample integration times but, as an example, for the Uranus-2007 data the SL modules have 25 exposure cycles, LL and SH both have 15 cycles and LH has 4 cycles. The sample integration time per exposure is around 1 second for every module apart from SH that has a sample integration time of 4 seconds. The combined integration times (total exposure time) for each module and each campaign is listed in Table 3.3. The two nods were kept separate until the very end of the reduction process for all campaigns.

For SL, the sky subtraction uses the fact that when sub-module SL1 is pointed at the source, SL2 is pointed at blank sky, and vice versa. Subtracting them from one another required no other sky-subtraction technique, unlike Orton et al. (2014a) who also subtracted the sky directly from the opposite end of the slit from the source. This method of subtracting directly from the slit provided negligible changes to the final spectra, so was omitted. For LL, subtraction of the two separate nods was required because LL1 was unavailable due to expected detector saturation. This method was used rather than subtracting directly from the slit due to the source visibly occupying the majority of the length of the slit with no consistent area to subtract from. Subtracting the nods is a proven method for background subtraction (Sloan, 2004), and it replicates the approach used for the SL modules. In most cases, SH and LH both had campaign-specific off-source pointings that could be directly subtracted from the on-source pointings. When these were not available, a campaign-suitable off-source pointing was chosen. This had to be a background campaign with a comparable ecliptic latitude just like the method used in Meadows et al. (2008) for their SH data.

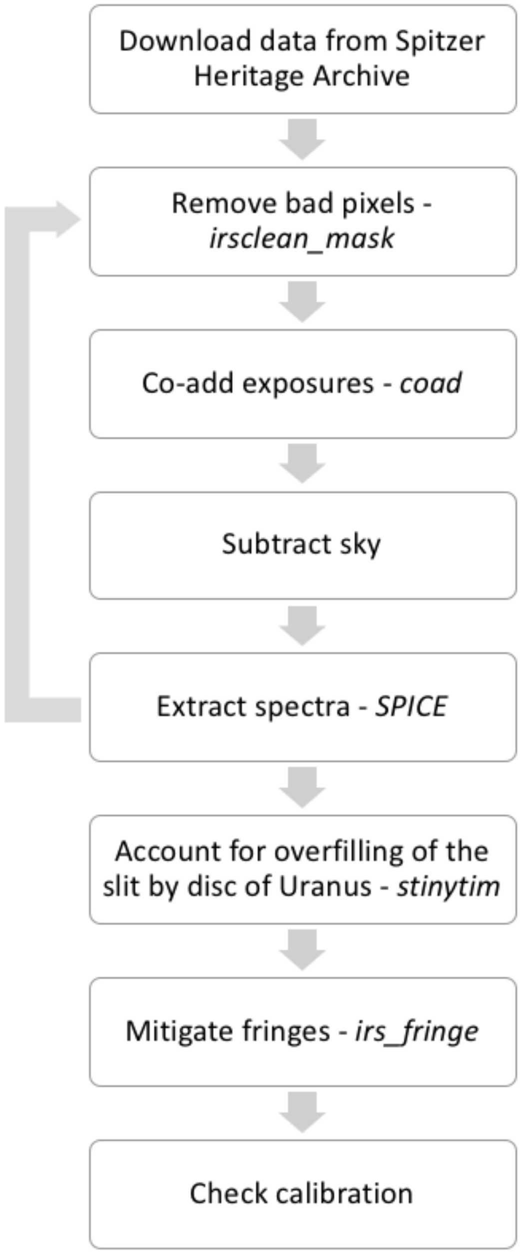

Figure 3.9: Data reduction process flow diagram. The spectra are checked after being extracted using *SPICE* to make sure all obvious bad pixels were masked. If any anomalies were detected then the cleaning, coadding and sky subtraction steps were repeated until we were satisfied with the spectrum in the loop shown.

The SSC-provided SPitzer IRS Custom Extractor (*SPICE v2.5.1*) extracts the spectra from the co-added, cleaned and sky-subtracted detector images. The settings used ('point source with regular extract') are the same as in Orton et al. (2014a) although the version of the software was updated in August 2013. A combination of the SSC contributed software *stinytim v2.0* and methods by Orton et al. (2014a) accounts for the overfilling of the slit by the disc of the planets by generating a point-spread function (PSF) for the IRS as a function of wavelength (0.5 μm increments were used). Unlike in the previous reduction of Orton et al. (2014a), we also corrected the LL spectra for this overfilling factor as we found it had an effect, with details described in Section 3.4.2. This same method was used for all other modules in the Uranus data but due to the smaller disc of Neptune it was not necessary to apply *stinytim* to the LH Neptune data. SSC software *IRSFRINGE v1.1* was used on the LH data as in Orton et al. (2014a) to defringe the orders and correct for this effect that originates from the detector substrates.

Data are converted from flux in Janskys into radiance and brightness temperature using an angular diameter from the vantage point of Spitzer of Uranus of 3.35 arcsec for 2007 and Neptune of 2.22 arcsec for 2005. The data show significant drop-outs at the edges of each order/sub-module. To compensate for this, two spectral points from either end of the low-resolution data were omitted from subsequent analysis. Ten points were omitted from high resolution data.

For the Uranus data, the spectra from the SH modules showed a slope that disagreed with the better-calibrated SL and LL data, so they were pivoted (i.e. corrected with a linear dependence on wavelength) and scaled to match at the same wavelengths using the same method as Orton et al. (2014a). The scaling factors used on each order were unchanged from the previous reduction but, due to the small changes in the data from the updated reduction pipeline, the pivoting factors required small changes. The need to scale up the SH data to the low-resolution modules by around 5% is also highlighted in Burgdorf et al. (2006) for the 2004 data. This scaling and pivoting of the SH data was not required for any of the Neptune data, most likely because it is brighter.

3.4.2 Errors and Calibration

The errors provided in the reduced data come from the Spitzer pipeline and are calculated in SPICE as a 1-sigma error. These errors do not take into account the reproducibility of the measurements so these were combined manually.

The following calculations are specific to the Uranus-2007 data but the methodology was used for all of the campaigns for both planets with very few differences in the numbers. For SL2 the average 1-sigma error from the pipeline is 6%, for SL1 and LL2 it is 1%. Additional error is added to account for the correction done by *stinytim*. This is estimated as the average correction factor for each module, where both SL modules are 7% and LL is 3%. These module-specific uncertainties are combined in quadrature with the 4% and 2% errors due to disagreements with standard stars (Sloan et al., 2014) and differences in the infrared calibration of the telescope respectively (Orton et al., 2014a). This yields a total radiance uncertainty of 6% for SL1, 7% for SL2 and 4% for LL2 for the Uranus data. Only SL was available for the Neptune data and both SL1 and SL2 were found to have errors of 6%. Each percentage error mentioned is the percentage of the measured radiance at every spectral point.

For the high-resolution modules, fringes were corrected for in the LH module. For Uranus, the pivoting and scaling of the SH module data to the low-resolution data are taken into account. By using the same methodology as the low-resolution with these additional errors added in quadrature we estimate an error of 9% for SH and 5% for LH for Uranus. For Neptune both the SH and LH modules were found to have errors of 5%. In Meadows et al. (2008) they estimated errors of around 3-sigma (10%) for the SH module of their 2004 data. The earlier campaigns in 2004 for both planets have a larger level of noise due to shorter exposure times and this will be taken into account in subsequent tests.

Fig. 3.10 compares the previously reduced Uranus-2007 data from Orton et al. (2014a) and provides the difference between the two in terms of brightness temperature, showing that the difference is within the total flux uncertainty of the reduction process in most regions. The entire spectrum exhibits a small upward shift (up to 0.3 K in the low-resolution and up to 1 K in the high-resolution) showing that the new reductions are slightly brighter than the old ones. For the LL module, this could be due to the corrections caused by the use of the *stinytim* tool. Otherwise, the extraction of a consistently brighter spectrum is most likely due to changes in the updated SSC tools and products. As previously mentioned, the factor used to scale the high-resolution data to the low was the same as used in Orton et al. (2014a) so the relative change across the modules has been consistent. This supports the idea that this brighter spectrum is a real change in the data due to improved calibration software and not an error that has propagated through the pipeline.

The bonus order (SL3) between 7.9-8.5 μm (1176 - 1266 cm^{-1}) was inconsistent with its neighboring orders and was not used, consistent with the previous investigation (Orton et al., 2014a). The large difference seen at around 8.5 μm (Fig. 3.10) is in a very low radiance region that exhibits a lot of noise. This region has also been omitted from subsequent analysis of the Uranus-2007 data. The SL3 bonus order was

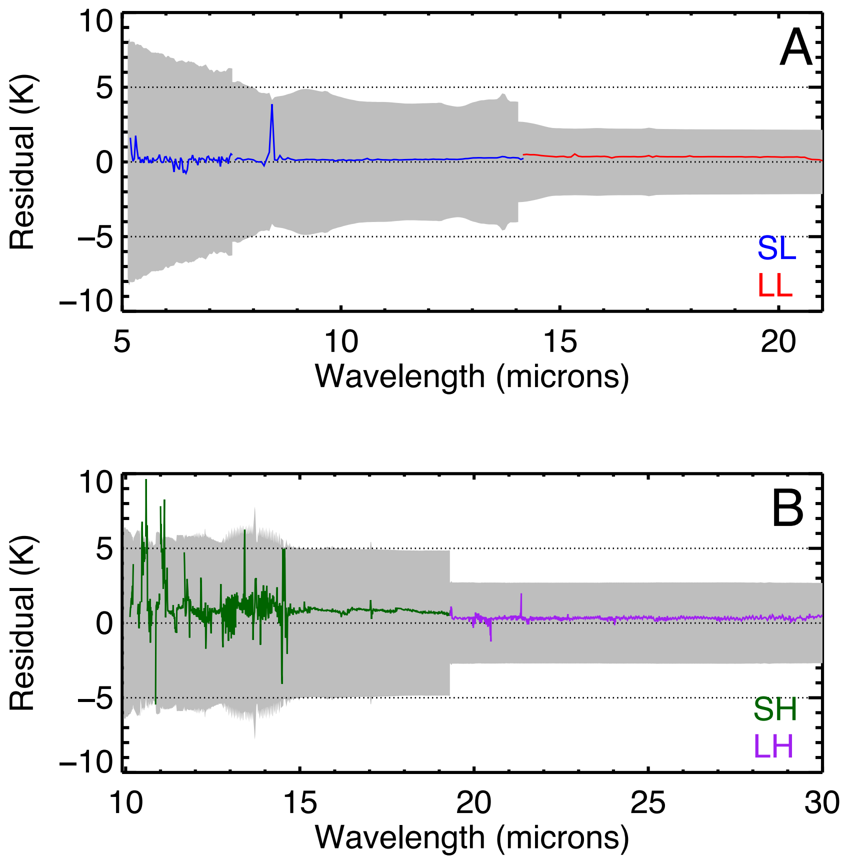

Figure 3.10: The difference between this current reduction of the Uranus-2007 data and the previously reduced data by Orton et al. (2014a) with low-resolution modules shown in panel A and high-resolution modules shown in panel B. The total flux uncertainties associated with the reduction are shown by the grey shaded regions (6% for SL1, 7% for SL2, 4% for LL2, 9% for SH, and 5% for LH, converted to brightness temperature).

found to be reliable in the Neptune data and has been used to bridge the small gap between SL1 and SL2 in all cases.

Orton et al. (2014a) found that the LL flux is 9% higher than the SL1 flux in the range in which they overlap. We found that the difference based upon this new reduction is around 15% for Uranus-2007. This is due to a combination of two factors: (i) The known discontinuity between the two Spitzer modules that has a standard deviation of around 9% (Sloan, 2004); and (ii) the 34-degree change in longitude caused by the time difference between each measurement (Table 4.1). This longitudinal change in brightness is the main focus of Chapter 4 and part of Chapter 5. No LL data was available to test if this difference was similar at Neptune.

The LH module data are well within the errors shown. The 10 - 12 μm region of the SH module has been omitted from subsequent analysis of Uranus due to noise. The high-resolution data have been used as a comparison but the most important scientific conclusions in Chapter 5 are based only on the low-resolution data due to their consistency and reliability.

The only comparison we can make to previous Neptune data is that presented by Meadows et al. (2008). They used the SH module data only and did not use a custom reduction process. They instead used the secondary pipeline product directly from Spitzer, know as PBCD files. Figure 3.11 compares the newly reduced Neptune-2004 SH module to these PBCD files. There is good agreement between the two being well within the measurement errors longwards of around 12 μm. The lower radiance region between 10-12 μm is noisy and consistently underfitting but is within errors over the majority of the region. The peak of the ethylene band at 10.5 μm has a better agreement than the lower radiances around it. This same region is noisy at Uranus and, as stated before, had to be omitted completely from analysis in Chapter 6.

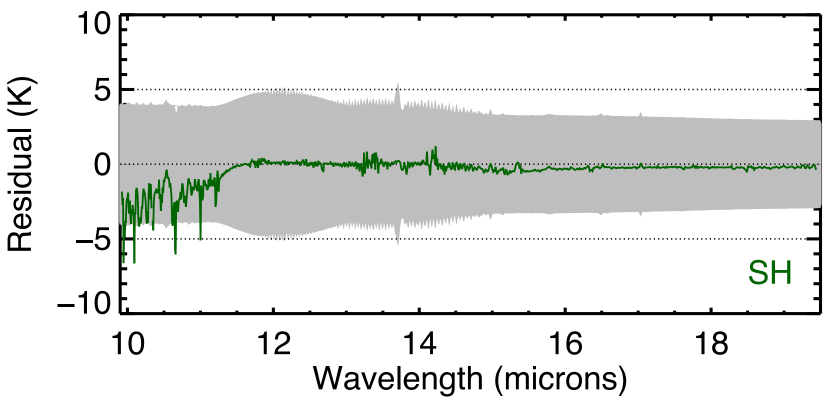

Figure 3.11: The difference between this current reduction of the Neptune-2004 SH module data from May and the data used by Meadows et al. (2008). The 5% total flux uncertainties associated with the reduction are shown by the grey shaded regions, converted to brightness temperature.

3.5 Summary

This chapter outlined the ice giant data available from the Spitzer Space Telescope Infrared Spectrometer and how it was processed so that it can be analysed and interpreted in the next results chapters. In the next chapter, the first of our results chapters, we separate the longitudes observed for each epoch in order to determine whether there is any variability at Uranus or Neptune.

Chapter 4

Longitudinal Variations in the Stratospheres of the Ice Giants

4.1 Introduction

The data from Spitzer IRS for both Uranus and Neptune outlined in Chapter 3 are analysed in this chapter to look at the variability of the planets as they rotate. The Uranus variability results have already been published in Rowe-Gurney et al. (2021). The Neptune results are in preparation for a future paper.

Given the 0.85-m diameter primary mirror, the Spitzer spectroscopy lacked the spatial resolution to show how temperature and composition varied across the planet, meaning that the results of Orton et al. (2014a,b) are considered as global averages of Uranus. The observations of Meadows et al. (2008) are also globally averaged results of Neptune. We analyse the differences in temperature and composition between the separate hemispheres to shed light on the variability of Uranus' stratosphere in 2007 and Neptune's stratosphere in 2005. We have also conducted the same study for 2005 and 2004 Uranus data as well as two sets of 2004 Neptune data. Analysing all the sets of data with multiple separate longitudes (Table 3.2) gives us a unique opportunity to compare the longitudinal variability of the two planets for the first time.

Figure 4.1 shows an example of the observable longitudes for a Spitzer campaign. As we have highlighted before, we have only disc-averaged spectra for each pointing centred at the sub-Spitzer point. The disc-averaged measurements represent the flux coming from the entire illuminated hemisphere. The circles in the figure show how portions of these hemispheres overlap for different pointings. Due to how the Spitzer modules are configured and fixed to the observatory, the spacecraft has to physically slew to expose different apertures. This means there is a time delay that would usually be considered a limitation but has instead become an advantage to this investigation by spreading the observations across the disc more evenly.

4.2 Variation at Uranus

4.2.1 2007

Due to the especially wide and even spread of longitudes in the Uranus-2007 data (Table 4.1, Fig. 4.1) we are able to look at the variation in detail. The observations were taken just 10 days after the exact equinox of Uranus allowing us a rare opportunity to see both the spring and autumn hemispheres equally.

Module	**Longitude**	**Date**	**Start Time**	**End Time**	**Mean Longitude (°E)**
SL	1	2007-12-16	17:40	18:18	209.45
SH	1	2007-12-16	18:18	19:33	229.11
LL	1	2007-12-16	19:34	19:38	243.20
LH	1	2007-12-16	19:42	19:44	245.64
SL	2	2007-12-17	00:06	00:43	343.60
SH	2	2007-12-17	00:44	01:59	3.43
LL	2	2007-12-17	02:00	02:07	18.05
LH	2	2007-12-17	02:08	02:10	19.97
SL	3	2007-12-17	06:46	07:24	122.97
SH	3	2007-12-17	07:24	08:39	142.63
LL	3	2007-12-17	08:40	08:47	157.25
LH	3	2007-12-17	08:48	08:50	159.16
SL	4	2007-12-17	13:15	13:52	258.17
SH	4	2007-12-17	13:53	15:08	278.00
LL	4	2007-12-17	15:09	15:16	292.62
LH	4	2007-12-17	15:17	15:19	294.53

Table 4.1: Spitzer-IRS Uranus-2007 campaign observing times (UT) and disc-centred longitudes (°East, system III) that are associated with each module as calculated by JPL Horizons with a 17.24 hr rotation period and sub-Spitzer point located at 2.69° S.

Before going into detail we looked at the four intervals of interest in the low resolution data shown in Figure 4.2 and see a clear pattern emerging between the longitudes. Longitude 3 is significantly dimmer than longitude 4 in every interval. These two longitude observations were taken 135 degrees apart with roughly 6.5 hours elapsing between observation mid-times. Longitude 1 and 2 show very similar radiance values despite nearly equivalent separations in longitude and time. In ranges of the spectrum where a variation can be seen, we see this same pattern across the low and high resolution spectra (Fig. 4.3). The acetylene region around 13 μm and the

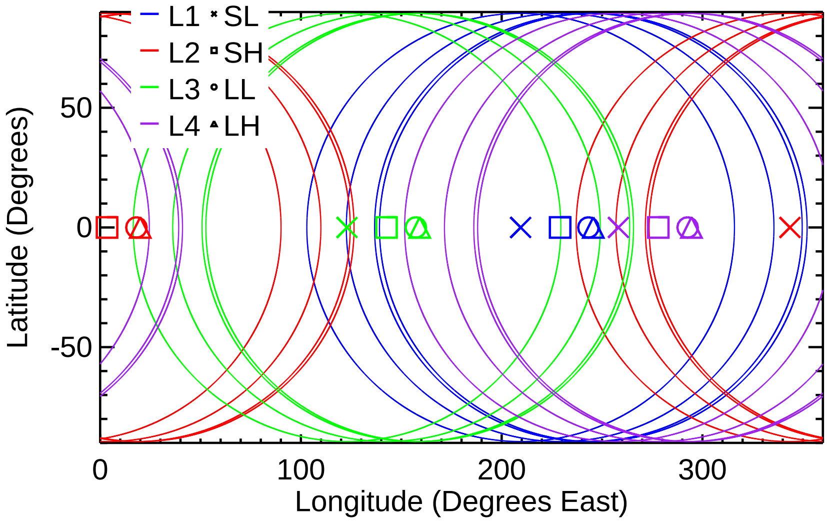

Figure 4.1: The Spitzer exposure ranges for all modules across all longitudes of Uranus for the 2007 campaign. Each longitude is displayed in a unique colour and each module is shown by a unique symbol. Relative latitude is centred on 2.69° South.

methane region around 8 μm show this pattern the most clearly above uncertainty values.

The next step we took was to assess the variations in discrete channels sensitive to the different emission features in Fig. 4.4. The radiances within each interval are averaged and compared to the global-average radiance to get a percentage radiance difference for each species at each observed longitude (Fig. 4.5). The intervals shown in Fig. 4.4 were selected using known central wavelengths for each species. The hydrocarbons were taken from GEISA-2003 compilation (Jacquinet-Husson et al., 2003). We use the locations and widths of the hydrogen quadrupole lines from Fouchet et al. (2003); Orton et al. (2014a); Fletcher et al. (2018). The widths over which to average were deduced from the widths of the features (slightly different for high and low resolutions). The hydrogen-helium CIA is present throughout the spectrum but was chosen to be represented by the wide ranges indicated because of a lack of other features in these regions. We chose two different wavenumber ranges for each resolution to gain two independent values of the continuum variation for analysis.

The complex hydrocarbons in the top panel of Figure 4.5 appear to vary from the mean in a noticeably sinusoidal fashion. There is a difference in radiance of up to 20% between the variations from 0° to 180° compared with those between 180° and 360°. The most variation occurs in acetylene with ethane also showing the same pattern. Diacetylene and propyne and the 16 μm region that encompasses both species in the

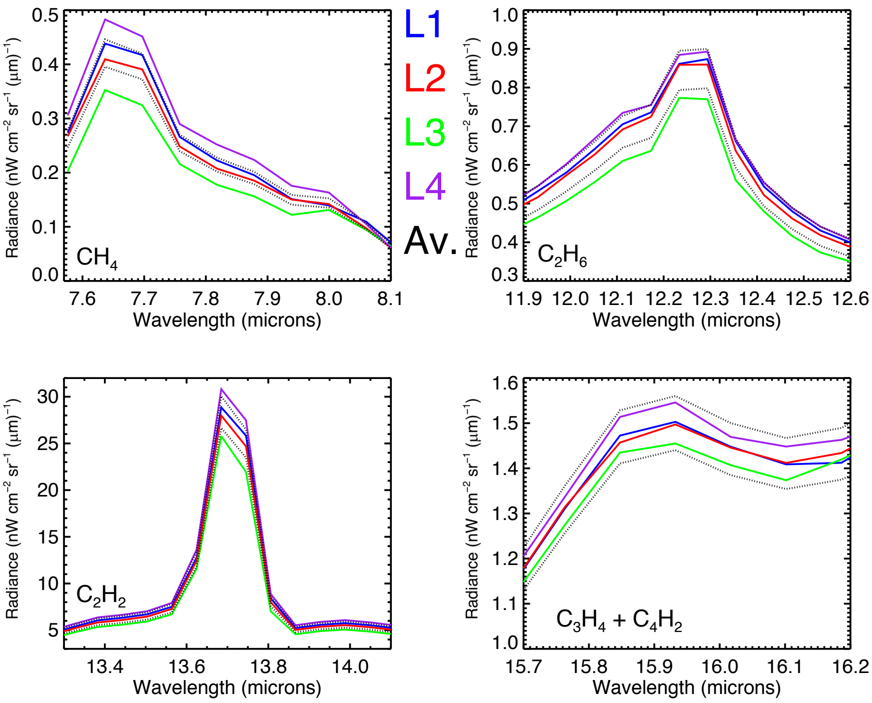

Figure 4.2: The radiances of the four different longitudes in the main hydrocarbon emission features for the low-resolution data from Spitzer-IRS in 2007. Longitude 1 to 4 are shown as blue, red, green and purple lines respectively. The upper and lower limits of the global-average radiance are shown as black dotted lines. The radiance is on a linear scale for direct comparison and features the same colour scheme as Fig. 4.1 for comparison.

low resolution observations show a small amount of variation that agrees with the overall trend of around 2 - 3%. The collision-induced continuum is also plotted for comparison, showing variations smaller than 1%.

With stratospheric methane emission showing the largest variation of up to 15% it is interesting to see it contrasted to the tropospheric species in the middle panel of Figure 4.5. The emission as a function of longitude from the hydrogen-helium continuum is relatively constant in both the high and low resolution bands, varying by less than 1%. Deuterated methane displays a variation that is similarly negligible ($< 2\%$), suggesting that this variation is only present in the stratosphere.

The different hydrogen quadrupole lines are associated with different altitudes (Orton et al., 2014a). S(1) has its maximum contribution near 0.1 mbar. S(2) and S(3) have maximum contributions at lower pressures of around 1 μbar. The bottom panel of Figure 4.5 shows a 4-5% variation in these lower-pressure quadrupoles than those sensing higher pressures. The S(4) quadrupole line shows the largest variation

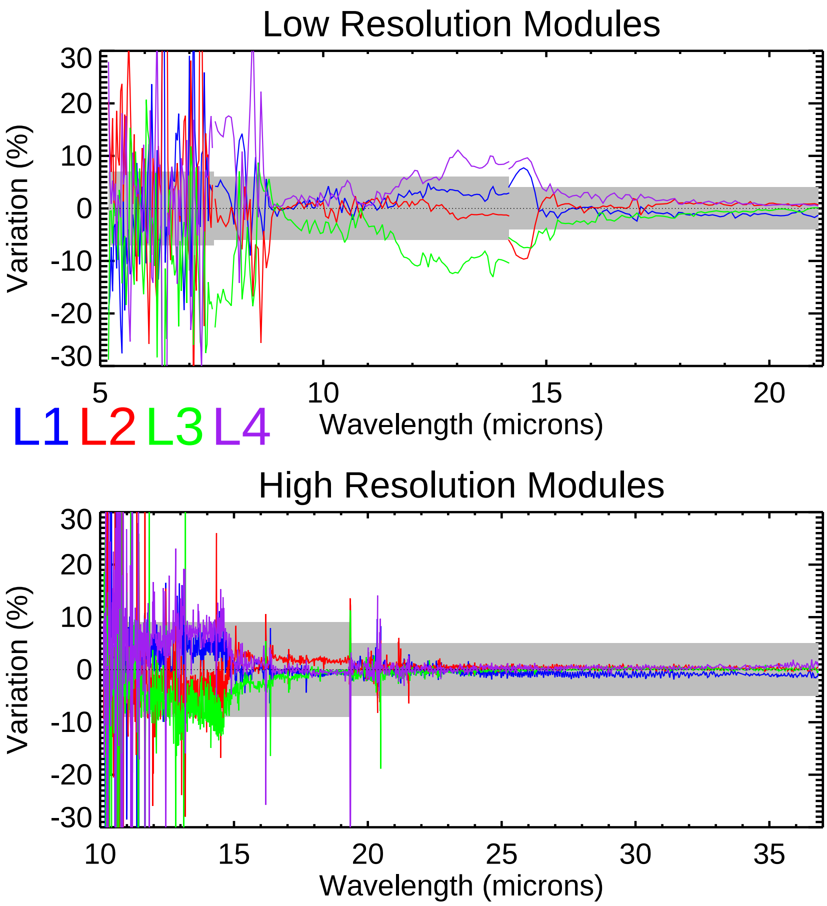

Figure 4.3: The percentage difference in radiance between the four separate longitudes for Uranus-2007 and the global average across both the low-resolution modules (top panel) and high-resolution modules (bottom panel). Measurement uncertainties for each module are shown as the grey shaded regions.

(10-13%) but this is most likely due to it being embedded in the highly variable methane feature. S(0) has only a very weak stratospheric contribution at its central peak of 28.2 μm (354 cm^{-1}) (Fletcher et al., 2018). Here it primarily senses the upper troposphere and so we have another confirmation of a lack of variation at these altitudes.

The apparent wavenumber-1 sinusoidal pattern is present in all three panels of Figure 4.5 with a minimum value consistently in the first longitudinal hemisphere and the maximum in the second hemisphere. It must be remembered that each point is just the mid-point of the disc that, in reality, spreads 90° east and west from that point as shown visually in Figure 4.1. Bias in the shape of the variation may be caused by the gap in the longitude spread of data between 18° E and 123° E. The variation is well above the standard error calculated, shown as error bars. Figure 4.3 shows

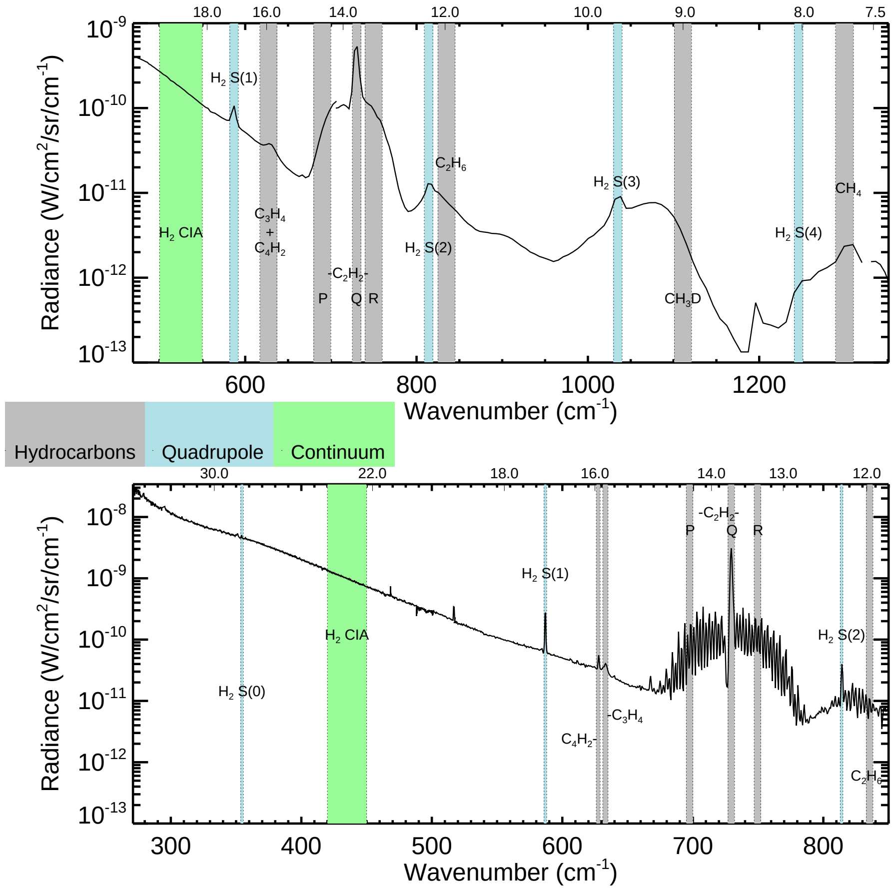

Figure 4.4: Wavenumber intervals selected for different species in longitudinal variation calculations at Uranus. The global-average low-resolution data for 2007 are shown in the top panel and the global-average high-resolution data for 2007 in the bottom panel. Wavelength values shown on top abscissa of both graphs in microns.

the acetylene, ethane and methane ranges also have variations that are above the measurement errors. There is consistency in the variations between the independently acquired modules in both resolutions. L1 and L4 (the clusters of points between 200° and 300°) show consistently higher average radiances for the stratospheric species even though these two campaigns were a full rotation apart assuming a rotation period defined by the Voyager magnetic field data (Table 4.1). This shows evidence of the variability being caused by a localised feature that is stable over short timescales.

4.2.2 2004 and 2005

We now seek to investigate whether the same variation was visible at different epochs. The 2005 data contain four separate longitude observations (Table 4.2), however the

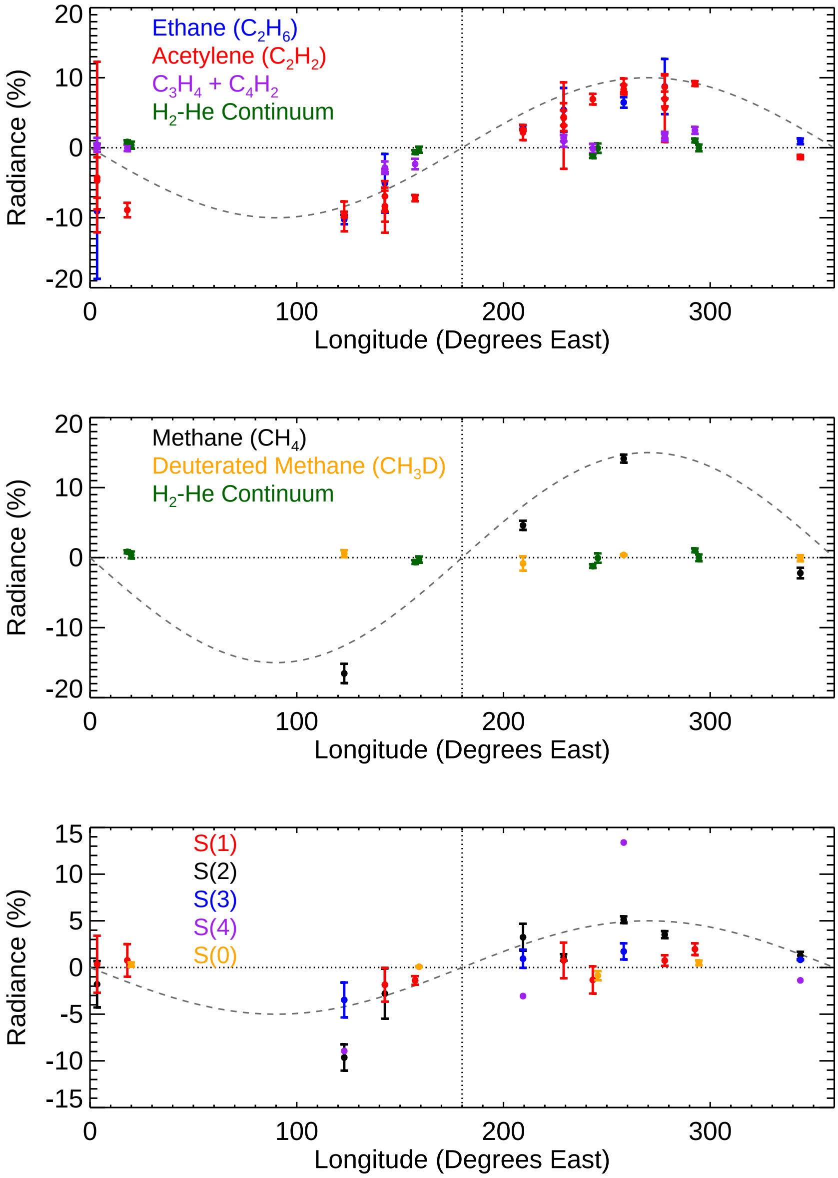

Figure 4.5: The percentage radiance difference from the global average of chemical species across 360° of Uranus in 2007 from all four Spitzer modules. Non-negligible standard errors are displayed not including measurement errors for clarity. Top panel: Complex hydrocarbon species and the hydrogen-helium continuum with 10% amplitude wavenumber-1 sinusoid displayed for reference. Middle panel: Methane variants and the hydrogen-helium continuum with 15% amplitude wavenumber-1 sinusoid. Bottom panel: hydrogen quadrupole species with 5% amplitude wavenumber-1 sinusoid displayed. It is merely coincidental that the sinusoidal pattern of the data has a phase-shift of zero, this is only there as a guide, and no fitting has actually taken place.

small 6° separation between longitude 1 and 4 gives us three distinguishable longitudes and one longitude where we can check for internal consistency. The 2004 data have three longitudes that are evenly separated. We have decided to look at only the low-resolution data because of the need to scale and pivot the high-resolution data to the low-resolution results. The 2004 variation of emission has error bars that are much larger, indicating the much larger standard deviation in the data (Fig. 4.6). This is caused by noise from the much shorter integration times (Table 3.3) and makes drawing any conclusions from the 2004 results difficult.

Year	Longitude	Date	Start Time	End Time	Mean Longitude (°E)
2005	1	2005-07-06	21:39	22:16	236.20
	2	2005-07-07	03:01	03:38	348.28
	3	2005-07-07	08:41	09:18	106.62
	4	2005-07-07	14:37	15:14	230.53
2004	1	2004-11-12	20:03	20:07	1.87
	2	2004-11-13	02:06	02:10	128.19
	3	2004-11-13	08:12	08:17	255.73

Table 4.2: The observing time (UT) and disc-centred longitude (°East, system III) associated with the SL module of the Uranus data collected in 2005 and 2004 as calculated by JPL Horizons with 17.24 hr rotation period. The sub-Spitzer point is located at latitudes 7.03 - 7.04°S for 2005 and 15.22 - 15.23°S for 2004.

There is less variation in the 2005 observations over the longitude spread compared to 2007 with changes smaller than 5% (Fig. 4.6). Longitude 1 (236°) and 4 (230°) in the 2005 data are only 6° different but were taken 17 hours apart, after one full rotation of the planet. The data points from these adjacent longitudes in Figure 4.6 are in agreement in their variation from the mean showing that the magnitude and location of the deviation is consistent over short timescales as was observed in 2007. The sparse spread of longitudes make a pattern similar to 2007 impossible to determine.

We have included deuterated methane (CH_3D) in the analysis to try to contrast the stratospheric and tropospheric variations. In the 2005 data, we see a similar pattern of variation for this tropospheric species as for the stratospheric ones. Longitude 1 and 4 both show higher CH_3D radiances compared to longitude 2 (348°) and 3 (106°), suggesting a variation that is deeper in the atmosphere in 2005 than in 2007. The variation is greatest in methane and acetylene just as it was in 2007. The uncertainties in the 2004 data make this level of analysis non-viable. We conclude that a variation was indeed present in 2005 in excess of the level of noise, although it was smaller than in 2007.

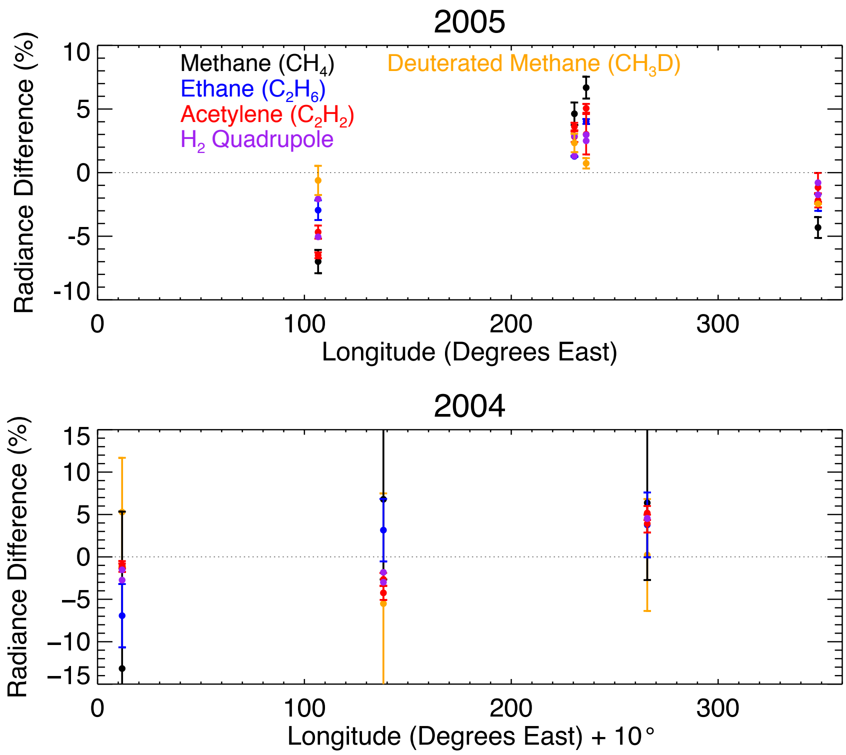

Figure 4.6: The percentage radiance difference from the global average of chemical species across 360° of Uranus from SL modules of 2005 and 2004 data. Non-negligible standard errors are displayed. The 2004 data has been shifted east by 10° for clarity.

4.2.3 Discussion

The variation will be investigated more, via optimal estimation retrievals, in chapter 5 but it is already clear that this variation is present and is either a change in temperature, composition or both. We investigated both near- and mid-infrared ground based observations of Uranus to determine whether a cause could be deduced by gaining much-needed spatial resolution.

4.2.3.1 Comparison to VLT Mid-IR Images Post-Equinox

Mid-infrared images from VLT-VISIR at 13 μm (Roman et al., 2020) revealed warm mid-latitude bands of acetylene emission in 2009, two years after the Spitzer observations (Figure 4.7). Taken over two nights, this series of images appear to show hints of zonal variation with marginally greater emission at some longitudes. Although the signal-to-noise ratio in these data was too low to offer conclusive evidence of longitudinal variation, similar future imaging data at higher signal-to-noise from the ground and JWST should be able to help determine whether discrete features or

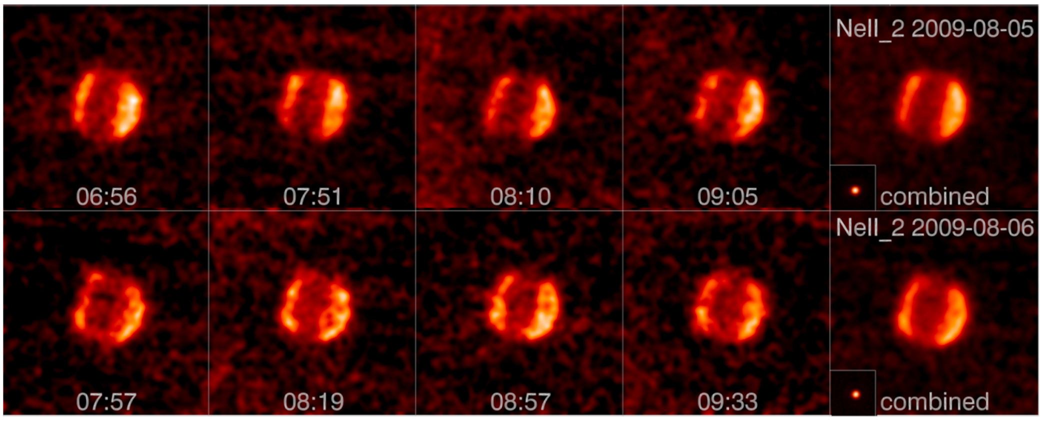

Figure 4.7: Images of Uranus from (Roman et al., 2020) showing variation in 2009 in the acetylene band from the VLT/VISIR NeII_2 [13.04 μm] filter. The top row shows images from August 5th 2009, the bottom row shows August 6th 2009. The 'combined' images in the rightmost column smears roughly 2 hours of rotation. Images shown here have been low-pass filtered with a 1 pixel standard deviation Gaussian blur for image clarity. Insets show the stars representative of the average spatial resolution of the seeing disk.

larger planetary waves are responsible for the variation seen in the Spitzer data.

We discuss this more in the discussion section of Chapter 5 after we have investigated the possible causes of the variation.

4.2.3.2 Comparison to Keck NIR Images at Equinox

The near-infrared images in Figure 4.8 were taken with NIRC2 coupled to the adaptive optics system on the Keck II telescope. They were acquired one week after the equinox and 4 days before the Spitzer data on 2007-12-12 and 2007-12-13. The H-band (1.6 μm) images sense down to several bars and are dominated by scattering at 1-3 bars (Sromovsky et al., 2009; de Pater et al., 2011). Clouds at pressures less than 1 bar are visible in the 2.1 μm K′ band (de Pater et al., 2013).

The two observed dates show approximately opposite hemispheres with the 2007-12-12 observation revealing a more meteorologically active hemisphere than the 2007-12-13 observation. The activity in both spectral bands show that a few discrete cloud features exist at pressures less than 1 bar. These clouds show regions of condensation located high above the main cloud layers and likely indicate local perturbations in the temperatures or dynamics (from below). We therefore speculate that they could also influence the stratosphere, either by direct advection of mass, or by generating waves that propagate vertically (such as during Saturn's 2010-2011 storm, Fletcher et al., 2012).

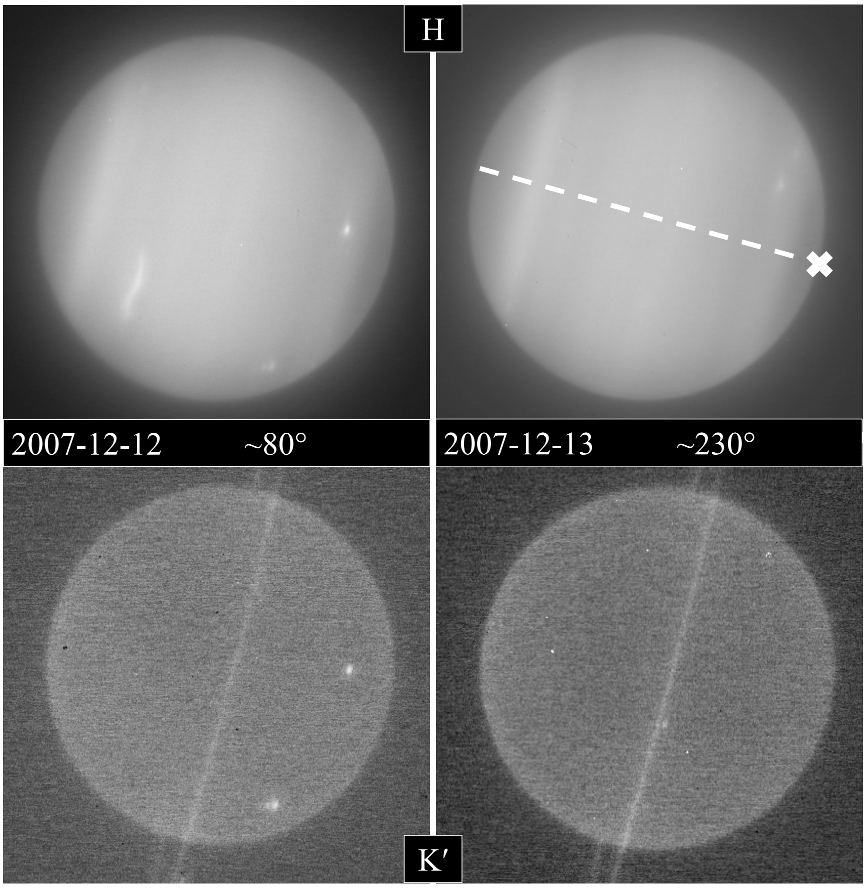

Figure 4.8: Images of Uranus at 1.6 μm (H band, top) and 2.1 μm (K′ band, bottom) taken with Keck II NIRC2 instrument on two dates in December 2007. Approximate central meridian longitude of each image is displayed in degrees east (de Pater et al., 2011, 2013). Orientation of the planet indicated by an X at the northern pole and a dashed line along the north-south meridian.

The central longitudes roughly correspond to the longitudes in the Spitzer observations (Fig. 4.1). We calculated the locations of the features during the Spitzer observations using drift speeds at their respective latitudes assuming constant wind velocities (Sromovsky et al., 2009). The minimum in the stratospheric emission and temperature at longitude 3 coincides with the hemisphere where the troposphere exhibits more meteorological activity.

This activity may be the direct cause of our observed variation and it is possible that one of these bright features is associated with a much larger and invisible dark spot like the one supposed in Hammel et al. (2009). The dark spot has been linked to the intense and long-lasting feature named the "Bright Northern Complex" (BNC) that was visible from 2005 (Sromovsky et al., 2007) through to 2007 (Sromovsky et al., 2009). The BNC was located at around 30° N in August of 2007 and it is likely that it is one of the two northern-hemisphere features seen in the left panels of Figure 4.8. These clouds are located between 200 and 600 mbar (Hammel et al., 2009; Roman et al., 2018) and provide circumstantial evidence that long-lived tropospheric disturbances may be related to the longitudinal variations we see in the stratosphere.

The large southern-hemisphere feature in the Figure 4.8 H-band image is referred to as the "Berg" (Hammel et al., 2001; de Pater et al., 2002; Sromovsky et al., 2009). This long-lived feature was located at 1.8–2.5 bars in 2007 and has been speculated to be linked to a vortex in the same way as the BNC (de Pater et al., 2011). It is therefore reasonable to deduce that, despite the clouds being located slightly deeper, similar dynamical processes could be at work at this location. The drift speeds of the Berg are similar to those of the BNC as they are located at similar latitudes of opposite hemispheres. It is impossible to deduce which feature could be a cause, or if it is a combination of the two, without spatial resolution at mid-infrared wavelengths.

Just as with the VLT observations, we discuss this more in the discussion section of Chapter 5 after we have investigated the possible causes of the variation.

4.3 Variation at Neptune

4.3.1 2005

We applied the same methodology to the Neptune-2005 data as we did to the Uranus data in the previous section. Table 4.3 and Figure 4.9 show the longitudes of the observations from each module and, as with Uranus, the spread of longitudes allows us to search for variability. The different modules are more closely clustered than at Uranus and we only have three separate longitude campaigns to use but it is still enough to deduce a general pattern.

Unlike Uranus, Neptune was not near to its equinox during the Spitzer campaigns and the sub-Spitzer point is at around 29°S. This means the south pole is prominent in the disc-averaged spectra and the north pole is obscured. It is still possible to observe the longitudinal variability with this viewing geometry.

The variation between longitudes does not go above the uncertainty levels of the data (Figure 4.10). There are only three exceptions. (i) At short wavelengths in the low-resolution, reflected sunlight and upper atmospheric effects are a large influence and variation is no longer reliably linked to the temperature and composition of the stratosphere and upper troposphere. (ii) The region of the SH module between 10 and 12 microns is the noisiest due to its low radiance. (iii) The sharp spikes at 19

Module	Longitude	Date	Start Time	End Time	Mean Longitude (°W)
SL	1	2005-11-19	19:22	19:43	35.86
SH	1	2005-11-19	19:44	20:11	45.17
LH	1	2005-11-19	20:12	20:15	51.13
SL	2	2005-11-20	01:49	02:09	179.79
SH	2	2005-11-20	02:10	02:38	189.10
LH	2	2005-11-20	02:39	02:41	195.06
SL	3	2005-11-20	07:48	08:08	313.49
SH	3	2005-11-20	08:14	08:42	324.66
LH	3	2005-11-20	08:42	08:45	330.43

Table 4.3: Spitzer-IRS Neptune-2005 campaign observing times (UT) and disc-centred longitudes (°West, system III) that are associated with each module as calculated by JPL Horizons with a 16.11 hr rotation period and sub-Spitzer point located at 29.06°S.

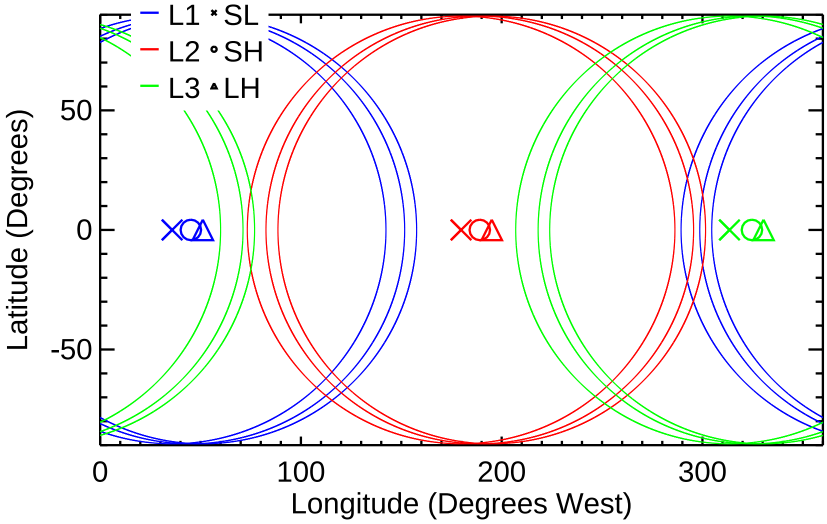

Figure 4.9: The Spitzer exposure ranges for all modules across all longitudes of Neptune for the 2005 campaign. Each longitude is displayed in a unique colour and each module is shown by a unique symbol. Relative latitude is centred on 29.06°South.

microns are where the SH and LH module join and some processing artifacts may remain in the data that will be removed before further analysis in later chapters.

To affirm the lack of variation that we see in Figure 4.10 we adapted the same method of assessing the variation in discrete channels as we did for Uranus. The spectral intervals chosen for the analysis of the species variation were the same as for Uranus with the added ethylene band located around 950 cm^{-1} (10.5 μm) in the SL data. The hydrogen-CIA band is difficult to locate in the SL data due to the much stronger hydrocarbon features, we only sampled the CIA using the LH module at

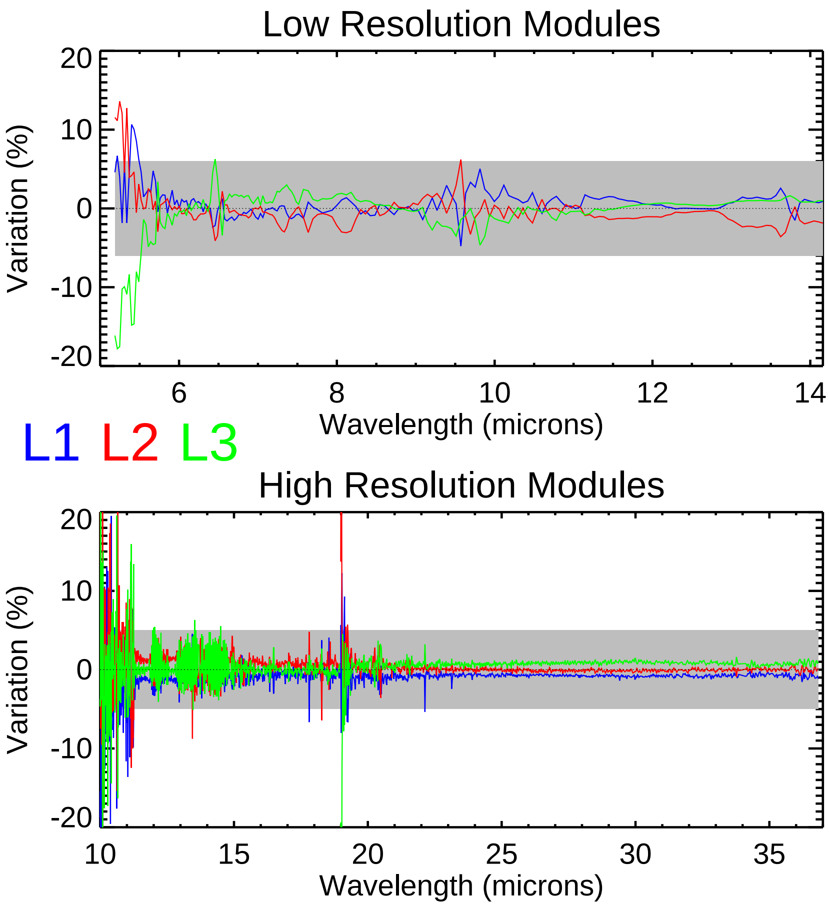

Figure 4.10: The percentage difference in radiance between the three separate longitudes for Neptune-2005 and the global average across both the low-resolution modules (top panel) and high-resolution modules (bottom panel). Measurement uncertainties for each module are shown as the grey shaded regions.

longer wavelengths.

We see a less than 3% variation across all species in all modules. Figure 4.12 is plotted with the same panels as the Uranus equivalent (Fig. 4.5) for comparison. Neptune in 2005 shows no sign of any significant longitudinal variation in any species.

4.3.2 2004

For both campaigns in 2004 there is a good spread of longitudes to analyse (Table 4.4). We had no need to pivot and scale the SH spectra to that of the SL spectra at Neptune but for consistency, and because the SH data are noisier, we used mostly the SL data to look at the variation. The LH data were used for the hydrogen and helium CIA and a clear example of the hydrogen quadrupole (H_2 S(0) at 28.2 μm

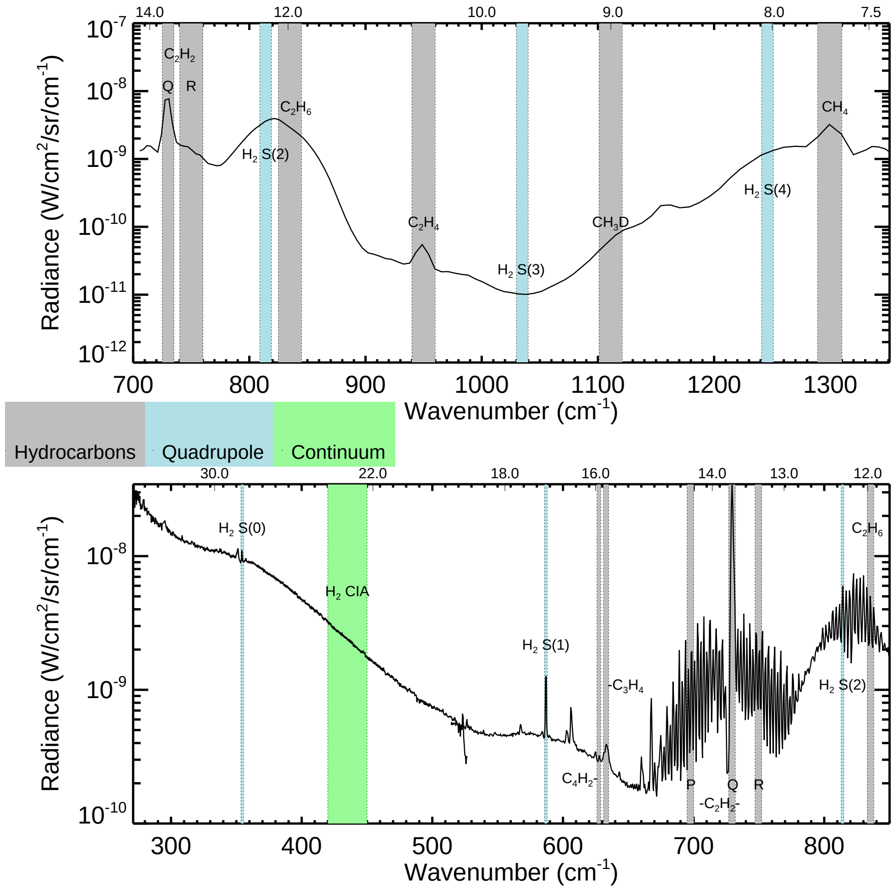

Figure 4.11: Wavenumber intervals selected for different species in longitudinal variation calculations for Neptune. The global-average low-resolution data for 2005 are shown in the top panel and the global-average high-resolution data for 2005 in the bottom panel. Wavelength values shown on top abscissa of both graphs in microns.

(354 cm^{-1})).

The November 2004 data show a variation of less than 3% that is consistent with the 2005 data.

The May 2004 data (Meadows et al., 2008) has a significant deviation at all three discrete longitudes. At longitude 1 the decrease in the stratospheric emission is almost 20%. At the other two longitudes (2 and 3) there is around a 10% increase in the stratospheric emission. The quadrupole (located in the upper stratosphere) and the tropospheric hydrogen-CIA have a negligible variation at all longitudes. This confines the variation to the stratosphere just like at Uranus in 2007 and 2005. The data spread is narrower compared to the other epochs so a pattern cannot be determined. This data is also the noisiest of the four Neptune campaigns but the variations are above standard deviation errors. Though tentative, we have a variation present in the mid-

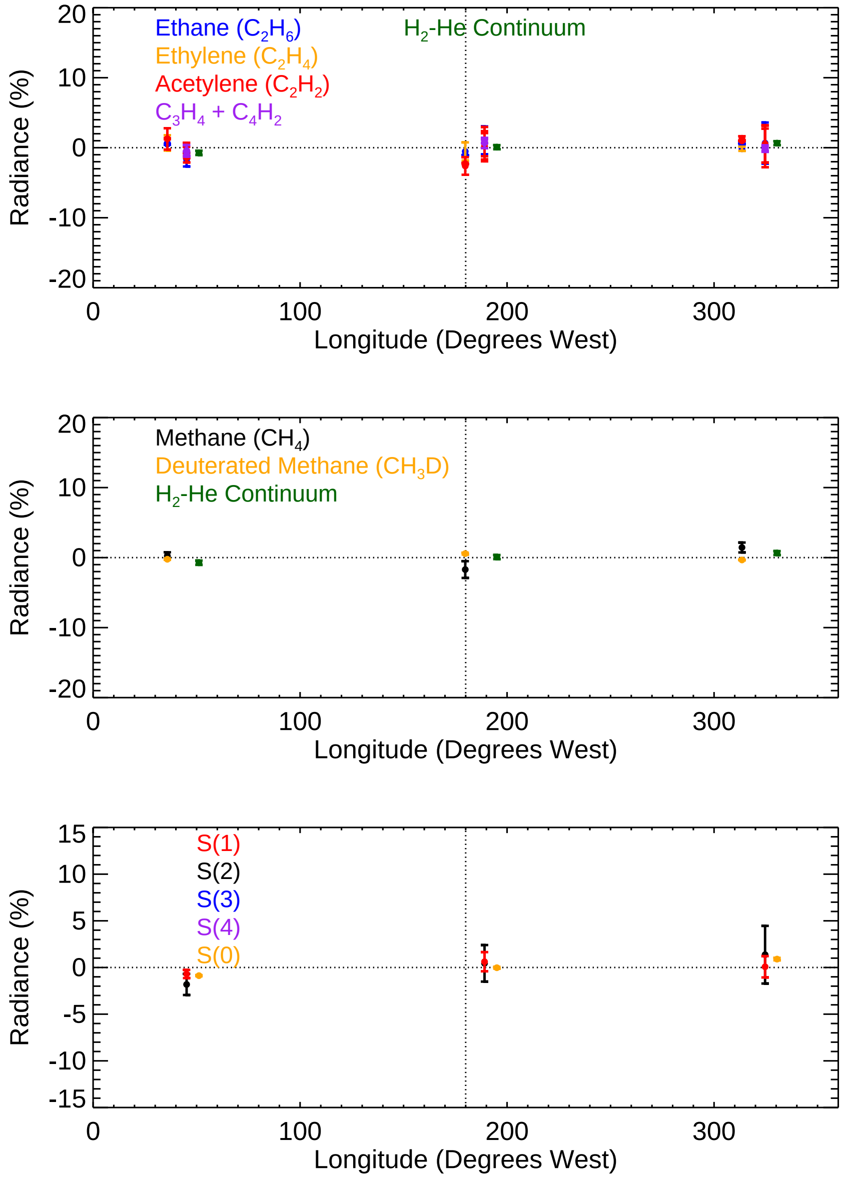

Figure 4.12: The percentage radiance difference from the global average of chemical species across 360° of Neptune in 2005 from all three available Spitzer modules. Non-negligible standard errors are displayed not including measurement errors for clarity. Top panel: Complex hydrocarbon species and the hydrogen-helium continuum. Middle panel: Methane variants and the hydrogen-helium continuum. Bottom panel: hydrogen quadrupole species.

stratospheric hydrocarbons in the May 2004 data previously analysed in Meadows et al. (2008).

Year	Longitude	Date	Start Time	End Time	Mean Longitude (°W)
Nov-2004	1	2004-11-15	22:38	22:46	209.14
Cycle 1	2	2004-11-16	03:14	03:22	311.93
	3	2004-11-16	07:52	08:00	55.45
	4	2004-11-16	12:39	12:47	162.33
May-2004	1	2004-05-15	01:00	01:05	40.97
Meadows	2	2004-05-15	06:18	06:23	159.41
	3	2004-05-15	12:14	12:18	291.83

Table 4.4: The observing time (UT) and disc-centred longitude (°West, system III) associated with the SL module of the Neptune data collected in the two epochs of 2004 as calculated by JPL Horizons with 16.11 hr rotation period. The sub-Spitzer point is located at latitudes 29.02°S for 2004 cycle 1 and 29.26°S for 2004 Meadows (et al.).

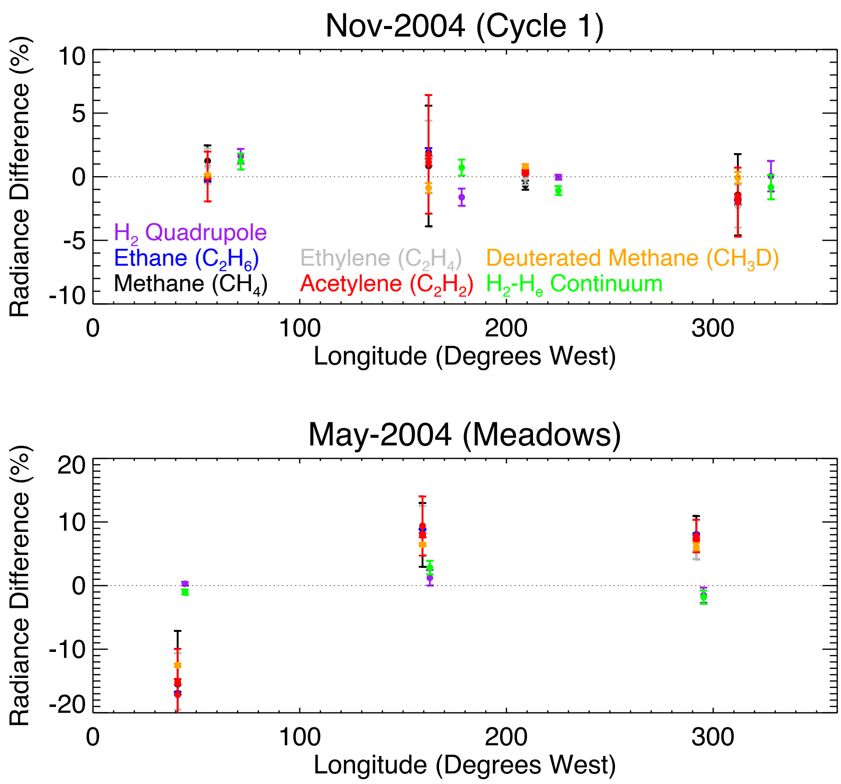

Figure 4.13: The percentage radiance difference from the global average of chemical species across 360° of Neptune from SL and LH modules of two sets of the 2004 data. The continuum and the hydrogen quadrupole line (S(0)) are taken from the LH module due to these features not being easily identified in the SL module. Non-negligible standard errors are displayed.

4.3.3 Discussion

The lack of variation that we see at Neptune (with the exception of May 2004) is not an expected result. Neptune is viewed as the more dynamic ice giant between the two due its higher internal heat and subsequent active meteorology. It was expected that we would see higher levels of variation, not lower.

Images of Neptune from the mid infrared and near infrared from July 2005 (Hammel et al., 2007) show two contrasting hemispheres (between around 50 to 80 degrees apart) in multiple wavelength bands (Figure 4.14). These observations are half way between the Nov-2004 and 2005 observations and could give us an insight into the state of the planet around this time. We can see only small levels of variation in the mid-infrared images (at the level of the noise, and certainly nothing to suggest a 20% change anywhere) and a lot of cloud activity in the near-infrared images.

Just like we explained at Uranus, the activity in the troposphere could be influencing the stratosphere. These images in the near-infrared show reflectivity around the tropopause level that could indicate this activity. There is strong evidence that convective activity could be transporting excess methane into the stratosphere that increases abundances of higher-order hydrocarbons or influences the temperature.

There is evidence in the mid-infrared of the bright southern pole shifting in latitude and creating a hot spot at certain longitudes (Orton et al., 2012). This polar 'wander' is seen in multiple ground-based images between 2006 and 2010 but does not appear to be a long-lived feature. Instead, it seems to appear episodically and may be linked to deeper dynamical activity or planetary waves. The south pole is very prominent in the Spitzer data and so it is possible that in May 2004 the variation we see is caused by a polar hot spot.

We have no images of the planet from May of 2004. The closest we could find was from the Hubble Space Telescope (HST) (Fig. 4.15) from July 2004, which we can also compare to November 2004. There appear to be a few discernible differences in the cloud coverage. In July there are two bright cloud features in the southern hemisphere that are no longer visible in November. The northern hemisphere appears brighter in the November images also. Bright features can be seen in both the August-2005 image and the June-2006 image, so the bright features in July 2004 do not appear unique to this epoch. We only have one longitude at most epochs and don't have images during May of 2004 so cannot deduce reliably what is happening to cause the deviation of early 2004 from the trend of the other epochs. The cloud activity at Neptune is incredibly dynamic and can change from day-to-day (Simon et al., 2016)

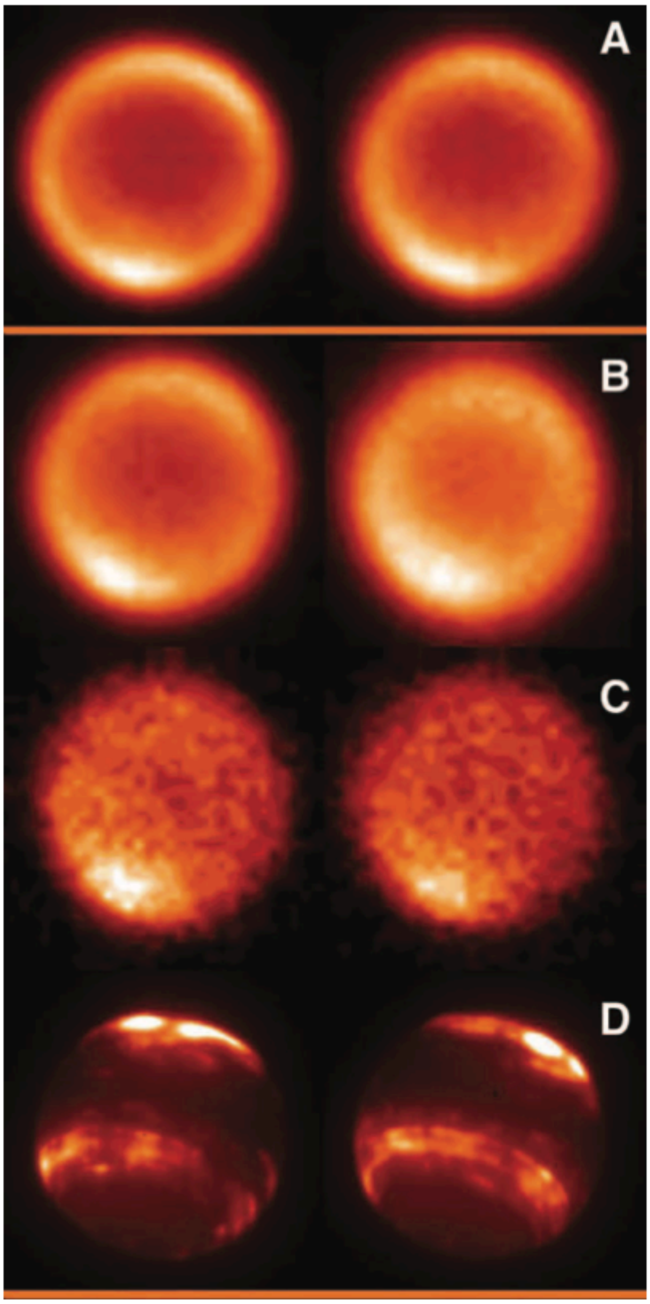

Figure 4.14: Images of Neptune at mid- and near-infrared wavelengths in mid-2005 from Hammel et al. (2007). The left images are between 50 to 80 degrees in longitude different from the right images. A: Mid-infrared images from Gemini Michelle at 11.7 μm on July 4 showing stratospheric ethane emission. B: Mid-infrared Gemini Michelle images on July 5 at the same wavelength showing a similar pattern of ethane emission. C: Mid-infrared Gemini Michelle images at 7.7 μm on July 5 showing methane emission. D: Near-infrared images from Keck NIRC2 at 1.6 μm on July 5 showing tropospheric clouds predominantly at mid-latitudes in both hemispheres.

so it would be unlikely that we would directly see the cause of the suspected variation in the May-2004 data.

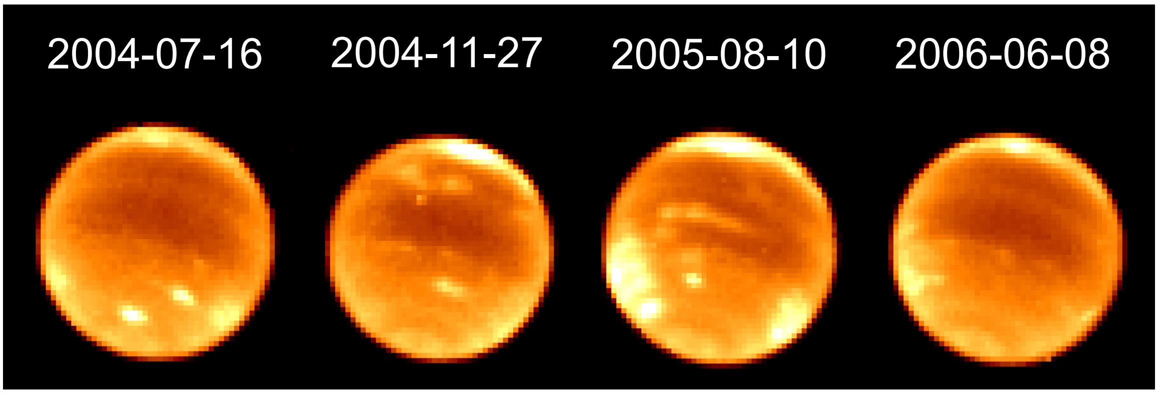

Figure 4.15: Images of Neptune from the Hubble Space Telescope WFPC2 619 nm filter from four different epochs that correspond to the Spitzer data the best.

Near-infrared images from Keck II NIRC2 from 2001 (Martin et al., 2012), 2009 (Fitzpatrick et al., 2014) and 2013/14 (Tollefson et al., 2018) look very much like Figure 4.14 panel D. Cloud features are prevalent at all longitudes and show this is the usual state of Neptune's upper troposphere.

One explanation for the contrasting lack of variation and frequent cloud activity could be that the more dynamic atmosphere causes every hemisphere to be active to the same degree. This homogeneity in activity would therefore cause the perceived lack of variation in this study.

4.4 Summary

A variation is not present at Neptune in 2005 or late 2004. In May 2004 a stratospheric variation is present at Neptune though it is tentative due to the larger uncertainties on this early dataset. If the variation is real then it could be caused by stratospheric methane injection by clouds or perturbations of the south polar warm vortex.

It is clear that a longitudinal variation is present in the stratosphere of Uranus in 2007 and in 2005. The next chapter will help in finding a cause for this variation by retrieving the individual longitudes to see if it is more likely a change in temperature, composition or a combination of both.

Chapter 5

Uranus' Stratospheric Temperatures and Composition in 2007

5.1 Introduction

In this chapter, we continue our use of the data from the Spitzer IRS detailed in chapter 3 and investigate it using the NEMESIS retrieval algorithm explained in chapter 2. We focus on the data from Uranus in 2007 and build on the previous investigation from Orton et al. (2014a,b) in retrieving the global average. We take this further by attempting to simultaneously retrieve the entire spectral range for the first time. We also retrieve the separate longitudes investigated in chapter 4 to investigate the cause of the variation in Uranus' stratosphere. The content of this chapter is all part of the published article by Rowe-Gurney et al. (2021).

5.2 Radiative Transfer Model/Method

The goal of this investigation is to develop a consistent retrieval framework for ice giant middle atmospheres. We slowly build up the complexity of the retrieval as we see improvements in the quality of the fits. The data ranges considered in the retrieval for low-resolution spectra are between 7.4 μm and 21.1 μm (472 - 1350 cm^{-1}) with three parameters (temperature, acetylene and ethane) that have full profile retrievals during the optimisation process.

For the high-resolution spectra, the range was constrained to between 12.0 μm and 19.0 μm (526 - 833 cm^{-1}) to omit overly noisy ranges without excluding the important features. The addition of the LH data beyond 19 μm increased the computation time significantly and so was omitted from this study. The following parameters were retrieved as full vertical profiles: temperature, acetylene, ethane and diacetylene. The high-resolution spectra did not cover the methane emission near 7 μm. This constraint, combined with the fact that the data were scaled to the low-resolution observations, limited our ability to derive temperatures independently from the high-resolution spectra and was why the low-resolution data were chosen as the main data to analyse.

Our Uranus reference atmosphere has 161 pressure levels and a pressure-temperature profile based on the nominal model from Orton et al. (2014a) with the assumption that temperatures reach just over 450K at a top pressure of 0.1 μbar. Alternative temperature profiles, including those mentioned in Orton et al. (2014a), were tested and this nominal model was found to provide the best *a priori* for our purpose (see sub-section 5.3.3). The gases included in the model are hydrogen, helium, methane ($^{12}CH_4$, $^{13}CH_4$ and CH_3D), acetylene (C_2H_2), ethane (C_2H_6), methylacetylene (C_3H_4), diacetylene (C_4H_2) and carbon dioxide. The different isotopes of methane were kept constant with respect to the vertical profile of $^{12}CH_4$. The CH_3D/CH_4 ratio used was 3.0×10^{-4} as in Orton et al. (2014b) corresponding to a D/H ratio of 4.4×10^{-5}. The $^{13}C/^{12}C$ value used is the terrestrial value of 1.12×10^{-2} (Marty et al., 2013).

The contribution function shows the vertical sensitivity of the Spitzer spectra, and is the product of the transmission weighting function and the Planck function (shown in Fig. 5.1 and explained more fully in Chapter 2). These are the altitudes we are most likely sensing at each low-resolution wavelength modelled by NEMESIS. At this resolution we find we cannot fit the narrow emission features of the hydrogen quadrupole without changes to the temperature prior (see sub-section 5.3.3 for details). The wavelengths at which these features occur have been omitted from any subsequent low-resolution retrievals. The quadrupoles that are in the selected high-resolution range have been, instead, covered in the high-resolution retrievals and in subsequent upper stratospheric testing. These features include the H_2 quadrupole S(1) line at 587 cm^{-1} (17.0 μm), S(2) at 814 cm^{-1} (12.3 μm), S(3) at 1034 cm^{-1} (9.7 μm) and S(4) at 1246 cm^{-1} (8.0 μm) (Orton et al., 2014a). The S(0) line, present in the LH data at 28.2 μm (354 cm^{-1}), has also be omitted from analysis due to us choosing not to use the data beyond 19 μm for the retrievals.

The calculation of the contribution function requires the abundances of the principal absorbers in the spectral intervals chosen. The molecular abundances are derived from those presented in Appendix A of Orton et al. (2014b) with some small modifications made throughout the process to improve the fit. We use the nominal gas model directly from Orton et al. (2014a,b) as our *prior*, then allow NEMESIS to vary temperature, acetylene and ethane to fit the low-resolution spectrum. These small deviations from the Orton et al. (2014a,b) model are discussed in subsequent sections.

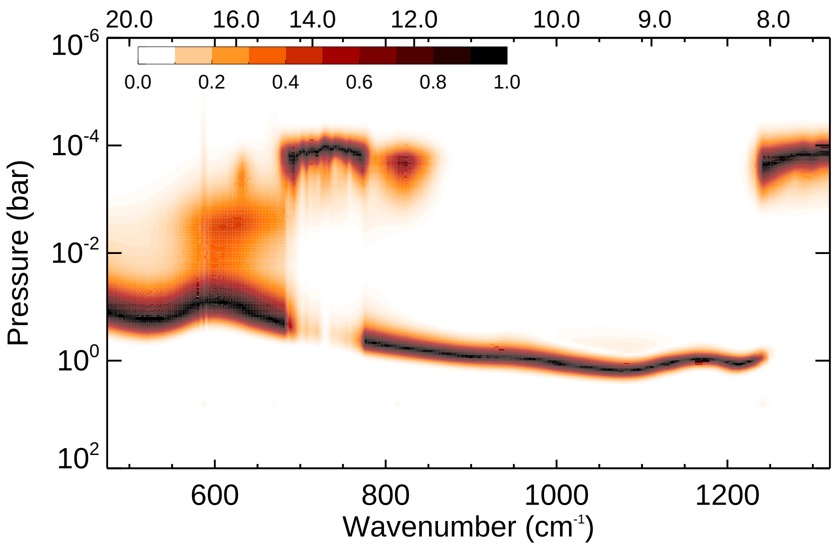

Figure 5.1: Low-resolution contribution function contour plot showing sensitivity to different altitudes for different portions of the disc-integrated spectrum for the reference atmosphere. The top x-axis shows the corresponding wavelengths in microns. Forward modelled using NEMESIS.

The low-signal region in the SL spectrum near 8-8.5 μm contains multiple sharp features that are not associated with real gaseous bands and therefore were not included in the model constraints. This region is sensitive to the carbon-13 isotopologue of methane and part of the monodeuterated methane band. The 5 to 7.4 μm section of the SL region was removed due to uncertainties in the available line data, excessive noise on the data, and the complex contribution of reflected sunlight at the shortest wavelengths. This wavelength range at Uranus has not been the subject of investigation in the past and will be the topic of subsequent analysis.

The errors used to constrain the spectral fit are the same as the measurement errors stated in subsection 3.4.2. The only limitation to the use of percentage errors is that the inversion is weighted towards the low radiance data. This biases the findings by not allowing the model as much freedom for what are usually noisier regions of the spectrum. Additional forward modelling error (0.019 nW/cm^2/sr/μm) was added to the methane band between 7 and 9 μm to allow the fit to the especially noisy, low-radiance regions more freedom during the retrieval. The subsequent fit to the data is close enough for this method of errors to be considered adequate. The uncertainties on the *priors* were set to 100% of the mole fraction for each gas (at each pressure level), with temperature *a priori* uncertainties of ±3 K to prevent substantial deviation from the model of Orton et al. (2014a). The typical number of iterations for the retrievals to converge on a reduced chi-squared value close to unity is nine for the low resolution and five for the high resolution.

NEMESIS is capable of generating synthetic spectra using line-by-line and also correlated-k approximation methods. The previous analysis of Orton et al. (2014a) used the former, but to compute the whole low resolution spectrum efficiently we used the correlated-k method. This has been explained in detail in chapter 2.

5.2.1 Disc Averaging

To convert the spectral radiance units (W/cm^2/sr/μm) into spectral power units (W/μm), a Uranian radius of 26000 km is assumed. This adds a 441 km limb extension of the atmosphere above the 1-bar pressure level at radius 25559 km.

The weightings in Table 5.1 are calculated using equation 2.11 using the same Uranian radius, r, that includes the 441 km limb from Teanby and Irwin (2013).

i	x (km)	Tangent altitude (km)	Emission angle (°)	w_i
1	0	-	0.0	0.0
2	5000	-	11.28	0.08876
3	12000	-	28.00	0.23077
4	18000	-	44.77	0.26627
5	22000	-	59.40	0.19527
6	24000	-	69.88	0.10651
7	25000	-	77.99	0.05766
8	25559	0	90	0.02269
9	25600	41	90	0.00913
10	25800	241	90	0.01527
11	26000	441	90	0.00769

Table 5.1: Field-of-view averaging points used to produce the synthetic reference spectra for Uranus, adapted from Teanby et al. (2013) where w_i is the weight calculated using equation 2.11.

5.2.2 Eddy Diffusion

The eddy diffusion coefficient profile is a major free parameter in chemical models (see Chapter 2). We use the assumption that the coefficient is the same at every altitude for Uranus (Moses et al., 2018). There is a significant effect from the vertical eddy diffusion coefficient (K_{zz}) on the distribution of gases in the Uranian stratosphere (Moses et al., 2018). A nominal value of $K_{zz} = 2430$ cm^{2}s^{-1} with a methane tropopause mole fraction (f_{CH4}) of 1.6×10^{-5} is stated in Orton et al. (2014b), but they could not independently constrain these values. Different $K_{zz} - f_{CH4}$ pairs were found to fit the data with higher K_{zz} values needing less methane and vice-versa. The two extremes of the K_{zz} values suggested by Orton et al. (2014b) Fig. 4 are 1020 cm^{2}s^{-1} and 3270 cm^{2}s^{-1}. The different K_{zz} values influence the shape of the vertical profiles of the main gases. The vertical hydrocarbon abundances calculated using these three K_{zz} values were used as priors for three independent retrievals, to see which one worked best (Fig. 5.5). For the retrieved gases, acetylene and ethane, the retrieved profiles fit the differing *priors* with no significant changes to the fit of the spectrum or the temperature. All three of these values were acceptable eddy diffusion coefficients and agrees with the findings in Orton et al. (2014b) and is the reason we chose to use their nominal value. This assumption places the methane homopause at the 7×10^{-2} mbar pressure level (Moses et al., 2018).

5.3 Disc-averaged Results

5.3.1 Low-Resolution Retrievals

To fit the globally-averaged low-resolution data we allow the full profiles of temperature, acetylene and ethane to vary. We retrieved from spectra in the range between 7.4 μm and 21.1 μm (472 - 1350 cm^{-1}) with the hydrogen quadrupole features and the noisy region around 8 μm omitted. We could not achieve an adequate fit when allowing the acetylene and ethane abundances or temperature profile to vary in isolation, and so we needed to allow all three parameters to depart from the *prior* profiles of Orton et al. (2014b) (Fig. 5.2). The best-fit retrieval, that allows variation from both sets of parameters, can be seen in the top panel of Figure 5.3 with a reduced chi-squared value of 0.77.

The retrieved temperature profile (Fig. 5.4) is consistent with the *a priori* from Orton et al. (2014a) at most altitudes. A 3 K and 2 K increase occurs at 0.4 mbar and 1.75 bar respectively. A 2 K cooling occurs at 0.1 mbar with other deviations within the retrieved errors. We also tested alternative temperature profiles. An isotherm at $p < 0.1$ mbar was proposed by Orton et al. (2014a) based on the findings from Lindal et al. (1987). We tested similar isotherms at different temperatures and found the best fit at 110 K, but the retrieval showed the need for 7 K heating just above the 0.1 mbar level, thus diverging from the isothermal shape. We discuss the impact

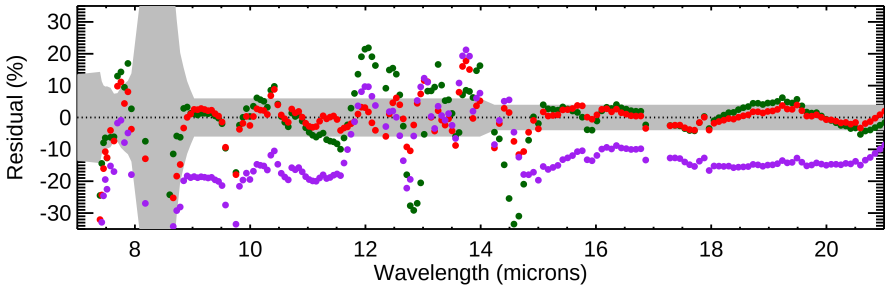

Figure 5.2: The residuals between the low-resolution data and the retrievals for temperature change only (green circles), acetylene and ethane abundance change only (purple circles) and the temperature, acetylene and ethane retrieval used in subsequent analysis (red circles). Retrieval errors are shown as the grey shaded regions.

of this profile (and other alternatives) to the upper-stratosphere and the hydrogen quadrupole in sub-section 5.3.3.

The P and R branches of acetylene fit well in the low resolution but the fit to the Q-branch has a higher radiance than the data, at the upper limits of the errors (Figure 5.6). The retrieved profile has a significant increase in abundance compared to the *prior*, peaking at 0.3 mbar. This peak is slightly deeper than the *a priori* peak. Above and below the new peak there is depletion relative to the *prior*. This is likely due to the lack of resolution for the sharp peak and the potential for saturation at this most radiant point in the data.

We tested the correlation-length parameter inside NEMESIS and a standard value of 1.5 was chosen. This parameter controls the smoothing of the profile fits. Higher values, that allowed more smoothing, had no significant effect on any of the profiles, including the overall chi-squared. If we force heavy smoothing of the acetylene profile, this results in an unusual vertical temperature structure in compensation. The multivariate problem is complex, and in this case we attempt to achieve a reasonable balance between the smoothness of both profiles. When we tested the acetylene, ethane, and methane priors resulting from the extremes of the vertical eddy diffusion coefficient in Orton et al. (2014b), we found that both solutions converged on the same abundance profile as the nominal model (Figure 5.5). Furthermore, scaling the acetylene prior to as little as 0.1 times and as much as 10 times the nominal acetylene abundance, we also found a convergence to the same nominal profile, lending confidence that our retrieval is driven by the data rather than being sensitive to the prior, at least over the 0.1-1.0 mbar range.

The ethane profile shows a depletion in the maximum stratospheric abundance

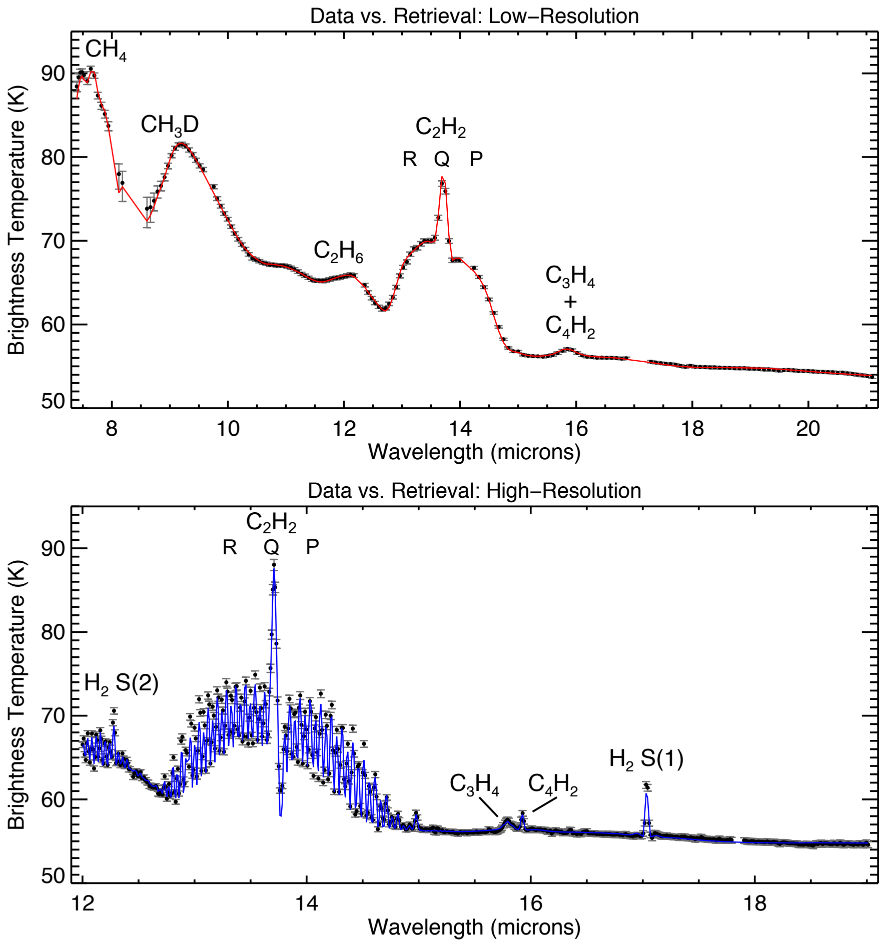

Figure 5.3: Full spectrum retrievals for the Spitzer-IRS Uranus-2007 global average spectra (black dots with associated errors). The top panel shows the low-resolution (SL and LL) modules between 7.4 and 21.2 μm (red) where temperature, acetylene and ethane are allowed to vary freely. The methane region between 7.4 and 9 μm has had a fixed forward-modelling error added to account for uncertainties. The bottom panel shows the high-resolution (SH) module between 12 and 19 μm (blue) where temperature, acetylene, ethane and diacetylene are allowed to vary freely.

at around 0.2 mbar with a fit within errors across the entire wavelength range (Fig. 5.7).

The spectral fit shows a difficulty in fitting the 7.4 - 7.6 μm region (Fig. 5.8) that was also seen by Orton et al. (2014b). They suggested that this is caused by other emission features being present and the model not containing the necessary line data. Our fit to this region is similar in shape and so we can assume that the same problem persists in our model, most likely as a result of incomplete line databases. The forward modelling errors added to the spectrum across the methane range were necessary to allow the temperature profile to fit realistically. This region is one of the

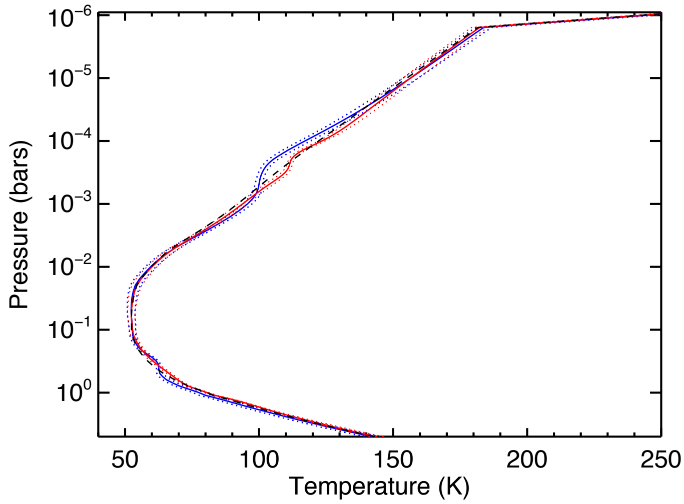

Figure 5.4: Retrieved vertical temperature profile for the global average of the low-resolution data (red solid line) with retrieval errors (red dotted line) compared to the *prior* (black dashed line). The high-resolution retrieved profile is also displayed (blue solid line).

dimmest in the entire spectrum (refer back to Figure 3.5 panel B) and so the larger uncertainty is expected.

All deviations from the *priors* greater than their associated errors occur in the same region of the stratosphere between 1 mbar and 0.01 mbar. The temperature and hydrocarbon fits are degenerate so we would expect any deviations from one profile of Orton et al. (2014a) to also affect the other.

5.3.2 High-Resolution Retrievals

In addition to the low-resolution dataset, the high-resolution observations show a similar longitudinal variability. We initially tried to forward-model at high resolution, using the low-resolution retrieval results, to see if we could reproduce the same variations that were observed in the high-resolution data. Figure 5.9 shows the percentage variation of the species that are present in both the high-resolution (green circles) and low-resolution (blue circles) spectral settings at each longitude. There are discrepancies between the modelled (red crosses) and the SH data variations. The variation between the model and the SL, however, is much smaller at all longitudes. This offset between the high-resolution forward model and the SH data is due to the shift in the longitude between observations with the SL and SH modules (Table 4.1). This 20° is enough to cause a significant change in the spectra. Thus the low-resolution results are not perfectly suited to model the high-resolution data, even if we were to assume

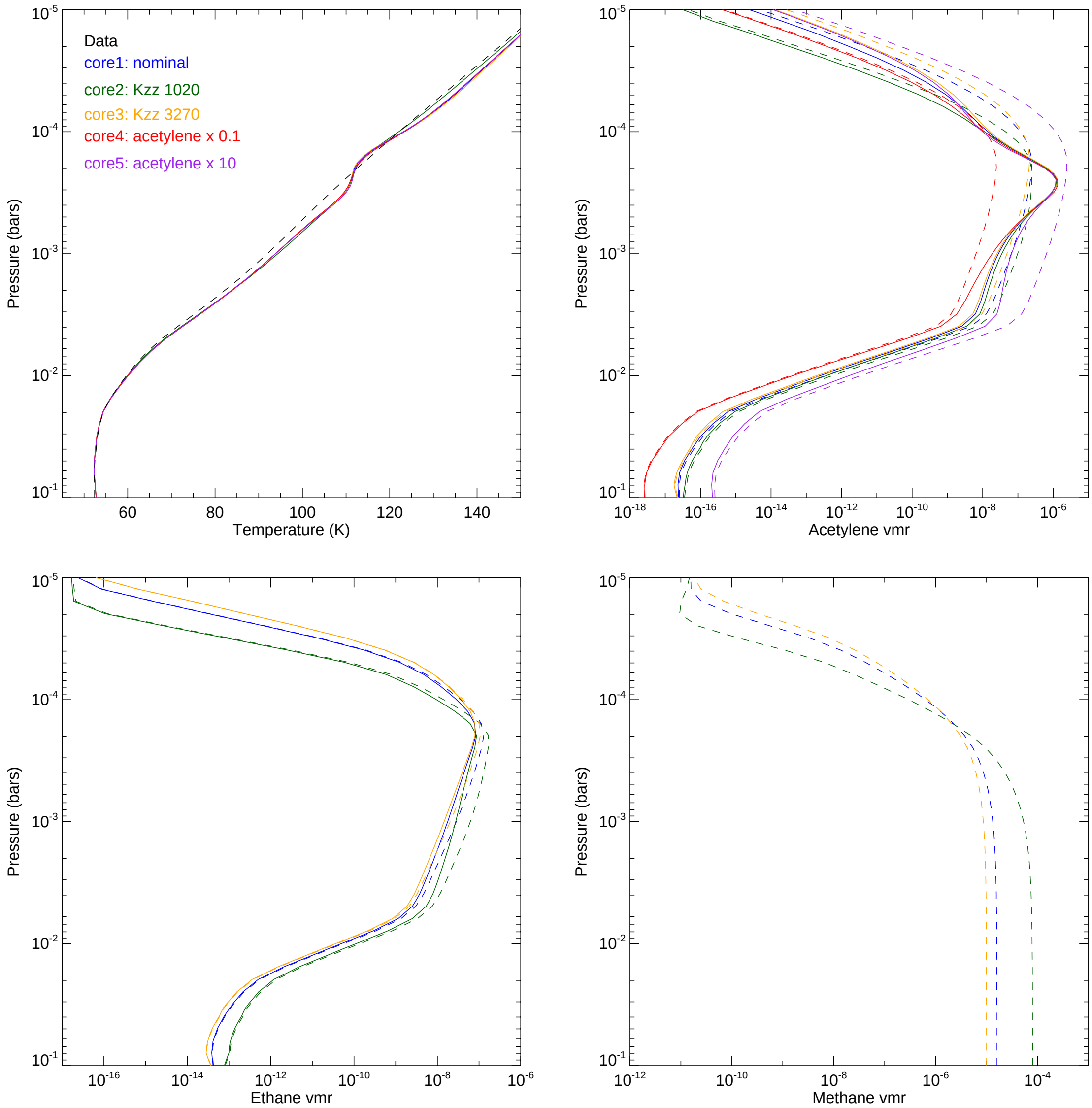

Figure 5.5: Results of the eddy diffusion and the extremes of the acetylene abundance tests for the low-resolution global average retrieval. Dashed lines are the *a priori* profiles, solid lines are the retrieved values showing good convergence in the 0.1-1.0 mbar range, despite starting from rather different priors.

that the high-resolution data are perfectly calibrated. The change in the brightness was too much for this test to be meaningful so we therefore attempted to invert the high-resolution data as a further test of the source of the variations.

When inverting the high-resolution data we encountered several challenges: (i) The data had to be scaled and pivoted to the low-resolution during calibration; (ii) the wavelength ranges do not contain the necessary information to constrain the variation of methane; (iii) the resolution is estimated at $R \sim 600$ but is found to vary

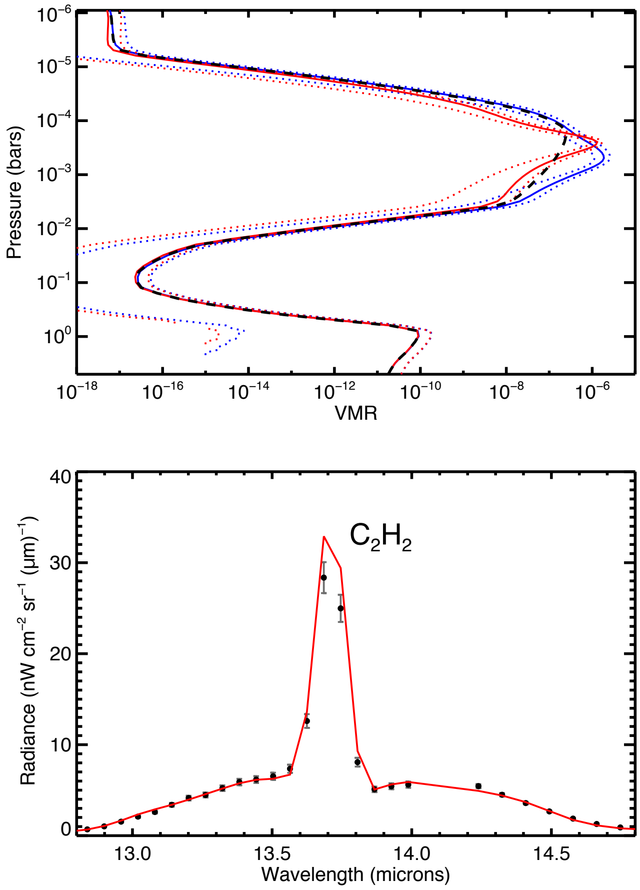

Figure 5.6: Acetylene vertical profile retrieval and spectral fit to the global average of the data. Low-resolution retrieval result shown as red solid lines in both panels. The top panel shows the volume mixing ratio (VMR) vertical profile where the *prior* is shown by the black dashed line and the retrieval uncertainties shown as red dotted lines. The high-resolution retrieval result is shown for comparison (blue solid line). The bottom panel shows the spectral fit to the data (black dots) with error bars, for the relevant acetylene wavelength range.

considerably as a function of wavelength (Orton et al., 2014a). Nevertheless, here we attempt to make use of the high-resolution data to study the longitudinal variation.

We attempt to fit the globally-averaged high-resolution data to identify how they might differ from the low-resolution results. The bottom panel of Figure 5.3 shows our best fit to the full high-resolution spectrum. The differences between the low-resolution (red lines) and the high-resolution (blue lines) retrieval results can be seen in the temperature, ethane and acetylene profiles (Figures 5.4, 5.7 and 5.6 respectively). The temperature profile shows cooling of around 7 K compared to the *prior* at around 0.1 mbar. For acetylene, the deviation from the *prior* is similar in magni-

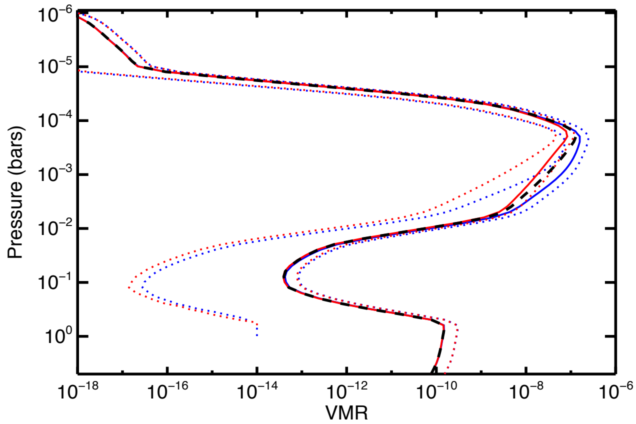

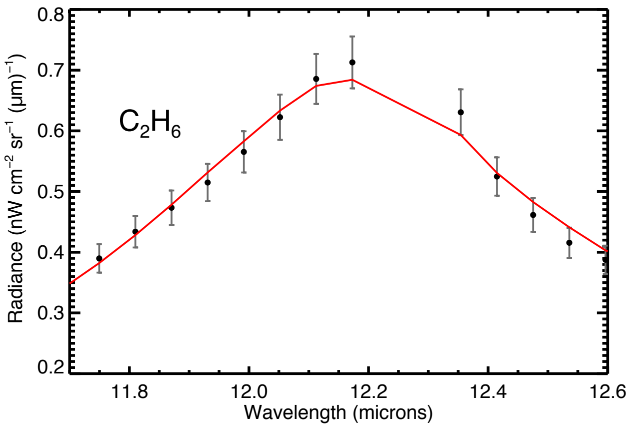

Figure 5.7: Same as Figure 5.6 but for ethane.

tude to the low-resolution result but peaks slightly deeper (0.3 mbar). The cooling and the increase in acetylene in this same altitude range indicates a level of degeneracy between these two parameters that was also identified in the low resolution inversions. For ethane, instead of a depletion at stratospheric altitudes (between 0.1 and 10 mbar) there is an increase in abundance. At the 1 mbar level the ethane abundance is increased compared to the *prior* by a factor of 1.3 for the high-resolution spectrum compared to a depletion by a factor of 0.3 for the low-resolution spectrum. These differences in temperature, acetylene and ethane could be real and related to the $\sim 20°$ change in the longitude between modules (Table 4.1), but could just as likely be due to the several modelling challenges we listed above. All of the retrieved profiles peak slightly deeper than in the low resolution results and could be due to differing vertical resolution causing differences in the high-resolution contribution functions.

Fits to the spectra are shown in some important regions in Figure 5.10. Ethane shows a good fit across the range with the embedded H_2 S(2) line clearly visible.

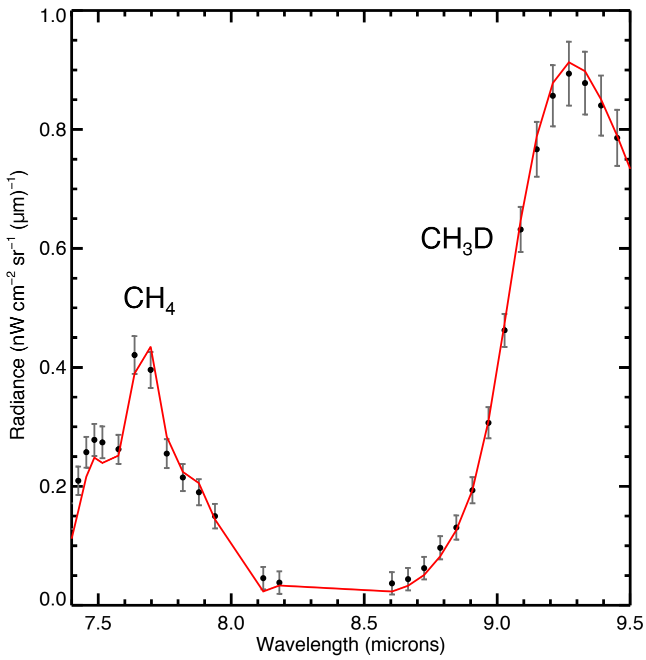

Figure 5.8: Methane retrieval fit to the low-resolution data (black dots with associated errors) for the relevant wavelength range for both methane variants labelled.

This modelled line is dim compared to the data which may suggest that the fitted temperature never quite gets warm enough to explain this emission when fitting the whole spectrum. The H_2 S(1) is also dim and we discuss this further in sub-section 5.3.3.

The fitted acetylene bands P and R are consistently lower than the observed brightness. This underfitting could be caused by the k-tables being sampled at a fixed spectral resolving power of 600 even though the resolution is variable across the wavelengths. However, although several different resolution k-tables were created to try to improve this fit, no real improvements were seen. We also tried to fit narrower sub-ranges of the acetylene emission, treating the P, Q and R branches independently, but had the same issue. The low-resolution acetylene fit also had some issues, though not as severe, and this was reasoned to be caused by saturation of the bright Q-band peak. The same can be reasoned for this range in high resolution.

Diacetylene and methylacetylene (propyne) both fit well. Diacetylene had to be varied in the retrieval to stop consistently underfitting. A very small increase in abundance of a factor of 1.6 between 0.2 and 1 mbar was necessary to fit this feature but was within the retrieved errors. Carbon dioxide at 667 cm^{-1} (15.0 μm) also fits within errors. The unknown feature at 640 cm^{-1} (15.6 μm) was observed by Orton

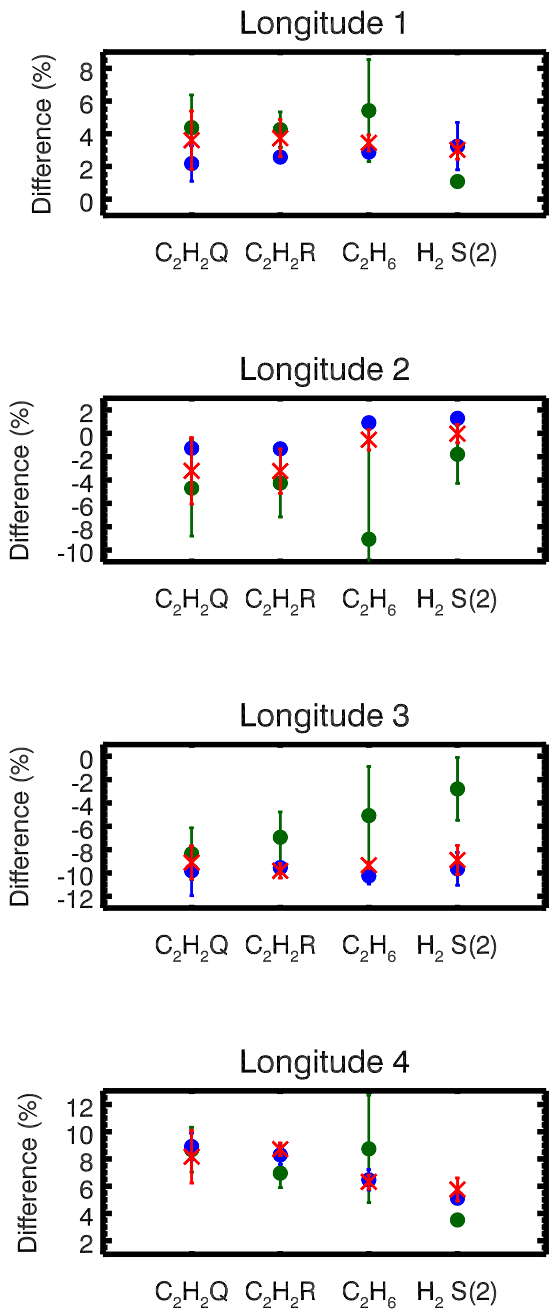

Figure 5.9: The longitudinal variations of certain species with the high-resolution forward model variations (red crosses) compared to the SH data variations (green circles) and SL data variations (blue circles). Errors shown are the standard errors over the wavelength range variations. Species were chosen due to their spectral range overlapping in both the SL and SH modules.

et al. (2014b) and can be seen in the bottom panel of Figure 5.10. This same feature also shows up in ISO data of Saturn in Moses et al. (2000). Another, small unknown feature is also present at 624 cm^{-1} (16.0 μm). Both unknown features are within the uncertainty of the data.

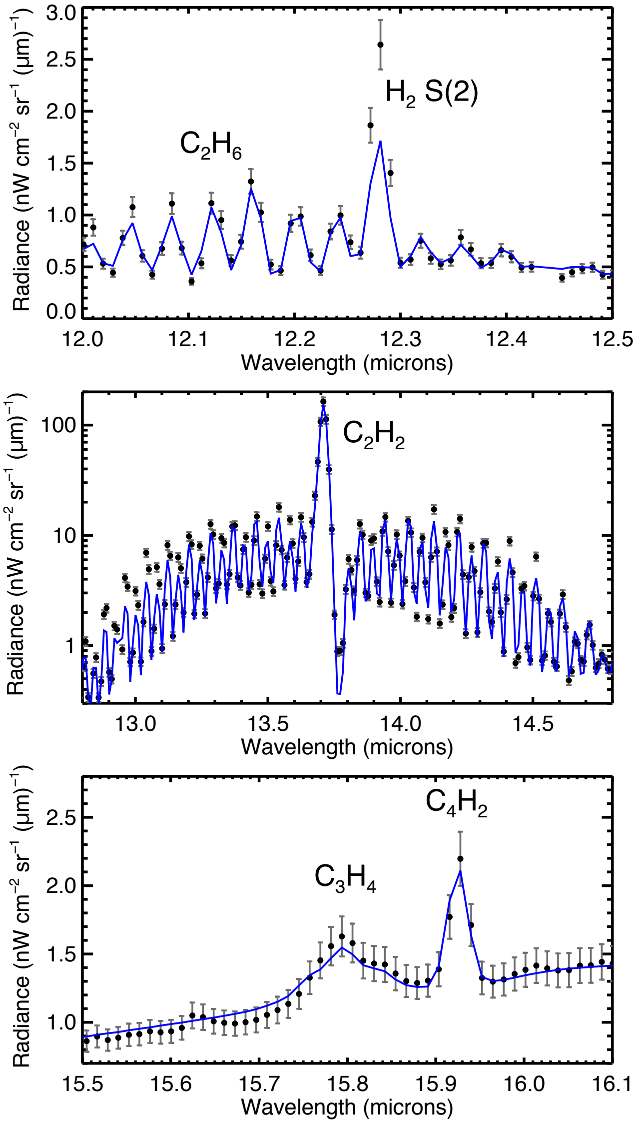

Figure 5.10: The spectral fit of the high-resolution retrieval (blue solid lines) to the data (black dots) with 9% error bars. Top panel: Ethane region with embedded H_2 S(2) feature. The poor fit of the model to this feature is discussed in sub-section 5.3.3. Middle panel: Acetylene P, Q and R band regions. Bottom panel: Methylacetylene and diacetylene region with unknown feature visible at 15.6 μm.

The full high-resolution inversions suggest slightly modified temperatures and gas profiles compared to the low-resolution data. This deviation could be caused by the longitudes being sampled up to 20° apart (Table 4.1) though the calibration of the SH data is sufficiently challenging that it is understandable that more weight is to be placed on the variations revealed by the better-calibrated low-resolution results.

5.3.3 Upper-Stratospheric Temperatures and the Hydrogen Quadrupole

The hydrogen quadrupole features present in the data include the S(1) line at 587 cm^{-1} (17.0 μm), S(2) at 814 cm^{-1} (12.3 μm), S(3) at 1034 cm^{-1} (9.7 μm) and S(4) at 1246 cm^{-1} (8.0 μm) (Orton et al., 2014a). S(1), S(2) and S(3) are clearly visible in the low-resolution data. The S(4) line is within the noisy range of the spectrum and therefore we have omitted it. The SH module data feature the S(1) and S(2) lines.

The quadrupole lines are all consistently underfitting in both the high- and low-resolution retrievals when we restrict ourselves to the Orton et al. (2014a) *prior*. This is why we have omitted the quadrupole spectral ranges in the global and longitudinal study of the low-resolution spectra, after clarifying that their omission does not impact our findings for the longitudinal variations.

Orton et al. (2014a) found that to successfully model the quadrupole they had to extend the temperature profile into the upper stratosphere up to 1 nanobar. The nominal temperature profile used in the main investigation cuts off at 0.1 μbar so we have extended it in Figure 5.11. This extended temperature profile reaches 700 K in the thermosphere, consistent with Voyager UV occultation measurements (Herbert et al., 1987). We increased the number of pressure levels to 200 and used an equivalent disc-averaging method that was extended up to a radius of 27000 km (a limb of 1441 km above the 1 bar level). The nominal fits to the quadrupole have the same differences to their respective spectral data as the nominal values in Figure 5.3, despite the extension into the upper atmosphere. Modelling of the quadrupoles alone does require the upper extension to be accurate but when retrieving the entire spectrum it does not make a difference outside of uncertainties. As we found it made no significant difference to the full spectrum retrievals to include these upper altitudes, we tested the alternative temperature profiles in Figure 5.11.

Although we cannot fit the quadrupoles with the Orton et al. (2014a) *prior*, we can get closer if we adjust the *prior* by warming it at the upper stratospheric pressures that the quadrupoles are sensitive to (Figure 5.11). These alternative temperature *priors* allow better quadrupole fits without affecting the fit elsewhere in the spectrum. The retrieved temperature fits were all within uncertainties of the nominal temperature retrieval, apart from at the altitudes that are warmed, where they are within the uncertainties of the adjusted *prior*. We have displayed two of the profiles in Figure 5.11. One has a smoothed slope starting to warm beyond the nominal profile at 10 μbar and the other starting at 28 μbar. They show that whilst we can fit the S(1) and S(3) lines together, this will then overfit the S(2) line as a consequence. We are assuming thermal equilibrium para-hydrogen fractions at the warm temperatures of the upper stratosphere, and this could be evidence that equilibrium is not the right solution for the quadrupoles (Conrath et al., 1998; Fouchet et al., 2003). The degree of disequilibrium could tell us a lot about atmospheric circulation and would be a good topic for future study.

This is why we chose to omit the quadrupoles from our low-resolution investigation and rely on the temperature *prior* found from Orton et al. (2014a). The quadrupoles only represent a small number of spectral points so the retrieval is favouring the richer data of the hydrocarbon bands, sacrificing the fit to the narrow lines. We have found that the extension into the upper stratosphere and accurate modelling of the hydrogen quadrupole do not affect the conclusions about relative changes from longitude to longitude in the following section.

As mentioned previously, we also experimented with a range of *a priori* with isotherms at $p < 0.1$ mbar. All *priors* tried to move away from the isotherm shape, heating by up to 7 K just above the 0.1 mbar level. The best fit quasi-isotherm (at 110 K) was found to fit the majority of the spectrum but it makes the fit to the quadrupole worse (see Fig. 5.11). A heating of the upper stratosphere is favourable over this solution in order to fit the quadrupole along with the rest of the spectrum in both the high and low resolution.

5.4 Retrievals at Separate Longitudes

We have demonstrated that NEMESIS is capable of fitting the globally-averaged Spitzer spectrum at low resolution with vertical profiles that are slightly modified from those of Orton et al. (2014a,b). We now investigate the four individual longitudes, fitting each low-resolution spectrum separately. Panel A in Figure 5.12 shows the difference between the retrieved spectra and the data if we allow temperature, acetylene and ethane to vary. When all parameters are free, they vary together due to the degeneracy between temperature and gas abundance. To test whether the change could come from changes to gases or temperatures alone we set up two additional experiments. These are the same as we tested for the global average (Fig. 5.2) but this time the chosen parameter is fixed to the global average retrieval result and run

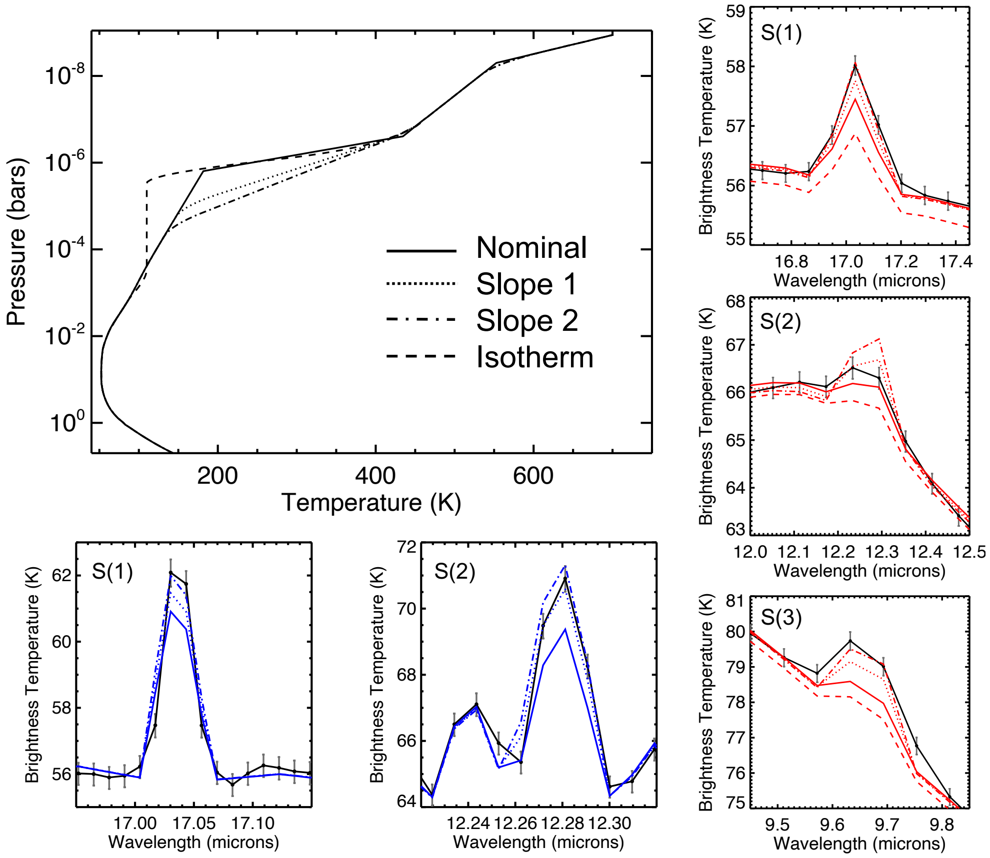

Figure 5.11: Temperature profile *a priori* that were used to test the quadrupole fits and the upper stratosphere extended up to 1 nanobar. The nominal temperature profile with extension is shown with the solid line, the profile with a smoothed slope starting at 10 μbar (Slope 1) is shown by the dotted line and the profile starting at 28 μbar (Slope 2) is shown by the dashed-dot line. The dashed line shows the low-resolution isotherm test at 110 K. The quadrupole fits during the full spectral retrieval for each temperature *prior* are shown for the low resolution (red) and high resolution (blue). The line styles match the temperature profile that they represent. The quadrupole line S(1) is at 17.0 μm (587 cm^{-1}), S(2) at 12.3 μm (814 cm^{-1}) and S(3) at 9.7 μm (1034 cm^{-1}).

with the other parameter as the only retrieved variable. Panel B shows the residuals when temperature is the only parameter changing. Panel C shows the residuals where only acetylene and ethane are allowed to vary.

Panel A and B (Fig. 5.12) have residuals and chi-squared values that are almost identical to each other. Panel C, however, shows that the model is less able to fit the data within errors when only gases are varied, and has discrepancies in the fits between longitudes. The chi-squared values are higher for longitudes 3 and 4 that exhibit the largest variation from the average.

From the fits shown in Fig. 5.12, we see that temperature variations are all that is required to fit the spectra to the same accuracy as when we change all of the variables. There is no known reason for chemical abundances to change with longitude, as photochemical time scales are extremely long, except perhaps if there are localized regions of vertical mixing. The small temperature perturbations retrieved here will have no effect on the chemical kinetics rates. We can therefore assume that temperature is the only parameter changing to cause the longitudinal variations observed in the emissions of the photochemical constituents of the stratosphere.

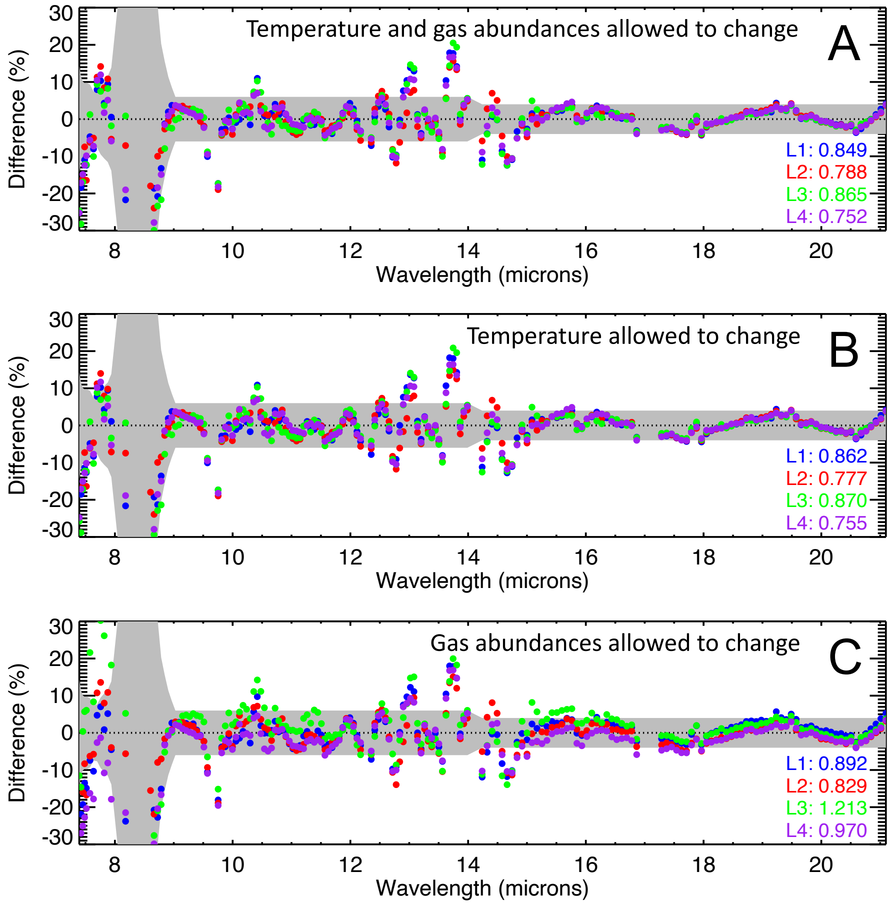

Figure 5.12: Percentage residuals between the low-resolution spectra and the retrieved fits for each individual longitude. The three panels show three different assumptions made during the modelling process. Panel A shows the results when both temperatures and gases are allowed to vary, panel B shows temperature change only and panel C shows gas change only. Longitude 1, 2, 3 and 4 are shown in blue, red, green and purple respectively. Global-average retrieval errors are shown by the grey shaded region. The chi-squared value for each longitude retrieval is shown in the bottom right corner of each panel.

If we assume that the longitudinal variability is caused solely by changes in temperature, then the temperatures required to cause the spectral changes in the four longitude observations are reasonable. Figure 5.13 shows a 3 K difference at 0.1 mbar between the most extreme longitudes. Longitude 3 is cooled by 2 K at 0.1 mbar. Longitude 4 is heated by 1.2 K just below the same altitude where longitude 2 also shows a cooling of 1.3 K. These three extremes of temperature change are the only altitudes at which the temperature difference exceeds the associated retrieval uncertainties of the global average retrieval.

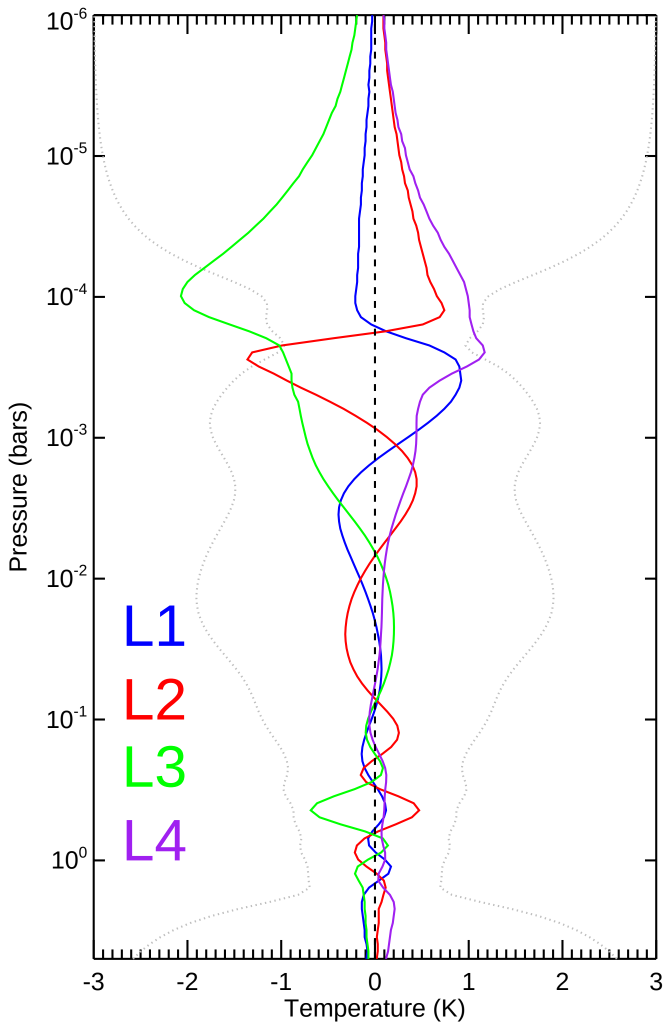

Figure 5.13: Temperature differences from the global mean at each pressure for each longitude retrieval, assuming the temperature is the only variable that is changing (corresponding to hypothesis B in Figure 5.12). Retrieved errors of the global average temperature are shown as grey dotted lines.

5.5 Discussion

5.5.1 Comparison to Orton *et al.*

Our reanalysis of the Spitzer/IRS globally-averaged spectrum converged on similar temperature and hydrocarbon profiles as Orton et al. (2014a), with the exception of deviations near the 0.1-mbar level and at even lower pressures to allow us to fit the quadrupole features. This is an independent fit to the newly reduced Spitzer data with a different spectral model that largely supports the results of Orton et al. (2014a,b) with some refinements. For example, Orton *et al.* modelled individual features separately with a line-by-line model, whereas we have inverted the entire range simultaneously with k-distributions to reproduce the newly reduced, and slightly brighter, Spitzer data.

The retrieval was only successful in replicating the data with adjustments to the acetylene and ethane profiles. This suggests that there is a real deviation from the gas *priors*, mainly acetylene, within this range. The increase in acetylene is required to allow NEMESIS to achieve an adequate fit across the whole spectral range. This sharp peak in abundance cannot be easily explained by photochemistry, and we cannot discount issues related to saturation at the peak of this relatively bright feature. There could also be hidden parameters contributing to this fit, such as systematic problems related to calibration of the data, and the effect of a non-uniform disc on the disc-averaging process. Non-LTE effects could also potentially explain these differences if they were factored into the retrievals. These anomalies at around 0.1 mbar are also present in the high-resolution retrievals but, with the data having such challenging reduction and calibration, they cannot be relied upon. We used this global fit as a baseline to study the relative variability that should be unaffected by any discrepancies from Orton *et al.*.

5.5.2 Longitudinal Temperature Changes

Having demonstrated the longitudinal variation occurring at Uranus is real and consistent with temperature changes in the stratosphere, we discuss where these variations may have originated from. It is still possible that temperature and abundances are both changing to cause the variation, but the fact that we can simultaneously reproduce the spectral emission from several molecular species by adjusting the temperature profile alone, suggests that a simple temperature perturbation may be responsible for the observed differences between longitudes.

Temperature change in the stratosphere of giant planets has been known to originate from intense storm activity that causes upwelling of cold material from the troposphere into the lower stratosphere. Voyager 2's IRIS instrument observed an intense and localised cold region in the lower stratosphere at Neptune (Conrath et al., 1989) that was thought to be associated with the Great Dark Spot. In 2006, a possible dark spot at Uranus was observed using HST (Hammel et al., 2009). If a dark spot or other large vortex was discovered and persisted through to December 2007, it is possible that this could cause a tropospheric temperature anomaly like that observed at Neptune, but the influence of tropospheric vortices on stratospheric temperatures is uncertain. Chapter 4 shows that the variability seems to occur in 2005, though it is weaker and seemingly at higher pressures than in 2007. This either shows that this type of anomaly occurs at Uranus frequently, or that this is the same feature (this possible dark spot) that has persisted, evolved and strengthened through to 2007. The 2004 data is so noisy that no conclusions can be drawn about whether the variation was present at that time. More frequent and repeated observations in the mid-infrared are necessary to make future insights.

If the variation is caused by a dark spot then this would mean a suspected stratospheric cold anomaly would exist at Longitude 2 and 3. We can assume that any localised cold region would be located between 0° and 180°. Conversely, we cannot discount the possibility that a hot region was located in the opposite hemisphere, much like the Saturn stratospheric beacon (Fletcher et al., 2012; Moses et al., 2015; Cavalié et al., 2015).

An alternative origin for the thermal variation could be a stratospheric wave with wavenumber 1. Waves are common in the stratospheres of Jupiter (Fisher et al., 2016; Fletcher et al., 2016), Saturn (Achterberg and Flasar, 1996) and Neptune (Sinclair et al., 2020a). It was postulated that the Great Dark Spot at Neptune was driving a stratospheric wave that then caused the cold temperature anomaly observed by Voyager 2 (Conrath et al., 1989).

We can not be sure if this change is isolated to one location or is a global phenomenon. JWST will provide us with the spatial resolution at mid-infrared wavelengths that is required to give us insight into what is happening. We can, however, use spatially-resolved images from ground-based instruments in the near- and mid-infrared to give us clues to this stratospheric anomaly.

5.5.3 Comparison to Ground-Based Images

We have now speculated that it is a temperature change in the stratosphere and therefore the two comparisons to ground-based images we discussed in chapter 4 can be evaluated based on this.

In the Keck II images the minimum in the stratospheric emission and temperature at longitude 3 coincided with the hemisphere where the troposphere exhibited more meteorological activity, such that upwelling and adiabatic expansion might explain the 3-K cooling of stratospheric temperatures. However, the individual features are small compared to the overall size of the disc, and no such large temperature perturbations have been observed in upper tropospheric temperatures of Uranus to date (Orton et al., 2015; Roman et al., 2020). Thus direct convective overshooting into the stratosphere seems unlikely but it is possible that one of these bright features is associated with a much larger and invisible dark spot mentioned in chapter 4 (Hammel et al., 2009).

The VLT-VISIR images, though taken years after the Spitzer observations, provide us with a clue to the possible spatial extent of the longitudinal variation observed with Spitzer. The observed features were at the edge of detectability in the ground-based 13 μm images, but appeared to be limited to the brighter mid-latitude band, and extended over half the visible longitudes. This shows it is feasible that the variation is localised on a small portion of the disc such that the 3-K contrasts we measure in the disc-averages could be a lower limit on the actual temperature perturbations in Uranus' stratosphere. However, any conclusions would be speculative at best until the Uranian stratosphere is observed with the spatial resolution and sensitivity of JWST.

This data suggests that tropospheric meteorology could be influencing stratospheric temperatures in subtle ways that either persist over long timescales or have been observed coincidentally two years apart. We also have tentative evidence of a connection between direct upwelling in the troposphere and the stratospheric temperatures during the time of the Spitzer observations.

5.6 Summary

In this chapter, we have adapted the NEMESIS spectral inversion algorithm to provide a full, simultaneous retrieval from 7-21 μm disc-averaged spectra of Uranus. This work builds upon that of Orton et al. (2014a,b), where an average over multiple longitudes was used to characterise the vertical temperature and composition. The longitudinal variation in emission detected at Uranus during the 2007 equinox can be explained as a physical change in the stratosphere of the planet, possibly due to a localised cold feature associated with a tropospheric vortex and its bright companion cloud, or a stratospheric wave.

The next chapter will apply the same methodology to the Spitzer IRS data of Neptune.

Chapter 6

Neptune's Stratospheric Temperatures and Composition in 2005

6.1 Introduction

This chapter uses the global average of the three separate longitude observations from the Spitzer IRS 2005 Neptune data (Chapter 3). We have conducted retrievals using NEMESIS in a similar fashion to the 2007 Uranus data in the previous chapter. We attempt to simultaneously retrieve the low- and high-resolution data using the three modules available (SL, SH and LH). The Short-Low (SL) module has wavelengths between 5.13 - 14.29 μm, the Short-High (SH) module is between 9.89 - 19.51 μm and the Long-High (LH) module is between 18.83 - 37.14 μm. There is no variation from longitude to longitude like at Uranus but, unlike the Uranus 2007 data, this data is currently unpublished and so many novel results have come from the global average alone.

6.2 Radiative Transfer Model/Method

Unlike the Uranus data, the Neptune data have lower noise at high resolution due to the planet being brighter. This means we can take advantage of all three modules (SL, SH and LH) in the retrievals. This brightness also causes disadvantages. The LL module would be saturated if used and so the only low-resolution data are from the SL module. The data ranges considered in the retrieval for low-resolution spectra are between 7.5 μm and 32.0 μm (313 - 1333 cm^{-1}). For the high-resolution retrievals, the range was constrained between 11.4 μm and 19.4 μm (515 - 877 cm^{-1}). The reasons for these specific ranges are stated below.

The thermal spectrum of Uranus is dominated by the tropospheric continuum (refer back to Figure 5.1) but Neptune's spectrum contains a lot more stratospheric hydrocarbons (Figure 6.1). Constraining the continuum with just the SL data has therefore been a challenge and we have had to combine it with the high-resolution module data longwards of 14 μm. We were careful to only sample the places in the SH and LH modules that contain continuum only and that is why our low-resolution retrievals go all the way out to 32 μm. This also partially solved the problem of the lack of LL module.

For the low-resolution retrievals, three parameters (temperature, acetylene and ethane) were allowed to vary during the optimisation process. All three parameters vary over their full profiles as simply scaling these profiles was found to be inadequate. As at Uranus, the 5 - 7.5 μm region was omitted due to uncertainties in the line data available and suspected reflected sunlight at these short wavelengths.

The high-resolution data do not contain the 7.7 μm methane band that helps to constrain the temperature profile. For this reason, we used the results from the low-resolution retrievals as priors for the high-resolution optimisation process. Temperature, acetylene and ethane were allowed to vary over their full profiles and a number of gases were allowed to vary by a scaling factor. These gases are methylacetylene, diacetylene, CO_2, propane and CH_3.

In both resolutions we omit the region around 10 μm containing the ethylene feature because we were not able to fit it realistically with the rest of the spectrum. The SH module has much less noise seen in the 10 - 11.5 μm region for Neptune compared to Uranus and the ethylene feature is very clear but we still had trouble fitting it. It could be reproduced, but only with a sharp warming in the troposphere at around 1 bar where both the contribution function plots show sensitivity in these regions (Fig. 6.1 and refer back to Fig. 3.7). The ethylene features are too deeply embedded in these regions of tropospheric emission that they could not be taken out. This is why both entire regions had to be omitted from analysis. We will discuss this further in section 6.3.

The Neptune reference atmosphere has 180 pressure levels with 13 gases included in the model. These gases are hydrogen, helium, methane ($^{12}CH_4$, $^{13}CH_4$ and CH_3D), acetylene (C_2H_2), ethane (C_2H_6), ethylene (C_2H_4), carbon dioxide, diacetylene (C_4H_2), propane (C_3H_8), methylacetylene/propyne (C_3H_4) and methyl (CH_3). We tested two *a priori* models with slightly different temperature and gas profile values. The first

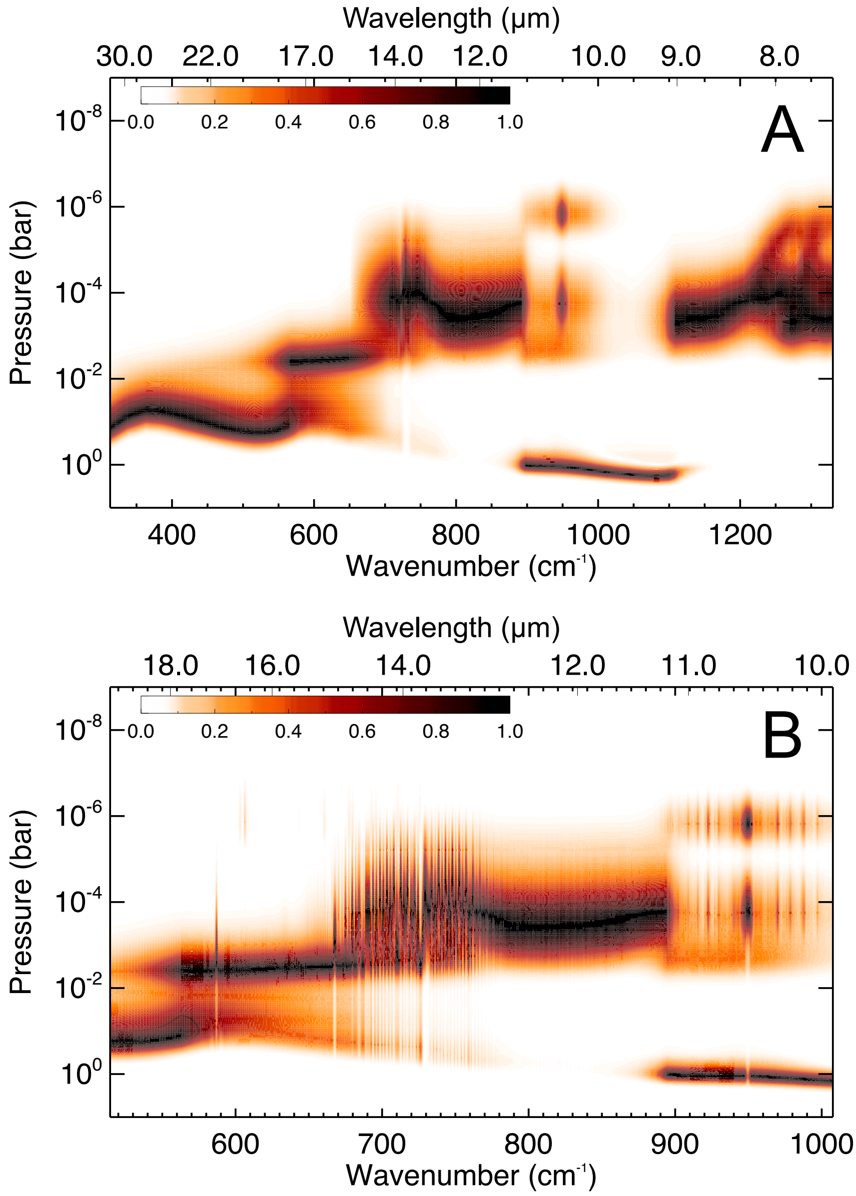

Figure 6.1: Contribution function contour plots showing sensitivity to different altitudes for different portions of the disc-integrated spectrum for the reference atmosphere using the priors from Moses et al. (2005) Model C. Panel A shows the low-resolution module (SL) range from 7.5 - 14.1 μm combined with the continuum sampled at low resolution from the high-resolution modules (SH and LH) in the range 16.1 - 32.0 μm. Panel B shows the high-resolution (SH) module range. Forward modelled using NEMESIS.

is Model C from Moses et al. (2005) and the second is from the AKARI observations from Fletcher et al. (2010). From here on, these are respectively called the *Moses* and *AKARI* models. The Moses model is the direct output from the photochemical model.

The AKARI model used the Moses profiles as a starting point then tweaked them to fit their observations in the mid-infrared. To account for the sub-Spitzer point in November 2005, the model profiles used are the ones centred on $-27°$ planetocentric latitude. The contribution functions in Figure 6.1 are modelled using the Moses model.

The different isotopes of methane were kept constant with respect to the vertical profile of $^{12}CH_4$. The CH_3D/CH_4 ratio used was 3×10^{-4} reported from NIR and MIR analyses of Neptune conducted independently by Irwin et al. (2014) and Fletcher et al. (2010). We found we were sensitive to the CH_3D/CH_4 ratio in the stratosphere and so the best-fit D/H ratio determined from our experiments and how it impacts our retrievals is discussed later in section 6.4. The $^{13}C/^{12}C$ value used is 1.11×10^{-2}, within errors of the terrestrial value (Marty et al., 2013).

Unlike Uranus, these data have yet to be analysed and therefore we do not have one temperature *a priori* that is considered the best. This is why we need to test multiple temperature profiles (see Figure 6.2) including the two from the Moses and AKARI models. The third main temperature profile that was tested was an average of both the Moses model and the nominal CH_4 results from the TEXES observations done by Greathouse et al. (2011). The Moses gas profiles were used alongside this profile. The Greathouse temperature profile was not used alone due to their investigations sensitivity being reliable only at certain altitudes in the stratosphere. In their investigation they also use the Moses model as their prior. By averaging them both this takes advantage of the Greathouse sensitivity to the hydrogen S(1) and methane ν_4 band whilst not compromising on sensitivity to the other altitude levels. This same profile is used in Roman et al. (in prep) where the variation of Neptune's MIR emission is observed from ground based imaging. The temperatures below 1 bar are taken from Voyager-2 radio occultation data (Lindal, 1992). The rapidly increasing temperatures above 10^{-7} bar are from Yelle et al. (1993) where they assumed the profile reached thermospheric temperatures of 550 K. This profile fit their model of hydrocarbon densities from Voyager-2 UVS data.

The quadrupole features are not as defined in the data as at Uranus. The brighter hydrocarbons overwhelm the dimmer quadrupole lines in the Neptunian stratosphere. The only quadrupole line that appears clearly in the data is the S(1) line at 17.0 μm (587 cm^{-1}) and is therefore only available in the SH data range.

The errors used to constrain the spectral fit are the same as the measurement errors stated in subsection 3.4.2. For the low-resolution retrievals this error allowed a good fit to the data with reasonable chi-squared values. For the high-resolution

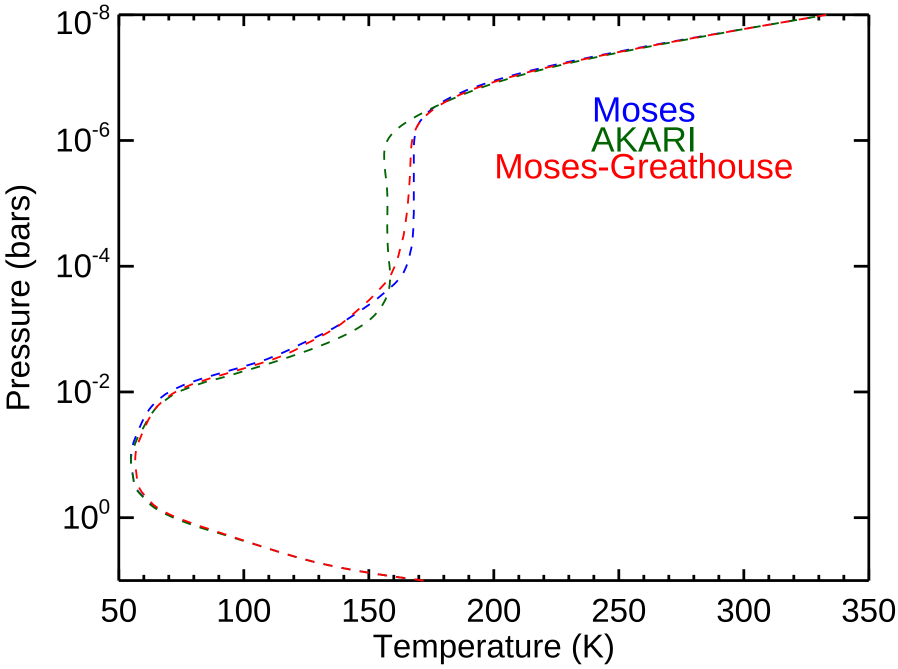

Figure 6.2: The three main temperature priors for Neptune used in this investigation. The Moses model in blue is from Moses et al. (2005) Model C. The AKARI model in green is from the investigation by Fletcher et al. (2010). The Moses-Greathouse profile in red is an average of the Moses model and the results from TEXES observations from Greathouse et al. (2011).

data, additional forward modelling error was added to the entire range to allow the fit more freedom during the retrieval. For the shorter wavelengths up to 14.8 μm 7.73 nW/cm^2/sr/μm was added and for the longer wavelengths we added less error (3.87 nW/cm^2/sr/μm). These converted values are round numbers in the units of the retrievals (2×10^{12} and 1×10^{12} W/μm respectively). We found that increasing the forward modelling error did not detrimentally affect the fit to the spectrum but drastically improved the smoothness of the retrieved profiles. This split between longer and shorter wavelengths was needed because the sharp transitions of the acetylene and ethane branches required more freedom in their fits than the smooth continuum dominated region past 15 μm. The uncertainties on the gas *priors* were set to 100% of the mole fraction at each pressure level, with temperature *a priori* uncertainties of $\pm$3 K. The typical number of iterations for the retrievals to converge on a reasonable fit is four for the low resolution and seven for the high resolution.

As in Chapter 5, we used the correlated-k method instead of line-by-line (explained in Chapter 2). We used 50 g-ordinates and a resolving power of 600, the same that was used at Uranus. It was just as challenging to fit to the data due to the dependence of resolution on the wavelength but it was found after some experimentation that this value was adequate. We ran multiple retrievals with different values of R and found that the fits did not improve on the overall spectrum. This process will be discussed more in Section 6.3.2, where we analyse the high-resolution results.

6.2.1 CH_3 k-tables

An additional CH_3 k-table was added to the list of k-tables for Neptune. CH_3 at Neptune has not been fit with NEMESIS before so we used the parameters developed by Sinclair et al. (2020b) at Jupiter adopted from Bézard et al. (1998) and Bézard et al. (1999) with updates from Stancu et al. (2005). We are measuring the opacities of many lines so we had to include the whole line database instead of their single line method. They assumed a broadening width of 0.035 $cm^{-1}atm^{-1}$ and a temperature dependence of 0.75 (as in Bézard et al. 1999 and Robinson et al. 1996). The partition function calculation assumed a symmetric top molecule and the modes and degeneracies taken from Bézard et al. (1999). Our prior profile for CH_3 at Neptune is from the Moses model.

The bottom panel of Figure 6.3 shows the distribution of lines that the new k-tables add to the model. The features at 15.15 μm, 15.55 μm, 16.00 μm and 17.62 μm were shown in Meadows et al. (2008) as unidentified and we show that all these features are CH_3 along with some others at 18.25 μm, 18.88 μm and 19.00 μm. The retrieval results for CH_3 are discussed in section 6.4.

6.2.2 Shifted Spectra

It became apparent that multiple orders in preliminary SH retrieval results exhibited signs of a slight difference in the wavelength reported by the IRS data pipeline and the actual wavelength. This is likely due to calibration errors in the SH module arising from minute changes in the telescope's internal temperature. To counteract this, we fitted both our initial spectral retrievals from NEMESIS and our Spitzer data to cubic splines on a per-order basis. We then found the wavelength 'lag' associated with each order through cross-correlation, restricted to within half of a wavelength step. After this we recalculated our Spitzer cubic spline by shifting our observed wavelengths and resampled the new spline for flux values at the original Spitzer wavelengths. This method was developed by Coy et al. (in prep) for use on Spitzer IRS Titan data and has enabled significant improvements on the fit for their data.

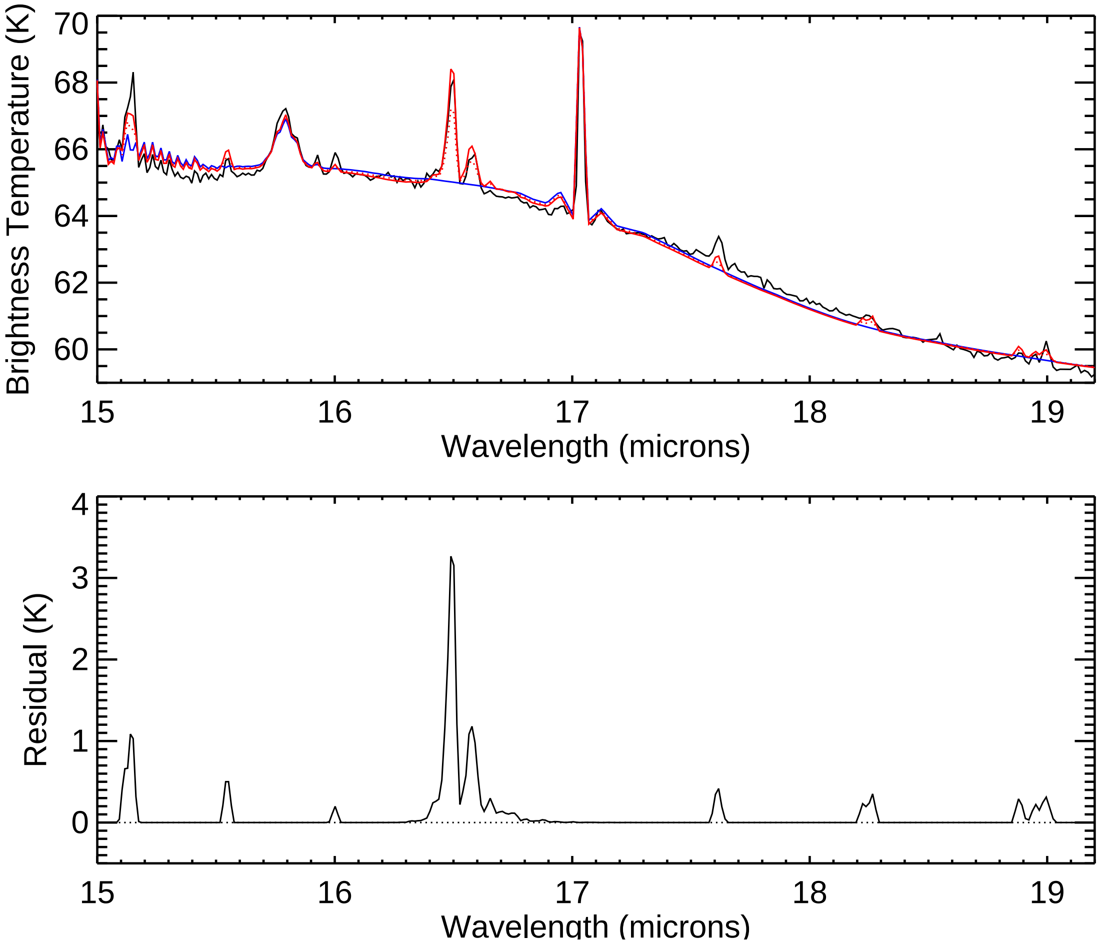

Figure 6.3: Top panel: the black line is the data, the blue line is the retrieval without CH_3 and the red lines are the retrieval with CH_3. The dotted red line shows the amount of CH_3 in the Moses model and the red solid line shows when the profile is allowed to scale by a factor during optimisation. Bottom panel: the residual from the forward model with and without CH3 to show the synthetic CH_3 lines based only on the Moses model used as the prior in the top panel.

Lags at Neptune occurred in order 14, 15 and 17 of the SH module, across the acetylene and ethane features where we see the sharpest features, and were on the order of around 0.001 μm. We applied these shifts to the data in the affected orders and reran the retrievals. This reduced the residuals between the model fit and the data by a small amount but the retrieved profiles were unaffected. The small shift in the data is therefore assumed to be within the errors of the model and would not need to be corrected in future Spitzer analysis for Neptune.

6.2.3 Disc Averaging

Just as with Uranus, we chose to compute the integrated spectral power of the planet in W/μm converted from the spectral radiance in units of W/cm^2/sr/μm. To do this, we used a Neptune radius of 25600 km, adding a 836 km limb extension onto the 1-bar level radius of 24764 km. A value of 836 was chosen for Neptune as this created a rounded value that was just below the maximum altitude specified in the reference atmosphere file.

The weightings in Table 6.1 are calculated using equation 2.11 using the same radius of Neptune, r, that includes the added limb. This method was successful at Uranus and after testing, has also been successful at reproducing the disc averaged spectrum at Neptune.

i	x (km)	Tangent altitude (km)	Emission angle (°)	w_i
1	0	-	0.0	0.0
2	5000	-	11.65	0.07570
3	10000	-	23.82	0.15140
4	15000	-	37.28	0.22710
5	20000	-	53.86	0.24224
6	23000	-	68.24	0.13929
7	24000	-	75.73	0.06410
8	24764	0	90	0.04499
9	25200	436	90	0.02808
10	25500	736	90	0.01544
11	25600	836	90	0.00388

Table 6.1: Field-of-view averaging points used to produce the synthetic reference spectra for Neptune, adapted from Teanby et al. (2013) where w_i is the weight calculated using equation 2.11.

6.2.4 Eddy Diffusion

In the Moses model, and therefore the basis of the other models, the eddy diffusion coefficient (K$_{zz}$) is assumed to be different at different altitude pressures (P):

$$\begin{aligned} K_{zz} &= 10^5 \left(\frac{0.1}{P}\right)^{0.55}, \text{ for P} < 0.1 \text{ mbar} \\ &= 10^5 \left(\frac{0.1}{P}\right)^{0.98}, \text{ for 28 mbar} < \text{P} < 0.1 \text{ mbar} \\ &= 400, \text{ for P} > 28 \text{ mbar} \end{aligned} \tag{6.1}$$

These values are dependent on the CH_4 mixing ratio and the homopause value, which is placed at around 8×10^{-5} mbar (Moses et al., 2018). This is unlike Uranus that had a fixed value at all altitudes. We did not experiment with this profile in this investigation and used the nominal CH_4 profile in all cases.

6.3 Disc-averaged Results

6.3.1 Low-Resolution Retrievals

We used the retrieval model to fit the data in the range 7.5 μm to 32.0 μm (312 - 1333 cm^{-1}). The SL data were used up to 14.1 μm and combined with the continuum (H_2-CIA) sampled at low resolution from the high-resolution modules (SH and LH) in the range 16.1 - 32.0 μm with the 10 μm region omitted. We allowed the full profiles of temperature, acetylene and ethane to vary as this produced the best fits to the data and the smoothest temperature profiles.

The best-fit retrieval for the low-resolution data was when we used the *priors* from the Moses-Greathouse model (Fig. 6.4, top panel). The chi-squared value of the best-fit was 0.82 with brightness-temperature residuals all within ± 1.5 K (Fig. 6.5).

The temperature profile is consistent with the *a priori* from Moses-Greathouse (Fig. 6.6) at tropospheric altitudes and above where the gradient increases into the upper stratosphere. The pressures where the retrieval deviates are between 1 mbar and 1 μbar where the profile is quasi-isothermal. There is a consistent 5-15 K heating, compared to the prior, to the whole region with the most isothermal section at 169 ± 3 K instead of the 165 K in the prior.

As well as the temperature profile from Moses-Greathouse, we tested the alternative temperature profiles from Moses, AKARI and scaled versions of Moses-Greathouse (Fig. 6.2). In all of these scenarios the retrieved temperatures converged to within errors of the chosen nominal profile below the altitude of the 10 μbar level. Above this level they shift towards their different priors.

Ethane and acetylene are the two most dominant gases in the emission present in the low-resolution data. Acetylene (C_2H_2) with its Q-band peak at around 13.7 μm is visible next to ethane (C_2H_6) at 12.0 μm in the low-resolution data in the top panel of Figure 6.4. The model shows a good fit to both species and Figure 6.8 shows the fit in the stratosphere for the vertical abundance. For acetylene, there is an increase in abundance compared to the prior at 2 mbar and at this same pressure region there is a depletion in ethane compared to the prior. Both gases have deviations from the prior that are within the retrieval errors.

As an extra test of the sensitivity to these gas abundances we conducted a bracketed retrieval on both by setting the *prior* to ±50% of the Moses model (Fig. 6.8). We found a convergence to the same regions that deviate from the prior in our nominal retrieval, showing confidence that our retrieval is driven by the data rather than sensitive to the prior. The lowest chi-squared values for each retrieval were the nominal Moses *prior* by a small margin and the fits to temperature were unchanged.

10-μm Region

The region between 9.0 μm and 11.4 μm was omitted. When this region was included in the retrieval there was a large 20 K spike in the temperature in the troposphere at the 1 bar level to allow a fit to the data. Ethylene is present at 10.5 μm but due to it being embedded in this region it had to also be omitted from analysis. Figure 6.9 shows the fit to this region when it is forward modelled using the results of our best fits. There is an up to 5 K deficit in emission across the band.

Before omitting this region we did attempt to fit it using multiple methods. The addition of the continuum from the SH and LH data was first used to check if it was the continuum fit that was struggling. In the end it did smooth the tropospheric temperatures so was kept as a useful addition but it did not help the poor fit of the 10-μm band. We tried to constrain the gases (acetylene, ethane and ethylene) in the troposphere by setting their priors to negligible levels below the tropopause but this was not successful in improving the anomalous temperature. The tropospheric temperature errors were reduced to force the model to remain close to a realistic prior but this increased the chi-squared and caused the model in that region to not fit the data. We did a full retrieval on the para-hydrogen fraction but this also did not affect the temperature fit in the troposphere.

We do not include clouds/aerosols in the nominal model but they may be a contributing factor around the 1-bar pressure level for Neptune (Toledo et al., 2020). We tested two types of cloud at the altitudes that seem to be affected by the heating. A methane-ice cloud and a grey cloud were both tested at 1 bar with the optical depth allowed to scale during the retrieval. Both types of cloud had no effect on the model. As a last resort, we also tested the helium abundance to see if freeing up this fundamental parameter would solve the fitting problem. It did not, and this is why we chose to omit the region from analysis altogether.

This region has weak emission (see radiance in bottom panel of Figure 3.7) and what few observations of this region exist have very low signal to noise ratios (de Pater et al., 2014; Fletcher et al., 2014, Roman et al., in-prep). The shape and structure of the data suggest this is not the case with the Spitzer data because we see the ethylene feature clearly above the noise. This seems to be, instead, a systematic offset in the brightness, most likely caused by issues with calibration at very low signal.

6.3.2 High-Resolution Retrievals

For the high-resolution, we retrieved from spectra in the range between 11.4 μm and 19.4 μm (515 - 877 cm^{-1}). Temperature, acetylene and ethane were allowed to vary over their full profiles with the results from the low-resolution retrieval as priors due to the lack of the 7.7 μm methane region that would be required to constrain the stratospheric temperature profiles. It is useful to have the results from the high resolution because the spectrum contains more spectral features that we can use to determine abundances. A number of gases not available in the low resolution were allowed to vary by a scaling factor. These gases were methylacetylene, diacetylene, CO_2, propane and CH_3.

The best fit is shown in Figure 6.4 (bottom panel) and has a chi-squared of 0.99. The temperature profile (Fig. 6.6) displays the same pattern as the low resolution but is closer to the original Moses-Greathouse *a priori* with warming of only 5 K at pressures of around 1 mbar. At all other altitudes the retrieval agrees with the prior (set as the low resolution retrieval result) but the difference at 1 mbar will be the subject of further scrutiny later on.

For acetylene and ethane, their profiles match the ones from the low resolution that are set as the priors (Fig. 6.10, top two panels) but the changes in abundance are more exaggerated in the high-resolution. The largest increase in the scaled gases is from propyne/methylacetylene with a factor of 5.7 ± 1.8 needed to fit the data. The CO_2 profile is decreased by a factor of 0.6 ± 0.1 and CH_3 is increased by 1.9 ± 0.3. Diacetylene and propane match the Moses priors within uncertainties. These scale factors are relative to the Moses model that was computed specifically to the Moses temperature profile. To check that these changes were not caused by the change in temperature profile, we also tested the Moses profile and came to these same scale factors within uncertainties.

The resolving power of the SH data is estimated at $R \sim 600$. As we know from the Uranus retrievals in chapter 5, this value varies considerably with wavelength, is highly uncertain and therefore introduces complications. We tested multiple different resolution k-tables ranging from a resolving power of 550 up to 1150. $R \sim 600$ had the best chi-squared value over the entire SH range we tested. We tested fitting just the hydrogen quadrupole S(1) line (Fig. 6.11) and found the best fit by a small margin to be at $R \sim 750$ but at $R \sim 600$ the retrieved temperature profile was the same. The challenges we had with fitting the resolution across the whole range may be the cause of the differences we see in acetylene and ethane profiles between the low- and high-resolution data. We attempted to remove different branches of acetylene to see if omitting these areas of suspected saturation would improve the fit. No improvements were made in the fit, temperature profiles or acetylene abundance profiles.

The same problems in the 10 μm region shortwards of 11.4 μm were seen in the high resolution as the low (Fig. 6.9). Including this band caused the same 20 K hot spike in the troposphere at 1 bar so we know that the systematic offset in the data is consistent independent of the instrument module.

6.4 Discussion

For the low-resolution retrieval, we achieved an adequate fit across the whole spectral range, including the continuum region sampled from the high-resolution data. The tropospheric temperature fits were very stable throughout the retrieval process and are in good agreement with the prior from the Moses-Greathouse model.

Stratospheric temperatures are harder to pin down though they have been inferred previously from disk-averaged observations by Orton et al. 1992; Marten et al. 2005; Hammel et al. 2006; Fletcher et al. 2010; Greathouse et al. 2011, etc.. Orton et al. (1992) used NASA/IRTF observations from 1989 and 1990 to infer temperatures in the stratosphere of 168 ± 10 K at the pressure levels of our quasi-isotherm. These temperatures were consistent with observations from Hammel et al. (2006). They attributed the ethane intensity variation between years to a variation in stratospheric effective temperature. In 2003 a temperature of 176 ± 3 K was inferred but that decreased to 165 ± 3 K in 2004. Fletcher et al. (2014) used ground-based imaging from 2003 through to 2007, therefore encompassing the 2005 period of our data and found temperatures of the quasi-isotherm ranged from 162 - 167 K and is in basic agreement with our findings (169 ± 3 K between 0.1 and 0.001 mbar).

Due to the absence of the 7.7 μm methane region, the low-resolution retrieval temperature results are more reliable at altitudes above the 0.3-mbar level in the stratosphere but at these levels the two priors have a good agreement anyway. It is below these levels (between 0.3 - 3 mbar), in the region where the hydrogen quadrupole S(1) line is sensitive, that we have the most variation between the priors. The S(1) line is only visible in the high-resolution at 17.04 μm and so the temperatures at these altitudes may be more reliable from the high-resolution retrievals. The high-resolution temperature is closer to the original prior and has the same shape and therefore lapse rate at these altitudes.

Due to the resolution difficulties, the acetylene and ethane retrievals from the low-resolution results are better fit to the data, meaning that the abundances are more trustworthy. The high-resolution results are sufficiently similar in shape that they compound the low-resolution results and show that the gas abundances are reliable.

Ethane is the most abundant hydrocarbon after methane in the Neptunian atmosphere. The ethane volume mixing ratio (VMR) determined at 0.3 mbar from the low-resolution retrieval is 1.0×10^{-6}. This value is within errors of the AKARI results from Fletcher et al. (2010) at the same altitude pressure. Observations from 2007, from the TEXES instrument at Gemini North, found a meridionally constant VMR of 9.3×10^{-7} at 1 mbar, only slightly higher than what we have determined at that level (4.3×10^{-7}).

For acetylene we have derived a VMR of 5.4×10^{-8} at 0.5 mbar from the low-resolution retrieval. This increase in the acetylene profile compared to the prior is not expected because no known chemical process could cause it at this altitude. We had similar problems for acetylene on Uranus, hinting that this is a problem with the model rather than a real increase in abundance. This problem could come from uncertainties in the linedata or other systematic retrieval uncertainties that we list in Chapter 2. Further testing would be needed in future to narrow down the underlying cause.

The less abundant hydrocarbons in our high-resolution model, methylacetylene/propyne (C_3H_4) and diacetylene (C_4H_2) were observed by Meadows et al. (2008) using the 2004 Spitzer Neptune data. They reported a VMR of $(1.2 \pm 0.1)\times10^{-10}$ at 0.1 mbar for C_3H_4. Our value at this level is slightly higher at $(2.2\pm0.7)\times10^{-10}$. For C_4H_2 our value at 0.1 mbar is within errors of the Moses prior with a value of $(1.7\pm0.9)\times10^{-12}$, which brings our upper limit within the lower limit of Meadows et al. (2008), $(3\pm1)\times10^{-12}$. The differences in these hydrocarbon species could be from noise in the 2004 data being greater due to shorter integration times (see Chapter 3), or real changes in abundance happening over the 18 months between the two datasets.

The VMR of CO_2 at 0.1 mbar was found to be $(6.9\pm1.2)\times10^{-10}$. Oxygen bearing species at the ice giants are thought to be from external sources such as comets and ring debris (Moses and Poppe, 2017; Moses et al., 2018). A lower value than the Moses model predicts suggests a lack of these sources.

6.4.1 Methyl - CH_3

The first detection of methyl at Neptune was by Bézard et al. (1999) using the Short-Wavelength Spectrometer of the Infrared Space Observatory (ISO). They observed the Q-branch of the molecule that we also see at 16.5 μm. The top panel of Figure 6.3 shows how the full high-resolution retrieval changes with and without the CH_3 k-tables.

Methyl (CH_3) is visible in the data for Neptune with a clear double feature at 16.5 μm (Fig. 6.3) previously identified in Meadows et al. (2008). Other unknown features were also visible in the 15 - 19 μm range that were not identified at the time of submission of their paper, but once we fit for CH_3 it was clear that all of the most prominent features were just minor branches of methyl.

We needed a 1.9$\pm$0.3 factor increase in the full profile abundance of CH_3 compared to the *a priori* from Moses et al. (2018) in order to fit our data and gives us a peak VMR of $(9.7 \pm 2.9)\times10^{-8}$ at 0.3 μbar. This value was consistent throughout the testing process.

Photodissociation of CH_4 produces CH_3 radicals and so an increase in this product suggests an increase in the production process or a longer lifetime between production of methyl and the reactions that reconstitute it to form more complex hydrocarbons. The methyl radical is thought to be the sole photochemical source of ethane, an intermediate between the break down of methane and production of this complex hydrocarbon (Bézard et al., 1999). We see a slight increase in ethane abundance compared to the Moses model between 0.1 mbar and 1 μbar in both resolution retrievals (Fig. 6.10). This increase is exaggerated in the high-resolution where we are sensitive to methyl. Methyl is most abundant around the 1 μbar level so an increase in both would be expected.

Observations of CH_3 can be used as a diagnostic tool to constrain the location of the homopause, however, it requires a precise knowledge of the CH_3 recombination rates, as well as its sources and sinks (Bézard et al., 1998). These new observations of bands at Neptune could help to determine the CH_4 homopause value like the investigation by Sinclair et al. (2020b) but is outside the scope of this investigation.

6.4.2 D/H

Initial findings showed that we were sensitive to the stratospheric D/H ratio (derived from the methane D/H and the relative abundances of CH_4 and CH_3D) and therefore we attempt to constrain this value by finding the best fit for our model. We used the low-resolution retrieval model that provided our best fit and only changed the relative abundance profile of CH_3D with respect to the fixed CH_4 abundance profile. We then completely re-ran the retrieval with these new ratios. Figure 6.12 shows the chi-squared values obtained from this experiment.

The best-fit value was found to be 5×10^{-4} with 1-sigma limits at 4.5×10^{-4} and 5.7×10^{-4}. The nominal 3×10^{-4} value used in the retrieval fits is outside of the 3-sigma errors. This nominal value is from Fletcher et al. (2010) and has a errors of $\pm 1 \times 10^{-4}$. This means that their upper limit of 4×10^{-4} is within 3-sigma of our best-fit. Using the 3-sigma limits as our errors therefore makes our best-fit CH_3D/CH_4 value $(5^{+2.3}_{-1.3}) \times 10^{-4}$.

When we use this best-fit value for our low-resolution retrieval we see changes in the fit to the methane band of the spectrum (Fig. 6.13). The fit to the methane band is much better than when using the nominal value and is within the retrieval errors more consistently. The temperature profile of this fit is shown in Figure 6.6 by the red dot-dashed line. It follows the high-resolution retrieved temperature profile closely around the 1 mbar level then increases considerably above that level. This makes the quasi-isothermal part of the temperature profile 10 K warmer than the prior (175 K). The gas abundances of both ethane and acetylene were the same within errors for the two scenarios.

We then used the results from this low-resolution fit as priors for our high-resolution fit in the same method we used for the nominal. The temperature fit is shown in Figure 6.6 by the blue dot-dashed line and exhibits the same warming as the low-resolution above 1 mbar but below that it has a very good fit to the Moses-Greathouse temperature prior. Again, gas abundances are unchanged within errors, showing that the changes caused by a different D/H appear to be in temperature only.

The CH_3D/CH_4 is four times the methane D/H ratio, $(D/H)_{CH_4}$ (Blake et al., 2021). The D/H ratio is known to increase with heliocentric distance due to fractionation of deuterium in the formation of icy grains (Blake et al., 2021). The methane D/H can be used to derive the hydrogen D/H, $(D/H)_{H_2}$, as long we know the isotopic fractionation factor, f, where $f = (D/H)_{CH_4}/(D/H)_{H_2}$. This factor is under debate and has a value of 1.6 from Lecluse et al. (1996).

For context, the protosolar value of $(D/H)_{H_2} = 2.1 \times 10^{-5}$ (Geiss and Gloeckler, 1998). Our best fit $(D/H)_{CH_4} = (1.25^{+0.6}_{-0.3}) \times 10^{-4}$ and using an f of 1.6 gives us a $(D/H)_{H_2}$ of $(7.8^{+3.8}_{-1.8}) \times 10^{-5}$. This value is much higher than later estimations from Feuchtgruber et al. (2013) using Herschel, $(4.1 \pm 0.4) \times 10^{-5}$, but are within the limits of an earlier investigation by Feuchtgruber et al. (1999) using ISO, $(6.5^{+2.5}_{-1.5})\times10^{-5}$. Blake et al. (2021) states that an even higher fractionation factor of 1.8 may be at Neptune and this brings us even closer to those values.

The ice giants accreted greater quantities of ices during their formation compared to hydrogen gas so these larger than protosolar values and larger than gas giant values are expected. Without knowing the fractionation factor it is impossible to determine the absolute D/H value at Neptune. Roman et al., in their Neptune paper (currently in preparation) have forward modelled expected radiances assuming abundances from the Moses model and compared those to ground-based observations in the MIR. While the model appears comparable to the observations at 7.9 μm, sensitive to CH_4 emission, it appears too dark compared to the 8 - 9 μm emission. The difference suggests that their assumed ratio of CH_3D to CH_4 (2.64×10^{-4}) is likely too low. They tested a value of 4×10^{-4} within our uncertainties and at the upper limit of the AKARI investigation. This was much closer but even this value was considered a little too low.

The abundance of CH_4 may be changing with time, whereas we are assuming it is constant. There is still a lack of knowledge of the exact abundance of CH_4 in the stratosphere (Greathouse et al., 2011) but we are assuming a profile matching the Moses model throughout this investigation. A changing CH_4 profile would change the D/H ratio determined. The D/H ratio is also temperature dependent (as we see in Figure 6.6) so if there is a temperature change over time at these altitudes then this could change the perceived CH_3D/CH_4 given the assumption of the same temperature. This degeneracy between stratospheric temperature and D/H ratio is hard to break.

In our conclusions chapter in Section 8.3, we discuss how these assumptions could be tested in future work.

6.5 Summary

The Neptune Spitzer IRS data from 2005 have optimised exposure times, multiple observed longitudes, and therefore the smallest uncertainties. We use these data to derive the vertical structure of the temperature and composition in the stratosphere and upper troposphere (between around 1 nanobar and 2 bars of pressure). We presented full optimal estimation inversions of this globally averaged data with the aim of constraining the temperature profile and the abundances of the stratospheric hydrocarbons. We fit both the low-resolution and high-resolution module data, testing multiple temperature priors derived from chemical models from Moses and observations from AKARI and TEXES/Gemini-N.

The globally-averaged stratospheric temperature structure shows a good agreement with the chosen prior that is an average of the Moses model (Model C from Moses et al. 2005) and the observations from Greathouse et al. (2011). We see a slight warming compared to the prior with a quasi-isothermal structure in the stratosphere that is at 169 ± 3 K between 0.1 and 0.001 mbar in agreement with past disk-averaged observations.

The abundances of stratospheric hydrocarbons have been determined along with the ratio of D/H. We conducted the first ever retrieval of methyl (CH_3) for Neptune at these wavelengths. We identified multiple features that were previously designated as unknown between 15 and 19 μm as branches of methyl as well as fitting the brightest band at 16.5 μm (Meadows et al., 2008). The VMR at 0.3 μbar was determined as $(9.7 \pm 2.9)\times10^{-8}$, almost twice the value from the Moses model. The CH_3D/CH_4 ratio was used to determine the D/H ratio. We found a best fit value of $(5^{+2.3}_{-1.3})\times10^{-4}$ corresponding to a hydrogen D/H value of $(7.8^{+3.8}_{-1.8})\times10^{-5}$. This value changed the temperature profile during the retrieval process, allowing the methane band to fit better with this effect being subject to further testing.

The disc-averaged thermal and chemical structure from Spitzer will likely be our best characterisation of Neptune's thermal structure until JWST/MIRI has acquired spatially-resolved mid-infrared spectroscopy in 2022.

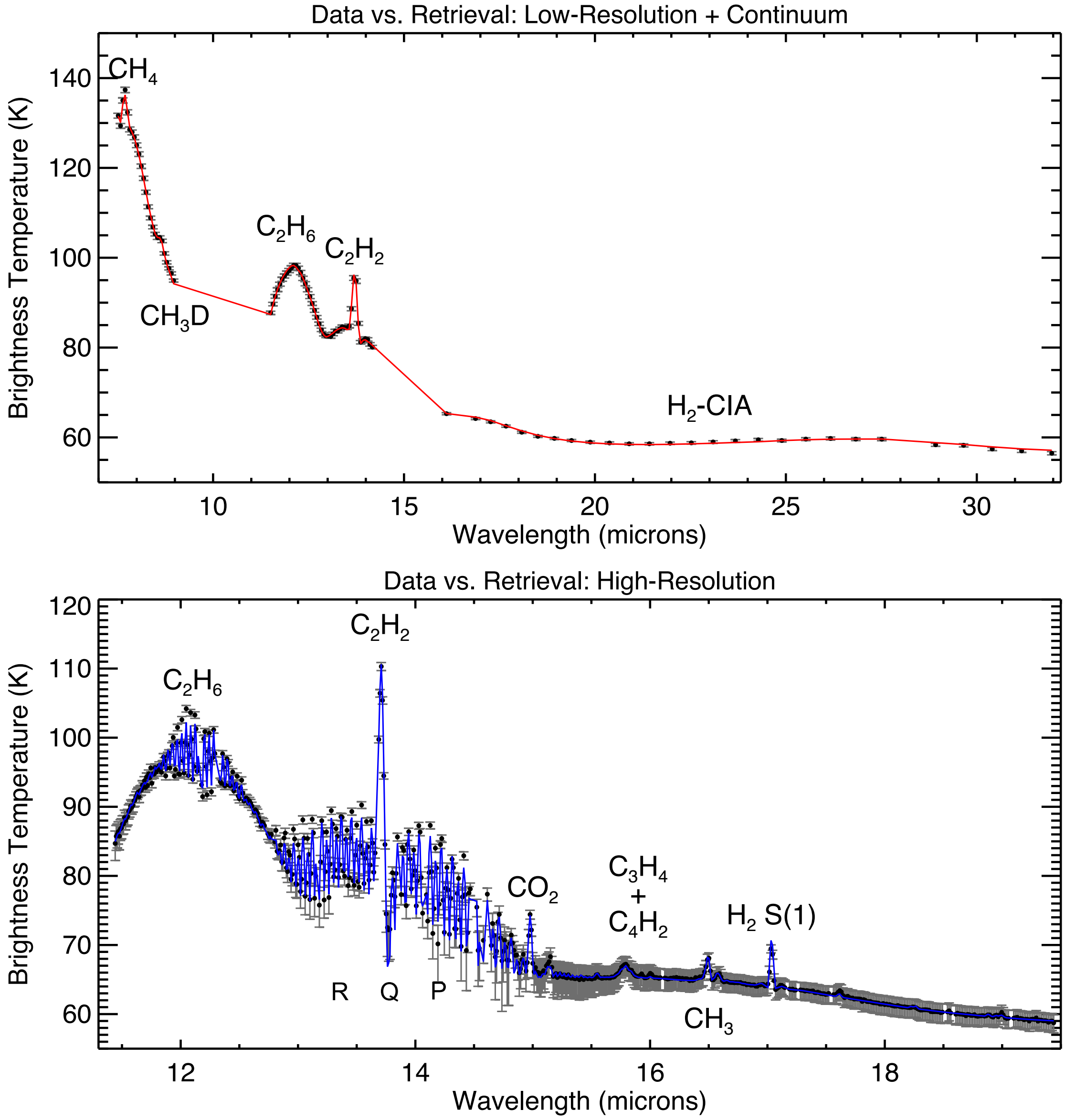

Figure 6.4: Best fit full spectrum retrievals for the Spitzer-IRS Neptune-2005 global average spectra (black dots with associated errors). The top panel shows the low-resolution (SL) module, 7.5 - 14.1 μm, combined with the continuum sampled at low resolution from the high-resolution modules (SH and LH) in the range 16.1 - 32.0 μm (red) where temperature, acetylene and ethane are allowed to vary freely. The bottom panel shows the high-resolution (SH) module between 11.4 and 19.4 μm (blue) where temperature, acetylene and ethane are allowed to vary freely over their full profiles and methylacetylene, diacetylene, CO_2, propane and CH_3 are allowed to vary by a scale factor. The entire range has had a fixed forward-modelling error added to account for uncertainties and allow the profile fits more freedom. The low-resolution fits use the Moses-Greathouse model as the prior and the high-resolution fits use these low-resolution retrieval results as the prior.

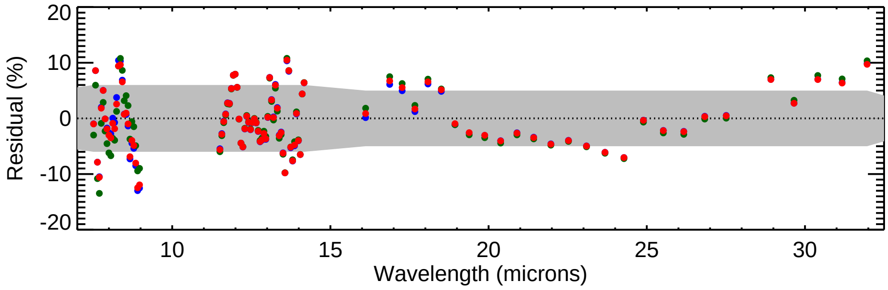

Figure 6.5: The residuals between the low-resolution data and the retrievals for the three main models, Moses-Greathouse (red circles), AKARI (green circles) and Moses (blue circles). Retrieval errors are shown by the grey shaded regions.

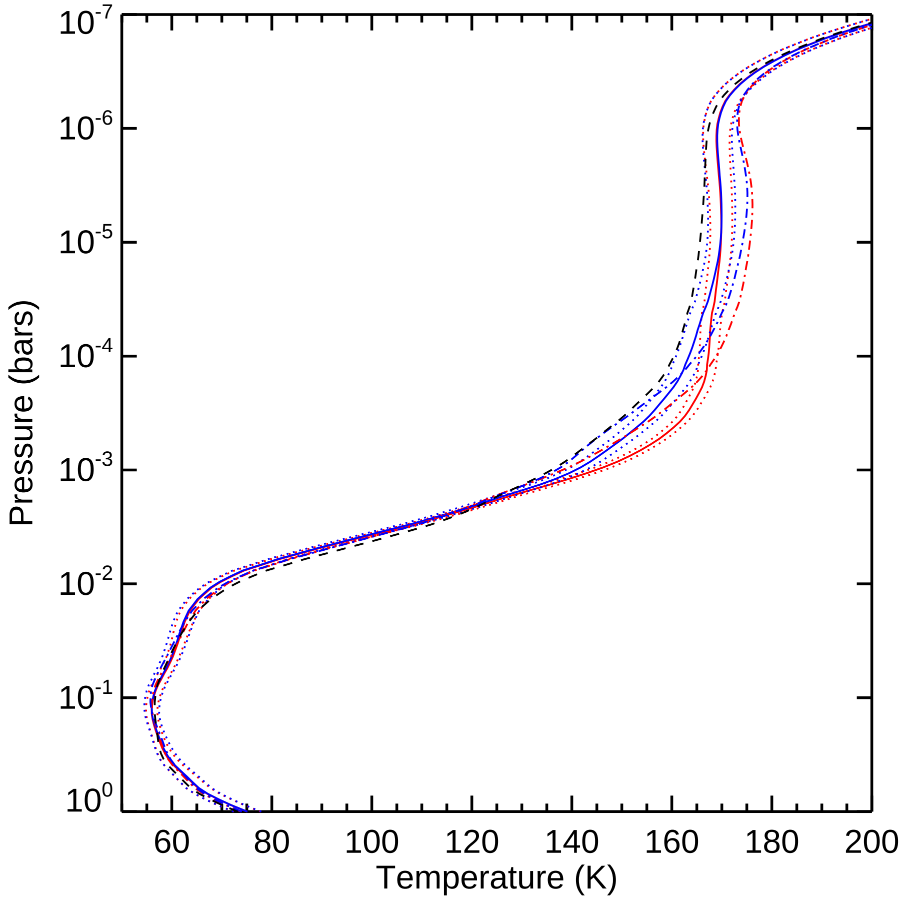

Figure 6.6: Retrieved vertical temperature profile for the global average of the low-resolution data (red solid line) with retrieval errors (red dotted line) compared to the *prior* from the Moses-Greathouse model (black dashed line). The high-resolution retrieved profile is shown by the blue solid line with errors (blue dotted line). The low-resolution fit with the best-fit D/H value is also displayed (red dash-dot line) along with the high-resolution version (blue dash-dot line). The *priors* for the high-resolution fits are their equivalent low-resolution fits.

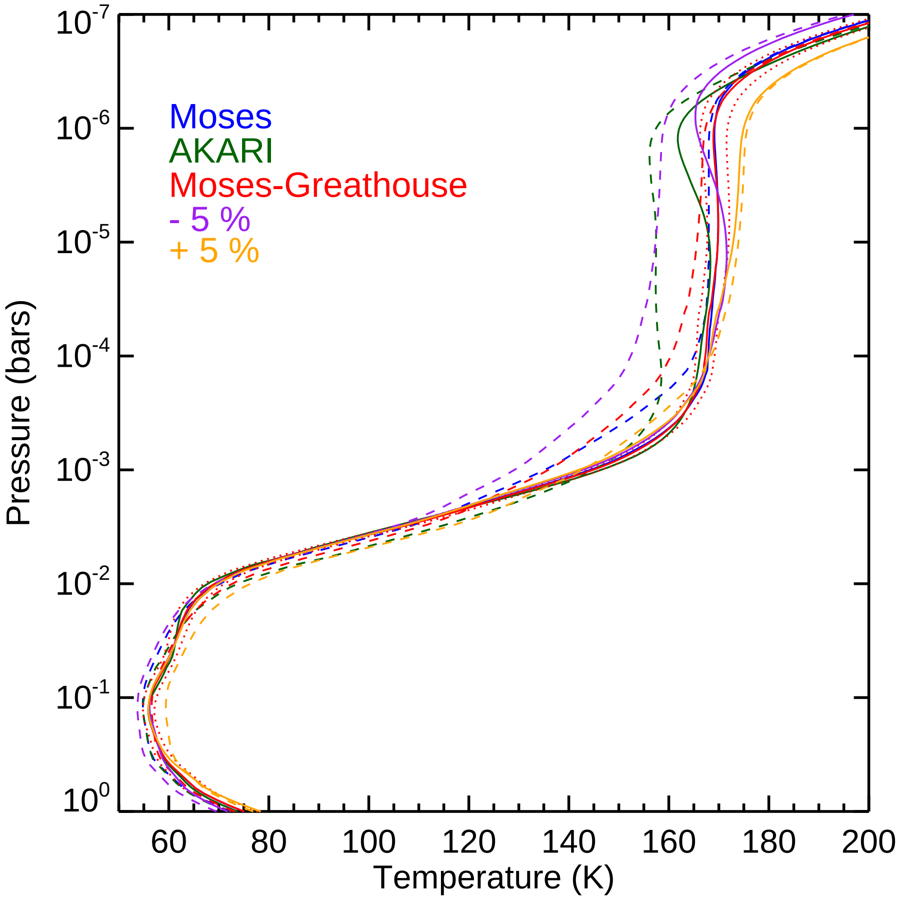

Figure 6.7: Low-resolution retrieval fits to temperature using the three main models along with a bracketed retrieval for the Moses-Greathouse model with scalings of 0.95 and 1.05. The retrievals converge where we have good information content, but diverge at the low pressures.

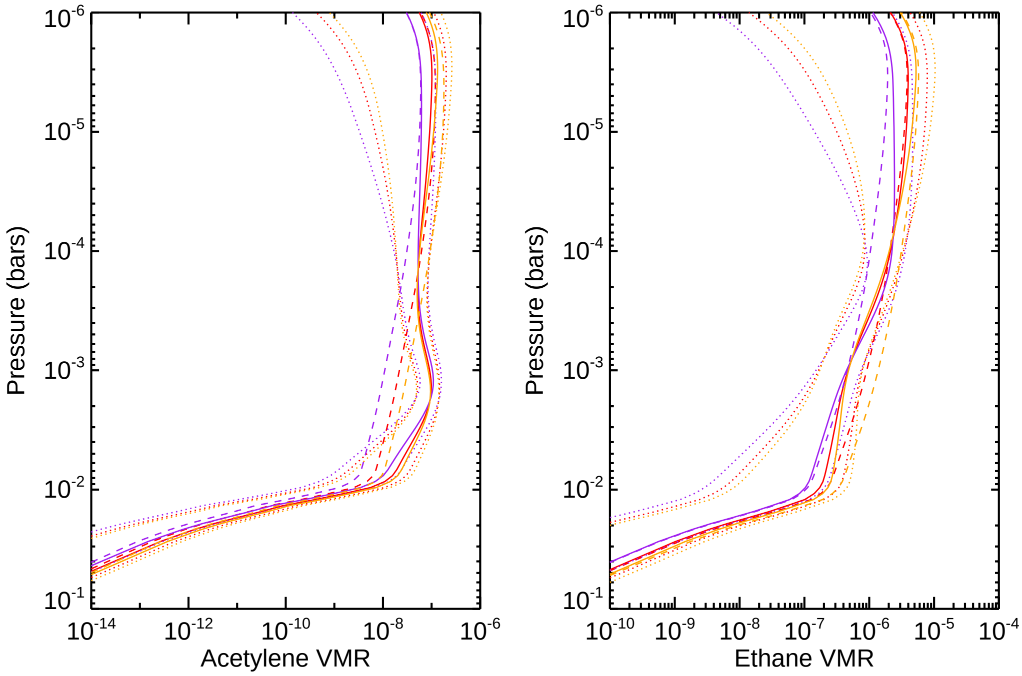

Figure 6.8: Gas vertical profiles for acetylene and ethane with plus and minus 50% abundance tested in the low-resolution retrievals. Plus 50% is shown in orange, minus 50% is shown in purple and the nominal gas profiles from the Moses model are shown in red. The priors are shown by dashed lines, the retrieved profiles are shown by solid lines and the retrieved errors are shown by the dotted lines.

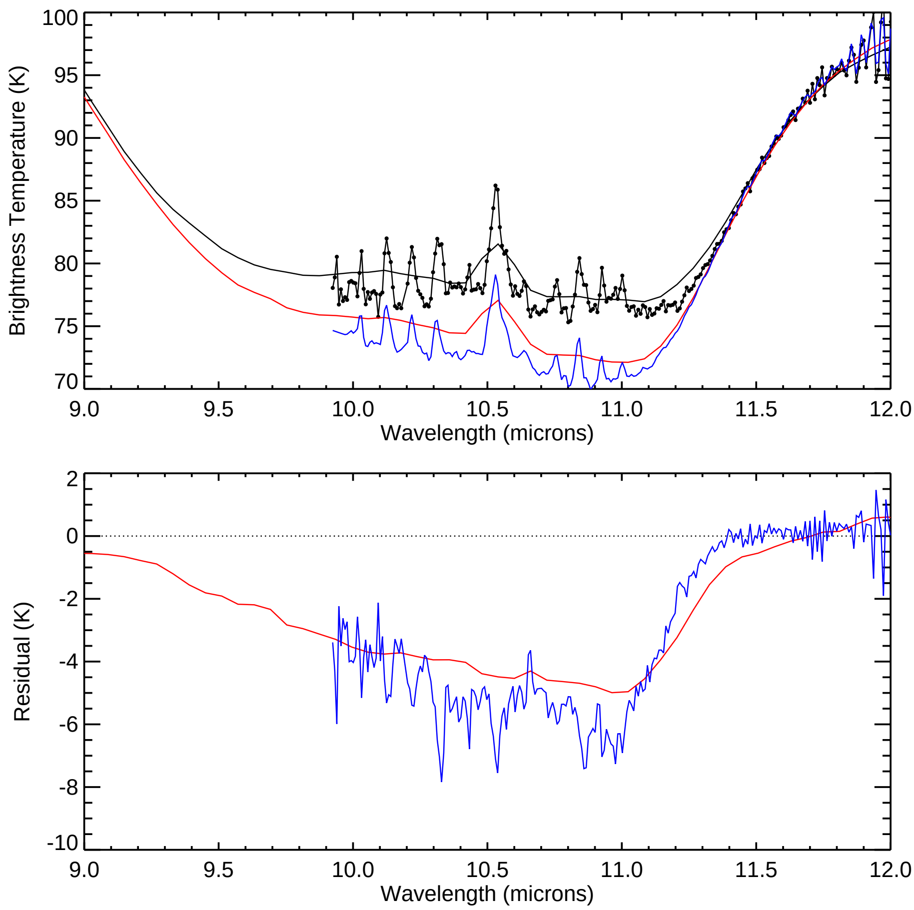

Figure 6.9: Figure to show the lack of fit of the current model to the 10 micron region. Top panel: The low-resolution data is shown by the black solid line and the high-resolution data is shown by the black connected dots. The model is shown in the coloured lines (red is low-resolution, blue is high-resolution). Bottom panel: Same colour scheme as the top panel showing the residual between the data and the model for both resolutions.

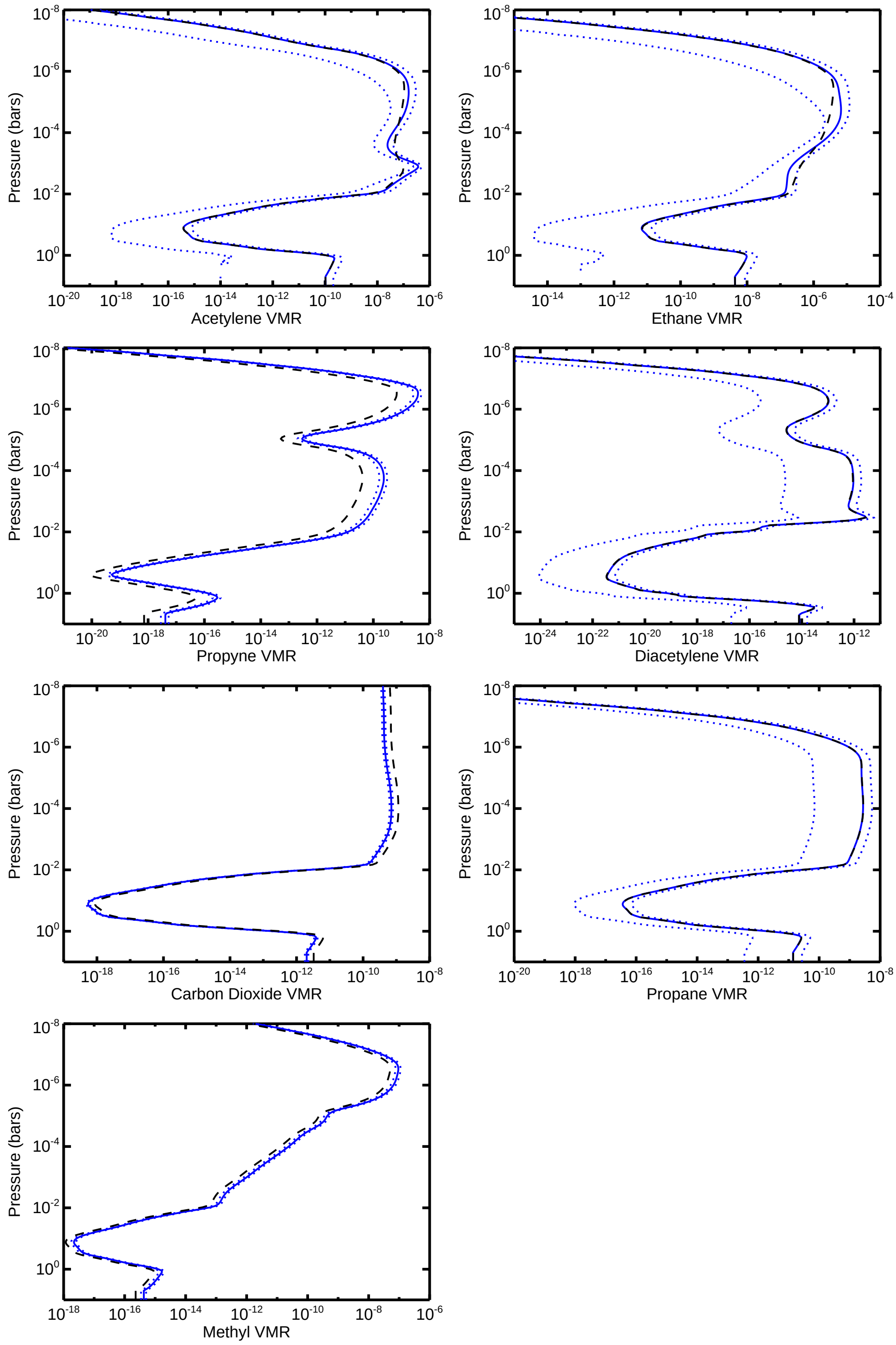

Figure 6.10: Retrieved gas profiles from the high-resolution model. The priors are shown by the black dashed line, the retrieved profiles are shown by the blue solid line and the retrieved errors are shown by the blue dotted lines. Acetylene and ethane are free to vary over their full profiles and the other five gases are free to vary by a scale factor.

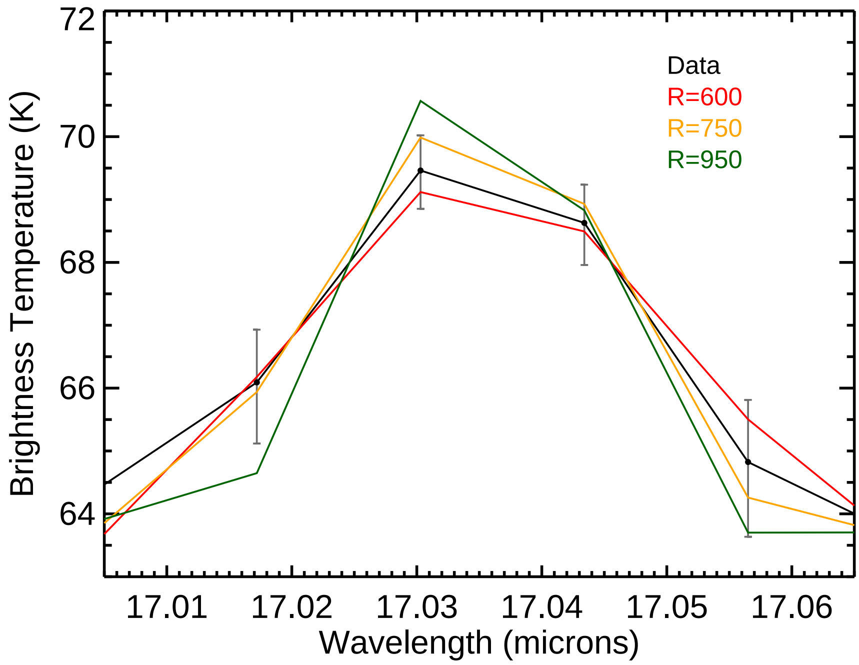

Figure 6.11: Fits to the data when we did a retrieval of just the hydrogen S(1) line using k-tables of different spectral resolving power, R, shown in different colours.

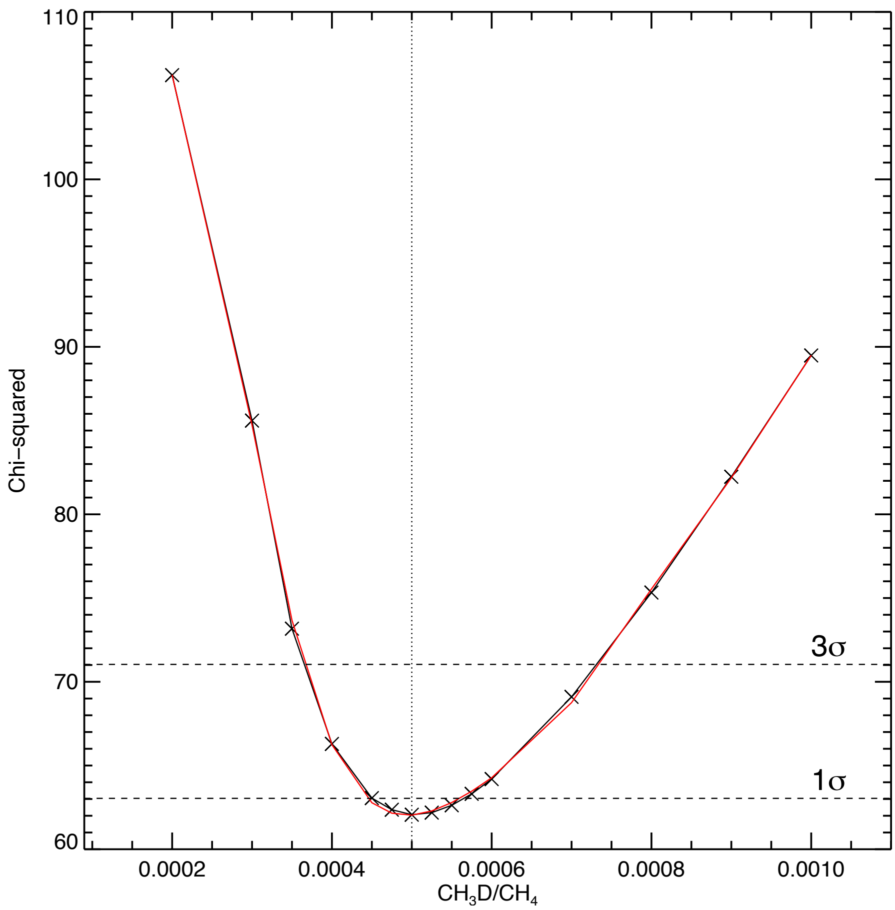

Figure 6.12: The chi-squared values for different fits to the CH_3D/CH_4 ratio shown by black crosses with a 7-degree polynominal fit shown by the red solid line. The best-fit value is shown by the vertical dotted line at 0.0005. The 1-sigma and 3-sigma limits are show by the horizontal dashed lines.

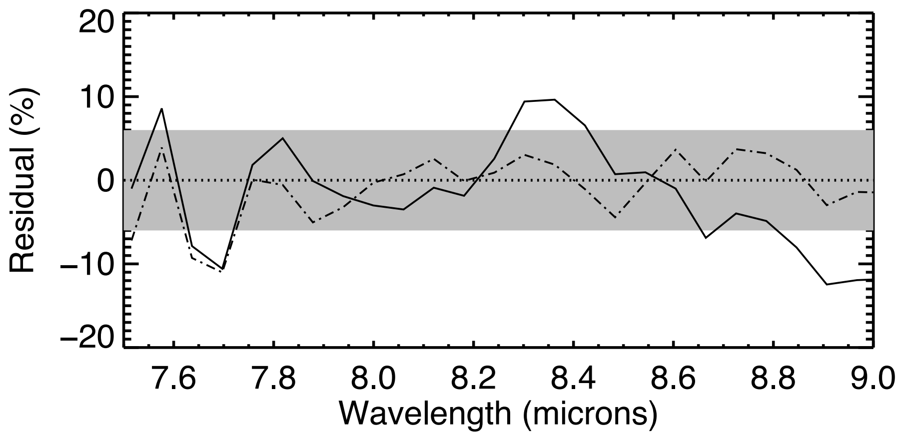

Figure 6.13: Low-resolution residuals for the fit to the methane band for two different values of the D/H ratio for the Moses-Greathouse model. The nominal CH_3D/CH_4 value is 3×10^{-4} (solid line) and the best-fit value is 5×10^{-4} (dot-dashed line).

Chapter 7

Predictive Model of JWST MIRI Observations

7.1 Introduction

The Spitzer IRS data can provide us with a lot of detail but without accompanying spatial resolution it is impossible to observe the latitudinal variability that is key to understanding atmospheric circulation and seasonal chemistry, or come to a definitive conclusion as to the origins of the longitudinal variability discussed throughout chapters 4 and 5. The James Webb Space Telescope (JWST), when it launches in 2021, will provide much improved spectral and spatial resolution in the mid-infrared band using its Mid-Infrared Instrument (MIRI). This will help to provide answers to many outstanding ice giant science questions (Norwood et al., 2016; Moses et al., 2018). It aims to explore the middle atmospheric circulation of Neptune and reveal contrasts in atmospheric temperatures and chemical tracers at Uranus during the first 12 months of operation in Heidi B. Hammel's Guaranteed Time Observations (GTO).

Prior to the launch of JWST and any planned ice giant observations, it is vital to know the instruments' capabilities for these planets. We generate synthetic data cubes using the spatial and spectral resolution and wavelength range of MIRI, specifically its Medium Resolution Spectrometer (MRS). We also use the JWST Exposure Time Calculator (ETC) to calculate the expected signal-to-noise using the Spitzer data as a base. This chapter represents a work-in-progress to show the start of work that will be continued after this thesis and to give context to the work done with Spitzer and how that will help with future Webb observations.

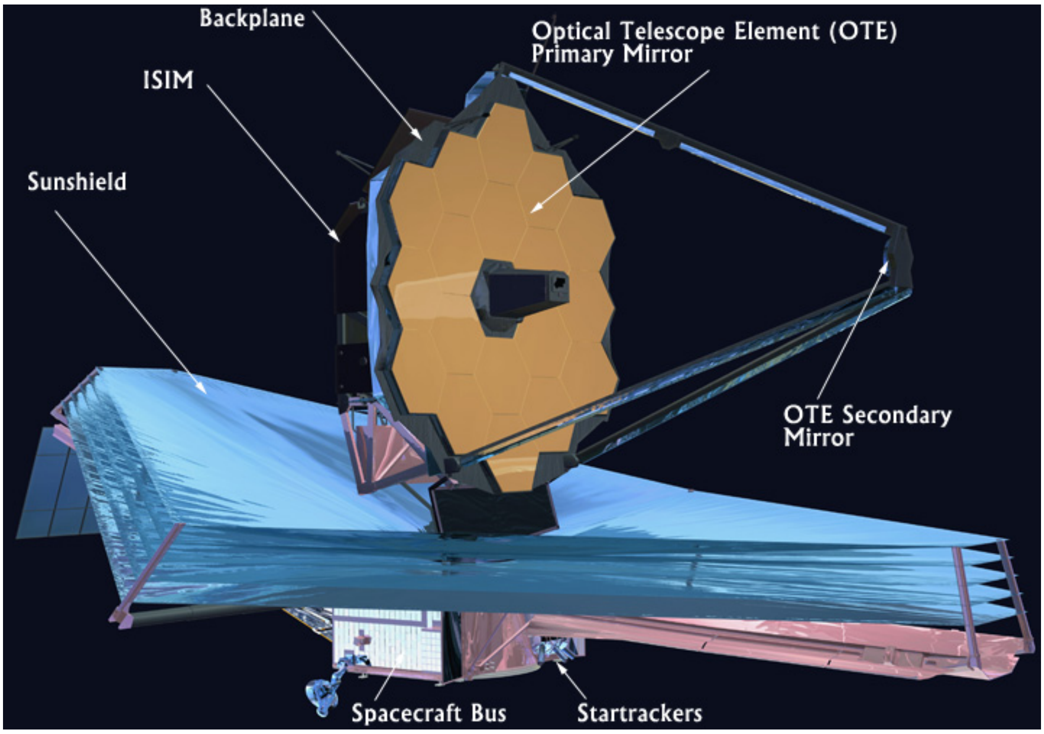

Figure 7.1: Schematic showing the front view of the James Webb Space Telescope with main elements labelled. Image from NASA: `www.jwst.nasa.gov`.

7.2 MIRI instrument

The James Webb Space Telescope is the premier observatory of the next decade. It is an infrared telescope with a 6.5 m diameter primary mirror made of 18 separate movable segments (Fig. 7.1). It houses four science instruments with both imaging and spectroscopic capabilities from 0.6 microns in the near-infrared out to 28 microns in the mid-infrared. The only instrument observing in the mid-infrared, at similar wavelengths to the Spitzer IRS, is MIRI. It has three Arsenic-doped Silicon (Si:As) detector arrays and a wide-field broadband imager with 9 broad-band filters covering the wavelength ranges from 5.6 to 25.5 microns. MIRI also has a medium-resolution spectrometer (MRS) that has an integral field unit with capabilities from 4.9 - 28.8 microns. It can also obtain spectra with a low spectral resolving power mode from 5 - 12 microns that includes both slitted and slitless options. The MRS is the most exciting instrument for use when observing the ice giants because it will give us the first three-dimensional spectroscopic maps of the planets at these wavelengths.

The ice giants are both distant and cold, making the signal-to-noise of most observations extremely low, especially in the thermal emission of the mid infrared. The integrated field units (IFUs) of the MIRI MRS provide data cubes of simultaneous spatial and spectral information. The MRS has four channels of varying wavelength range, each with their own IFU. Each channel is separated into three different rotations/grating settings (A - *SHORT*, B - *MEDIUM* and C - *LONG*) giving 12 observing channels in total. Each channel has a number of slices that are used to split up the footprint as can be seen for channel 4 in Figure 7.2. Channel 1, 2, 3 and 4 have 21, 17, 16 and 12 slices respectively. All of the *SHORT* observations are taken simultaneously then rotated to *MEDIUM* and then *LONG*. The wavelength coverage of each can be seen in Figure 7.3.

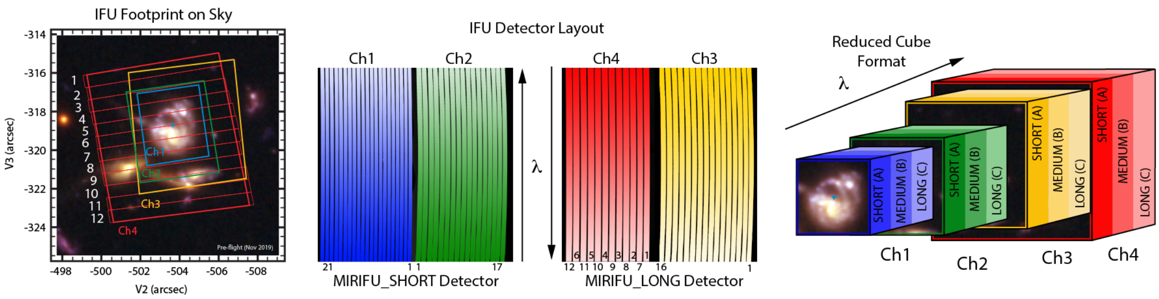

Figure 7.2: Left: Effective rectangular footprint of each of the four MRS channels on the sky with twelve slices shown for channel 4 as an example. Middle: The layout of the two detectors containing all four channels and their slices. Right: Illustration of the post-calibration pipeline 3D cube format showing how the channels, rotations and slices are combined. Channels 1, 2, 3 and 4 are shown in blue, green, yellow and red respectively (STScI, 2016, MIRI Medium Resolution Spectroscopy).

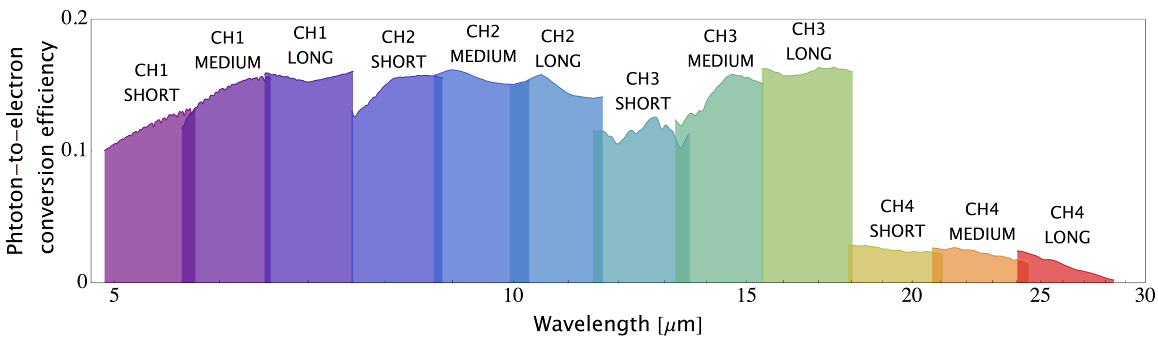

Figure 7.3: The MRS filter bandpasses showing the wavelength coverage of the MIRI MRS channels (STScI, 2016, MIRI Medium Resolution Spectroscopy).

The entire spectral range can be utilized for observations of both Uranus and Neptune without reaching saturation limits (Fig. 7.4A). The instrument has field of view capabilities of up to 7.7" x 7.7" (for channel 4), which is perfectly suited to the approximate 3.6" and 2.2" diameters of Uranus and Neptune respectively (Fig. 7.4B). It has spectral resolving powers that change between each MRS band ranging from 1300 to 3700 (Wells et al., 2015). To put into context, the Spitzer IRS high-resolution module had resolving powers of around 600 (Houck et al., 2004). The signal-to-noise capabilities will also be much improved compared to Spitzer.

7.2.1 Guaranteed Time Observations (GTO)

The guaranteed time observations (GTO) campaign for both ice giants are likely to occur in the first twelve months of operation (2022). Three separate pointings spaced by 120° longitude are embedded into the GTO plan for Uranus and two pointings 180° apart are planned for Neptune. This is so the data acquired will provide the necessary information for determining the source of variations hinted at by the Spitzer data. With the planned launch date in November of 2021 the first window to conduct the observations are in August 2022 and so we are using this window in our calculations. This window is driven by the Webb requirement for observation targets to be at an apparent solar elongation angle of between 85 and 135 degrees (STScI, 2016, JWST Target Viewing Constraints). This happens in two discrete windows in 2022. For Uranus, window 1 is between August and September and window 2 is between December and February of 2023. For Neptune, window 1 is from June to August and window 2 is from October to December (Fletcher et al., 2021).

The observations with MIRI will map temperatures and composition from the troposphere to the stratosphere, exploring the middle atmospheric circulation in unprecedented detail. Near-simultaneous Near-infrared Spectrometer (NIRSpec) 1.6 - 5.3 μm spectroscopy of Uranus will be used to understand connections to the dynamics below (e.g., aerosols, clouds and storms) and the energetics of the ionosphere (via H_3^+ emission), permitting a comprehensive view of energy flow through ice giant atmospheres.

With these observations happening at both ice giants we want to be able to use our current knowledge of the planets to make our best guess of what could be detected in their atmospheres using MIRI. For this we plan to simulate the MIRI observations using the results we have obtained from our analysis on the Spitzer IRS data.

7.3 Simulation Tools

This section gives a short description of the tools we have used or plan to use to simulate the MIRI ice giant data. In brief, we used NEMESIS to generate synthetic

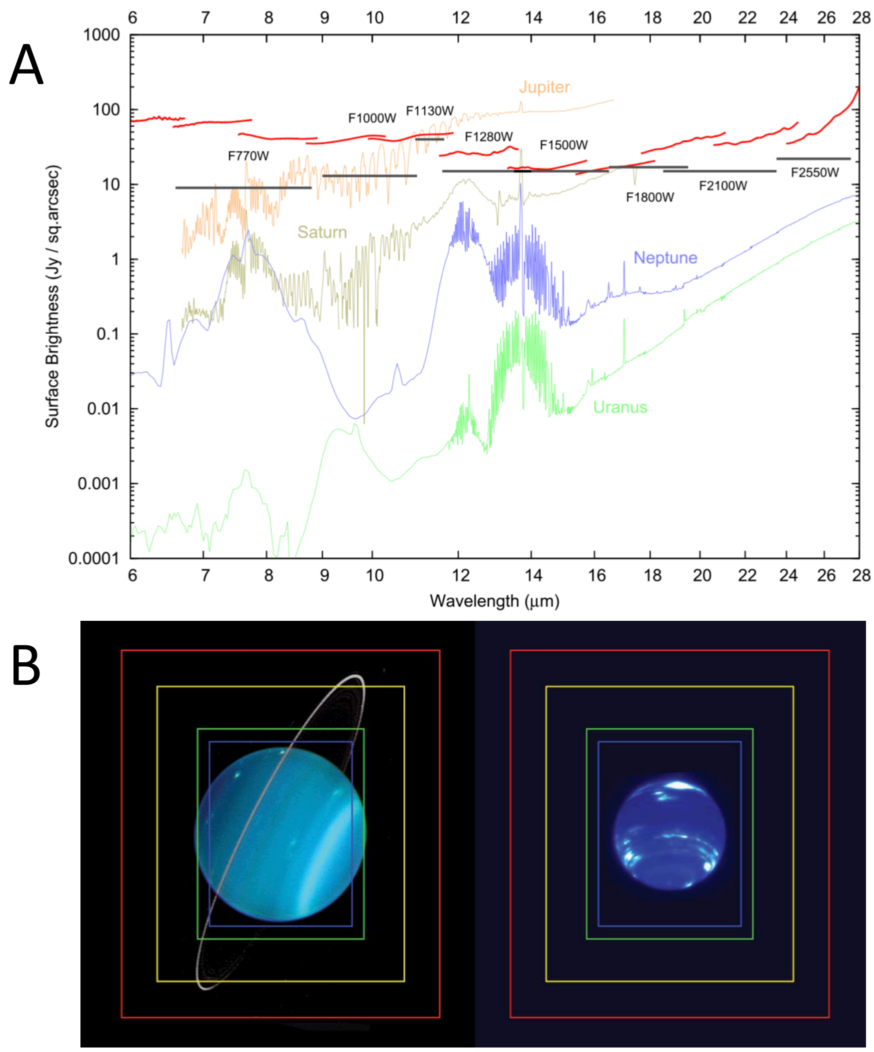

Figure 7.4: Panel A: The mid-infrared spectra of the four giant planets compared to the saturation limits of the filters on the MIRI MRS (red lines) and the MIRI imager (black lines). Uranus and Neptune are observable via imagery and spectroscopy over the entire spectral range of the instrument. The spectral resolution of the ice giant spectra displayed is that of Spitzer and will be much higher for the MRS. Panel B: Sample viewing geometry of Uranus and Neptune through the JWST MIRI MRS IFUs. Different color boxes show the four different IFU sizes of the channels with the colours corresponding to those in Figure 7.2. The typical sizes and orientations of Uranus and Neptune are shown for 2018. Figure adapted from Norwood et al. (2014, 2016).

data cubes of Uranus and will do the same for Neptune in the future. These images will then be input into the software that simulates the MIRI detector. This software produces the synthetic data as 'detector images' with all the individual slices laid out on the detector. The data reduction pipeline then recombines these to create the 3D data cubes that are equivalent to the cleaned data that we would use to do science. By doing all this synthetically we are ready for the real data and aware of any future issues with the pipeline. The last step would then be to use NEMESIS to analyse the processed simulations.

7.3.1 NEMESIS

NEMESIS is described in Chapter 2 and has been used in the past by Moses et al. (2018) to generate synthetic data cubes of both planets (Figure 7.7). We have used a similar method to generate cubes like this for Uranus.

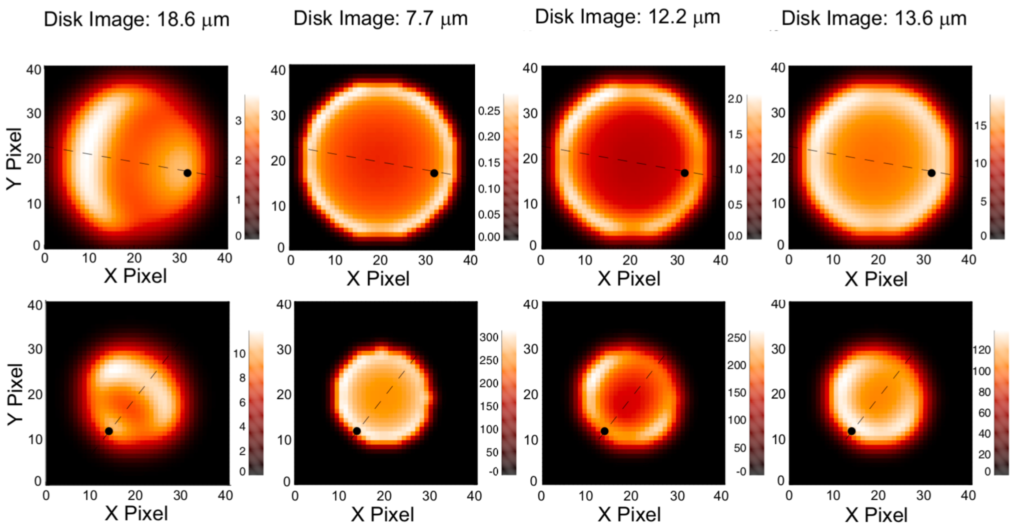

Figure 7.5: Selected ranges from the synthetic data cubes of Uranus (top row) and Neptune (bottom row) simulating what the JWST MIRI MRS would see at significant wavelength bands in 2018. The black dots mark the position of the poles and the dashed lines mark the central meridian. These images are adapted from Moses et al. (2018).

The forward modelling mode of NEMESIS is used along with suitable k-tables to generate the cubes of Uranus containing the time-dependent, latitude-dependent and altitude-dependent hydrocarbon and temperature profiles. The k-tables were generated for 8 gases, hydrogen, helium, three isotopes of methane ($^{12}CH_4$, $^{13}CH_4$ and CH_3D), acetylene, ethane and ethylene. The spatial orientation and size of the disk corresponds to an estimated date of the 31st August 2022 with an observer sub-latitude of 61.3° and an angular diameter of 3.6”. The latitude-dependence is taken from the results of Roman et al. (2020) taking into account the hemispheric asymmetry in acetylene emission that they detected. The altitude-dependence is taken from the vertical profiles from Orton et al. (2014a,b) with 161 pressure levels.

These profiles are used to simulate the expected spectral radiance and brightness temperatures that could be observed by MIRI for the full range from 5 to 28 μm over all 12 sub-bands.

Now, thanks to our Spitzer results (Chapter 4 and 5 and Rowe-Gurney et al. 2021), we can add longitude-dependence as a property to add to these model Uranus data in future. We have not yet started the work on creating synthetic data cubes for Neptune. To update the Moses et al. (2018) simulations in Figure 7.5 we will use the Spitzer spectra best-fit vertical profiles from chapter 6 as the foundation and update the spatial orientation and size of the disk to the 2022 JWST viewing window.

7.3.2 MIRISim

MIRISim is a simulator for the MIRI instrument on JWST that is based in the Python 3 environment (Geers et al., 2019). It was developed by the MIRI team at the UK Astronomy Technology Centre (UK-ATC) and managed by the Space Telescope Science Institute (STScI). It can simulate the MRS by producing FITS files consistent with data that would be output by JWST. These data can be read into the JWST pipeline because they are representative of what can be expected from MIRI observations. This gives us a sense of what MIRI is capable of and is representative of the current understanding of the instrument with new products being added regularly as effects are being actively studied by the instrument team.

To be able to simulate an observation, we create an astronomical scene using the cubes generated from NEMESIS. These cubes are first generated in units of radiance and are converted to units of μJy/arcsec^2 to be compatible with the MIRISim input. MIRISim then adds in flux from instrument optics, electronics and background, simulates the image slicer for MRS and the geometric deformations. It then disperses the image slices, adds in stochastic cosmic ray hits, photon noise and read noise and outputs the simulated observations.

7.3.3 JWST Data Pipeline

The JWST data reduction pipeline is a Python software suite that processes data taken by all of the JWST instruments, automatically removing instrumental signatures from the observations.

There are three stages in the pipeline. Stage 1, also called *Detector1*, does detector level corrections and ramp fitting for individual exposures that is universal for nearly all modes. Stage 2 is divided into separate modules for imaging and spectroscopic modes to do calibrations for individual exposures. Stage 3 is also module specific and combines data from multiple exposures within an observation.

We input the MIRI MRS simulations made by MIRISim that are already in the format needed for the pipeline. There are multiple output files for each stage with the final stage 3 outputs including fully processed 3D cubes and extracted 1D spectra.

7.3.4 ETC - Exposure Time Calculator

MIRISim combined with the JWST data pipeline cannot be used as a sensitivity calculator, which is why the ETC must be used alongside these tools. The ETC performs signal-to-noise ratio (SNR) calculations for all observing modes and is mostly used to calculate the number of integrations and total exposure time possible without saturating the different instrument channels.

We have used version 1.6 of the ETC for both Uranus and Neptune that is available online via a graphical user interface. The ETC is capable of using custom spectra from the user (User Supplied Spectra) supplied in wavelength (μm) and flux density (mJy) units. We used the disc-averaged high-resolution spectra used in Chapter 5 for Uranus (2007) and 6 for Neptune (2005) and the same exposure times as proposed in the GTO plans. These plans include a 4-point dither pattern and a total exposure time of 333 seconds per detector, per longitude. We used a circular aperture centred on the source with an aperture radius of 0.26 arcsec. The size of the aperture determines how the background noise is estimated and investigations into the best size per wavelength/channel are ongoing.

Channel 3B is used as an example as it is in the brightest region of both spectra (13.36 - 15.65 μm) covering the acetylene band. This is the band that would show any signs of saturation if the wrong observing modes were chosen. No saturation was seen at either Uranus or Neptune when doing these calculations with the new Spitzer data. We also tested channel 2C (9.99 - 11.71 μm). This band is, in contrast to 3B, very dim and therefore has much lower SNR. It is a band that has been difficult to observe using Spitzer and contains the ethylene band visible at Neptune. Our calculations for both bands are discussed below when we talk about the application to both planets.

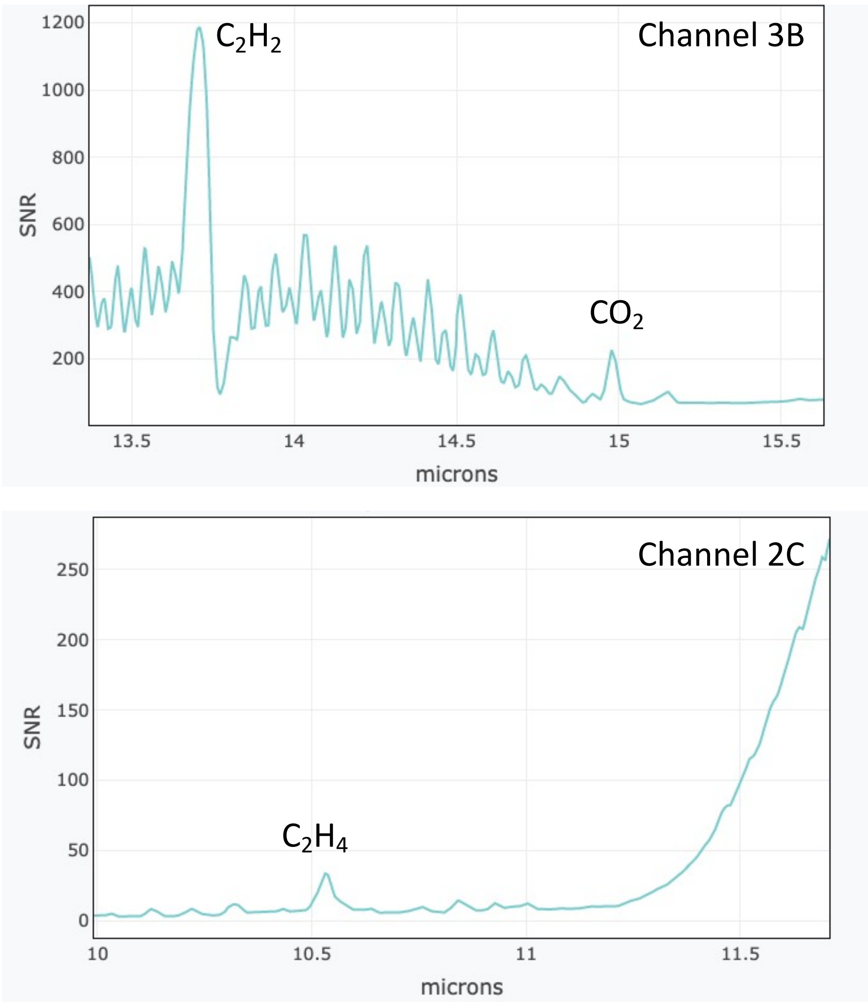

Figure 7.6: Example SNRs of Neptune calculated for channel 3B and 2C using the ETC, the Spitzer disc-averaged high-resolution spectrum from 2005 and the exposure times as proposed in the Cycle 1 GTO plans. Species present in the spectra are labelled.

7.4 Detectability of Spatial Gradients in Temperature and Chemistry

Ground-based telescopes can currently spatially resolve Uranus and Neptune in the MIR with higher spatial and spectral resolution in cases where the mirror is on the order of 10-m in diameter. The JWST has better sensitivity and wavelength coverage and the MIRI MRS can provide spatially-resolved spectroscopic maps of both planets (Norwood et al., 2016). How detectable certain science outcomes are from these maps is what will be useful to know before the data starts coming back from the observatory.

We can start to ascertain how detectable spatial structure of temperature and chemistry are on the ice giants by using the images generated from the first NEMESIS step. The images in Figure 7.7 incorporate the latitudinal changes in emission from Roman et al. (2020). These changes are modelled in acetylene emission only. From this preliminary experiment, we can see that latitudinal variation in acetylene is very visible in comparison to the images by Moses et al. (2018) in Figure 7.5 at two of the same wavelength bands. The 13.6 μm (acetylene) image of Uranus by Moses et al. (2018) is dominated by limb brightening but no other structure is visible. Our image has clear latitudinal variation with the bright polar cap visible in this emission band. The image in ethane emission (12.2 μm) looks very similar to the image by Moses et al. (2018) with strong limb brightening but no visible latitudinal variation. This assumes that ethane and stratospheric temperature are uniform, which may or may not be the case. This shows that we will be able to detect variations in the abundances of specific species and see on a global map where these variations are occurring on the disk but a full retrieval study is still needed and the first glimpses of Uranus at 12.2 μm will confirm or refute this.

7.4.1 Application to Uranus

The sub-observer latitude is around 60°N for the Uranus GTO viewing window. This orientation can be seen visually in the 13.6 μm image showing the bright northern polar cap acetylene emission (Fig. 7.7). This allows a large portion of the longitudes of the planets to still be seen even with the north pole slowly rotating into view on its way to northern summer solstice.

Figure 7.7 shows visually the best-case scenario MIRI MRS pixel scale for Uranus. The individual slices have coarser resolution than this but the planned dithering can improve the image quality. The blurring and other instrument effects from MIRI have not been added to the model yet but this gives us a good idea of the spatial resolution we will see when generating the 3-dimensional spectroscopic maps of the planet. Each pixel in the image will be associated with a spectrum like that in the top panel of the figure that has over four times the resolving power of the Spitzer IRS high-resolution module. The exact spectral resolution used in the model is as stated for each of the 12 sub-bands, varying with wavelength linearly from one end of the band to the other. The spectrum in Figure 7.7, therefore, has the spectral resolving power range of channel 3A (2,530–2,880) approximately R$\sim$ 2700.

Using the ETC and the high-resolution Spitzer spectra as a base, we calculated the SNR as 622 for the brightest wavelength range of the acetylene band, channel

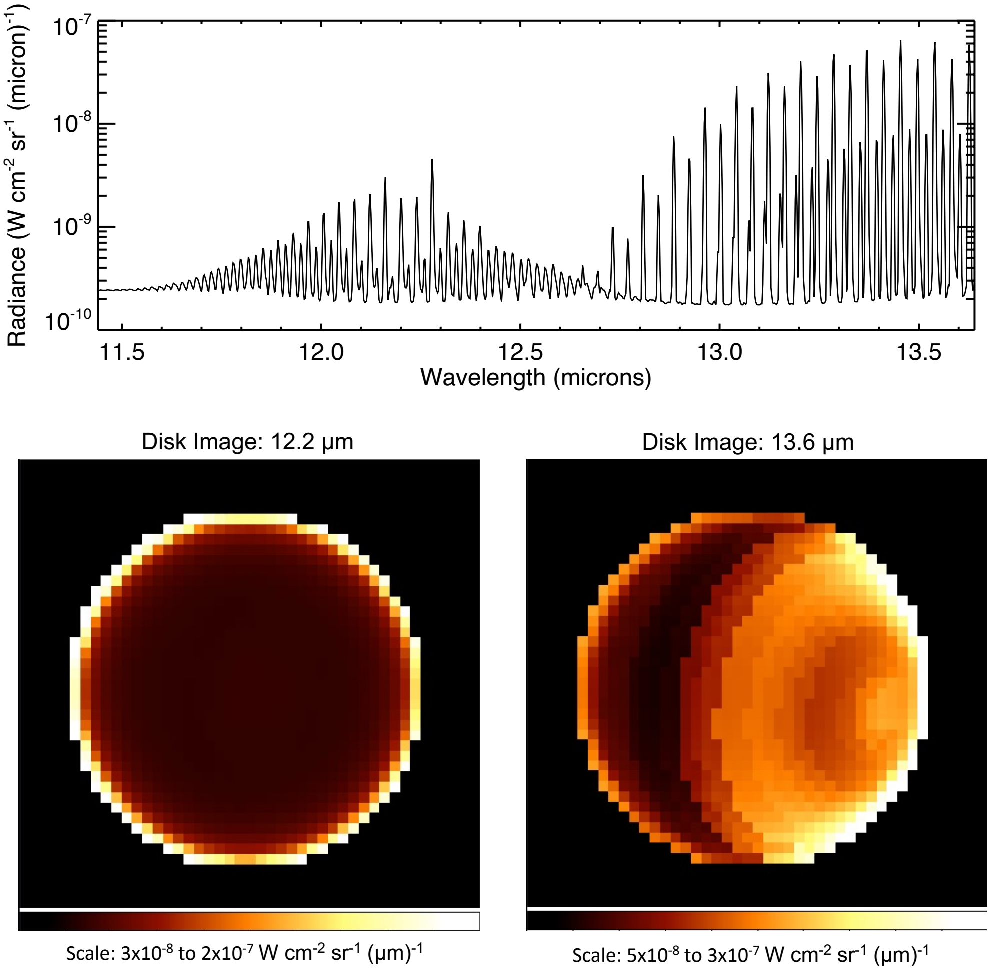

Figure 7.7: Top panel: An example spectrum extracted from a synthetic data cube of Uranus showing the ethane and acetylene bands at the approximate latitude of the sub-observer point generated in radiance units for the August 2022 GTO viewing window. Bottom two images: Slices of the same synthetic data cube in the two different hydrocarbon bands with the latitudinal emission variations in acetylene from Roman et al. (2020) incorporated. The best-case scenario pixel scale of the MIRI MRS can be seen in the images.

3B. This means the signal is over 600 times the noise level for the MIRI observations without reaching saturation. Channel 2C, the low-signal region that we had to cut out of our Spitzer analysis completely for Uranus, has an SNR of 5.3. This still means we have 5 times the signal over the noise and information from this band at high resolution could mean the discovery of ethylene at Uranus. Neither Orton et al. (2014b) or Rowe-Gurney et al. (2021) could detect this species over the noise of the Spitzer data.

7.4.2 Application to Neptune

We used our globally-averaged high-resolution Spitzer spectra from 2005 for the user supplied spectra in the ETC. We calculated a signal-to-noise of 1170 for the brightest acetylene band range (channel 3B). This is almost double that of Uranus, because the spectrum of Neptune is brighter overall and yet, it is still within instrument saturation limits. Channel 2C's SNR is 13.2 giving us a good chance of successfully extracting the abundance of ethylene from the MIRI data (see Figure 7.6).

Neptune has a smaller disk than Uranus but is also brighter due to its significant internal heat source. A similar level of analysis can be conducted at both planets and once this has been completed we will know more about the application of these methods and their effectiveness at Neptune.

7.5 Future Work

The work in this chapter is still in progress. The synthetic data cubes of Uranus will have the longitudinal changes added and the ones of Neptune will be built with their vertical profiles updated from the Spitzer results.

Once the data cubes are created, we will input them into MIRISim with the output being the equivalent of what MIRI will output when doing the real observations. These synthetic observations will then be processed using the data pipeline before being analysed using the radiative transfer and retrieval methods used in Rowe-Gurney et al. (2021) guided by photochemical models (Moses et al., 2018). This will allow us to do a sensitivity study to understand the degeneracies inherent in the MIRI spectra, and ultimately - with the real data - reveal information about the atmospheric composition and temperature profiles.

Longitudinal variations may be visible during the GTO, the extent of which can be modelled. Observations of Uranus taken at different longitudes will be simulated with a variation like that observed and analysed in Chapter 4. Four different longitude temperature profiles will be modelled into the synthetic data and then sampled at the three longitudes of the GTO plan. This will enable us to ascertain exactly what can be extracted with confidence from the data and therefore what scientific conclusions can be made. If longitudinal variations are present then MIRI will be able to determine where on the disk they originate and therefore narrow down their suspected source.

7.6 Summary

In this chapter we have shown how the Spitzer data analysed in previous chapters can be used to model future observations with the James Webb Space Telescope Mid-Infrared Instrument Medium-Resolution Spectrometer. The synthetic spectra of Uranus generated using the forward modelling mode of NEMESIS have had the latitudinal changes in acetylene abundance added from the study by Roman et al. (2020) and the spatial orientation updated for the current GTO plans. This is an ongoing study but we have described the tools, methods, preliminary results and expected findings. The next step is to pass the synthetic data cubes into the MIRISim pipeline to understand how to work with the MIRI detector outputs.

The James Webb Space Telescope will give us the first global spectroscopic maps of both of ice giants in the mid-infrared and will advance our understanding of the composition and evolution of their atmospheres. These simulations will also allow effective and efficient preparation of the software and analytical tools necessary to process the real JWST data.

Chapter 8

Conclusion

8.1 Overview

This thesis uses data from the Spitzer Infrared Spectrometer to investigate the temperature structure and composition of the stratosphere and upper troposphere of both the ice giants, Uranus and Neptune. In the introduction, we set out the following questions that we hoped this thesis would answer:

1. Is there a longitudinal variation at Uranus and Neptune from Spitzer IRS data?
2. Is there a connection between the troposphere and stratosphere in the variability?
3. What is the thermal structure and composition of Uranus' stratosphere in 2007 and can this tell us the likely cause of the variation?
4. What is the thermal structure and composition of Neptune's stratosphere in 2005?
5. How will spatially-resolved MIR observations from JWST MIRI extend the disc-integrated analysis described in this thesis?

This chapter will conclude by addressing the answers to each question and by describing the results in each case. Finally, we make some suggestions for future work.

8.2 Conclusions

1. Is there a longitudinal variation at Uranus and Neptune from Spitzer IRS data?

Both the Uranus and Neptune data were processed using an updated reduction pipeline that is described in Chapter 3. In Chapter 4, we analysed these disc-averaged spectra from Spitzer IRS at separate longitudes to shed light on the the variability of the planets as they rotate. A variability of up to 15% at stratospheric altitudes sensitive to the hydrocarbon species at around the 0.1-mbar pressure level was detected at Uranus in 2007. The tropospheric hydrogen-helium continuum, and the monodeuterated methane that also arises from these deeper levels, both exhibit a negligible variation smaller than 2%, constraining the phenomenon to the stratosphere. A similar variation was detected in 2005 and may have been detected in 2004 if there had not been a considerable amount of noise caused by short integration times. In 2005 the variation in emission was smaller (around 5%) but had a sparser set of longitudes and therefore a pattern could not be determined. This longitudinal variation on Uranus was reported in Rowe-Gurney et al. (2021), and the causes are discussed below.

A variation is not present at Neptune in 2005 or late 2004, when all the separate longitudes displayed the same brightness temperature. In May 2004 a stratospheric variation is present, although it is tentative due to the deviation only appearing at a single longitude and because there are larger uncertainties on this early dataset with short integration times.

2. Is there a connection between the troposphere and stratosphere in the variability?

The longitudinal variation detected at Uranus during the 2007 equinox is an observed physical change in the stratosphere of the planet, most likely a temperature change associated with the band of bright stratospheric emission observed in ground-based images. The variation showed evidence of being caused by a localised feature that is stable over short timescales. The Spitzer IRS data can provide much detail but without accompanying spatial resolution it is impossible to come to a definitive conclusion as to the origins of the changes. In chapter 4, we investigated both near- and mid-infrared ground based observations of Uranus to determine whether a cause could be deduced by gaining this much-needed spatial resolution.

We used observations from Keck II NIRCII in December 2007 (Sromovsky et al., 2009; de Pater et al., 2011) and VLT/VISIR in 2009 (Roman et al., 2020) which suggested possible links to these variations in the form of discrete meteorological features. Roman et al. (2020) identified discrete patches of brightness in 13-μm (acetylene) emission within a broad stratospheric band at mid-latitudes, which could be related to the variability observed by Spitzer. The NIR images from Keck sense the cloud tops in the troposphere. The more meteorologically active hemisphere seen in these observations coincided with the minimum in stratospheric emission and could indicate a connection between the stratosphere and troposphere. An invisible *dark spot*-like tropospheric feature, with its observed companion clouds, provide circumstantial evidence of a connection with the longitudinal variations we see in the stratosphere.

At Neptune, the activity in the troposphere could once again be influencing the stratosphere. Images in the NIR from Gemini and HST show reflectivity around the tropopause level that could indicate this. If the variation in May 2004 is real, then it could be caused by stratospheric methane injection by clouds or perturbations of the south polar warm vortex.

It is impossible to provide a definitive answer to this question due to the lack of spatial resolution in the Spitzer data. However, with the advances of the JWST at MIR wavelengths, accompanied by NIR observations from JWST or the ground, this question can be answered and should be a focus of future investigations into both planets.

3. What is the thermal structure and composition of Uranus' stratosphere in 2007 and can this tell us the likely cause of the variation?

Building on the forward-modelling analysis of the global average study of Uranus by Orton et al. (2014a,b), we presented full optimal estimation inversions (using the NEMESIS retrieval algorithm, Irwin et al. 2008) in Chapter 5. We did this for the global average and also at each longitude to distinguish between thermal and compositional variability.

More weight was placed on the results of the retrievals from the better-calibrated low-resolution data. We used the results from the investigation by Orton et al. (2014a) as *priors* and found that all deviation from these occurred in the same region of the stratosphere (between 1 mbar and 0.01 mbar). This hinted at some degeneracy in our global average results. The data were best reproduced by models with atmospheric mixing via eddy diffusion that was weaker than that assumed by Orton et al. but still within the confines of a realistic fit according to their model. An eddy diffusion coefficient value of 1020 $cm^2 sec^{-1}$ and a tropopause methane mole fraction of 8.0×10^{-5} provides the best fit to the temperature structure and the methane vertical profile whilst also maintaining the closest chi-squared value for the spectral fit (Moses et al., 2018). The high-resolution results had slightly modified temperatures and gas profiles compared to the low-resolution, caused by the challenges we had in calibration and also the longitudinal changes in emission that occurred between modules.

The model suggested that the variations can be explained solely by changes in stratospheric temperatures. A temperature change of less than 2 K is needed to reproduce the observed variation. This is compounded by results from high-resolution forward models (primarily sounding the ethane and acetylene emission) constructed using the parameters retrieved from the low-resolution spectra. Temperature change in the stratospheres of giant planets has been known to originate from intense storm activity like that from the vortex systems associated with dark spots. We postulated that this could be the cause of the temperature anomaly but it could also be thermal variation caused by a stratospheric wave. Any conclusions drawn would be speculative at best until the Uranian stratosphere is observed with the spatial resolution and sensitivity of JWST.

The Uranus variability results from Chapter 4 and 5 have already been published in Rowe-Gurney et al. (2021).

4. What is the thermal structure and composition of Neptune's stratosphere in 2005?

The data from 2005 have optimised exposure times, multiple observed longitudes, and therefore the lowest noise. We used these data to derive the vertical structure of the temperature and composition in the stratosphere and upper troposphere (between around 1 nanobar and 2 bars of pressure). In Chapter 6, we do full optimal estimation inversions (using NEMESIS) of the globally averaged November 2005 data.

We fit both the low-resolution and high-resolution module data, and tested multiple temperature priors derived from chemical models (Moses et al., 2005) and observations from AKARI (Fletcher et al., 2010) and TEXES/Gemini-N (Greathouse et al., 2011). The temperature structure showed a good agreement with the chosen prior, an average of Moses model C (Moses et al., 2005) and the TEXES observations from Greathouse et al. (2011). There was a slight warming compared to the prior with a quasi-isothermal structure in the stratosphere that is at 169 ± 3 K between 0.1 and 0.001 mbar in agreement with past disk-averaged observations.

The abundances of stratospheric hydrocarbons were determined, including acetylene and ethane from the low-resolution data. Methylacetylene/propyne, diacetylene, CO_2 and propane abundances were determined from the high-resolution data. We conducted the first ever retrieval of methyl (CH_3) for Neptune at these wavelengths. We identified multiple features that were previously designated as unknown between 15 and 19 μm as branches of methyl as well as fitting the brightest band at 16.5 μm (Meadows et al., 2008). The VMR at 0.3 μbar was determined as $(9.7 \pm 2.9)\times10^{-8}$, almost twice the value from the Moses model.

We found sensitivity to the stratospheric D/H ratio (derived from the relative abundances of CH_4 and CH_3D) and constrained this value by finding the best fit to our model, $(5^{+2.3}_{-1.3})\times10^{-4}$. This corresponded to a hydrogen D/H value of $(7.8^{+3.8}_{-1.8})\times10^{-5}$ that is higher than expected but in agreement with a past investigation by Feuchtgruber et al. (1999).

The Neptune results from this chapter are being prepared for a future publication.

5. How will spatially-resolved MIR observations from JWST MIRI extend the disc-integrated analysis described in this thesis?

The James Webb Space Telescope will give us the first global spectroscopic maps of both of the ice giants in the mid-infrared and will advance our understanding of the composition and evolution of their atmospheres. In Chapter 7, we showed how the Spitzer data analysed in previous chapters can be used to model future observations with the James Webb Space Telescope Mid-Infrared Instrument Medium-Resolution Spectrometer. We added the latitudinal changes in acetylene abundance from the study by Roman et al. (2020) to generate synthetic spectra of Uranus using the forward modelling mode of NEMESIS.

Using Uranus as an example, we showed that we are able to detect variations in the abundances of specific species and see on a global map where these variations are occurring on the disk. However, a full retrieval study is still needed to understand the sensitivity to small variations in each gaseous species, and the inherent degeneracies. This question is not yet fully answered because this project is ongoing. Future work was highlighted in this chapter and will also be summarised below in Section 8.3. These simulations, once complete, will allow effective and efficient preparation of the software and analytical tools necessary to process the real JWST data.

These modelling results are in preparation for a future publication.

8.3 Future Work

8.3.1 The Ice Giant Spectrum Between 5 and 7 Microns

We omitted the 5 to 7 μm region of the SL spectrum in both Chapter 5 for Uranus and Chapter 6 for Neptune. This was due to not only noise in the data at these short wavelengths but also uncertainties in the line data for this region. The region has a complex contribution of reflected sunlight and so both sunlight and thermal emission need to be accounted for. This region contains the wing of the main 7.7 μm methane band that is used for temperature constraint. Instruments typically struggle to cover that range because a different detector type is needed below and above the area around 5 μm (where the indistinct boundary between MIR and NIR lies). With more information in this region, connections between the photochemical processes of the stratosphere and the clouds of the troposphere could be drawn more easily. At the ice giants, and even at the more explored gas giants, it has not been the subject of much investigation in the past and should be the topic of a future investigation.

8.3.2 Non-LTE Effects at the Ice Giants

The current version of NEMESIS assumes Local Thermodynamic Equilibrium (LTE, see Chapter 2). Evidence suggests that this is suitable for the gas giants at MIR wavelengths but not for the extreme cold of the ice giants (Orton et al., 2014b). This means corresponding atmospheric temperatures can differ significantly from the local kinetic temperature assumed, which could generate a systematic offset in retrieved temperatures and abundances at low pressures. For example, Appleby (1990) found that a temperature difference of up to 20 K is possible at Uranus due to non-LTE effects at pressures of around 0.1 μbar. As the Source functions for the hydrocarbons remain poorly constrained under ice giant conditions, a hybrid radiative transfer code combining LTE and non-LTE effects is planned.

8.3.3 Para-Hydrogen Fraction Disequilibrium Testing

Fitting the hydrogen quadrupole in the Spitzer data in Chapter 5 and 6 was found to be challenging. One solution to this problem could be the ortho-para ratio and the assumptions we used for both planets. We assumed thermal equilibrium at the warm temperatures of the upper stratosphere where we are sensitive to the quadrupoles. The lack of fit could be telling us that equilibrium is not the right solution and the degree of disequilibrium could tell us a lot about atmospheric circulation. As we stated in Chapter 1, circulation, chemistry and temperatures are all interlinked and an in-depth study on the effects of the para-hydrogen fraction would investigate all of them.

8.3.4 Methyl at Uranus

Methyl was unsuccessfully sought out by Burgdorf et al. (2006) in the earlier Spitzer data. It was then tentatively observed by Orton et al. (2014b) in the 2007 Uranus data at the fundamental 16.5 μm band. We did not report this observation in our findings in Chapter 5, but we do report of two unknown features at 15.6 μm and 16.0 μm. This coincides with two of the smaller features identified at Neptune in Chapter 6 at 15.55 μm and 16.0 μm. It is possible that this is methyl at Uranus but further testing is needed to confirm. It would be useful to go back with the knowledge gained from the later investigation into methyl at Neptune and prove a definite detection.

Methyl radicals are directly produced by the photodissociation of methane, usually around the homopause level. Observations of CH_3 can be used as a diagnostic tool to constrain the location of the homopause (Bézard et al., 1998). These new observations at Uranus could help to determine the CH_4 homopause value like the investigation by Sinclair et al. (2020b). CH_3 is the intermediate product between methane and ethane production and can help us to understand the formation of ethane (Bézard et al., 1999). Knowing more about methyl can therefore lead to a better understanding of ice giant stratospheric photochemical processes.

8.3.5 Further Neptune D/H Testing

In Chapter 6, we introduced the possibility that changing the D/H gives a better temperature profile and methane fit. The temperature profile fits with the best-fit D/H also have the best similarity between high and low resolution. What would be useful as an extension of the D/H testing that has already been done would be to observe the methane region and the quadrupole, adjusting the methane, the D/H, and atmospheric temperature priors until we came up with something that worked in both regions. Once we've found a good compromise for D/H and the temperature profile, this could be used to fit the full low-resolution and high-resolution ranges and produce refined temperature and gas retrievals.

Methane could be changing with time, whereas we have assumed a constant methane level throughout testing. This is a parameter that could be tested along with the eddy diffusion coefficient, which directly impacts the methane profile as it did at Uranus. We did not test the eddy diffusion coefficient assumptions or the methane profile at Neptune. We also have access to other epochs of Spitzer data, and this would be useful to check if the D/H levels are consistent for all of them.

8.3.6 Continuing with JWST MIRI Modelling for the Ice Giants

The work of Chapter 7 needs to be continued and the future work section at the end of the chapter details this. In summary, the synthetic data cubes of Uranus will have the longitudinal changes added and the ones of Neptune will be built with their vertical profiles updated from the Spitzer results. These cubes will then be input into MIRISim with the output synthetic observations then processed using the data pipeline. A sensitivity study would then be conducted using NEMESIS to understand the degeneracies inherent in the MIRI spectra, and ultimately - with the real data - reveal information about the atmospheric composition and temperature profiles.

8.3.7 Preparing for Future Missions to the Ice Giants

There is a lot of enthusiasm surrounding the idea of a mission to the ice giants in the coming decades. The international science community are collectively pushing towards a dedicated mission to one or both of the ice giants (Mousis et al., 2018; Hofstadter et al., 2019; Guillot, 2019; Fletcher et al., 2019; Dahl et al., 2020; Fletcher et al., 2020, etc.). This would be the first dedicated mission to the last remaining class of planet to be explored and the first time we have been to the systems since Voyager-2 in the late 1980s. A return to the ice giants is hoped to combine orbital exploration of the planets, rings, satellites and magnetospheres. It is hoped that it would also include an atmospheric entry probe, following the legacy of Cassini-Huygens at Saturn and Titan. The work in this thesis and the future work listed above will all help to motivate the exploration of both planetary systems by bringing new information and also new questions about the planet's atmospheres.

8.4 Final Comments

This thesis used the archived mid-infrared spectra from the now decommissioned Spitzer Space Telescope to investigate the middle atmosphere of the ice giants, Uranus and Neptune. This was done in preparation for the James Webb Space Telescope. At the time of writing, this observatory is due to launch in around 3 months. The data obtained will provide high spatial resolution observations in the mid-infrared that will improve our understanding of ice giant atmospheric evolution, processes and dynamics. This will, in turn, improve our understanding of planetary formation and our own solar system, and therefore planetary systems throughout the universe.

Bibliography

Achterberg, R. K. and Flasar, F. M. (1996). Planetary-scale thermal waves in saturn's upper troposphere. *Icarus*, 119(2):350–369.

Appleby, J. F. (1990). Ch4 nonlocal thermodynamic equilibrium in the atmospheres of the giant planets. *Icarus*, 85(2):355–379.

Atreya, S. K. (2013). *Atmospheres and Ionospheres of the Outer Planets and their Satellites*, volume 15. Springer Science & Business Media.

Baines, K. H. and Hammel, H. B. (1994). Clouds, hazes, and the stratospheric methane abundance in neptune. *Icarus*, 109(1):20–39.

Baines, K. H., Mickelson, M. E., Larson, L. E., and Ferguson, D. W. (1995). The abundances of methane and ortho/para hydrogen on uranus and neptune: Implications of new laboratory 4-0 h2 quadrupole line parameters. *Icarus*, 114(2):328–340.

Batalha, N. M., Rowe, J. F., Bryson, S. T., Barclay, T., Burke, C. J., Caldwell, D. A., Christiansen, J. L., Mullally, F., Thompson, S. E., Brown, T. M., et al. (2013). Planetary candidates observed by kepler. iii. analysis of the first 16 months of data. *The Astrophysical Journal Supplement Series*, 204(2):24.

Bézard, B., Feuchtgruber, H., Moses, J., and Encrenaz, T. (1998). Detection of methyl radicals (ch3) on saturn. *Astronomy and Astrophysics*, 334:L41–L44.

Bézard, B., Romani, P., Feuchtgruber, H., and Encrenaz, T. (1999). Detection of the methyl radical on neptune. *The Astrophysical Journal*, 515(2):868.

Bishop, J., Atreya, S., Herbert, F., and Romani, P. (1990). Reanalysis of voyager 2 uvs occultations at uranus: Hydrocarbon mixing ratios in the equatorial stratosphere. *Icarus*, 88(2):448 – 464.

Blake, J. S., Fletcher, L. N., Greathouse, T. K., Orton, G. S., Melin, H., Roman, M. T., Antuñano, A., Donnelly, P. T., Rowe-Gurney, N., and King, O. (2021). Refining saturn's deuterium-hydrogen ratio via irtf/texes spectroscopy. *Astronomy and Astrophysics*.

Blass, W., Halsey, G., and Jennings, D. (1987). Self-and foreign-gas broadening of ethane lines determined from diode laser measurements at 12 μm. *Journal of Quantitative Spectroscopy and Radiative Transfer*, 38(3):183–184.

Borysow, A. and Frommhold, L. (1986). Theoretical collision-induced rototranslational absorption spectra for the outer planets-h2-ch4 pairs. *The Astrophysical Journal*, 304:849–865.

Borysow, J., Frommhold, L., and Birnbaum, G. (1988). Collison-induced rototranslational absorption spectra of h2-he pairs at temperatures from 40 to 3000 k. *The Astrophysical Journal*, 326:509–515.

Bouanich, J.-P., Blanquet, G., Walrand, J., and Lepère, M. (2003). H2-broadening in the $\nu 7$ band of ethylene by diode-laser spectroscopy. *Journal of molecular spectroscopy*, 218(1):22–27.

Bouanich, J.-P., Blanquet, G., Walrand, J., and Lepère, M. (2004). Hydrogen-broadening coefficients in the $\nu 7$ band of ethylene at low temperature. *Journal of molecular spectroscopy*, 227(2):172–179.

Broadfoot, A., Atreya, S., Bertaux, J., Blamont, J., Dessler, A., Donahue, T., Forrester, W., Hall, D., Herbert, F., Holberg, J., et al. (1989). Ultraviolet spectrometer observations of neptune and triton. *Science*, 246(4936):1459–1466.

Broadfoot, A., Herbert, F., Holberg, J., Hunten, D., Kumar, S., Sandel, B., Shemansky, D., Smith, G., Yelle, R., Strobel, D., et al. (1986). Ultraviolet spectrometer observations of uranus. *Science*, 233(4759):74–79.

Brown, L. R., Benner, D. C., Champion, J.-P., Devi, V. M., Fejard, L., Gamache, R., Gabard, T., Hilico, J., Lavorel, B., Loete, M., et al. (2003). Methane line parameters in hitran. *Journal of Quantitative Spectroscopy and Radiative Transfer*, 82(1-4):219–238.

Burgdorf, M., Orton, G., van Cleve, J., Meadows, V., and Houck, J. (2006). Detection of new hydrocarbons in Uranus' atmosphere by infrared spectroscopy. *Icarus*, 184(2):634–637.

Burgdorf, M., Orton, G. S., Davis, G. R., Sidher, S. D., Feuchtgruber, H., Griffin, M. J., and Swinyard, B. M. (2003). Neptune's far-infrared spectrum from the iso long-wavelength and short-wavelength spectrometers. *Icarus*, 164(1):244–253.

Cavalié, T., Dobrijevic, M., Fletcher, L. N., Loison, J.-C., Hickson, K., Hue, V., and Hartogh, P. (2015). Photochemical response to the variation of temperature in the 2011- 2012 stratospheric vortex of saturn. *Astronomy & Astrophysics*, 580:A55.

Conrath, B., Flasar, F., Hanel, R., Kunde, V., Maguire, W., Pearl, J., Pirraglia, J., Samuelson, R., Gierasch, P., Weir, A., et al. (1989). Infrared observations of the neptunian system. *Science*, 246(4936):1454–1459.

Conrath, B. J., Gierasch, P. J., and Leroy, S. S. (1990). Temperature and circulation in the stratosphere of the outer planets. *Icarus*, 83(2):255–281.

Conrath, B. J., Gierasch, P. J., and Ustinov, E. A. (1998). Thermal Structure and Para Hydrogen Fraction on the Outer Planets from VoyagerIRIS Measurements. *Icarus*, 135(2):501–517.

Dahl, E. K., Brueshaber, S., Cosentino, R., Palotai, C., Rowe-Gurney, N., Sankar, R., Sayanagi, K., Aslam, S., Baines, K., Barth, E., et al. (2020). Ice giant atmospheric science: A white paper for nasa's planetary science decadal survey 2023-2032. *arXiv preprint arXiv:2010.08617*.

de Pater, I., Dunn, D. E., Stam, D. M., Showalter, M. R., Hammel, H. B., Min, M., Hartung, M., Gibbard, S. G., Dam, M. A. V., and Matthews, K. (2013). Keck and VLT AO observations and models of the uranian rings during the 2007 ring plane crossings. *Icarus*, 226(2):1399–1424.

de Pater, I., Fletcher, L. N., Luszcz-Cook, S., DeBoer, D., Butler, B., Hammel, H. B., Sitko, M. L., Orton, G., and Marcus, P. S. (2014). Neptune's global circulation deduced from multi-wavelength observations. *Icarus*, 237:211–238.

de Pater, I., Gibbard, S., Macintosh, B., Roe, H., Gavel, D., and Max, C. (2002). Keck adaptive optics images of uranus and its rings. *Icarus*, 160(2):359–374.

de Pater, I., Sromovsky, L. A., Fry, P. M., Hammel, H. B., Baranec, C., and Sayanagi, K. M. (2015). Record-breaking storm activity on Uranus in 2014. *Icarus*, 252:121–128.

de Pater, I., Sromovsky, L. A., Hammel, H. B., Fry, P. M., Lebeau, R. P., Rages, K., Showalter, M., and Matthews, K. (2011). Post-equinox observations of Uranus : Berg ' s evolution , vertical structure , and track towards the equator. *Icarus*, 215(1):332–345.

Encrenaz, T. (2002). Iso observations of planetary atmospheres. *Advances in Space Research*, 30(9):1967–1970.

Encrenaz, T., Combes, M., Atreya, S., Romani, P., and Fricke, K. (1986). A study of the upper atmosphere of uranus using the iue. *Astronomy and Astrophysics*, 162:317–322.

Encrenaz, T., Feuchtgruber, H., and Atreya, S. K. (1998). Letter to the Editor ISO observations of Uranus : The stratospheric distribution of C 2 H 2 and the eddy diffusion coefficient. *ASTRONOMY AND ASTROPHYSICS*, 46:43–46.

Feuchtgruber, H., Lellouch, E., Bézard, B., Encrenaz, T., de Graauw, T., and Davis, G. (1999). Detection of hd in the atmospheres of uranus and neptune: a new determination of the d/h ratio. *Astronomy and Astrophysics*, 341:L17–L21.

Feuchtgruber, H., Lellouch, E., Orton, G., De Graauw, T., Vandenbussche, B., Swinyard, B., Moreno, R., Jarchow, C., Billebaud, F., Cavalié, T., et al. (2013). The d/h ratio in the atmospheres of uranus and neptune from herschel-pacs observations. *Astronomy & Astrophysics*, 551:A126.

Fisher, B. M., Orton, G. S., Liu, J., Schneider, T., Ressler, M. E., and Hoffman, W. F. (2016). The organization of jupiter's upper tropospheric temperature structure and its evolution, 1996–1997. *Icarus*, 280:268–277.

Fitzpatrick, P. J., de Pater, I., Luszcz-Cook, S., Wong, M. H., and Hammel, H. B. (2014). Dispersion in neptune's zonal wind velocities from nir keck ao observations in july 2009. *Astrophysics and Space Science*, 350(1):65–88.

Flasar, F. M., Conrath, B. J., Gierasch, P. J., and Pirraglia, J. A. (1987). Voyager infrared observations of uranus' atmosphere: Thermal structure and dynamics. *Journal of Geophysical Research: Space Physics*, 92(A13):15011–15018.

Fletcher, L., Hammel, H., Milam, S., de Pater, I., Fouchet, T., Orton, G., Roman, M., Rowe-Gurney, N., Melin, H., Wong, M., Fry, P., Antuñano, A., Hueso, R., Tiscareno, M., Irwin, P., Moses, J., Holler, B., Stansberry, J., , and Glasse, A.

(2021). The jwst giant planet atmospheres programme. *European Planetary Science Congress 2021*. EPSC2021-39.

Fletcher, L. N., de Pater, I., Orton, G. S., Hammel, H. B., Sitko, M. L., and Irwin, P. G. (2014). Neptune at summer solstice: zonal mean temperatures from ground-based observations, 2003–2007. *Icarus*, 231:146–167.

Fletcher, L. N., de Pater, I., Orton, G. S., Hofstadter, M. D., Irwin, P. G., Roman, M. T., and Toledo, D. (2020). Ice giant circulation patterns: implications for atmospheric probes. *Space science reviews*, 216(2):1–38.

Fletcher, L. N., Drossart, P., Burgdorf, M., Orton, G., and Encrenaz, T. (2010). Neptune's atmospheric composition from akari infrared spectroscopy. *Astronomy & Astrophysics*, 514:A17.

Fletcher, L. N., Greathouse, T., Orton, G., Sinclair, J., Giles, R., Irwin, P., and Encrenaz, T. (2016). Mid-infrared mapping of jupiter's temperatures, aerosol opacity and chemical distributions with irtf/texes. *Icarus*, 278:128–161.

Fletcher, L. N., Gustafsson, M., and Orton, G. S. (2018). Hydrogen dimers in giant-planet infrared spectra. *The Astrophysical Journal Supplement Series*, 235(1):24.

Fletcher, L. N., Helled, R., Roussos, E., Jones, G., Charnoz, S., André, N., Andrews, D., Bannister, M., Bunce, E., Cavalié, T., et al. (2019). Ice giant systems, the scientific potential of orbital missions to uranus and neptune: A white paper submitted to esa's voyage 2050 call. *arXiv preprint arXiv:1907.02963*.

Fletcher, L. N., Hesman, B. E., Achterberg, R. K., Irwin, P. G. J., Bjoraker, G., Gorius, N., Hurley, J., Sinclair, J., Orton, G. S., Legarreta, J., García-melendo, E., Sánchez-lavega, A., Read, P. L., Simon-miller, A. A., and Flasar, F. M. (2012). The origin and evolution of Saturn ' s 2011 – 2012 stratospheric vortex. *Icarus*, 221(2):560–586.

Fortney, J. J., Ikoma, M., Nettelmann, N., Guillot, T., and Marley, M. (2011). Self-consistent model atmospheres and the cooling of the solar system's giant planets. *The Astrophysical Journal*, 729(1):32.

Fouchet, T., Lellouch, E., and Feuchtgruber, H. (2003). The hydrogen ortho-to-para ratio in the stratospheres of the giant planets. *Icarus*, 161(1):127–143.

Geers, V., Klaassen, P., Beard, S., Consortium, E., et al. (2019). Mirisim: The jwst-miri simulator. *ASPC*, 523:641.

Geiss, J. and Gloeckler, G. (1998). Abundances of deuterium and helium-3 in the protosolar cloud. *Primordial Nuclei and their Galactic evolution*, pages 239–250.

Gillett, F. and Rieke, G. (1977). 5-20 micron observations of uranus and neptune. *The Astrophysical Journal*, 218:L141–L144.

Goody, R. M. and Yung, Y. L. (1995). *Atmospheric radiation: theoretical basis*. Oxford university press.

Greathouse, T. K., Richter, M., Lacy, J., Moses, J., Orton, G., Encrenaz, T., Hammel, H., and Jaffe, D. (2011). A spatially resolved high spectral resolution study of neptune's stratosphere. *Icarus*, 214(2):606–621.

Guillot, T. (2019). Uranus and neptune are key to understand planets with hydrogen atmospheres: A white paper for esa's voyage 2050. *arXiv preprint arXiv:1908.02092*.

Hadland, N., Sankar, R., LeBeau Jr, R. P., and Palotai, C. (2020). Epic simulations of neptune's dark spots using an active cloud microphysical model. *Monthly Notices of the Royal Astronomical Society*, 496(4):4760–4768.

Halsey, G., Hillman, J., Nadler, S., and Jennings, D. (1988). Temperature dependence of the hydrogen-broadening coefficient for the $\nu 9$ fundamental of ethane. *Journal of Quantitative Spectroscopy and Radiative Transfer*, 39(6):429–434.

Hammel, H., Lynch, D., Russell, R., Sitko, M., Bernstein, L., and Hewagama, T. (2006). Mid-infrared ethane emission on neptune and uranus. *The Astrophysical Journal*, 644(2):1326.

Hammel, H., Rages, K., Lockwood, G., Karkoschka, E., and de Pater, I. (2001). New measurements of the winds of uranus. *Icarus*, 153(2):229–235.

Hammel, H. B. and Lockwood, G. (2007). Long-term atmospheric variability on uranus and neptune. *Icarus*, 186(1):291–301.

Hammel, H. B., Sitko, M. L., Lynch, D. K., Orton, G., Russell, R., Geballe, T., and De Pater, I. (2007). Distribution of ethane and methane emission on neptune. *The Astronomical Journal*, 134(2):637.

Hammel, H. B., Sromovsky, L. A., Fry, P. M., Rages, K., Showalter, M., Pater, I. D., Dam, M. A. V., and Lebeau, R. P. (2009). The Dark Spot in the atmosphere of Uranus in 2006 : Discovery , description , and dynamical simulations. *Icarus*, 201(1):257–271.

Hanel, R., Conrath, B., Flasar, F. M., Kunde, V., Maguire, W., Horn, L., and Schulte, P. (1986). Infared Observations of the Uranian System. *Science Magazine*, 2931(1966).

Helled, R. and Bodenheimer, P. (2014). The formation of uranus and neptune: Challenges and implications for intermediate-mass exoplanets. *The Astrophysical Journal*, 789(1):69.

Helled, R. and Fortney, J. J. (2020). The interiors of uranus and neptune: current understanding and open questions. *Philosophical Transactions of the Royal Society A*, 378(2187):20190474.

Helled, R., Nettelmann, N., and Guillot, T. (2020). Uranus and neptune: origin, evolution and internal structure. *Space Science Reviews*, 216(3):1–26.

Herbert, F. and Sandel, B. R. (1999). Ultraviolet observations of uranus and neptune. *Planetary and space science*, 47(8-9):1119–1139.

Herbert, F., Sandel, B. R., Yelle, R. V., Holberg, J. B., Broadfoot, A. L., Shemansky, D. E., Atreya, S. K., and Romani, P. N. (1987). The upper atmosphere of uranus: Euv occultations observed by voyager 2. *Journal of Geophysical Research: Space Physics*, 92(A13):15093–15109.

Herzberg, G. (1952). Spectroscopic evidence of molecular hydrogen in the atmospheres of uranus and neptune. *The Astrophysical Journal*, 115:337–340.

Hofstadter, M., Simon, A., Atreya, S., Banfield, D., Fortney, J. J., Hayes, A., Hedman, M., Hospodarsky, G., Mandt, K., Masters, A., et al. (2019). Uranus and neptune missions: A study in advance of the next planetary science decadal survey. *Planetary and Space Science*, 177:104680.

Hofstadter, M. D. and Butler, B. J. (2003). Seasonal change in the deep atmosphere of uranus. *Icarus*, 165(1):168–180.

Houck, J. R., Roellig, T. L., Van Cleve, J., Forrest, W. J., Herter, T., Lawrence, C. R., Matthews, K., Reitsema, H. J., Soifer, B. T., Watson, D. M., et al. (2004). The infrared spectrograph (irs) on the spitzer space telescope. *The Astrophysical Journal Supplement Series*, 154(1):18.

Hueso, R., De Pater, I., Simon, A., Sánchez-Lavega, A., Delcroix, M., Wong, M., Tollefson, J., Baranec, C., de Kleer, K., Luszcz-Cook, S., et al. (2017). Neptune long-lived atmospheric features in 2013–2015 from small (28-cm) to large (10-m) telescopes. *Icarus*, 295:89–109.

Hueso, R. and Sánchez-Lavega, A. (2019). Atmospheric dynamics and vertical structure of uranus and neptune's weather layers. *Space Science Reviews*, 215(8):52.

Irwin, P. (2009). *Giant planets of our solar system: atmospheres, composition, and structure*. Springer Science & Business Media.

Irwin, P., Lellouch, E., De Bergh, C., Courtin, R., Bézard, B., Fletcher, L., Orton, G., Teanby, N., Calcutt, S., Tice, D., et al. (2014). Line-by-line analysis of neptune's near-ir spectrum observed with gemini/nifs and vlt/crires. *Icarus*, 227:37–48.

Irwin, P., Teanby, N., De Kok, R., Fletcher, L., Howett, C., Tsang, C., Wilson, C., Calcutt, S., Nixon, C., and Parrish, P. (2008). The nemesis planetary atmosphere radiative transfer and retrieval tool. *Journal of Quantitative Spectroscopy and Radiative Transfer*, 109(6):1136–1150.

Irwin, P. G., Fletcher, L. N., Teanby, N. A., Orton, G. S., Toledo, D., Braude, A., and Bezard, B. (2019a). Latitudinal variation in abundance of hydrogen sulphide (h2s) and methane (ch4) in the atmosphere of neptune. In *Geophysical Research Abstracts*, volume 21.

Irwin, P. G., Toledo, D., Garland, R., Teanby, N. A., Fletcher, L. N., Orton, G. A., and Bézard, B. (2018). Detection of hydrogen sulfide above the clouds in uranus's atmosphere. *Nature Astronomy*, 2(5):420–427.

Irwin, P. G., Toledo, D., Garland, R., Teanby, N. A., Fletcher, L. N., Orton, G. S., and Bézard, B. (2019b). Probable detection of hydrogen sulphide (h2s) in neptune's atmosphere. *Icarus*, 321:550–563.

Irwin, P. G., Wong, M. H., Simon, A. A., Orton, G., and Toledo, D. (2017). Hst/wfc3 observations of uranus' 2014 storm clouds and comparison with vlt/sinfoni and irtf/spex observations. *Icarus*, 288:99–119.

Jacquinet-Husson, N., Armante, R., Scott, N., Chédin, A., Crépeau, L., Boutammine, C., Bouhdaoui, A., Crevoisier, C., Capelle, V., Boonne, C., et al. (2016). The 2015 edition of the geisa spectroscopic database. *Journal of Molecular Spectroscopy*, 327:31–72.

Jacquinet-Husson, N., Crepeau, L., Armante, R., Boutammine, C., Chédin, A., Scott, N., Crevoisier, C., Capelle, V., Boone, C., Poulet-Crovisier, N., et al. (2011). The 2009 edition of the geisa spectroscopic database. *Journal of Quantitative Spectroscopy and Radiative Transfer*, 112(15):2395–2445.

Jacquinet-Husson, N., Scott, N., Chédin, A., and Chursin, A. (2003). The geisa spectroscopic database system revisited for iasi direct radiative transfer modelling. *Atmos. Oceanic Opt*, 16(3):256–261.

Karkoschka, E. (2011). Neptune's rotational period suggested by the extraordinary stability of two features. *Icarus*, 215(1):439–448.

Karkoschka, E. (2015). Uranus' southern circulation revealed by voyager 2: unique characteristics. *Icarus*, 250:294–307.

Karkoschka, E. and Tomasko, M. (2009). The haze and methane distributions on uranus from hst-stis spectroscopy. *Icarus*, 202(1):287–309.

Karkoschka, E. and Tomasko, M. G. (2011). The haze and methane distributions on neptune from hst–stis spectroscopy. *Icarus*, 211(1):780–797.

Klein, M. and Hofstadter, M. (2006). Long-term variations in the microwave brightness temperature of the uranus atmosphere. *Icarus*, 184(1):170–180.

Lacis, A. A. and Oinas, V. (1991). A description of the correlated k distribution method for modeling nongray gaseous absorption, thermal emission, and multiple scattering in vertically inhomogeneous atmospheres. *Journal of Geophysical Research: Atmospheres*, 96(D5):9027–9063.

Lamy, L., Prangé, R., Hansen, K., Clarke, J., Zarka, P., Cecconi, B., Aboudarham, J., André, N., Branduardi-Raymont, G., Gladstone, R., et al. (2012). Earth-based detection of uranus' aurorae. *Geophysical Research Letters*, 39(7).

Lecluse, C., Robert, F., Gautier, D., and Guiraud, M. (1996). Deuterium enrichment in giant planets. *Planetary and space science*, 44(12):1579–1592.

Lellouch, E., Hartogh, P., Feuchtgruber, H., Vandenbussche, B., de Graauw, T., Moreno, R., Jarchow, C., Cavalié, T., Orton, G., Banaszkiewicz, M., et al. (2010). First results of herschel-pacs observations of neptune. *Astronomy & astrophysics*, 518:L152.

Li, C., Le, T., Zhang, X., and Yung, Y. L. (2018). A high-performance atmospheric radiation package: With applications to the radiative energy budgets of giant planets. *Journal of Quantitative Spectroscopy and Radiative Transfer*, 217:353–362.

Lindal, G. F. (1992). The atmosphere of neptune-an analysis of radio occultation data acquired with voyager 2. *The Astronomical Journal*, 103:967–982.

Lindal, G. F., Lyons, J. R., Sweetnam, D. N., Eshleman, V. R., Hinson, D. P., and Tyler, G. L. (1987). The atmosphere of uranus: Results of radio occultation measurements with voyager 2. *Journal of Geophysical Research: Space Physics*, 92(A13):14987–15001.

Line, M. R., Wolf, A. S., Zhang, X., Knutson, H., Kammer, J. A., Ellison, E., Deroo, P., Crisp, D., and Yung, Y. L. (2013). A systematic retrieval analysis of secondary eclipse spectra. i. a comparison of atmospheric retrieval techniques. *The Astrophysical Journal*, 775(2):137.

Lunine, J. I. (1993). The atmospheres of uranus and neptune. *Annual review of astronomy and astrophysics*, 31(1):217–263.

Margolis, J. S. (1993). Measurement of hydrogen-broadened methane lines in the $\nu 4$ band at 296 and 200 k. *Journal of Quantitative Spectroscopy and Radiative Transfer*, 50(4):431–441.

Marten, A., Matthews, H., Owen, T., Moreno, R., Hidayat, T., and Biraud, Y. (2005). Improved constraints on neptune's atmosphere from submillimetre-wavelength observations. *Astronomy & Astrophysics*, 429(3):1097–1105.

Martin, S. C., de Pater, I., and Marcus, P. (2012). Neptune's zonal winds from near-ir keck adaptive optics imaging in august 2001. *Astrophysics and Space Science*, 337(1):65–78.

Marty, B., Alexander, C. M. O., and Raymond, S. N. (2013). Primordial origins of earth's carbon. *Reviews in Mineralogy and Geochemistry*, 75(1):149–181.

Meadows, V. S., Orton, G., Line, M., Liang, M.-C., Yung, Y. L., Van Cleve, J., and Burgdorf, M. J. (2008). First spitzer observations of neptune: Detection of new hydrocarbons. *Icarus*, 197(2):585–589.

Melin, H. (2020). The upper atmospheres of uranus and neptune. *Philosophical Transactions of the Royal Society A*, 378(2187):20190478.

Molter, E. M., de Pater, I., Luszcz-Cook, S., Tollefson, J., Sault, R. J., Butler, B., and de Boer, D. (2020). Tropospheric composition and circulation of uranus with alma and the vla. *arXiv preprint arXiv:2010.11154*.

Moses, J., Cavalié, T., Fletcher, L., and Roman, M. (2020). Atmospheric chemistry on uranus and neptune. *Philosophical Transactions of the Royal Society A*, 378(2187):20190477.

Moses, J., Fouchet, T., Bézard, B., Gladstone, G., Lellouch, E., and Feuchtgruber, H. (2005). Photochemistry and diffusion in jupiter's stratosphere: constraints from iso observations and comparisons with other giant planets. *Journal of Geophysical Research: Planets*, 110(E8).

Moses, J. I., Armstrong, E. S., Fletcher, L. N., Friedson, A. J., Irwin, P. G., Sinclair, J. A., and Hesman, B. E. (2015). Evolution of stratospheric chemistry in the saturn storm beacon region. *Icarus*, 261:149–168.

Moses, J. I., Bézard, B., Lellouch, E., Gladstone, G. R., Feuchtgruber, H., and Allen, M. (2000). Photochemistry of saturn's atmosphere: I. hydrocarbon chemistry and comparisons with iso observations. *Icarus*, 143(2):244–298.

Moses, J. I., Fletcher, L. N., Greathouse, T. K., Orton, G. S., and Hue, V. (2018). Seasonal stratospheric photochemistry on Uranus and Neptune. *Icarus*, 307:124–145.

Moses, J. I. and Poppe, A. R. (2017). Dust ablation on the giant planets: Consequences for stratospheric photochemistry. *Icarus*, 297:33–58.

Moses, J. I., Rages, K., and Pollack, J. B. (1995). An analysis of neptune's stratospheric haze using high-phase-angle voyager images. *Icarus*, 113(2):232–266.

Mousis, O., Atkinson, D. H., Cavalié, T., Fletcher, L., Amato, M., Aslam, S., Ferri, F., Renard, J.-B., Spilker, T., Venkatapathy, E., et al. (2018). Scientific rationale for uranus and neptune in situ explorations. *Planetary and Space Science*, 155:12–40.

Nettelmann, N., Wang, K., Fortney, J. J., Hamel, S., Yellamilli, S., Bethkenhagen, M., and Redmer, R. (2016). Uranus evolution models with simple thermal boundary layers. *Icarus*, 275:107–116.

Norwood, J., Hammel, H., Milam, S., Stansberry, J., Lunine, J., Chanover, N., Hines, D., Sonneborn, G., Tiscareno, M., Brown, M., et al. (2014). Solar system observations with jwst. *ArXiv e-prints*, 1403.

Norwood, J., Moses, J., Fletcher, L. N., Orton, G., Irwin, P. G., Atreya, S., Rages, K., Cavalié, T., Sánchez-Lavega, A., Hueso, R., et al. (2016). Giant planet observations with the james webb space telescope. *Publications of the Astronomical Society of the Pacific*, 128(959):018005.

Orton, G., Griffin, M. J., Ade, P. A., Nolt, I., Radostitz, J., Robson, E., and Gear, W. K. (1986). Submillimeter and millimeter observations of uranus and neptune. *Icarus*, 67(2):289–304.

Orton, G. S., Aitken, D. K., Smith, C., Roche, P. F., Caldwell, J., and Snyder, R. (1987). The spectra of uranus and neptune at 8–14 and 17–23 μm. *Icarus*, 70(1):1–12.

Orton, G. S., Fletcher, L. N., Encrenaz, T., Leyrat, C., Roe, H. G., Fujiyoshi, T., and Pantin, E. (2015). Thermal imaging of Uranus: Upper-tropospheric temperatures one season after Voyager. *Icarus*, 260:94–102.

Orton, G. S., Fletcher, L. N., Liu, J., Schneider, T., Yanamandra-Fisher, P. A., de Pater, I., Edwards, M., Geballe, T. R., Hammel, H. B., Fujiyoshi, T., et al. (2012). Recovery and characterization of neptune's near-polar stratospheric hot spot. *Planetary and Space Science*, 61(1):161–167.

Orton, G. S., Fletcher, L. N., Moses, J. I., Mainzer, A. K., Hines, D., Hammel, H. B., Martin-Torres, F. J., Burgdorf, M., Merlet, C., and Line, M. R. (2014a). Mid-infrared spectroscopy of uranus from the spitzer infrared spectrometer: 1. determination of the mean temperature structure of the upper troposphere and stratosphere. *Icarus*, 243:494–513.

Orton, G. S., Gustafsson, M., Burgdorf, M., and Meadows, V. (2007). Revised ab initio models for h2–h2 collision-induced absorption at low temperatures. *Icarus*, 189(2):544–549.

Orton, G. S., Lacy, J. H., Achtermann, J. M., Parmar, P., and Blass, W. E. (1992). Thermal spectroscopy of neptune: The stratospheric temperature, hydrocarbon abundances, and isotopic ratios. *Icarus*, 100(2):541–555.

Orton, G. S., Moses, J. I., Fletcher, L. N., Mainzer, A. K., Hines, D., Hammel, H. B., Martin-Torres, J., Burgdorf, M., Merlet, C., and Line, M. R. (2014b). Mid-infrared spectroscopy of uranus from the spitzer infrared spectrometer: 2. determination of the mean composition of the upper troposphere and stratosphere. *Icarus*, 243:471–493.

Pearl, J. and Conrath, B. (1991). The albedo, effective temperature, and energy balance of neptune, as determined from voyager data. *Journal of Geophysical Research: Space Physics*, 96(S01):18921–18930.

Pearl, J., Conrath, B., Hanel, R., Pirraglia, J., and Coustenis, A. (1990). The albedo, effective temperature, and energy balance of uranus, as determined from voyager iris data. *Icarus*, 84(1):12–28.

Podolak, M., Helled, R., and Schubert, G. (2019). Effect of non-adiabatic thermal profiles on the inferred compositions of uranus and neptune. *Monthly Notices of the Royal Astronomical Society*, 487(2):2653–2664.

Reinhardt, C., Chau, A., Stadel, J., and Helled, R. (2020). Bifurcation in the history of uranus and neptune: the role of giant impacts. *Monthly Notices of the Royal Astronomical Society*, 492(4):5336–5353.

Robinson, G. N., Zahniser, M. S., Freedman, A., and Nelson Jr, D. D. (1996). Pressure-broadened linewidth measurements in the $\nu 2$ band of the ch3 radical. *Journal of Molecular Spectroscopy*, 176(2):337–341.

Rodgers, C. D. (2000). *Inverse methods for atmospheric sounding: theory and practice*, volume 2. World scientific.

Roman, M. T., Banfield, D., and Gierasch, P. J. (2018). Aerosols and methane in the ice giant atmospheres inferred from spatially resolved, near-infrared spectra: I. Uranus, 2001 – 2007. *Icarus*, 310:54–76.

Roman, M. T., Fletcher, L. N., Orton, G. S., Rowe-Gurney, N., and Irwin, P. G. (2020). Uranus in northern midspring: Persistent atmospheric temperatures and circulations inferred from thermal imaging. *The Astronomical Journal*, 159(2):45.

Romani, P. N. and Atreya, S. K. (1988). Methane photochemistry and haze production on neptune. *Icarus*, 74(3):424–445.

Romani, P. N., Bishop, J., Bézard, B., and Atreya, S. (1993). Methane photochemistry on neptune: Ethane and acetylene mixing ratios and haze production. *Icarus*, 106(2):442–463.

Rothman, L. S., Gordon, I. E., Babikov, Y., Barbe, A., Benner, D. C., Bernath, P. F., Birk, M., Bizzocchi, L., Boudon, V., Brown, L. R., et al. (2013). The hitran 2012 molecular spectroscopic database. *Journal of Quantitative Spectroscopy and Radiative Transfer*, 130:4–50.

Rothman, L. S., Gordon, I. E., Barbe, A., Benner, D. C., Bernath, P. F., Birk, M., Boudon, V., Brown, L. R., Campargue, A., Champion, J.-P., et al. (2009). The hitran 2008 molecular spectroscopic database. *Journal of Quantitative Spectroscopy and Radiative Transfer*, 110(9-10):533–572.

Rowe-Gurney, N., Fletcher, L. N., Orton, G. S., Roman, M. T., Mainzer, A., Moses, J. I., De Pater, I., and Irwin, P. G. (2021). Longitudinal variations in the stratosphere of uranus from the spitzer infrared spectrometer. *Icarus*, 365:114506.

Sanchez-Lavega, A. (2010). *An introduction to planetary atmospheres.* Taylor & Francis.

Sánchez-Lavega, A., Pérez-Hoyos, S., and Hueso, R. (2004). Clouds in planetary atmospheres: A useful application of the clausius–clapeyron equation. *American Journal of Physics*, 72(6):767–774.

Sánchez-Lavega, A., Sromovsky, L., Showman, A. P., Del Genio, A., Young, R., Hueso, R., Garcia-Melendo, E., Kaspi, Y., Orton, G. S., Barrado-Izagirre, N., et al. (2019). *Gas Giants*, chapter 4. Cambridge University Press.

Schulz, B., Encrenaz, T., Bézard, B., Romani, P., Lellouch, E., and Atreya, S. (1999). Detection of c2h4 in neptune from iso/pht-s observations. *Astronomy and Astrophysics*, 350:L13–L17.

Simon, A., Wong, M., and Hsu, A. (2019). Formation of a new great dark spot on neptune in 2018. *Geophysical Research Letters*, 46(6):3108–3113.

Simon, A. A., Rowe, J. F., Gaulme, P., Hammel, H. B., Casewell, S. L., Fortney, J. J., Gizis, J. E., Lissauer, J. J., Morales-Juberias, R., Orton, G. S., et al. (2016). Neptune's dynamic atmosphere from kepler k2 observations: implications for brown dwarf light curve analyses. *The Astrophysical Journal*, 817(2):162.

Sinclair, J., Orton, G., Fletcher, L., Roman, M., de Pater, I., Encrenaz, T., Hammel, H., Giles, R., Velusamy, T., Moses, J., et al. (2020a). Spatial structure in neptune's 7.90-μm stratospheric ch4 emission, as measured by vlt-visir. *Icarus*, page 113748.

Sinclair, J. A., Greathouse, T. K., Giles, R. S., Antuñano, A., Moses, J. I., Fouchet, T., Bézard, B., Tao, C., Martín-Torres, J., Clark, G. B., et al. (2020b). Spatial variations in the altitude of the ch4 homopause at jupiter's mid-to-high latitudes, as constrained from irtf-texes spectra. *The Planetary Science Journal*, 1(3):85.

Sloan, G. (2004). Irs-tr 04002: Discontinuities between the low-resolution modules on the irs. *Infrared Spectrograph Technical Report Series.*

Sloan, G., Herter, T., Charmandaris, V., Sheth, K., Burgdorf, M., and Houck, J. (2014). Spectral calibration in the mid-infrared: Challenges and solutions. *The Astronomical Journal*, 149(1):11.

Smith, B. A., Soderblom, L., Beebe, R., Bliss, D., Boyce, J., Brahic, A., Briggs, G., Brown, R. H., Collins, S., Cook, A., et al. (1986). Voyager 2 in the uranian system: Imaging science results. *Science*, 233(4759):43–64.

Smith, B. A., Soderblom, L. A., Banfield, D., Basilevsky, A., Beebe, R., Bollinger, K., Boyce, J., Brahic, A., Briggs, G., Brown, R., et al. (1989). Voyager 2 at neptune: Imaging science results. *Science*, 246(4936):1422–1449.

Smith, M. D. and Gierasch, P. J. (1995). Convection in the outer planet atmospheres including ortho-para hydrogen conversion. *Icarus*, 116(1):159–179.

Sromovsky, L., de Pater, I., Fry, P., Hammel, H., and Marcus, P. (2015). High s/n keck and gemini ao imaging of uranus during 2012–2014: new cloud patterns, increasing activity, and improved wind measurements. *Icarus*, 258:192–223.

Sromovsky, L., Fry, P., and Baines, K. (2002). The unusual dynamics of northern dark spots on neptune. *Icarus*, 156(1):16–36.

Sromovsky, L., Hammel, H., de Pater, I., Fry, P., Rages, K., Showalter, M., Merline, W., Tamblyn, P., Neyman, C., Margot, J.-L., Fang, J., Colas, F., Dauvergne, J.-L., Gómez-Forrellad, J., Hueso, R., Sánchez-Lavega, A., and Stallard, T. (2012). Episodic bright and dark spots on uranus. *Icarus*, 220(1):6 – 22.

Sromovsky, L., Karkoschka, E., Fry, P., Hammel, H., de Pater, I., and Rages, K. (2014). Methane depletion in both polar regions of uranus inferred from hst/stis and keck/nirc2 observations. *Icarus*, 238:137–155.

Sromovsky, L. A. and Fry, P. M. (2005). Dynamics of cloud features on Uranus. *Icarus*, 179(2):459–484.

Sromovsky, L. A., Fry, P. M., Hammel, H. B., Ahue, W. M., de Pater, I., Rages, K. A., Showalter, M. R., and van Dam, M. A. (2009). Uranus at equinox: Cloud morphology and dynamics. *Icarus*, 203(1):265–286.

Sromovsky, L. A., Fry, P. M., Hammel, H. B., de Pater, I., Rages, K. A., and Showalter, M. R. (2007). Dynamics, evolution, and structure of Uranus' brightest cloud feature. *Icarus*, 192(2):558–575.

Sromovsky, L. A., Fry, P. M., and Kim, J. H. (2011). Methane on Uranus: The case for a compact CH4 cloud layer at low latitudes and a severe CH4 depletion at high-latitudes based on re-analysis of Voyager occultation measurements and STIS spectroscopy. *Icarus*, 215(1):292–312.

Sromovsky, L. A., Limaye, S. S., and Fry, P. M. (1993). Dynamics of neptune's major cloud features. *Icarus*, 105(1):110–141.

Stancu, G., Röpcke, J., and Davies, P. (2005). Line strengths and transition dipole moment of the ν 2 fundamental band of the methyl radical. *The Journal of chemical physics*, 122(1):014306.

Stone, E. and Miner, E. (1986). The voyager 2 encounter with the uranian system. *Science*, 233(4759):39–43.

Stone, E. and Miner, E. (1989). The voyager 2 encounter with the neptunian system. *Science*, 246(4936):1417–1421.

Stratman, P. W., Showman, A., Dowling, T., and Sromovsky, L. (2001). Epic simulations of bright companions to neptune's great dark spots. *Icarus*, 151(2):275–285.

STScI (2016). *JWST User Documentation*.

Taylor, F. W. (2005). *Elementary climate physics*, volume 234. Oxford University Press Oxford.

Taylor, F. W. (2010). *Planetary Atmospheres*. Oxford University Press.

Teanby, N., Irwin, P., Moses, J., and Helled, R. (2020). Neptune and uranus: ice or rock giants? *Philosophical Transactions of the Royal Society A*, 378(2187):20190489.

Teanby, N. A. and Irwin, P. G. J. (2013). An External Origin for Carbon Monoxide on Uranus from Herschel/SPIRE. *The Astrophysical Journal Letters*, 49.

Teanby, N. A., Irwin, P. G. J., Nixon, C. A., Courtin, R., Swinyard, B. M., Moreno, R., Lellouch, E., Rengel, M., and Hartogh, P. (2013). Constraints on Titan's middle atmosphere ammonia abundance from Herschel / SPIRE sub-millimetre spectra. *Planetary and Space Science*, 75:136–147.

Toledo, D., Irwin, P. G., Rannou, P., Fletcher, L. N., Teanby, N. A., Wong, M. H., and Orton, G. S. (2020). Constraints on neptune's haze structure and formation from vlt observations in the h-band. *Icarus*, 350:113808.

Toledo, D., Irwin, P. G., Teanby, N. A., Simon, A. A., Wong, M. H., and Orton, G. S. (2018). Uranus's northern polar cap in 2014. *Geophysical Research Letters*, 45(11):5329–5335.

Tollefson, J., de Pater, I., Luszcz-Cook, S., and DeBoer, D. (2019). Neptune's latitudinal variations as viewed with alma. *The Astronomical Journal*, 157(6):251.

Tollefson, J., de Pater, I., Marcus, P. S., Luszcz-Cook, S., Sromovsky, L. A., Fry, P. M., Fletcher, L. N., and Wong, M. H. (2018). Vertical wind shear in neptune's upper atmosphere explained with a modified thermal wind equation. *Icarus*, 311:317–339.

Trilling, D. E., Lisse, C., Cruikshank, D. P., Emery, J. P., Fernández, Y., Fletcher, L. N., Hamilton, D. P., Hammel, H. B., Harris, A. W., Mueller, M., et al. (2020). Spitzer's solar system studies of asteroids, planets and the zodiacal cloud. *Nature Astronomy*, 4(10):940–946.

Vander Auwera, J., Moazzen-Ahmadi, N., and Flaud, J.-M. (2007). Toward an accurate database for the 12 μm region of the ethane spectrum. *The Astrophysical Journal*, 662(1):750.

Varanasi, P. (1992). Intensity and linewidth measurements in the 13.7 μm fundamental bands of 12c2h2 and 12c13ch2 at planetary atmospheric temperatures. *Journal of Quantitative Spectroscopy and Radiative Transfer*, 47(4):263–274.

Vazan, A. and Helled, R. (2020). Explaining the low luminosity of uranus: a self-consistent thermal and structural evolution. *Astronomy & Astrophysics*, 633:A50.

Wells, M., Pel, J.-W., Glasse, A., Wright, G., Aitink-Kroes, G., et al. (2015). The mid-infrared instrument for the james webb space telescope, vi: The medium resolution spectrometer. *Publications of the Astronomical Society of the Pacific*, 127(953):646.

Werner, M. W., Roellig, T., Low, F., Rieke, G. H., Rieke, M., Hoffmann, W., Young, E., Houck, J., Brandl, B., Fazio, G., et al. (2004). The spitzer space telescope mission. *The Astrophysical Journal Supplement Series*, 154(1):1.

Wright, D. (1987). Uranus in antiquity. *Quarterly Journal of the Royal Astronomical Society*, 28:79.

Yelle, R. V., Herbert, F., Sandel, B. R., Vervack Jr, R. J., and Wentzel, T. M. (1993). The distribution hydrocarbons in neptune's upper atmosphere. *Icarus*, 104(1):38–59.